

National Technical University of Ukraine “Igor Sikorsky Kyiv Polytechnic Institute”

Ministry of Education and Science of Ukraine

University of Palermo

Ministry of Universities and Research of the Republic of Italy

National Technical University of Ukraine “Igor Sikorsky Kyiv Polytechnic Institute”

Ministry of Education and Science of Ukraine

Qualifying scientific work on manuscript rights

KOVINCHUK IRYNA VASYLIVNA

UDC [546.711-3+549.623.9]-022.532:544.526.5](043.3)

DISSERTATION

COMPOSITES OF MANGANESE OXIDES AND OXIDEHYDROXIDES WITH HALLOYSITE AS DEGRADATION PHOTOCATALYSTS

161 – Chemical technologies and engineering

16 – Chemical and bioengineering

Applying for the Doctor of Philosophy degree

The dissertation contains the results of own research. The use of ideas, results and texts of other authors are linked to the corresponding source

_____ I.V. Kovinchuk

Research supervisors:

Sokolskyi Heorhii Volodymyrovych, Doctor of Chemical Sciences, professor

Lazzara Giuseppe, Doctor of Chemical Sciences, professor

Kyiv – 2025

ANNOTATION

Kovinchuk I.V. Composites of manganese oxides and oxidehydroxides with halloysite as degradation photocatalysts. – Qualification scientific work in the form of a manuscript. Joint doctoral thesis for the degree of Doctor of Philosophy in specialty 161 “Chemical Technologies and Engineering”. – National Technical University of Ukraine “Igor Sikorsky Kyiv Polytechnic Institute”, Ministry of Education and Science of Ukraine and Doctor of Philosophy in “Physical and Chemical Sciences”. – University of Palermo (Italy), Kyiv, 2025.

The dissertation is devoted to the study of the influence of synthesis conditions, phase composition, and structure on the functionality of composites based on manganese oxides and oxidehydroxides for the photocatalytic degradation of model organic compounds: aqueous solutions of dyes and polyethene films under UV- and Vis. light irradiation. The work considers the relationship between synthesis conditions and phase composition, morphology, band gap width, and specific surface area of the products with their efficiency as photocatalysts. In addition, the influence of halloysite aluminosilicate nanotubes on the physicochemical properties and photocatalytic activity of composite materials, as well as the behavior of manganese oxides and oxyhydroxides relative towards their surface, was investigated.

The photocatalytic activity of standard materials MnO_2 , TiO_2 and their mechanical mixture was studied at the photocatalytic degradation of polyethylene films under the influence of UV- and visible light irradiation. This study included a comparison of the mass loss of containing photocatalyst PE films with the pure film. The $\text{MnO}_2/\text{TiO}_2$ mixture demonstrated the highest efficiency with a film mass loss of 21.3% after 90 hours of irradiation. The degradation mechanism was evaluated by the relative intensity of the peaks of the FTIR spectra corresponding to the carbonyl, hydroxyl and ether indices. It was established that the mechanical mixture of $\gamma\text{-MnO}_2$ with TiO_2 causes synergy action with a greater degree of degradation at all intermediate stages of PE oxidation since the vibrations of functional groups of the intermediates are more intense compared with the PE/TiO_2 film. In addition, the carbonyl index shows a relatively more significant accumulation of the corresponding groups. Therefore, the conversion occurs much faster

than in other samples at all stages, which indicates the nonspecificity of the catalytic action of the formed radicals towards PE oxidation intermediates on the γ -MnO₂ photocatalyst with TiO₂.

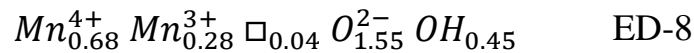
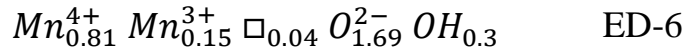
It was found that during chemical precipitation from MnSO₄ solution using hydrogen peroxide as an oxidant composite material with different ratios of manganese oxides and oxidehydroxides with valences from +2 to +4 are formed. The medium's acidity and the presence of NH₄⁺ dopants in the reaction medium play a decisive role. It was shown that at pH = 10 the main phase formed are the low-valent manganese oxides hausmannite Mn₃O₄ in the presence of excess ammonium ions, and bixbyite Mn₂O₃ in its absence. While at lower pH values = 5-7 the main product is manganite γ -MnOOH and groutite α -MnOOH with traces of manganese oxide 4+ in excess NH₄⁺. The nature of the interaction of manganese oxides with the surface of halloysite nanotubes was studied by the transmission electron microscopy. It was found that in TEM images of samples synthesized in the presence of an excess of ammonium ions in the reaction mixture (CS-2 and CS-6), a darkening of the lumen area of the nanotubes is observed, which may indicate its filling, while in the absence of an excess of ammonium (CS-1 and CS-7), particles of manganese oxides and oxidehydroxides decorate the outer surface of halloysite. The measured specific surface area of the synthesized samples is by 3-3.5 times higher (55-66 m²/g) compared to the standard MnO₂ PCP sample. At the same time, the presence of halloysite nanotubes did not significantly affect this parameter. The diffuse reflection spectra were recorded and the band gap width using the Tauk plot was calculated. The band gap values of $E_g = 2.28$ -2.38 eV were established for samples CS-5-CS-9. In turn, the values of 2.52 and 2.7 eV were measured for the lower-valence samples CS-1 and CS-2, respectively. Thus, in accordance with semiconductor properties of these composites, their potential photocatalytic activity belongs to the visible light range. The dynamic light scattering method data on the average size of composite material aggregates and the TEM image analysis data of sizes of individual nanoparticles were evaluated. In both cases, the synthesized samples exhibit smaller sizes compared to the standard MnO₂ PCP sample, ranging between 117–175 nm for aggregates and 7–12 nm for nanoparticles.

A series of electrochemically deposited samples was synthesised to expand the range of phase states of the materials studied. The influence of acidity and the presence of dopant ions of NH_4^+ and Cr^{3+} on the synthesised samples' morphology, phase composition, and physicochemical properties was investigated. X-ray diffraction analysis confirmed the formation of composite oxide materials consisting of α -, γ -, ε - and δ -phases of MnO_2 in various proportions. It was established that NH_4^+ ions in excess stabilise the electrodeposition of hollandite, α -, and birnessite, δ -, phases of MnO_2 , while their absence favours the formation of the ramsdellite γ - and ε - MnO_2 phases. The samples with a predominant hollandite phase of MnO_2 demonstrated the highest specific surface area, reaching a maximum of $215 \text{ m}^2/\text{g}$ for sample ED-12, indicating the achievement of a diffusion-controlled deposition regime. In comparison, samples with a predominant ε - MnO_2 phase exhibited smaller surface areas, specifically $65.65 \text{ m}^2/\text{g}$ for ED-13 and $82.88 \text{ m}^2/\text{g}$ for ED-2. The particle size distribution and morphology of MnO_2 were evaluated using scanning electron microscopy images. For samples ED-2 and ED-6, which are composites of γ - and ε - MnO_2 , plate-like formations with an average nanoparticle size of $70 \pm 15 \text{ nm}$ were observed. Samples with a predominant alpha-phase exhibited a needle-like morphology.

The synthesized manganese dioxide electrodeposited (ED) samples are semiconductors with a band gap width ranging from 2.16 to 2.36 eV. Doping with Cr^{3+} ions reduced the band gap by approximately 0.3–0.5 eV due to introducing new electron donor levels. The Mulliken electronegativity and the positions of the valence and conduction bands were calculated for the electro-synthesized samples. Sample ED-6 demonstrated a conduction band position at 0.12 eV (vs the standard hydrogen electrode, SHE) and a valence band at 2.49 eV (SHE), with the broadest band gap of 3.36 eV, indicating the potential of this sample for photocatalytic water splitting to produce hydrogen.

Differential scanning calorimetry combined with mass spectrometry was performed on selected electro-synthesized samples. This analysis enabled the identification of the thermal decomposition products and temperature intervals of their release. These findings provide insight into defect levels based on the Ruetschi cation vacancy model.

According to this model, the content of cation vacancies (\square) in manganese dioxide samples, predominantly of the ramsdellite modification, can be estimated. As energetically non-equivalent positions, these crystal lattice defects being in the material's surface layers can significantly enhance its catalytic activity. The calculated formulas for the electrodeposited samples are presented below.



Both γ -MnO₂ (ED-6) and α -MnO₂ (ED-8) Samples (see the names of Samples in the text below) exhibit the same content of cation vacancies; however, ED-8 is distinguished by two times higher Mn³⁺ content.

It was established that the composite samples of low-valent manganese oxides, CS-2 and CS-1, exhibit the highest photocatalytic activity toward the cationic dye Methylene Blue. This is likely due to the presence of halloysite nanotubes in the composites, which feature is a negatively charged outer surface. This provides a synergistic effect, facilitating pollutant degradation by more efficient transport of the dye from the solution bulk to the photocatalyst surface. For the anionic dye Congo Red, the highest efficiency was demonstrated by sample CS-8, which consists of higher valent α -MnOOH and γ -/ β -MnO₂. This sample has the narrowest band gap (1.99 eV) among all chemically synthesized samples. The further insight was made by analysis of the band gap potential diagrams of CS-series of samples and MO-diagram with HOMO and LUMO of a dye. It was revealed that CS-1, CS-2 samples have well aligned E_C edges of HNTs, Mn_xO_y and LUMO MB levels. It can be suggested that this feature is responsible for the positive influence of HNT's surface decoration by Mn_xO_y on photocatalytic activity of MB degradation due to new option of direct electron transfer of photoelectron from E_C of both HNTs & Mn_xO_y and following MB dye reduction. It is also evident from this diagram for CR dye that only CS-8 Sample has favorably aligned E_V to HOMO level of CR dye and, probably, this feature can be responsible for the faster direct oxidation of CR by holes from the valence band of CS-8 as a photocatalyst. Thus, distinctly active behavior of CS-

1&CS-2 photocatalysts toward MB degradation as well as CS-8 Sample high activity toward CR destruction can be explained by the semiconducting properties of these photocatalysts.

According to the results obtained, it was proposed to apply the materials synthesized in this work for photodegradable coatings on PE surface, compared to their incorporation into the bulk of a film. A method of attaching nanomaterials onto polyethylene films through the partial dissolution of their surface has been developed. The introduction of 2.59% by mass of halloysite nanotubes was achieved when immersing the PE film in a suspension of HNTs in cyclohexane at 50°C for 120 s, and 2.51% at a suspension temperature of 60°C for 60 s. The decrease in the contact angle in the first case is more pronounced than in the second one. Considering the hydrophilic properties of halloysite, it can be assumed that treatment at 50°C leaves a greater amount of HNTs onto the surface, while at 60°C, the nanomaterial penetrates in-depth of the film. In addition, an adhesive composition was developed for applying nanomaterials to PE films without the need to dissolve polyethylene and heat. Polyvinylpyrrolidone was chosen as the base, polyethylene glycol was added as a plasticizer in a ratio of 7:1 by weight. The optimal ratios of solvent and polymer base for applying the composition to PE films using a spray and a sponge were determined. For the spray, they were 1 to 18, for the sponge - 1 to 15. Studies of decorated films using an optical microscope confirmed the uniform distribution of nanomaterial over the entire surface of the film using the developed compositions.

A block diagram for the chemical synthesis of a composite material for further use as a photocatalyst for the degradation of aqueous solutions of organic pollutants (dyes) has been developed. The material balance for the synthesis of 1 kg of the sample was calculated and the heat of its formation was estimated.

The practical significance is confirmed by the following. The developed methods for introducing photocatalysts into and onto polyethylene films are intended for practical use for the photodegradation of polymers. To achieve effective degradation, it is possible to coat an already manufactured film with composite materials with halloysite nanotubes and manganese oxides/oxyhydroxides. A promising candidate for such a coating, which is considered in this study, is a mechanical mixture of TiO_2 and MnO_2 . Electrostatic

interactions between metal ions and the HNT surface allow for controlled decoration of HNTs with deposited particles of Mn oxides and oxydehydroxides. This effect is especially relevant for the development of new functional materials in photocatalysis and catalysis. The study showed that composites CS-2 and CS-1 exhibit high activity in the photodegradation of methylene blue dye, while CS-8 and CS-9 effectively photodegrade Congo red. This opens up promising opportunities for practical application. A technology for the synthesis of manganese oxides and oxide-hydroxide photocatalytic material with halloysite CS-2 is proposed.

Keywords: MANGANESE DIOXIDE, MANGANESE OXYDEHYDROXIDE, HAYSMANNITE, ELECTRODEPOSITION, CHEMICAL SYNTHESIS, PHOTOCATALYSIS, HALLOYSITE, DECORATION, CATIONIC DYES, ANIONIC DYES, METHYLENE BLUE, CONGO RED, POLYETHYLENE FILM, DEGRADATION.

List of publications

Articles:

1 **I. Kovinchuk**, N. Haiuk, G. Lazzara, G. Cavallaro, and G. Sokolskyi, ‘Enhanced photocatalytic degradation of PE film by anatase/ γ -MnO₂’, *Polym. Degrad. Stab.*, vol. 210, p. 110295, Apr. 2023, doi: 10.1016/j.polymdegradstab.2023.110295. The journal is cited by the scientometric databases SCOPUS and Web of Science (Q1). *Personal contribution is analysis of literary sources, conducting experimental research, processing and formatting results, writing the article.*

2. **I. Kovinchuk**, G. Sokolsky, and G. Lazzara, ‘Single-stage and simple fabrication of PE films decorated with halloysite nanotubes’, *KPI Sci. News*, vol. 136, no. 1–4, Apr. 2024, doi: 10.20535/kpissn.2023.1-4.297046. Journal adopted by the Ministry of Education & Science of Ukraine as professional ones in specialty 161 Chemical technology and engineering. *Personal contribution is analysis of literary sources, conducting experimental research, processing and formatting results, writing and submitting the article.*

3 **I. V. Kovinchuk**, G. Lazzara, Ragulya, A.V., M. M. Kržmanc, and G. V. Sokolsky, 'Evaluation of nanoparticles' size characteristics of manganese oxide/hydroxide based photocatalysts', *Visnyk Kherson Natl. Tech. Univ.*, vol. 4, no. 91, pp. 52–59, 2024.

Journal adopted by the Ministry of Education & Science of Ukraine as professional ones in specialty 161 Chemical technology and engineering. *Personal contribution is analysis of literary sources, conducting experimental research, processing and formatting results, writing and submitting the article.*

Conference materials:

4. Sokolsky G.V., Ivanova N.D., Zudina L.V., Gayuk N.V., **Kovinchuk I.V.** Electrolytic doping and implementation of a bifunctional electrochemical system, *9th Ukrainian Congress of Electrochemistry Achievements Problems and Prospects, 2021, P. 56-57.* <https://doi.org/10.33609/978-966-8398-64-3.01.2021.1-191>. *Personal contribution is analysis of literary sources, conducting experimental research.*

5. Sokolsky G., Paineau E., Zahornyi M., Gayuk N., Ragulya A., **Kovinchuk I.** INTs/MnO₂/TiO₂/PANI composites: toward new applications and enforced functionality, *2021 IEEE 11th International Conference Nanomaterials: Applications & Properties (NAP), 2021, P. NSS-A-03.* <https://doi.org/10.1109/NAP51885.2021.9568504>. *Personal contribution is analysis of literary sources, conducting experimental research.*

6. **Kovinchuk I.**, Lazzara G., Cavallaro G., Sokolsky G. MnO₂/TiO₂ Nanopowders-Assisted Photocatalytic Degradation of Low-Density Polyethylene Films, *2022 IEEE 12th International Conference Nanomaterials: Applications & Properties, 2022 P. 10nee–27.* <https://doi.org/10.1109/NAP55339.2022.9934707>. *Personal contribution is analysis of literary sources, conducting experimental research, processing and formatting results, writing and submitting the abstract.*

7. Sokolsky G.V., **Kovinchuk I.V.**, Ragulya A.V., Spreitzer M., Kržmanc M.M. Electrodeposition of nanodispersed α/δ - & γ/α -manganese dioxide composites for visible light photocatalytic applications, *10th Ukrainian Congress of Electrochemistry Achievements Problems and Prospects, 2, 2024, P. 32-36.* <https://doi.org/10.33609/elchimcongr.2024.09.1-210>. *Personal contribution is analysis*

of literary sources, conducting experimental research, processing and formatting results, writing.

Abstracts of conference presentations:

8. Haiuk N.V., Sokolsky H.V., Svyntsova A.V., **Kovinchuk I.V.** (2021) Fotokatalitychna destruktsiia polietylenovykh plivok dioksydamy tytanu i manhanu. [Photocatalytic destruction of polyethylene films by titanium and manganese dioxides] *Materialy XV mizhnarodnoi naukovo-tekhnichnoi konferentsii «AVIA-2021»*. m. Kyiv, (Ukraine). P. 19.1-19.4. *Personal contribution is analysis of literary sources, conducting experimental research, processing results.*

9. Sokolsky H.V., Chyhyrynets O.E., Haiuk N.V., **Kovinchuk I.V.**, Melnyk A.V. (2021) Dioksyd tytanu: fototoksychnist ta shliakhy yii podolannia dlia kosmetychnykh zastosuvan [Titanium Dioxide: Phototoxicity and Ways to Overcome It for Cosmetic Applications]. *International Scientific Online Conference «Modern Advances in Organic Synthesis, Polymer Chemistry and Food Additives»*. m. Lviv, (Ukraine). P. 40. *Personal contribution is analysis of literary sources, conducting experimental research, processing results.*

10. Haiuk N.V., Dmitriieva Y., **Kovinchuk I.V.**, Sokolsky H.V. (2021) Tverdofazna fotokatalitychna destruktsiia polietylenovykh plivok oksydnymy materialamy manhanu ta tytanu [Solid-phase photocatalytic destruction of polyethylene films by manganese and titanium oxide materials]. *Materialy I Mizhnarodnoi naukovo konferentsii «Aktualni problemy khimii, materialoznavstva ta ekolohii»*. m. Lutsk, (Ukraine). S. 119–122. *Personal contribution is analysis of literary sources, conducting experimental research, processing and formatting results.*

11. **Kovinchuk I.V.**, Sokolskyi H.V., Haiuk N.V. (2021) Vyznachennia serednoho diametru nanostryzheniv Manhan (IV) oksydu riznoho pokhodzhennia v prohramnomu seredovyshchi ImagJ ta SciDAVi [Determination of the average diameter of Manganese (IV) oxide nanorods of various origins in the ImagJ and SciDAVi software environments]. *Materialy shkoly-konferentsii molodykh vchenykh suchasne materialoznavstvo: fizyka, khimiia, tekhnolohii*. m. Uzhhorod, (Ukraine). P. 245–246. *Personal contribution is analysis of literary sources, conducting experimental research,*

processing and formatting results, writing and submitting the abstract.

12. **Kovinchuk I.**, Haiuk N., Cavallaro G., Lazzara G., Sokolsky G. (2022) Thermogravimetric study of PE films containing TiO₂, MnO₂ photocatalysts, and their composites. *Book of abstracts of the 13 European Symposium on Thermal Analysis and Calorimetry*. Palermo, (Italy). P. 214. *Personal contribution is analysis of literary sources, conducting experimental research, processing and formatting results, writing and submitting the abstract.*

13. Svintsova A.V., Sokolsky G.V., Hlukhova P.I., **Kovinchuk I.V.**, Lazzara G., Sokolsky G. (2022) Encapsulated by Ascorbic Acid Halloysite Nanotubes combined with Rutile Nanoparticles for Cosmetic Applications. *Book of abstracts of the Ukrainian conference with international participation "Chemistry, physics and technology of surface"*. Kyiv, (Ukraine). P. 78. *Personal contribution is analysis of literary sources, conducting experimental research, data curation.*

14. **Kovinchuk I.**, Hlukhova P., Sokolskyi H. (2023) Otsinka mozhyvosti vykorystannia oksydneykh fotokatalitychnykh system dlia pisliavoiennoho vidnovlennia terytoriii [Assessment of the possibility of using oxide photocatalytic systems for post-war restoration of territories]. *Materialy konferentsii Synerhiia nauky i biznesu y povoiennomu vidnovlenni Khersonshchyny*. m. Odesa, (Ukraine). P. 391–395. *Personal contribution is analysis of literary sources, processing and formatting results, writing and submitting the abstract.*

15. **Kovinchuk I.**, Sokolsky G., Lazzara G. (2023) Single stage and simple fabrication of PE films Impregnated with halloysite nanotubes. *Book of abstracts. International Conference on Chemistry, Chemical Technology and Ecology*. Kyiv, (Ukraine). P. 60–61. *Personal contribution is analysis of literary sources, conducting experimental research, processing and formatting results, writing and submitting the abstract.*

16. P. Hlukhova, **I.V. Kovinchuk**, Dzh. Lazzara, i H. V. Sokolskyi (2023) Fotokatalitychni vlastyvoli kompozytiv oksydiv-hidroksydiv manhanu z haluazytom, syntezyovanykh hidrokhimichnym metodom [Photocatalytic properties of manganese oxide-hydroxide composites with halloysite synthesized by the hydrochemical method]. *Zbirka tez dopovidei. Mizhnarodna konferentsiia z khimii, khimichnoi tekhnolohii ta*

ekolohii, prysviachenii 125-richchiu KPI im. Ihoria Sikorskoho. m. Kyiv, (Ukraine). P. 14–16. Personal contribution is analysis of literary sources, conducting experimental research, data curation.

17. Sokolsky G., **Kovinchuk I.**, Lazzara G., Zudina L., Hluhova P., Andriiko O. (2023) Comparison of chemical and electrodeposition pathways of manganese dioxide from NH_4^+ -containing electrolytes. *Book of abstracts. International Conference on Chemistry, Chemical Technology and Ecology*. Kyiv, (Ukraine). P. 87–88. *Personal contribution is analysis of literary sources, conducting experimental research, processing and formatting results.*

18. **Kovinchuk I.V.**, Hluhova P.I., Telina M.M., Khrebtan D.R., Vechirko E.R., Lazzara G., Sokolsky G.V. (2024) Halloysite nanotubes as components of nanocomposites with Mn oxides/hydroxides. *Book of abstracts. 12th International Conference "Nanotechnologies and Nanomaterials" NANO-2024*. Uzhgorod, (Ukraine). P. 77. *Personal contribution is analysis of literary sources, conducting experimental research, processing and formatting results, writing and submitting the abstract.*

19. **Kovinchuk I.**, Hluhova P., Lazzara G., Sokolsky G. (2024) Enhanced Photocatalytic Methylene Blue Degradation by $\text{Mn}_3\text{O}_4/\text{HNT}$ -based composite material. *Book of abstracts. XXVIII Congresso Nazionale della Società Chimica Italiana*. Milan, (Italy). P. FIS-PO-005. *Personal contribution is analysis of literary sources, conducting experimental research, processing and formatting results, writing and submitting the abstract.*

АНОТАЦІЯ

Ковінчук І.В. Composites of manganese oxides and oxidehydroxides with halloysite as degradation photocatalysts. – Кваліфікаційна наукова праця на правах рукопису. Дисертація на здобуття наукового ступеня доктора філософії за спеціальністю 161 «Хімічні технології та інженерія». – Національний технічний університет України «Київський політехнічний інститут імені Ігоря Сікорського», МОН України, Київ, 2024 та наукового ступеня доктора філософії «Фізичні і хімічні науки». – Університет Палермо (Італія), Київ, 2025.

Дисертаційна робота присвячена дослідженню впливу умов синтезу, фазового складу, структури на функціональність композитів на основі оксидів та оксидгідроксидів мангану для фотокаталітичної деградації модельних органічних сполук: водних розчинів барвників та поліетиленових плівок (ПЕ) під дією УФ-опромінення. В роботі також розглянуто взаємозв'язок умов синтезу та фазового складу, морфології, ширини забороненої зони, питомої поверхні продуктів з їх ефективністю як фотокаталізаторів. Крім цього було вивчено вплив наявності алюмосилікатних нанотрубок галуазиту на фізико-хімічні властивості та фотокаталітичну активність композитних матеріалів, а також характер взаємодії із манган оксидами та оксидгідроксидами.

Оцінено фотокаталітичну активність стандартних матеріалів MnO_2 , TiO_2 та їх механічної суміші для фотокаталітичної деградації поліетиленових плівок під впливом УФ-, видимого опромінення. Оцінка проводилася за втратою маси ПЕ плівок із внесеним фотокаталізатором у порівнянні із чистою плівкою. Найвищу ефективність продемонструвала суміш $\text{MnO}_2/\text{TiO}_2$ із втратою маси плівки 21.3% після 90 годин опромінення. Механізм деградації оцінювали за відносною інтенсивністю піків FTIR спектрів, що відповідають карбонільному, гідроксильному та етерному індексам. Виявилося, що механічна суміш $\gamma\text{-MnO}_2$ з TiO_2 спричиняє більшу ступінь деградації на усіх проміжних стадіях окиснення ПЕ, бо функціональні групи інтермедіатів є більш інтенсивними порівняно з плівкою ПЕ/ TiO_2 . Окрім того, карбонільний індекс показує відносно найбільше накопичення відповідних груп. Отже, перетворення відбувається набагато швидше

ніж у інших зразках на всіх стадіях, що свідчить про неспецифічність каталітичної дії утворених радикалів щодо інтермедіатів окиснення ПЕ на фотокаталізаторі γ - MnO_2 з TiO_2 .

Було встановлено, що при хімічному осадженні оксидів/оксидгідроксидів мангану із розчину MnSO_4 за використання як окисника гідроген пероксиду утворюються композитні матеріали із різним співвідношенням оксидів/оксидгідроксидів мангану валентності від +2 до +4. Вирішальну роль відіграє кислотність середовища та наявність допанта іонів NH_4^+ у реакційному середовищі. Показано, що при $\text{pH} = 10$ основною утворюваною фазою являються низьковалентні оксиди мангану гаусманіт Mn_3O_4 за присутності надлишку йонів амонію, та біксбіїт Mn_2O_3 за його відсутності. В той час, як при нижчих значеннях $\text{pH} = 5-7$ основним продуктом осадження являється манганіт γ - MnOOH та грутит α - MnOOH із домішками оксиду мангану 4+ за наявності надлишку NH_4^+ . Методом трансмісійної мікроскопії вивчено характер взаємодії оксидів мангану із поверхнею галуазитних нанотрубок. Встановлено, що на TEM зображеннях зразків синтезованих при наявності надлишку іонів амонію в реакційній суміші (CS-2 та CS-6) спостерігається затемнення області люмену нанотрубок, що може свідчити про його заповнення, в той час як за відсутності надлишку амонію (CS-1 та CS-7) частинки оксидів/оксидгідроксидів мангану декорують зовнішню поверхню галуазиту. Виміряна питома поверхня синтезованих зразків є в 3-3.5 разів вища в порівнянні із стандартним зразком MnO_2 PCP і склала 55-66 $\text{m}^2/\text{г}$, при чому внесення галуазитних нанотрубок не мало значного впливу на цей показник. Методом DRS було знято спектри дифузного відбиття та розраховано ширину забороненої зони за Тауком. Встановлено $E_g = 2.28-2.38$ еВ для зразків CS-5-CS-9, та 2.52 та 2.7 еВ для нижчевалентних зразків CS-1 та CS-2 відповідно. Що свідчить про напівпровідникові властивості композитів та їх потенційну фотокаталітичну активність у діапазоні видимого світла. Було проведено порівняння даних про середній розмір агрегатів композитних матеріалів отриманих методом дисперсійного розсіювання світла та окремих наночастинок методом оцінки за зображеннями TEM. Встановлено, що у обох випадках синтезовані зразки мають

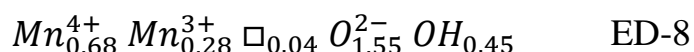
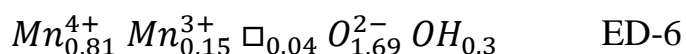
менший розмір в порівнянні із стандартним зразком MnO_2 РСР і коливаються в межах 117-175 нм для агрегатів та 7-12 нм для наночастинок.

Для розширення діапазону фазових станів досліджуваних зразків було синтезовано серію електрохімічно осаджених зразків. Досліджено вплив кислотності та наявності допант іонів NH_4^+ та Cr^{3+} в електроліті на морфологію, фазовий склад та фізико-хімічні властивості синтезованих зразків. Методом рентгенівської дифракції підтверджено отримання композитних оксидних матеріалів, що складаються із α -, γ -, ε - та δ -фаз MnO_2 у різних співвідношеннях. Встановлено, що надлишок іонів NH_4^+ стабілізують електроосадження голандитної α - та бірнеситної δ -фази MnO_2 , а за їх відсутності – рамсделітної γ - та ε - MnO_2 . Найбільш розвинену площу поверхні продемонстрували зразки із основною голандитною фазою MnO_2 яка досягла максимум $215 \text{ м}^2/\text{г}$ для зразка ED-12, що свідчить про досягнення дифузійного режиму осадження, порівняно меншу площу мають зразки із основною ε - MnO_2 фазою, а саме $65.65 \text{ м}^2/\text{г}$ ED-13 та $82.88 \text{ м}^2/\text{г}$ ED-2. Розподіл частинок MnO_2 за розміром та морфологія оцінювалися за зображеннями отриманими за допомогою скануючої електронної мікроскопії. Для зразків ED-2 ED-6, які є композитами α - та ε - MnO_2 , спостерігаються пластинчасті утворення із середнім розміром наночастинок $70 \pm 15 \text{ нм}$. Зразки з основною альфа-фазою демонструють голчасту морфологію.

Синтезовані оксидні зразки є напівпровідниками із шириною забороненої зони в межах 2.16–2.36 еВ. Допування іонами Cr^{3+} звузило E_g приблизно на 0,3 – 0,5 еВ завдяки введенню нових електронодонорних рівнів. Розраховані електронегативність MnO_2 по Маллікену та положення валентної і зони провідності для електросинтезованих зразів. Зразок ED-6 продемонстрував зону провідності на рівні 0.12 еВ (відносно нормального водневого електроду, СВЕ) та валентну – 2.49 еВ (СВЕ) з найширшою забороненою зоною 3.36 еВ, що свідчить про перспективність даного зразка для фотокаталітичного розщеплення води із утворенням водню. Проведено аналіз методом диференціальної скануючої калориметрії у поєднанні із мас-спектроскопією деяких електросинтезованих зразків, що дозволило ідентифікувати продукти термічного розкладу, встановити

температурні інтервали їх виділення для подальшої оцінки дефектності, керуючись моделлю катіонних вакансій Рутші.

Згідно цієї моделі, можна оцінити вміст катіонних вакансій (\square) у зразках діоксиду мангану переважно рацделітної модифікації. У свою чергу, дефекти кристалічної ґратки як енергетично нерівноцінні позиції приповерхневих шарів матеріалу здатні суттєво підсилювати його каталітичну активність. Розраховані формули для електроосаджених зразків представлені нижче:



γ -MnO₂ ED-6 та α -MnO₂ ED-8 мають однаковий вміст катіонних вакансій, в той час як ED-8 вирізняється вдвічі вищим вмістом Mn³⁺.

Встановлено, що найвищу фотокаталітичну активність по відношенню до катіонного барвника Метиленового Синього проявляють композитні зразки низьковалентних оксидів мангану CS-2 та CS-1, ймовірно, завдяки присутності у складі композитів галуазитних нанотрубок із негативно зарядженою зовнішньою поверхнею, що забезпечує синергетичний ефект і сприяє деградації забрудника за рахунок ефективнішого транспорту барвника із об'єму розчину до поверхні фотокаталізатора. По відношенню до аніонного барвника Конго Червоний найвищу ефективність показав зразок CS-8, що складається з α -MnOOH та γ -/ β -MnO₂ із найвужчою із всіх хімічно синтезованих зразків шириною забороненої зони 1.99 eV.

Подальший аналіз діаграм потенціалу забороненої зони та діаграм з рівнями НОМО та LUMO барвника дозволив виявити, що зразки CS-1 та CS-2 мають добре узгоджені крайні рівні E_c галуазитних нанотрубок, Mn_xO_y та рівень LUMO барвника метиленового синього. Можна припустити, що саме ця властивість обумовлює позитивний вплив декорування поверхні HNTs оксидами мангану Mn_xO_y на фотокаталітичну активність щодо деградації MB, завдяки новій можливості прямої передачі електронів від зони провідності HNTs та Mn_xO_y до

рівня LUMO MB з подальшим відновленням барвника. З діаграми також видно, що для Конго Червоного лише зразок CS-8 має сприятливо узгоджений рівень E_V з рівнем НОМО барвника, і, ймовірно, ця властивість може бути відповідальною за швидше пряме окислення CR дірками із валентної зони CS-8 як фотокаталізатора. Таким чином, виражена активність фотокаталізаторів CS-1 та CS-2 у деградації MB, а також висока активність зразка CS-8 у руйнуванні CR може бути пояснена напівпровідниковими властивостями цих фотокаталізаторів.

За результатами проведених досліджень, одержані в роботі матеріали запропоновано наносити для створення фотодеградуючих покриттів на поверхню ПЕ порівняно із їх введенням у склад плівки. Розроблено метод нанесення наноматеріалів на поліетиленові плівки через часткове розчинення їхньої поверхні. Досягнуто внесення 2.59% за масою галуазитних нанотрубок при зануренні ПЕ плівки в суспензію ГНТ в циклогексані при 50°C на 120 с., та 2.51% при температурі суспензії 60°C впродовж 60 с. Зменшення кута змочування при цьому у першому випадку виражене сильніше, ніж у другому. Враховуючи гідрофільні властивості галуазиту можна припустити, що обробка при 50°C залишає на поверхні більшу кількість ГНТ, в той час як при 60°C наноматеріал проникає вглиб плівки. Крім цього розроблено адгезивний склад для нанесення наноматеріалів на ПЕ плівки без необхідності розчинення поліетилену та нагрівання. В якості основи було обрано полівінілпіролідон, в якості пластифікатора вносили поліетиленгліколь у співвідношенні 7:1 за масою. Визначено оптимальні співвідношення розчинника і полімерної основи для нанесення композиції на ПЕ плівки із використанням спрея та губки. Для спрея вони склали 1 до 18, для губки - 1 до 15. Дослідження декорованих плівок за допомогою оптичного мікроскопа підтвердили рівномірне розподілення наноматеріалу по всій поверхні плівки за використання розроблених складів.

Розроблено принципову технологічну схему хімічного синтезу композитного матеріалу для подальшого використання як фотокаталізатора деградації водних розчинів органічних забрудників (барвників). Розраховано матеріальний баланс для синтезу 1 кг зразка та оцінено теплоту його утворення.

Практична значимість підтверджується наступним. Розроблені способи внесення фотокаталізаторів у та на поліетиленові плівки призначені для практичного використання для фотодеградації полімерів. Для досягнення ефективної деградації можна покрити вже виготовлену плівку композитними матеріалами з галуазитними нанотрубками та оксидами/оксидгідроксидами мангану. Перспективним кандидатом на таке покриття, яке розглядається в цьому дослідженні, є механічна суміш TiO_2 і MnO_2 . Електростатичні взаємодії між іонами металів і поверхнею ННТ дозволяють керувати декорувати ННТ осадженими частинками оксидів і оксидгідроксидів Mn. Цей ефект особливо актуальний для розробки нових функціональних матеріалів у фотокаталізі та каталізі. Дослідження показало, що композити CS-2 і CS-1 виявляють високу активність у фотодеструкції барвника метиленового синього, тоді як CS-8 і CS-9 ефективно фотодegradують конго червоний. Це відкриває багатообіцяючі можливості для практичного застосування. Запропоновано технологію синтезу оксидів мангану та оксидно-гідроксидного фотокаталітичного матеріалу з галуазитом CS-2.

Ключові слова: ДІОКСИД МАНГАНУ, ОКСИДГІДРОКСИД МАНГАНУ, ГАУСМАНІТ, ЕЛЕКТРООСАДЖЕННЯ, ХІМІЧНИЙ СИНТЕЗ, ФОТОКАТАЛІЗ, ГАЛУАЗИТ, ДЕКОРУВАННЯ, КАТІОННІ БАРВНИКИ, АНІОННІ БАРВНИКИ, МЕТИЛЕНОВИЙ СИНІЙ, КОНГО ЧЕРВОНИЙ, ПОЛІЕТИЛЕНОВА ПЛІВКА, ДЕГРАДАЦІЯ.

CONTENT

LIST OF ABBREVIATIONS, SYMBOLS, AND NOTATIONS	20
INTRODUCTION	22
SECTION 1. ORGANIC POLLUTANTS OF ENVIRONMENT AND METHODS OF THEIR REMOVAL	28
1.1 Dyes as water pollutants.....	28
1.2 Plastic pollution.....	33
1.3 AOPs for the removal of organic pollutants: photocatalysis and photocatalysts ..	35
1.3.1 Titanium dioxide	40
1.3.2 Manganese oxides and oxidehydroxides.....	40
1.3.3 Clays and Halloysite nanotubes.....	44
Conclusions to Section 1	47
SECTION 2. OBJECTS, SYNTHETIC, AND RESEARCH METHODS	53
2.1 Materials and reagents.....	53
2.2. Synthesis methods of photocatalysts studied	53
2.2.1 Chemical synthesis of manganese oxides and oxidehydroxides with halloysite composite materials	53
2.2.2 Electrodeposition of manganese dioxide materials	54
2.2.3 Preparation of PE/TiO ₂ and PE/TiO ₂ &MnO ₂ films.....	56
2.2.4 Preparation of PE films decorated with HNTs.....	57
2.2.5 Preparation of adhesive composition and its application for the decoration of PE films with photocatalyst.....	57
2.3 Physico-chemical research methods	58
2.3.1 Thermogravimetric Analysis	58
2.3.2 Thermogravimetric Analysis combined with Mass Spectrometry	60
2.3.3 Fourier Transform Infrared Spectroscopy	60
2.3.4 X-ray diffraction and X-ray Fluorescence analyses	61
2.3.5 ζ-potential and Dynamic light scattering analysis (DLS)	61
2.3.6 UV-Vis spectroscopy	62
2.3.7 Diffuse reflectance spectroscopy. Band gap calculation	62
2.3.8 Water Contact Angle Measurements	64
2.3.9 SEM and SEM combined with EDS analysis	64
2.3.10. Dynamic mechanical analysis.....	65

2.3.11 BET analysis	66
2.4. Methods for evaluation of photocatalytic activity	66
2.4.1. Photocatalytic degradation of PE films.....	66
2.4.2 Photocatalytic degradation and adsorption of organic dyes (Methylene Blue, Congo Red).....	66
Conclusions to Section 2	69
SECTION 3. PHYSICOCHEMICAL AND MECHANICAL PROPERTIES OF STANDARD MATERIALS OF MnO₂, TiO₂, PRISTINE HNTs, AND COMPOSITE PE FILMS	73
3.1 Characterization of standard materials of TiO ₂ , MnO ₂ in this study, and pristine HNTs	73
3.2 Characterization of PE films decorated with halloysite nanotubes	78
3.3 Characterization of PE films decorated with photocatalysis series CS1-9. Optical microscope investigation.....	81
Conclusions to Section 3	82
SECTION 4. PROPERTIES OF CHEMICALLY SYNTHESIZED MANGANESE OXIDES AND OXIDEHYDROXIDES COMPOSITES WITH HNTs	85
4.1 Characterization of manganese oxides and oxidehydroxides composites with HNTs	85
4.1.1 Characterization of manganese oxides and oxidehydroxides with HNTs composites aqueous dispersions: ζ potential, size distribution (DLS, TEM)	85
4.1.2 BET analysis	90
4.1.3 Phase and elemental composition of synthesized composites of manganese oxides and oxidehydroxides with halloysite	91
4.1.4 FTIR study	93
4.1.5 Thermal properties of samples in air and nitrogen atmosphere	96
4.1.6 DRS and band gap calculation.....	101
Conclusions to Section 4	103
SECTION 5. PROPERTIES OF ELECTROCHEMICALLY SYNTHESIZED MANGANESE DIOXIDE MATERIALS	105
5.1 Characterization of electrodeposited manganese dioxide materials	105
5.1.1 XRD study	107
5.1.2 SEM, EDS and size distribution	113
5.1.3 BET analysis	117

5.1.4 TGA/DTA/MS analysis.....	118
5.1.5 DRS analysis and calculation of band gap width, determination of energy level positions.....	125
5.2 Comparison of chemical and electrodeposition pathways of manganese dioxide from NH_4^+ -containing electrolytes	128
Conclusions to Section 5	129
CHAPTER 6. FUNCTIONALIZATION OF SAMPLES OF MANGANESE SYSTEM (III, IV)	132
6.1 Photocatalytic degradation of composite films: mass loss measurements, lifetime prediction and carbonyl index	132
6.2 Study of adsorption of Congo Red and Methylene blue on HNT's surface.....	141
6.3 Study of photocatalytic activity manganese oxides and oxidehydroxides with halloysite for degradation of dyes in aqueous solutions (Methylene Blue and Congo Red)	146
Conclusions to Section 6	158
CHAPTER 7. CHEMICAL PROCESS TECHNOLOGY FOR SYNTHESIS OF COMPOSITE PHOTOCATALYST.....	162
7.1 Block diagram for synthesis of photocatalytic material with halloysite nanotubes	162
7.2. Material balance	164
7.3. Energy balance	167
Conclusions to Section 7	170
CONCLUSIONS.....	172
ACKNOWLEDGMENTS	174
REFERENCES	175
APPENDIXES	193
Appendix A.....	193
Appendix B	194
Appendix C	196
Appendix D.....	197
Appendix E	198

LIST OF ABBREVIATIONS, SYMBOLS, AND NOTATIONS

ζ	zeta potential, mV;
AOP	Advanced Oxidation Processes;
BET	Brunauer-Emmett-Teller (method of surface area determination);
CB	Conduction Band;
CMC	Critical Micelle Concentration;
CR	Congo Red;
DMA	Dynamic Mechanical Analysis;
DRS	Diffuse Reflectance Spectroscopy;
DTA	Differential Thermal Analysis;
DTG	Differential Thermogravimetry;
E_{CB}	conduction band energy, eV;
E_g	energy gap of semiconductor, eV;
E_{VB}	valence band energy, eV;
FTIR	Fourier Transform Infrared (Spectroscopy);
LUMO	Lowest Unoccupied Molecular Orbital;
HNT	Halloysite Nanotube;
HOMO	Highest Occupied Molecular Orbital;
MB	Methylene Blue;

PE	Polyethylene;
PEG 300	Polyethyleneglycole 300;
PVP K90	Polyvinylpyrrolidone K 90;
ROS	Reactive Oxygen Species;
SEM	Scanning Electron Microscopy;
SHE	Standard Hydrogen Electrode
TEM	Transmission Electron Microscopy;
TG	Thermogravimetry;
UV	Ultraviolet (Irradiation);
VB	Valence Band;
XRD	X-Ray Diffraction (Analysis);
XRF	X-ray Fluorescence (Spectroscopy).

INTRODUCTION

Justification for choosing the research topic, the purpose and objectives of the research. The aim is to study the interrelationship between phase compositions, structure, and functionality of manganese oxides and oxidehydroxides with aluminosilicate nanotubes of halloysite in photocatalytic polyethene and aqueous dyes degradation.

To achieve the given goal, the following tasks were set:

1. Investigate the influence of acidity, the presence of halloysite nanotubes and the synthesis method on the physicochemical properties (phase and chemical composition, crystallite size, etc.) of manganese oxides and oxidehydroxides with halloysite as degradation photocatalysts.
2. To study the chemical and phase composition, size and morphology of particles, optical band gap, thermal behavior of synthesized samples.
3. To investigate the photocatalytic activity of materials towards polyethylene films and organic dyes of anionic and cationic types under the influence of UV irradiation and in the dark.
4. To develop methods for applying nanomaterials to the surface of films.
5. To develop a schematic diagram of the synthesis of a composite photocatalyst.

Object of the research includes chemically synthesized composite materials of manganese oxides and oxidehydroxides with halloysite nanotubes and electrodeposited manganese dioxide materials.

The subjects are photocatalytic and other physico-chemical properties of composite materials based on manganese oxides and oxidehydroxides with aluminosilicate nanotubes synthesized by the method of chemical codeposition and on electrodeposited manganese dioxide materials

Research methods. The phase composition and structural-crystalline parameters of the synthesized samples were studied by powder diffraction on a Rigaku, MiniFlex600 (Japan) X-ray diffractometer with Cu K α radiation (the tube voltage 40 kV, tube current 15 mA) and Bruker AXS D4 Endeavo (the tube voltage 40 kV, tube current 30 mA). The elemental composition was studied by Energy dispersive spectroscopy using a Quanta

650 Thermo Scientific SEM Oxford equipped Ultim Max 40 detector. The optical properties of photocatalyst suspensions, as well as dye solutions, were studied by absorption spectra using a Specord S600 spectrophotometer (Analytik, Jena, Germany). Differential reflectance spectra were recorded on a Shimadzu UV-3600 UV-VIS-NIR spectrophotometer (200 – 2000 nm). Fourier transform infrared spectra were recorded on a Frontier FTIR spectrometer PerkinElmer (400 – 4000 nm). The morphology and particle size of the synthesized photocatalysts were studied on a Scanning Electron Microscope of Thermo Scientific, Verios G4HP. Dynamic light scattering to determine particle size and zeta potential was studied using a Malvern Zetasizer Nano device. The temperature stability of the materials was determined by thermogravimetric analysis on a Thermogravimetric Analyzer Discovery TGA550 with TRIOS Software and Derivatograph Q1000 (MOM, Hungary). The specific surface area was measured using the BET method on a Gemini II 2370 Micromeritics analyzer. The research results were processed using Microsoft Excel, QtiPlot, ImageJ, Fityk software.

Scientific novelty of the results obtained

Photocatalytic behaviour of individual compounds of ramsdellite structure type MnO_2 and anatase TiO_2 was studied for PE-films degradation. The coupling effect of mechanically mixed MnO_2 and TiO_2 in the PE film with 1% by mass of a photocatalyst content was established. This mixed photocatalyst achieved 21.3% loss by mass versus pure MnO_2 (6.5%) and TiO_2 (14.6%) after 90 h of degradation under UV-light at $\lambda = 250 \text{ nm}$ as evidenced by the 1st type of $\text{TiO}_2@\text{MnO}_2$ heterojunction with faster accumulation of intermediates of PE oxidation as shown by FTIR data of Carbonyl, Hydroxyl, and C–O stretching vibration indexes.

Composites of oxides and oxidehydroxides of manganese with halloysite nanotubes were synthesised for the first time from solutions containing NH_4^+ -ions and at different pH (5-7 and 10). They possess the advantages of narrow band gap, good stability, and high photocatalytic activity of degradation of organics under the visible light range irradiation. Composites with aluminosilicate nanotubes of halloysite are shown to display the decoration and incorporation effects of manganese compound toward a nanotube,

improving functionality due to the role of HNTs as photocatalyst's support and enhanced reactant support to the photocatalyst interface.

It was revealed that chemically deposited oxides and oxidehydroxides of manganese actively decorate HNTs' interface in case of the presence of cationic species of Mn^{2+} in a reaction medium, and incorporation into HNT's lumen is observed for crystallisation of negatively charged Mn species of acid residues of the Tutton salts.

As demonstrated by energy band diagrams, the positive influence of HNT's surface decoration by Mn_xO_y on photocatalytic activity of MB degradation is explained by the new option of direct electron transfer of photoelectron from E_C of both HNTs & Mn_xO_y and following MB dye reduction. It is also evident from this diagram for CR dye that only CS-8 Sample has favorably aligned E_V to HOMO level of CR dye and, probably, this feature can be responsible for the faster direct oxidation of CR by holes from the valence band of CS-8 as a photocatalyst.

Electrodeposition of manganese dioxide under diffusion control has been provided at low Mn^{2+} concentrations (0.05 and 0.1 mol/L) from sulfate electrolytes that was confirmed by studied TEM deposits morphology revealed the close to maximal fraction of nanoparticles. The role of dopant-ions of NH_4^+ and Cr^{3+} was studied for the first time at these conditions. When moderate concentration of sulfuric acid (0.031 mol/L) is introduced into the reaction mixture and in the presence of dopant NH_4^+ ions, the main product consists of δ and α - MnO_2 , while when concentrated acid solutions (2 mol/L), a pure hollandite phase of needle-like morphology with a maximum surface area of 215 m^2/g is precipitated. Unlike fluoride-containing electrolytes, Cr^{3+} had no detectable influence on phase composition of products of electrodeposition in fluoride electrolytes.

Practical significance of the results obtained

The developed methods of incorporating photocatalysts into and onto polyethylene films are designated for practical use in photodegraded polymers. To achieve efficient degradation, it is possible to coat the already produced film with halloysite nanotubes with Mn oxides/oxidehydroxides. The promising candidate for such a coating considered in this study is a mechanical mixture of TiO_2 and MnO_2 .

The use of electrostatic interactions between species of metal ions and HNTs' surfaces allows controlling the decoration of HNTs by deposited particles of oxides and oxide hydroxides of Mn in this study and of other metals generally. This effect has practical significance for developing new functional materials in photocatalysis and catalysis, in particular.

It has been shown that the composites CS-2 and CS-1 are highly active in photodestructing Methylene Blue dye, while CS-8 and CS-9 are active in Congo Red photocatalytic degradation. This opens up prospects for their practical use.

A technology for the synthesis of manganese oxides/oxidehydroxide photocatalytic material with halloysite was proposed.

Personal contribution of the applicant

The determination of the direction of scientific research, the formulation of the task, goals and ways of their implementation, the planning of the main stages of work, the generalization and discussion of the results were carried out with the scientific supervisors H.V. Sokolskyi (Igor Sikorsky Kyiv Polytechnic Institute) and G. Lazzara (University of Palermo).

The author carried out: 1) a literature search and analysis of the literature on the topic of the dissertation; 2) established the conditions for the synthesis of composite photocatalysts based on manganese oxides and oxidehydroxides with and without Halloysite; 3) chemical and electrochemical synthesis of composite materials; 4) dynamic light scattering, thermal, dynamic mechanical analyses and water contact angle measurements of films; 5) UV-Vis, X-ray diffraction, differential reflectance, Fourier transform infrared spectroscopies of composite samples; 6) experiment on the photocatalytic degradation of PE films; 7) selected model organic pollutants and the parameters for studying the photocatalytic activity of composites in static condition.

The work uses scientific developments by Zudina L. [1] for the design of an experiment on the electrochemical synthesis of manganese oxide materials.

Part of the work on the synthesis and study of photocatalytic degradation of polyethylene films was carried out jointly with Haiuk, N. [2]. Personal contribution of the doctoral candidate: participation in preparation of films, conducting an experiment to study degradation, data processing, writing abstracts for the conference.

TEM investigations were done at the Collective Use Center of Electron Microscopy of National Academy of Sciences of Ukraine in M.G. Kholodny Institute of Botany with Dr. Klymchuk Dmytro. Characterisation of ED samples was partially done at Jožef Stefan Institute (Ljubljana, Slovenia) in collaboration with: Silvo Zupančič (BET analysis), Tina Radošević and Dr. Uroš Hribar (EDS analysis), Dr. Marjeta Maček Kržmanc (TGA&MS and XRD analysis). XRD patterns modelling and phase composition discussion was made together with supervisor G. Sokolsky.

Research papers published in co-authorship with G. Sokolsky, G. Lazzara, N. Haiuk, G. Cavallaro and others. Co-authors of scientific works are the scientific supervisor and scientists with whom the research was conducted.

Connection of work with scientific programs, plans, topics

The research was carried out at the Department of Physical Chemistry, Faculty of Chemical Technology, National Technical University of Ukraine “Igor Sikorsky Kyiv Polytechnic Institute” (Ukraine), and at the Faculty of Physics and Chemistry of the University of Palermo (Italy) in accordance with the agreement on dual supervision of the PhD thesis No. 0220/3 dated 02.28.2022.

As an executor, doctoral candidate was included in the research project “Physico-chemical foundations of the production, functionality and use of multicomponent nanodisperse systems and the use of additives in food and cosmetic products” with state registration number 0117U007592, 2018-2023, and “Physical Chemistry of Nanocomposite and Dispersed Systems of Functional Destination” of the Department of Physical Chemistry of Igor Sikorsky Kyiv Polytechnic Institute with state registration number 0124U001965, 2024-2026.

Mobility was completed at the University of Palermo (Italy) under the Erasmus + Programme, Key Action 1–Learning Mobility of Individuals, KA107 – Higher education, Grant Agreement No.2019-1-IT02-KA107-062108 during 28.02.2022-26.02.2023.

The part of the experiment was carried out in Advanced Materials Department, Jožef Stefan Institute, Ljubljana (Slovenia) according to Work Package 1 of the Marie Skłodowska-Curie Research and Innovation Staff Exchange action “Innovative Functional Oxide Materials for Green Hydrogen Energy Production – H-GREEN”.

Approbation of dissertation results

The results of the dissertation have been presented and discussed at 8 international conferences, including: 11th, 12th IEEE International Conference “Nanomaterials: Applications & Properties” (NAP-2021, NAP-2022); 13 European Symposium on Thermal Analysis and Calorimetry (ESTAC 2022); 12th International Conference "Nanotechnologies and Nanomaterials" NANO-2024; 2024 XXVIII National Congress of the Italian Chemical Society etc. The results of the work were also presented at three schools: School conference for young scientists “Modern materials science: physics, chemistry, technologies”, 4-8 October 2021, Uzhhorod, Ukraine; Summer School and Workshop in Calorimetry and Thermal Analysis 2022 - Calorimetry and thermal methods in material science, 19-24 June 2022, CNRS, Institut de Recherches sur la Catalyse et l'Environnement de Lyon, Université Lyon, Lyon, France; NATO ASI Summer school “Nanomaterials and Nanoarchitectures II. Composite Materials & Their Applications”, 28 June – 5 July 2024, Smolenice, Slovak Republic.

Publications

19 publications have been published on the topic of the dissertation, including: 3 papers (1 of which is cited by the SCOPUS scientometric database and belongs to the Scopus quartile Q1 journal and 2 were issued in journals adopted by the Ministry of Education & Science of Ukraine as professional ones in specialty 161 Chemical technology and engineering), 4 materials of international conferences, as well as 12 reports at conferences.

Structure and scope of the dissertation

The dissertation is presented on 198 pages of typewritten text, consists of an introduction, 7 chapters, general conclusions, a list of sources used and 5 appendices. The volume of the main text of the dissertation is 149 pages of printed text. The work is illustrated with 32 tables and 52 figures. The reference list contains 151 entries.

SECTION 1. ORGANIC POLLUTANTS OF ENVIRONMENT AND METHODS OF THEIR REMOVAL

1.1 Dyes as water pollutants

Water is a vital resource for human survival and development. Human development and industrialisation have given rise to rapid growth in industries whose waste products include antibiotics, hormones, pathogens, pesticides, heavy metals, oils, microplastics, and toxic dyes [3]. Dye contamination is mainly caused by such industries as textile and paper production, as well as printing products, food processing, and cosmetics. Getting into natural water flows - above ground, underground, they can reach the food chain of humans, causing irreparable damage to health, the full consequences of which are difficult to assess [4], [5].

The European Union has taken legislative steps to address the pressing issue of water pollution. Several documents, directives, and regulations have been put in place, with water reuse emerging as a promising solution. The Water Framework Directive (WFD), introduced in 2000, mandates European countries to enhance the performance of all surface and groundwater bodies by 2027. This includes reducing wastewater production and discharges of pollutants [6], [7]. The Circular Economy (CE) plan also underscores the importance of preserving and restoring water resources, offering hope for a sustainable future.

Among the chemical pollutants, organic dyes are one of the major contaminants of industrial wastewater due to toxic nature [8]. More than 1.6 million tons of synthetic dyes are produced annually for industrial purposes [9]. For example, the textile industry accounts for 20% of global wastewater pollution and is one of the most influential in terms of both water consumption and pollution. Dyeing one ton of textiles requires about 15 tons of water [9], of which more than 80% is wasted. Each type of dye has certain features that are used for dyeing certain types of materials.

There are several classifications of dyes based on various criteria, such as chemical structure, method of application, or properties. By origin, dyes are divided into organic

and inorganic. In turn, organic are divided into the following groups according to their chemical structure [10]:

- *Azo Dyes*. The most widely represented group of synthetic dyes in the industry. They differ from the others by the presence of one or more azo groups ($-N=N-$) in their structure. Azo dyes are known for their wide range of colours, which is why they are so actively used in industry. Examples are Congo red, Direct Black, Ponceau S, Sunset Yellow FCF, Methyl orange.
- *Anthraquinone Dyes*. This class of dyes are derivatives of anthraquinone and are widely used to obtain bright blue and red shades. They have a complex structure with aromatic rings attached to anthraquinone and are often used in textiles, artistic paints, hair dyes and for dyeing leather goods. The main advantage of the representatives of this group is their durability, especially under the influence of sunlight. Examples of this group are alizarin, anthrapyrimidine yellow (Pigment Yellow 108), anthraquinone red (Pigment Red 177), and Indanthrone blue (Pigment Blue 60).
- *Triarylmethane dyes* are synthetic organic dyes characterised by the presence of triarylmethane backbones. Typical representatives of this class are malachite green, methyl violet, and phenol dyes.
- *Indigoid Dyes*. The dye was first obtained from natural raw materials, but now it is synthesised by chemical means. It includes dyes like indigo, commonly used for dyeing denim due to their rich blue colour.

If consider the method of use as the main indicator, then the classification will be [11]:

- *Acid Dyes* dissociate in water to form negatively charged ions, which are responsible for dyeing fibres such as wool, silk, and nylon. They are resistant to biodegradation and have a wide range of bright colours.
- *Cationic or Basic Dyes*. Positively charged water soluble dyes bond with negatively charged synthetic fibres and are used for silk, acrylic, as well as non acrylic fibre dyeing. The dyeing process takes place effectively in a neutral environment with heating.

- *Nonionic or Disperse Dyes* are insoluble in water and suitable for hydrophobic fibres like polyester and acetate. For best results, fine dispersions require heating to fairly high temperatures of around 130-210°C at a pH of 5.5.
- *Direct Dyes*. Water-soluble dyes that have a high affinity to cellulosic fibres. They provide a wide colour range but have lower resistance to washing. Moreover, they are also used as organic pigments and pH indicators.
- *Reactive Dyes*. This class of dyes' colouring properties are due to the unique reactive groups that can form covalent bonds with cellulose fibres. The dyeing process takes place in a weakly alkaline dye bath. The dyed fibres have a stable colour and improved strength characteristics. They are commonly used for cellulosic fibres like cotton, wool, and nylon.
- *Vat Dyes*. These water-insoluble complex dyes are important in cellulose or cotton fibres' printing and dyeing industry. They are characterised by unique colour fastness.
- *Sulfur Dyes*. Sulfur dyes are obtained by sulfurisation or thionation of amino or nitro groups. Insoluble in water and typically used for staple, viscous, and yarn fibers, different types of leather, especially for dark shades like blacks and browns. They offer cost-effectiveness but have moderate wash fastness.

It is worth noting that azo dyes are the main class used in industry. According to [12], they are up to 60-70% of all dyes. Such high popularity is due to the excellent solubility in water, durability of colour, chemical stability and variety of colours. One of the representatives of the azo dyes is Congo red (Fig. 1.1). It is an anionic diazo dye (containing two -N=N- groups) consisting of sodium salt of benzdiazobis-1-naphthylamine-4-sulfonic acid with a molecular weight of 696.68 g mol⁻¹.

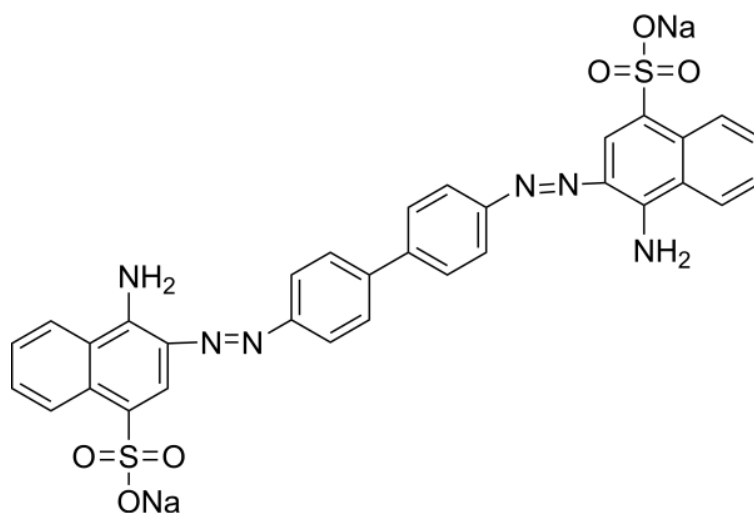


Figure 1.1. Congo Red chemical structure.

This dye is also known as CR 4B, Cotton Red B, Cotton Red C, Direct Red 28, Cosmos Red, Direct Red Y and Direct Red R [13]. It is soluble in acetone, ethanol, water (11.6 g/100ml) and is practically insoluble in ether. 1 mass% water solution has pH 6.7. [14] and has bright red colour in alkaline solution and blue in acid solution. Commonly used as an indicator, a biological stain, as a fabric and paper dye. A study of the dye's toxicity to animals and humans showed a high probability of allergic reactions, in addition, the dye can be metabolised to o-benzidine, a carcinogenic product [15]. From the point of view of photocatalytic degradation, it is important to consider the position of HOMO and LUMO. According to literature data [16] HOMO energy is -1.21 eV and LUMO 0.97 eV. However, at least 15% of the total volume of Congo Red used is untreated wastewater [17]. Considering all of the above, high toxicity, and poor biodegradability, eliminating dye from wastewater is an important topic for research.

Methylene Blue (tetramethylthionine chloride), a cationic thiazin dye from the phenothiazine family whose structure is shown in Figure 1.2. It has found wide application as an optical probe of biophysical systems, an indicator of oxidation-reduction reactions due to the bright colour change during reduction, and as a test material in photocatalysis. It is also used for therapeutic and diagnostic purposes in the clinic for the treatment of methemoglobinemia [18]. It is a solid, odourless, dark blue powder at room temperature. According to [14], solubility in water is 4.36 g per 100 g of water and is also

soluble in ethanol, ethylene glycol. Water solution exhibits maximum absorption at 664 nm. The positions of the LUMO and HOMO of MB were reported as -0.88 and 1.55 eV, respectively, while the bandgap is 2.43 eV [19].

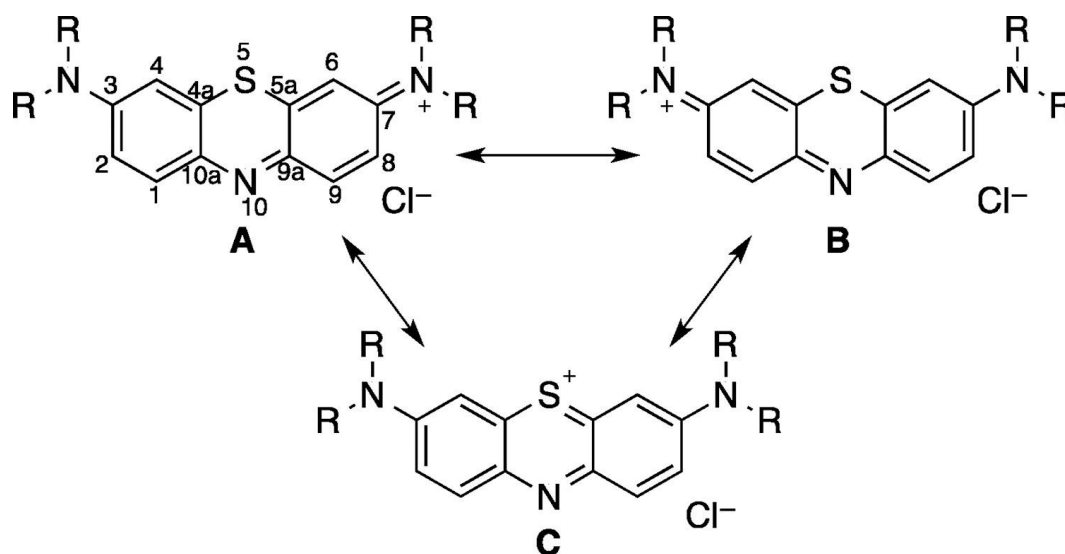


Figure 1.2. Resonance structures of MB derivatives [20].

The lethal dose for oral consumption for rats is set at LD₅₀ 1180 mg/kg. Poisonous when taken orally, intraperitoneally, intravenously and subcutaneously. When systemically ingested by the human body, it causes changes in the blood and has a toxic effect on the central nervous system. M. Albert et al. [21] report high toxicity of MB in premature infants resulting in hemolytic anaemia.

The most common methods of removal of organic contaminants are chemical, physical, and biological methods. Physical methods have the advantage of low levels of toxic additives used in the separation process. Such methods include filtration, sedimentation, adsorption, and coagulation-flocculation. The addition of coagulants promotes the enlargement of pollutant particles, allowing them to be subsequently separated by filtration or sedimentation. Solid particles are removed through filtration using membrane or carbon filters. Adsorption, which occurs on the surface of sorbent materials such as activated carbon and ion exchange resins, is particularly notable for its dye removal efficiency and cost-effectiveness. The efficiency of the adsorbent directly depends on the surface area and porosity of the material. The disadvantages of the method

is the need to manage or disposal water treatment residuals [22] as well as the path for effective reuse and recycle options of adsorbents, high dependence on the pH of the environment, time consuming, and the fact that the adsorbent is not capable of degrade dyes.

In chemical methods of water purification, reagents play a crucial role. These methods, which include oxidation, precipitation, electrochemical methods, photocatalysis, and photo electrocatalysis, use reagents to help decompose the pollutant in the aquatic environment. This decomposition process is essential for effectively removing organic contaminants from water.

Advanced oxidation processes (AOPs) photocatalysis, Fenton reactions effectively decompose organic pollutants using highly reactive species such as hydroxyl radicals. AOPs achieve decomposition efficiencies of pollutants up to trace levels, outperforming traditional chemical oxidation methods [4].

Another chemical method is electrochemical remediation. It is based on using electric current to initiate chemical reactions of decomposition. The limitations of these methods are the use of toxic substances and the formation of toxic secondary decay products.

Biological methods include using microbial and enzymatic treatments before the discharge of aqueous waste. These methods are non-toxic, but their efficiency is lower than alternatives, they are difficult to scale up, and they are often expensive.

Considering the potential for combined methods to enhance efficiency, there is a promising future for water purification. By carefully weighing the advantages and disadvantages of each method, it is possible to create a comprehensive approach that maximizes the benefits of each.

1.2 Plastic pollution

Plastics, including polyethene (PE), polypropylene (PP), polystyrene (PS), polyvinyl chloride (PVC), polyurethane (PU), and polyethene terephthalate (PET), are widely used and essential in every aspect of daily life due to their durability and low cost [23].

According to the UN Foundation, more than 430 million tons of plastic are produced annually (data for 2023), with a continuing trend of increasing from year to year. The increasing production, coupled with the lack of effective processing methods applied universally and uniformly, has made the problem of plastic pollution increasingly acute over the past decade. Laurent Lebreton et al. [24] estimated that 2060 global plastic waste volumes are expected to reach 270 million tons. According to the authors [23], about 8 million tons of plastic waste ends up in the world's oceans every year, while the authors [25] forecast suggests that about 1.2 billion tons of plastic waste will remain in landfills in 2050. Recognising this, the European Commission has adopted an EU Plan to make all plastic packaging recyclable by 2030. [26]. Being global, multidimensional, and affecting all spheres of human life, multidisciplinary collaboration is required to advance remediation technologies. When plastics are exposed to the open air, for example, in landfills, they release toxic substances into the air; when they get into rivers and oceans or soil, getting into food, they cause irreparable damage to the health of all living beings. It calls for a more careful attitude to resources.

The different methods of recycling plastic are often called "primary", "secondary", "tertiary", or "energy recovery", and "quaternary" [27]. Primary recycling involves using uncontaminated, identical plastic as raw material. This means that the quality of the product is not reduced, and it can be used for the same purposes as the original plastic. Secondary recycling is the transformation of material by mechanical means for less demanding products. Primary and secondary recycling involves mechanical processes such as sorting, shredding, washing and extrusion. These processes can result in varying levels of polymer degradation. Thus, recycled material costs are often higher than pristine plastic, and the quality of the processed material decreases with each cycle [28].

Polymers are known to be petroleum-based products [29]. Following the principles of energy sustainability, tertiary recycling allows for the recovery of petrochemical components from which the polymers were made. The main idea is to split the polymer into individual monomers through the depolymerisation process to produce a high-quality secondary product. Tertiary processing includes:

Tertiary processing includes:

- Chemical
 - Chemical recovery
 - Energy recovery
- Thermolysis
 - Pyrolysis
 - Gasification
 - Hydrogenation

While chemical methods speed up the process of plastic degradation to days compared to traditional hundreds of years, moreover the processed products can become valuable resources, they have a relatively high cost and are difficult to scale. Separately, it is worth mentioning photodegradation, photocatalytic oxidation and electrochemical oxidation methods of decomposing plastic into safe products such as water and carbon dioxide. Following multiple recycling cycles, once the plastic experiences a critical decline in quality, it may be directed to a landfill or utilised in quaternary recycling processes, such as incineration. Quaternary recycling is used for highly contaminated mixed waste for energy recovery [30].

However, the mentioned methods only meet some of the needs of processing. Each of them has critical shortcomings that lead to the emergence of no less important problems. For example, incineration releases volatile organic compounds and harmful chemical compounds [31] such as CO, NO_x and SO_x, furans, and dioxins into the atmosphere [32]. The most environmentally friendly method is the biological way of waste disposal – depolymerisation using enzymes, bacteria and fungi [33]. The disadvantage of bio recycling is its extremely long duration of process.

1.3 AOPs for the removal of organic pollutants: photocatalysis and photocatalysts

The advantages of degradation processes under the influence of ultraviolet radiation, sunlight and catalysts are undeniable and attract increased interest from researchers. The advanced oxidation process, namely heterogeneous photocatalysis, has attracted much

attention for environmental remediation because it can be applied without additional energy sources using only sustainable resources of solar energy to remove various pollutants. Moreover, they do not transfer pollutants from one phase to another (as in chemical precipitation and adsorption) and do not create a massive amount of dangerous sediment. AOPs are able to convert organic pollutants into harmless products. The result of such an intensive study of photocatalysis was using numerous metal oxide semiconductors, polymer semiconductors, and metalorganic substances. To improve their efficiency, various strategies are used. For example, the number of active sites can be influenced by changing the precursor for synthesis or by using extensive thermal etching. Changing the band gap or band-edge positions affects the efficiency of photocarrier transport and the efficiency of solar energy absorption. The design of heterojunctions, defects, cocatalyst loading, element doping, crystallinity, surface area, and interfacial interactions are also important parameters that affect the overall efficiency.

One of the important factors affecting the activity is the size of the nanoparticles. It is known that 0D-based quantum dots are useful as electron receiving/capturing centres, thereby increasing the separation efficiency of photogenerated electron-hole pairs. 1D nanomaterials (nanorods, nanotubes and nanowires) have a large surface area and numerous active centres, which increases the efficiency of adsorption and rapid charge separation and increases the intensity of interaction at the phase interface. [34]. One interesting property of 1D materials is their ability to direct charge transfer through channels, thereby facilitating electron (e^-) - hole (h^+) pairs transfer. [35]. (2D) tends to restack, which leads to weakening, so their ability to absorb light is lower compared to 1D. Moreover, although the layered structure of 2D nanomaterials can reduce carrier recombination in the bulk, the recombination on the surface will still be high. 3D nanostructures often have complex morphologies, resulting in several different reaction pathways.

The mechanism of classical heterogeneous photocatalysis involves a series of oxidation and reduction reactions on the surface of a semiconductor. Almost all reactions are based on the generation of reactive hydroxyl radicals ($\bullet OH$) with a redox potential of 2.8 eV. They attack organic pollutant molecules with rate constants on the order of 10^6

to $109 \text{ M}^{-1} \text{ s}^{-1}$ and initiate a series of oxidation reactions to AOP: ozonation, sonolysis, photocatalysis and humid air oxidation. Fenton and photo-Fenton oxidation generate $\bullet\text{OH}$ radicals by reacting ferrous ions (Fe^{2+}) and hydrogen peroxide with UV light or other activators. Unlike the Fenton reaction, ozone-based oxidation uses ozone to generate hydroxyl radicals by decomposing ozone in water, which subsequently decomposes pollutants [4].

In general, photocatalytic degradation of pollutants can be described in 5 stages [34]: The first stage is the adsorption of the target pollutant on the surface of the photocatalyst. This is followed by the absorption of a photon ($h\nu$) of sunlight by the photocatalyst, forming $e^- - h^+$ pair. A necessary condition for this is that the energy of a photon of light exceeds the width of the forbidden zone. Only in this case, electrons can migrate from the valence band to the conduction band. To participate in the oxidation-reduction process, the electron and hole migrate to the surface of the material, this process is accompanied by the recombination of electrons and holes on the surface and inside the photocatalyst. This process is shown schematically in Figure 1.4.

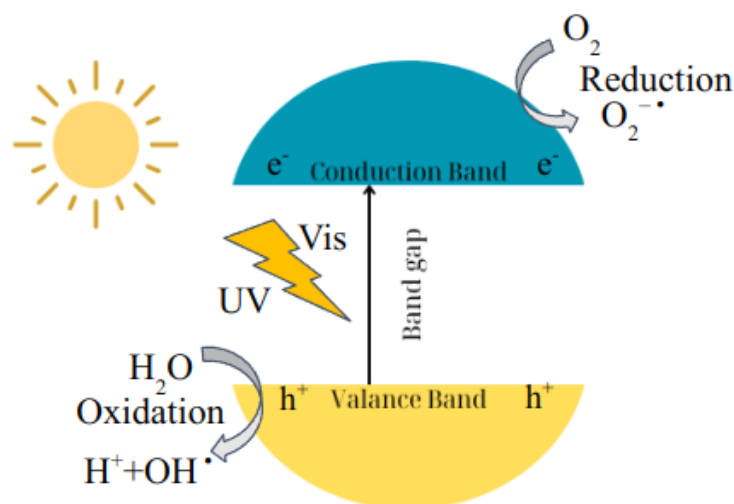


Figure 1.4. Schematic representation of the photochemical activation of material under UV light.

Due to the recombination, potential energy is released through heat or light. Under the influence of photogenerated carriers, oxidation and reduction of water and oxygen

molecules to hydroxyl ($\bullet\text{OH}$) and superoxide radicals ($\bullet\text{O}_2$) occur on the surface. At the same time, pollutant molecules can be broken down into simplest molecules up to H_2O and CO_2 (as a result of complete mineralisation of organics) that are later desorbed into the bulk of the solution [36]. The sequence of equations of chemical reactions is shown below (1.1-1.11):



Or in inert atmosphere



In addition, the oxidation-reduction potential of the pollutant must be lower than the conduction band potential and higher than the valence band of the photocatalyst [31]. For example, in the case of dyes, it is necessary to take into account the positions of HOMO and LUMO.

A disadvantage characteristic of many single-component photocatalysts is high charge carrier recombination and a compromise between the band gap and redox strength. To overcome these factors, it has been proposed that composite materials from two or more semiconductors can be created. A heterojunction is a surface between semiconductors through which charge carriers can pass. This way, electrons and holes will be separated and located in different catalyst bands. Heterojunction materials may be designed as a composite of different materials (multicomponent) or with the various phases of one material (multiphase). Based on the different alignments of the heterojunction bands, a distinction is made between type I heterojunctions, type II

heterojunctions, p–n-type heterojunctions, Schottky junctions, Z-type heterojunctions, and S-type heterojunctions [36]. Common types include Type I, Type II, and Type Z heterojunctions. They are shown schematically in Fig. 1.5, focusing on their energy levels and charge carriers following the photoexcitation process.

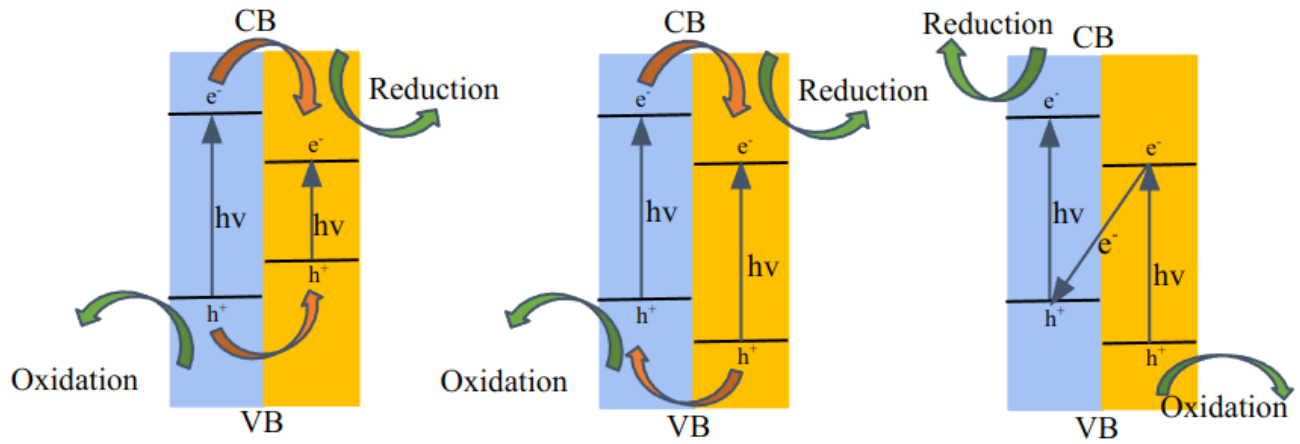


Figure 1.5. Schematic energy diagrams for type I heterostructure (a), type II heterostructure (b) and type Z-scheme system (c).

In composite semiconductors with heterojunction type I, the CB of semiconductor A is higher than the CB of semiconductor B, while the VB of semiconductor B is lower than that of semiconductor A, as depicted in Fig. 1.5a. When such materials are in sufficient contact, photoexcited electrons can move downwards from CB(A) to CB(B), gaining energy. At the same time, for holes, it is more energetically favourable to move upwards from VB (A) to VB (B). Since the charge carriers accumulate at the energy levels of one of the materials, charge separation does not occur, and thus, photocatalytic efficiency is not improved.

Type II, on the contrary, promotes charge separation and reduces the probability of recombination. This is achieved by creating materials whose energy levels are arranged in such a way that electrons move downwards to the CB of material B (Fig. 1.5b). Meanwhile, holes move upwards to the VB of material A. This type of heterojunction is most often found in literature [37] TiO_2/CdS [38], CdS/ZnO [39], $\text{TiO}_2/\text{SnO}_2$ [40].

In Z-type photocatalytic systems (Fig. 1.5c), electrons of material B (n-type semiconductor) recombine with holes of material A (p-type semiconductor), thus

increasing the distance between photogenerated electrons on CB (A) and holes on VB (B), giving both the high charge-separation and strong redox ability. This type of photocatalyst is usually composed of n-type and p-type semiconductors [41], [42].

Some of the first photocatalysts that found application in environmental pollutant degradation were TiO_2 , ZnO , SnO_2 , etc. [43] due to their chemical stability, strong oxidative properties, recyclability, and wide availability. However, the limitations associated with their use are worth mentioning: fast recombination, wide forbidden zones, and activity exclusively under UV irradiation [36].

1.3.1 Titanium dioxide

TiO_2 , being chemically and physically stable, relatively inexpensive, and widely available, is one of the most frequently used and promising semiconductor photocatalysts. In 1972, the photocatalytic process of water splitting in a photoelectrochemical cell using titanium dioxide as a single-crystal electrode was first described by A. Fujishima [44]. Titanium dioxide is a wide-gap n-type semiconductor with a band gap of 3.2 eV for anatase, 3.0 eV for rutile, 3.3 eV for brookite, 3.34 eV for metastable TiO_2 Ramsdellite modification, 3.6 eV — for the metastable hollandite form. The VB of TiO_2 is formed by the outer p-electrons of oxygen, and the bottom of the CB is mainly formed by excited titanium ions. The presence of partially reduced titanium (Ti^{3+}), the level of which is $\sim 0.2\text{--}0.8$ eV below the conduction band and which acts as an electron donor, is of particular importance for the manifestation of the electronic properties of titanium dioxide. The presence of Ti^{3+} determines the conductivity of TiO_2 in many cases [45], [46].

Conventional photocatalysts, e.g., TiO_2 and ZnO recently attained limited application owing to their weak visible light adsorption assigned to their wide bandgaps that encouraged research design of new and narrow bandgap semiconductors [47].

1.3.2 Manganese oxides and oxidehydroxides

Manganese oxides, encompassing various forms such as MnO , MnO_2 , Mn_2O_3 , Mn_3O_4 , Mn_5O_8 , among others, are of significant technological relevance owing to their

diverse crystalline structures. This structural variety directly results from the wide range of oxidation states from 2+ up to 7+ that manganese can have. Such variability gives these materials critical functionalities, making them essential in various applications, including energy storage devices, components of fuel cells, enhancement of supercapacitors and application for catalysis.

MnO₂ is an n-type semiconductor and exists in several crystallographic forms, i.e., α -, β -, γ -, δ -, λ - and ε - [48]. The ways in which MnO₆ octahedral interlinks in the MnO₂ nanostructures cause variation in crystallographic forms. Each crystallographic form possesses its unique tunnel structure or interlayers. The vertices and edges in MnO₆ octahedral sharing in several directions lead to tunnel structures forming with different dimensions.

1D tunnel structure can be found in α - (2×2), β - (1×1), and γ -MnO₂ (is regarded as the intergrowth of ramsdellite 1×2 and pyrolusite 1×1) while the δ -MnO₂ possess 2D layered in its structure and the λ -MnO₂ is a 3D spinel structure as depicted in Fig. 1.6.

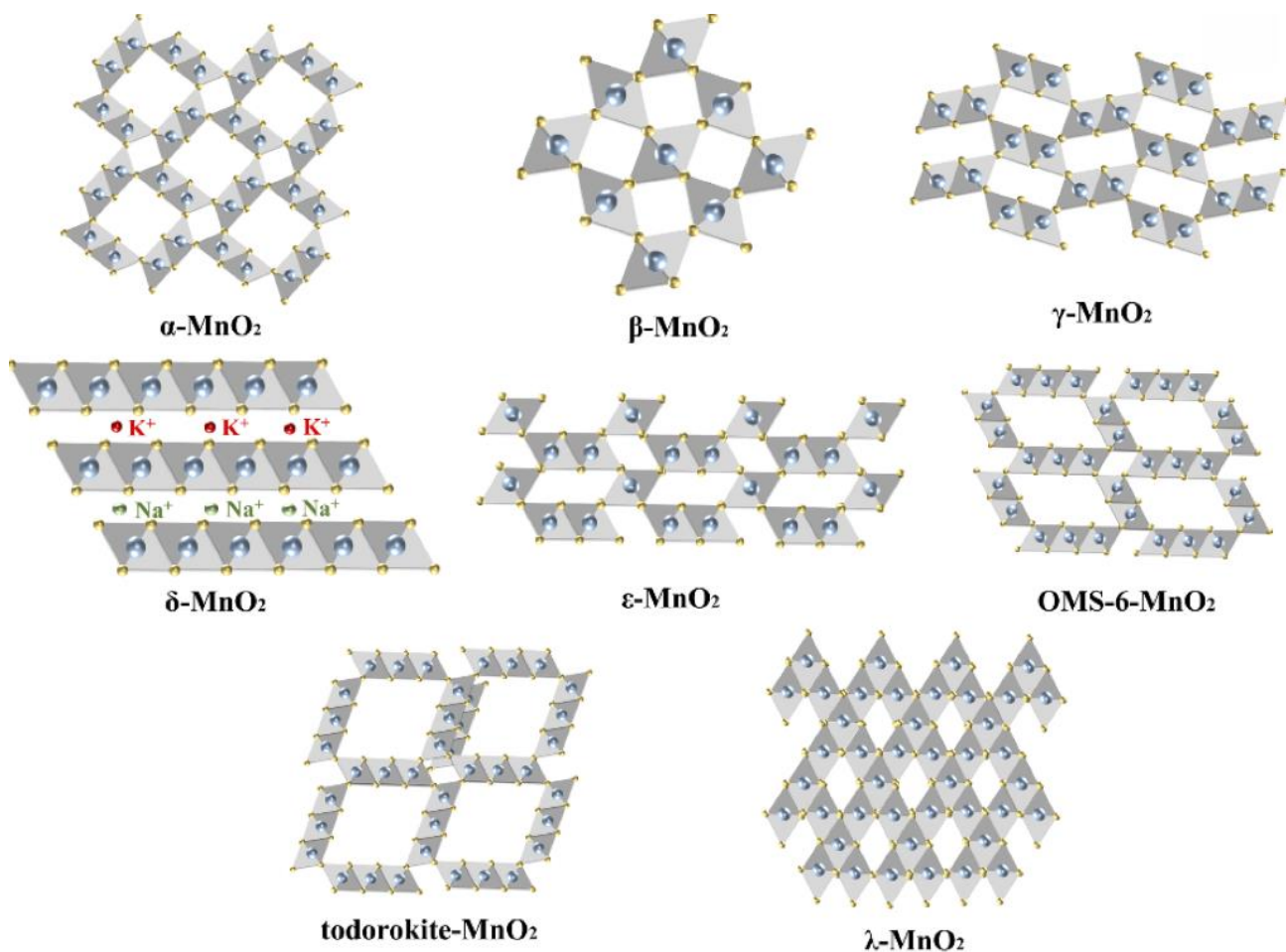


Figure 1.6. Overview of structural fragments in polymorphic modifications of MnO₂ [48].

They are characterised by the tunnel's size with the octahedral subunits' number ($n \times m$) [48]. γ - MnO_2 structure is characterised by an arrangement of $[\text{MnO}_6]$ octahedra connected via edges and corners, forming tunnels that extend along the c-axis of the structure. Within this framework exists a random microscopic intergrowth of tunnel structures, specifically the tunnels of pyrolusite and the tunnels of ramsdellite. This complicated network of tunnels is a defining feature of the γ - MnO_2 structure, illustrating the complex of different tunnel types within a single crystalline framework. Synthesis conditions such as the reaction temperature, precursor concentration, impurities and dopants, or coupling can easily alter the crystal structure. The most common methods for synthesis of manganese oxides are permanganate reduction, pyrolytic decomposition of manganese nitrate, electrochemical method, hydrothermal synthesis in a magnetic field or chemical precipitation. At temperatures above 460°C , manganese dioxide loses oxygen and transforms into α - Mn_2O_3 [49], and the crystal structure transforms from a tetragonal syngony to a cubic lattice, reaching a temperature of 970 - 1050 Mn_2O_3 loses oxygen to form Mn_3O_4 . For this reason, thermogravimetric analysis of manganese oxide compounds is a valuable tool for detecting the content of lower-valence Mn in the form of defects (Mn^{3+} ions), structural water and OH groups, cation vacancies, etc. [50].

Mn_2O_3 exhibits p-type semiconductor of direct bandgap. It exists in the form of two polymorphs known as minerals α -kurnakite and β -bixbyite [51]. Like other manganese oxides, it has found wide application as electrochemical sensor, photocatalyst for purification of wastewater contaminated with dyes [52] or hormones in medical wastewater [53], electrochemical supercapacitor [54], in lithium-ion batteries and in solar thermochemical water splitting [55]. As a component in composite materials it is used for photocatalytic H_2 evolution [56], the oxygen evolution reaction [57], as well as CO_2 reduction to CH_4 [58].

MnOOH is an oxyhydroxide of Mn^{3+} . It exists in 3 crystalline modifications: α -groutite, β -feitknechtite and γ -manganite. It found wide use as chemical catalysts, molecular sieves, and cathode materials in primary and rechargeable batteries [59]. According to authors [60] γ - MnOOH was considered the most stable trivalent manganese hydroxide. It is crucial to highlight that γ - MnOOH is structurally related to β - MnO_2

modification named pyrolusite, while α -MnOOH - to γ -MnO₂. γ -MnOOH is considered one of the simple and practical precursors for obtaining manganese oxides by thermal decomposition [61].

Mn₃O₄, known as hausmannite, is a p-type metal oxide that features a spinel-like crystal structure that comprises a unit cell with 32 oxygen atoms and 24 manganese atoms. In this structure, manganese exists in both divalent and trivalent cationic states, with Mn²⁺ ions occupying tetrahedral sites and Mn³⁺ ions residing in octahedral sites. Numerous studies have explored the effectiveness of hausmannite in the photodegradation of various dyes, including Alizarin Yellow, Methylene Blue, and Methyl Orange. It is reported as an excellent sensor material for identifying volatile organic compounds [62]. Furthermore, it is a significant energy storage medium, particularly as an anode material for lithium-ion batteries [63]. Additionally, its role as an efficient catalyst [64] in a wide range of oxidation and reduction reactions underscores its importance in catalysis.

Mn₅O₈, a particular manganese oxide composition, showcases Mn cations in Mn²⁺ and Mn⁴⁺ oxidation states. As a metastable oxide, its application, especially as a catalyst in denitration processes, has only gained attention recently. The unique combination of valence states and their antiferromagnetic nature enables the use of Mn₅O₈ in applications such as sensors for hard disks and devices utilising magnetic thin films. Coupled with MnO₂, it was usefully used for gaseous benzene photocatalytic degradation [65].

The crystalline nature of manganese oxides, in particular MnO₂ nanostructures has demonstrated an impact on the photocatalytic reaction. It was observed by S.-L.Chiam [66] that amorphous MnO₂ nanorods exhibit superior performance compared to their crystalline counterparts in photocatalytic reactions. This discrepancy may arise from defects, such as oxygen vacancies or surface irregularities facilitating the capture of excited electrons. Consequently, this prolongs the separation of charge carriers, thereby enabling more holes to migrate to the particle surface, subsequently enhancing the degradation of organic compounds

The combination of manganese dioxide with titanium dioxide has been extensively investigated for its potential in photocatalysis, with TiO₂ being a widely recognized semiconductor due to its exceptional photocatalytic properties. Coupling TiO₂ with MnO₂

may yield mutually beneficial outcomes. It addresses the challenges posed by MnO_2 , such as slow charge transfer rate and fast recombination of photogenerated electron-hole pairs. At the same time, it can help to expand the TiO_2 activity zone into the visible light region. Thus, coupling presents a synergistic approach to improving overall photocatalytic efficiency [67]. As shown by Xue et al [66], the synergy between MnO_2 and TiO_2 results in the formation of a photocatalytic system characterized by a larger surface area and larger pore size than the individual elements. Furthermore, when exposed to visible light irradiation, the $\text{MnO}_2/\text{TiO}_2$ composite exhibited outstanding performance.

1.3.3 Clays and Halloysite nanotubes

Clays are fine-grained natural minerals available in a wide variety of morphologies and physical properties. Typically, clays become plastic when mixed with water and hard when fired. Chemically, clays are aluminium phyllosilicates with variable amounts of iron, magnesium, alkali metals, alkaline earth metals and other cations. Due to its exceptional properties, such as high surface area and ion exchange capacity, clays have been widely used as adsorbents and catalysts [68], [69]. Clay-based nanocomposite materials are used as fillers in polymer composites to improve their mechanical properties, such as stiffness and strength. This is explained by the high surface area and the ability of clays to form strong interactions with polymers. In addition, clays can be used as carriers for drug delivery due to their high surface area and biocompatibility. The interlayer spaces of clays can be used to encapsulate drugs that can be released slowly over time. The most common types of clay minerals are zeolites, micas, spars, scapolites, and permutites.

One of the types of clays is halloysite with a tubular structure that distinguishes it from others. It was first described by the French geologist Pierre Berthier in 1826 and named after the Belgian geologist Omaluis d'Allois (1707-1789), who discovered it in the Angler lead-zinc deposits in Belgium [70]. It is fairly common mineral that occurs in various geological environments and is low-cost. It is found in weathered volcanic rocks and sedimentary rocks such as shales and sandstones. Halloysite is also found in soils,

where it forms as a result of the weathering of feldspar minerals. The largest deposits are located in the USA, Australia, China, Mexico, Turkey, and New Zealand.

Halloysite is a natural aluminosilicate of the kaolin group with Al : Si in a ratio of 1:1, having the chemical formula $\text{Al}_2\text{Si}_2\text{O}_5(\text{OH})_4 \cdot n\text{H}_2\text{O}$, where n can vary from 0 to 4. In the case of $n = 2$, the mineral is called halloysite – 10Å. When heated to 120°C an irreversible process of dehydration occurs until $n = 0$, such a mineral is called halloysite – 7Å, and the two varieties have different physical and chemical properties that affect their use in different industries [71]. The Sigma Aldrich halloysite used in this work contains two water molecules, according to the certificate of analysis provided by the supplier, the molecular weight is 294.19 g/mol. In general, halloysite consists of 10 – 15 bilayers spaced approximately 0.72 nm apart and has a density of 2,53 g·cm⁻³. Due to its layered structure, it has a large specific surface area in the range of 50 – 150 m²/g. The cavity volume is 10-20% of the total tube volume, which can be increased to 30-40% by treatment with sulfuric acid [72].

The outer surface mainly consists of groups O—Si—O, and the inner with Al—OH, on the edges of the tubes, there are both groups Al—OH and Si—OH (Fig. 1.7.). Both surfaces are polar, providing good hydrophilicity (the water contact angle on halloysite nanotubes is below 5°). The layers are interconnected by hydrogen bonds formed between the oxygen atoms of the tetrahedral layer and the OH groups on the inner surface of the octahedral layer. Rolled into a tube, these layers cause the presence of a negative charge on the outer surface of the tubes and a positive charge in the inner cavity [73] in the pH range from 3 to 8. Within the indicated pH, the electrical zeta potential of nanotubes is - 30 mV. The isoelectric point of the halloysite is at pH 2.5.

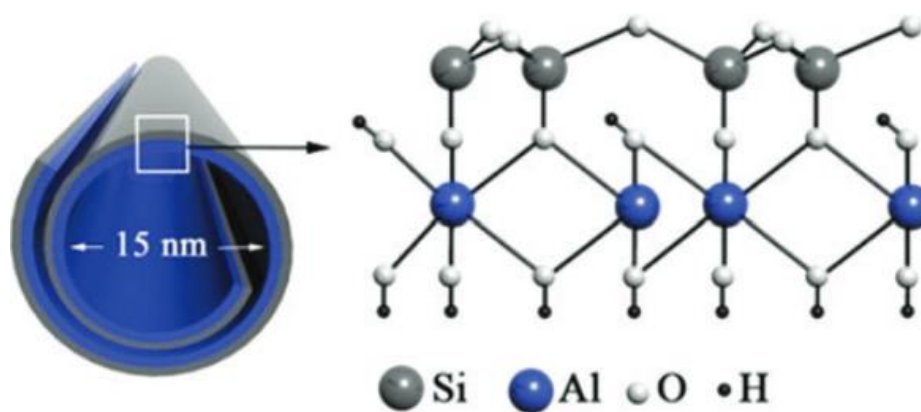


Figure 1.7. Schematic representation of halloysite structure [74].

The average dimensions depend on the deposit and ranges within such values: external diameter of 50-80 nm, lumen of 10-15 nm and length of about 1000 nm [75], [76].

Halloysite is white, light grey, or light yellow in colour and has a pearly lustre. Its colouring is due to impurities with Fe^{+3} , Cr^{+3} , and Ti^{+4} ions. Halloysite does not show toxic properties in relation to living organisms and plants [77].

At the same time, it is worth noting that the human body lacks mechanisms for the decomposition of aluminosilicate tubes, and intravenous injections cause thrombosis, so HNTs can be used mainly for oral administration or for the development of creams and composites for external use. The effect of oral halloysite was studied in mice [78]. HNT exhibits toxicity due to the accumulation of aluminium and, as a result, liver dysfunction. Therefore, it is important to control the intake of halloysite at the level of 20 mg/kg^{-1} of body mass. From the point of view of biocompatibility, short nanotubes are the most attractive. Halloysite is considered as a green alternative in various applications, including as nanoadditives, catalyst supports, and nanocarriers for the controlled release of agents, drugs, and proteins, owing to their natural, non-toxic, and biocompatible properties [79].

The distinct chemical compositions and the opposite charges of the inner and outer surfaces of halloysite nanotubes provide a wide range of possibilities for the development of HNT-based composite materials. This unique structure enables the functionalization

of the outer surface of the nanotubes with positively charged molecules, while the inner cavity can be loaded with negatively charged molecules. Consequently, the internal cavity of HNTs benefits as a reservoir for encapsulating various active substances, such as pharmaceuticals, proteins, surfactants, corrosion inhibitors, and catalysts. This facilitates the controlled release of these substances, offering potential applications in a wide array of fields, from drug delivery systems to materials science, highlighting the adaptability and utility of HNTs in creating sophisticated composite materials with targeted functionalities. Chemical agents release time may vary from 1-10 hours to days [80]. The combination of biomolecules with halloysite nanotubes offers a path toward the development of innovative materials with unique properties. This approach is particularly attractive due to its reliance on natural resources, fostering environmental sustainability and cost-efficiency. Beyond biomolecules, the potential for loading various inorganic salts [81], such as ammonium molybdate ($\text{NH}_4 \cdot 6\text{Mo}_7\text{O}_{24}$), potassium permanganate (KMnO_4), sodium silicate (Na_2SiO_3) and sodium chromate (Na_2CrO_4) can be loaded into HNTs from their saturated solution in water by vacuum cycling. The release of these salts is achieved within 1–2 hours.

Surface modification of nanotubes plays a crucial role in enhancing the performance of materials by influencing the stability of colloidal solutions, optimizing filler dispersion within polymer matrices, and expanding the effective surface area of catalysts [82]. Combining different methods of HNT modification allows to immobilize multiple functional groups on both the interior and exterior surfaces of the nanotube. Such dual-functionalization not only extends the range of potential applications for HNTs but also introduces a level of customization and effectiveness in materials design that harnesses the unique structural features of halloysite nanotubes.

Conclusions to Section 1

Thus, the demands of sustainable development regarding environmental pollution include the usage of green technologies. Various methods have been applied against pollution, and not all meet modern requirements. It can be seen that organic dyes and plastics can be considered as a simple model of liquid and solid waste material

degradation. It was shown that photocatalytic methods, despite their limitations of low substrate concentration, are prospective advanced oxidation approaches that answer sustainability goals. Conventional TiO₂ based photocatalysts are also limited with UV-irradiation wavelengths. The composites with manganese oxides and manganese oxidehydroxides have the advantages of photocatalytic activity in the visible range of light together with abundance in nature, stability, low price, etc. Their composites with other components like aluminosilicate nanotubes of halloysite could expand opportunities of a photocatalyst on its base due to the heterojunctions, decoration effects, lumen loading by active components, as well as photocatalyst support function. On the other hand, catalytic applications of aluminosilicate materials toward organic compound cracking and other degradation processes are well-known. Therefore, it is of scientific interest to study the photocatalytic activity of composites of manganese oxide - manganese oxidehydroxide-HNT system in organic compounds degradation.

Based on the analysis of scientific literature, the main directions of research were identified and scientific tasks were formulated to achieve the set aim of this study.

The results of the analysis of scientific literature conducted in the preparation of this section are presented in the following publications:

Articles:

1 **I. Kovinchuk**, N. Haiuk, G. Lazzara, G. Cavallaro, and G. Sokolskyi, ‘Enhanced photocatalytic degradation of PE film by anatase/ γ -MnO₂’, *Polym. Degrad. Stab.*, vol. 210, p. 110295, Apr. 2023, doi: 10.1016/j.polymdegradstab.2023.110295. The journal is cited by the scientometric databases SCOPUS and Web of Science (Q1). *Personal contribution is analysis of literary sources, conducting experimental research, processing and formatting results, writing the article.*

2. **I. Kovinchuk**, G. Sokolsky, and G. Lazzara, ‘Single-stage and simple fabrication of PE films decorated with halloysite nanotubes’, *KPI Sci. News*, vol. 136, no. 1–4, Apr. 2024, doi: 10.20535/kpissn.2023.1-4.297046. Journal adopted by the Ministry of Education & Science of Ukraine as professional ones in specialty 161 Chemical technology and engineering. *Personal contribution is analysis of literary sources,*

conducting experimental research, processing and formatting results, writing and submitting the article.

3 **I. V. Kovinchuk**, G. Lazzara, Ragulya, A.V., M. M. Kržmanc, and G. V. Sokolsky, 'Evaluation of nanoparticles' size characteristics of manganese oxide/hydroxide based photocatalysts', *Visnyk Kherson Natl. Tech. Univ.*, vol. 4, no. 91, pp. 52–59, 2024.

Journal adopted by the Ministry of Education & Science of Ukraine as professional ones in specialty 161 Chemical technology and engineering. *Personal contribution is analysis of literary sources, conducting experimental research, processing and formatting results, writing and submitting the article.*

Conference materials:

4. Sokolsky G.V., Ivanova N.D., Zudina L.V., Gayuk N.V., **Kovinchuk I.V.** Electrolytic doping and implementation of a bifunctional electrochemical system, *9th Ukrainian Congress of Electrochemistry Achievements Problems and Prospects*, 2021, P. 56-57. <https://doi.org/10.33609/978-966-8398-64-3.01.2021.1-191>. *Personal contribution is analysis of literary sources, conducting experimental research.*

5. Sokolsky G., Paineau E., Zahornyi M., Gayuk N., Ragulya A., **Kovinchuk I.** INTs/MnO₂/TiO₂/PANI composites: toward new applications and enforced functionality, *2021 IEEE 11th International Conference Nanomaterials: Applications & Properties (NAP)*, 2021, P. NSS-A-03. <https://doi.org/10.1109/NAP51885.2021.9568504>. *Personal contribution is analysis of literary sources, conducting experimental research.*

6. **Kovinchuk I.**, Lazzara G., Cavallaro G., Sokolsky G. MnO₂/TiO₂ Nanopowders-Assisted Photocatalytic Degradation of Low-Density Polyethylene Films, *2022 IEEE 12th International Conference Nanomaterials: Applications & Properties*, 2022 P. 10nee–27. <https://doi.org/10.1109/NAP55339.2022.9934707>. *Personal contribution is analysis of literary sources, conducting experimental research, processing and formatting results, writing and submitting the abstract.*

7. Sokolsky G.V., **Kovinchuk I.V.**, Ragulya A.V., Spreitzer M., Kržmanc M.M. Electrodeposition of nanodispersed α/δ - & γ/α -manganese dioxide composites for visible light photocatalytic applications, *10th Ukrainian Congress of Electrochemistry*

Achievements Problems and Prospects, 2, 2024, P. 32-36.
<https://doi.org/10.33609/elchimcongr.2024.09.1-210>. *Personal contribution is analysis of literary sources, conducting experimental research, processing and formatting results, writing.*

Abstracts of conference presentations:

8. Haiuk N.V., Sokolsky H.V., Svyntsova A.V., **Kovinchuk I.V.** (2021) Fotokatalitychna destruktsiia polietylenovykh plivok dioksydamy tytanu i manhanu. [Photocatalytic destruction of polyethylene films by titanium and manganese dioxides] *Materialy XV mizhnarodnoi naukovo-tekhnichnoi konferentsii «AVIA-2021»*. m. Kyiv, (Ukraine). P. 19.1-19.4. *Personal contribution is analysis of literary sources, conducting experimental research, processing results.*

9. Sokolsky H.V., Chyhyrynets O.E., Haiuk N.V., **Kovinchuk I.V.**, Melnyk A.V. (2021) Dioksyd tytanu: fototoksychnist ta shliakhy yii podolannia dlia kosmetychnykh zastosuvan [Titanium Dioxide: Phototoxicity and Ways to Overcome It for Cosmetic Applications]. *International Scientific Online Conference «Modern Advances in Organic Synthesis, Polymer Chemistry and Food Additives»*. m. Lviv, (Ukraine). P. 40. *Personal contribution is analysis of literary sources, conducting experimental research, processing results.*

10. Haiuk N.V., Dmitriieva Y., **Kovinchuk I.V.**, Sokolsky H.V. (2021) Tverdofazna fotokatalitychna destruktsiia polietylenovykh plivok oksydnymy materialamy manhanu ta tytanu [Solid-phase photocatalytic destruction of polyethylene films by manganese and titanium oxide materials]. *Materialy I Mizhnarodnoi naukovo konferentsii «Aktualni problemy khimii, materialoznavstva ta ekolohii»*. m. Lutsk, (Ukraine). S. 119–122. *Personal contribution is analysis of literary sources, conducting experimental research, processing and formatting results.*

11. **Kovinchuk I.V.**, Sokolskyi H.V., Haiuk N.V. (2021) Vyznachennia serednoho diametru nanostryzheniv Manhan (IV) oksydu riznoho pokhodzhennia v prohramnomu seredovyshchi ImagJ ta SciDAVi [Determination of the average diameter of Manganese (IV) oxide nanorods of various origins in the ImagJ and SciDAVi software environments]. *Materialy shkoly-konferentsii molodykh vchenykh suchasne*

materialoznavstvo: fizyka, khimiia, tekhnolohii. m. Uzhhorod, (Ukraine). P. 245–246. *Personal contribution is analysis of literary sources, conducting experimental research, processing and formatting results, writing and submitting the abstract.*

12. **Kovinchuk I.**, Haiuk N., Cavallaro G., Lazzara G., Sokolsky G. (2022) Thermogravimetric study of PE films containing TiO₂, MnO₂ photocatalysts, and their composites. *Book of abstracts of the 13 European Symposium on Thermal Analysis and Calorimetry*. Palermo, (Italy). P. 214. *Personal contribution is analysis of literary sources, conducting experimental research, processing and formatting results, writing and submitting the abstract.*

13. Svintsova A.V., Sokolsky G.V., Hlukhova P.I., **Kovinchuk I.V.**, Lazzara G., Sokolsky G. (2022) Encapsulated by Ascorbic Acid Halloysite Nanotubes combined with Rutile Nanoparticles for Cosmetic Applications. *Book of abstracts of the Ukrainian conference with international participation “Chemistry, physics and technology of surface”*. Kyiv, (Ukraine). P. 78. *Personal contribution is analysis of literary sources, conducting experimental research, data curation.*

14. **Kovinchuk I.**, Hlukhova P., Sokolskyi H. (2023) Otsinka mozhyvosti vykorystannia oksydneykh fotokatalitychnykh system dlia pisliavoiennoho vidnovlennia terytoriii [Assessment of the possibility of using oxide photocatalytic systems for post-war restoration of territories]. *Materialy konferentsii Synerhiia nauky i biznesu y povoiennomu vidnovlenni Khersonshchyny*. m. Odesa, (Ukraine). P. 391–395. *Personal contribution is analysis of literary sources, processing and formatting results, writing and submitting the abstract.*

15. **Kovinchuk I.**, Sokolsky G., Lazzara G. (2023) Single stage and simple fabrication of PE films Impregnated with halloysite nanotubes. *Book of abstracts. International Conference on Chemistry, Chemical Technology and Ecology*. Kyiv, (Ukraine). P. 60–61. *Personal contribution is analysis of literary sources, conducting experimental research, processing and formatting results, writing and submitting the abstract.*

16. P. Hlukhova, **I.V. Kovinchuk**, Dzh. Lazzara, i H. V. Sokolskyi (2023) Fotokatalitychni vlastyvoli kompozytiv oksydiv-hidroksydiv manhanu z haluazytom, syntezovanykh hidrokhimichnym metodom [Photocatalytic properties of manganese

oxide-hydroxide composites with halloysite synthesized by the hydrochemical method]. *Zbirka tez dopovidei. Mizhnarodna konferentsiia z khimii, khimichnoi tekhnolohii ta ekolohii, prysviachenii 125-richchiu KPI im. Ihoria Sikorskoho*. m. Kyiv, (Ukraine). P. 14–16. *Personal contribution is analysis of literary sources, conducting experimental research, data curation.*

17. Sokolsky G., **Kovinchuk I.**, Lazzara G., Zudina L., Hluhova P., Andriiko O. (2023) Comparison of chemical and electrodeposition pathways of manganese dioxide from NH_4^+ -containing electrolytes. *Book of abstracts. International Conference on Chemistry, Chemical Technology and Ecology*. Kyiv, (Ukraine). P. 87–88. *Personal contribution is analysis of literary sources, conducting experimental research, processing and formatting results.*

18. **Kovinchuk I.V.**, Hluhova P.I., Telina M.M., Khrebtan D.R., Vechirko E.R., Lazzara G., Sokolsky G.V. (2024) Halloysite nanotubes as components of nanocomposites with metal oxides/hydroxides. *Book of abstracts. 12th International Conference "Nanotechnologies and Nanomaterials" NANO-2024*. Uzhgorod, (Ukraine). P. 77. *Personal contribution is analysis of literary sources, conducting experimental research, processing and formatting results, writing and submitting the abstract.*

19. **Kovinchuk I.**, Hluhova P., Lazzara G., Sokolsky G. (2024) Enhanced Photocatalytic Methylene Blue Degradation by $\text{Mn}_3\text{O}_4/\text{HNT}$ -based composite material. *Book of abstracts. XXVIII Congresso Nazionale della Società Chimica Italiana*. Milan, (Italy). P. FIS-PO-005. *Personal contribution is analysis of literary sources, conducting experimental research, processing and formatting results, writing and submitting the abstract.*

SECTION 2. OBJECTS, SYNTHETIC, AND RESEARCH METHODS

2.1 Materials and reagents

The following reagents were used in this work: granules of pure low-density polyethylene (LDPE) 15803-020, P-xylene, Cyclohexane (Sigma Aldrich), MnO_2 of industrial production (Prydniprovsky Chemical Plant, Kamyanske, Ukraine); TiO_2 (anatase) produced by Institute for Problem of Material Science of NASU [46]; Polyvinylpyrrolidone K 90, Polyethylene glycol 300 from Sigma Aldrich, Halloysite $\text{Al}_2\text{Si}_2\text{O}_5(\text{OH})_4 \cdot 2\text{H}_2\text{O}$ nanotubes (I-Minerals Inc, USA and Sigma Aldrich), $\text{MnSO}_4 \cdot 5\text{H}_2\text{O}$, $(\text{NH}_4)_2\text{SO}_4$. All reagents were at least of chemically pure grade. These reagents were used as auxiliary: KCl ; BaSO_4 ; BaCl_2 ; KOH ; NaOH ; NH_4OH ; H_2SO_4 ; H_2O_2 . Distilled water was used to prepare the solutions.

2.2. Synthesis methods of photocatalysts studied

2.2.1 Chemical synthesis of manganese oxides and oxidehydroxides with halloysite composite materials

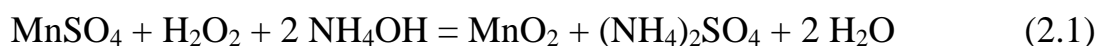
To expand the possibilities of electrodeposition well known for manganese oxide synthesis and the spectrum of the studied samples, a method of chemical synthesis was used from electrolyte solutions similar to those used in previous works, which differed in the acidity of the medium $\text{pH} = 5-6$ and higher. A typical synthesis of oxide materials was as follows: dissolution of 13.85 g of $\text{MnSO}_4 \cdot 5\text{H}_2\text{O}$ in 100 ml of water, adding $(\text{NH}_4)_2\text{SO}_4$ to achieve a ratio of ions $\text{Mn}^{2+}:\text{NH}_4^+$ equal 1:2 for samples CS-2, 3, 4, 6, 8, 9. Halloysite nanotubes of 1 g for samples CS-1, 2, 6, and 7 were also added. For samples with HNT, 1 hour of vacuuming was applied to achieve complete removing of air and fill the lumen with a solution. The addition of ammonium hydroxide was done dropwise alternately with hydrogen peroxide to maintain the required acidity level until the stoichiometric amount of ammonium hydroxide was added. Thus, it was determined that the required amount of hydrogen peroxide exceeds the stoichiometric amount by 4 times, considering the occurrence of a side reaction of catalytic decomposition of hydrogen peroxide on the

surface of manganese oxides. Only for sample CS-3 the air was used as an oxidant instead of H_2O_2 . The product was centrifuged, washed with distilled water and dried at 160°C until constant mass. Table 2.1 shows the composition of the reaction mixture and conditions of synthesis for each sample.

Table 2.1. Composition of reaction mixture and conditions of synthesis of CS series of samples

Sample name	Sample description	HNTs content, g	$[\text{NH}_4^+]$ 1.5 mol·L ⁻¹	pH
CS-1	Mn-HNT-pH10- H_2O_2	1		10
CS-2	Mn- NH_4^+ -HNT-pH10- H_2O_2	1	+	10
CS-3	Mn- NH_4^+ -pH10		+	10
CS-4	Mn- NH_4^+ -pH5-6- H_2O_2		+	5-6
CS-5	Mn-pH5-6- H_2O_2			5-6
CS-6	Mn- NH_4^+ -HNT-pH5-7.5- H_2O_2	1	+	5-7.5
CS-7	Mn-HNT-pH5-6- H_2O_2	1		5-6
CS-8	Mn- NH_4^+ -HNT-pH5-7.5- H_2O_2 slow (72h)		+	5-7.5
CS-9	Mn- NH_4^+ -HNT-pH5-8- H_2O_2 express (2h)		+	5-8

Possible synthesis route:



2.2.2 Electrodeposition of manganese dioxide materials

Electrodeposition of manganese dioxide samples was performed using Platinum electrodes, with the cathode area being approximately 3 to 5 times larger than that of the anode. The current was set at $10 \text{ A}\cdot\text{dm}^2$. Samples were synthesized from the MnSO_4 solution with the addition of dopant NH_4^+ and Cr^{3+} ions following the procedure we used before with fluoride electrolytes [83]. Subsequently, the methodology was created taking

into account the purpose of the work and literature data on the creation of nanomaterials of a given dispersion and with optimal heterojunctions.

The total volume of electrolyte was 1 L. To study the influence of acidity on the structure of samples, some electrolytes contained H_2SO_4 in different concentrations. The duration of the deposition process was 30 minutes. All samples were obtained at room temperature. Table 2.2 shows the general conditions of the synthesis procedure.

Table 2.2. Composition of electrolyte of ED series of samples

Sample	$\text{MnSO}_4 \cdot 5\text{H}_2\text{O}$ / $\text{mol} \cdot \text{L}^{-1}$	$(\text{NH}_4)_2\text{SO}_4$ / $\text{mol} \cdot \text{L}^{-1}$	H_2SO_4 / $\text{mol} \cdot \text{L}^{-1}$	$\text{Cr}_2(\text{SO}_4)_3$ / $\text{mol} \cdot \text{L}^{-1}$
ED-1	0.05	1.5	0.03	
ED-2	0.05	0	0.03	
ED-3	0.1	1.5	0.03	
ED-4	0.1	1.5	0	
ED-5	0.05	1.5	0	
ED-6	0.1	0	0.03	
ED-7	0.1	1.5	2	
ED-8	0.05	1.5	2	
ED-9	0.1	0	2	
ED-10	0.05	0	2	0.01
ED-11	0.1	0	2	0.01
ED-12	0.1	1.5	2	0.01
ED-13	0.1	0	0.03	0.01

After electrodeposition, samples were left in the electrolyte solution overnight for complete precipitation. Then the sediments were thoroughly washed with distilled water until a negative reaction to sulfate ions with subsequent drying at a temperature of 150 °C to a constant mass.

2.2.3 Preparation of PE/TiO₂ and PE/TiO₂&MnO₂ films

The film preparation process was adapted from [84] and schematically illustrated in Fig. 2.2. First, 0.5 g of PE granules were added to 25 ml of p-xylene, followed by heating in an oven at 110°C for 40–45 minutes. Once the PE melted, inorganic components — pure TiO₂ and TiO₂/MnO₂ mixture in ratio 1:1 were introduced at a concentration of 1% by mass. Sonication was performed for 60 minutes at a power of 50 W. The dispersions were then poured into a 9 cm diameter glass Petri dish. Finally, the solvent casting method was employed at 110°C to produce a film. The same procedure was used to prepare a film of pure PE dissolved in p-xylene. The resulting PE composite film had an average thickness of 50–70 μm. A schematic representation of the film synthesis sequence is shown in Figure 2.1.

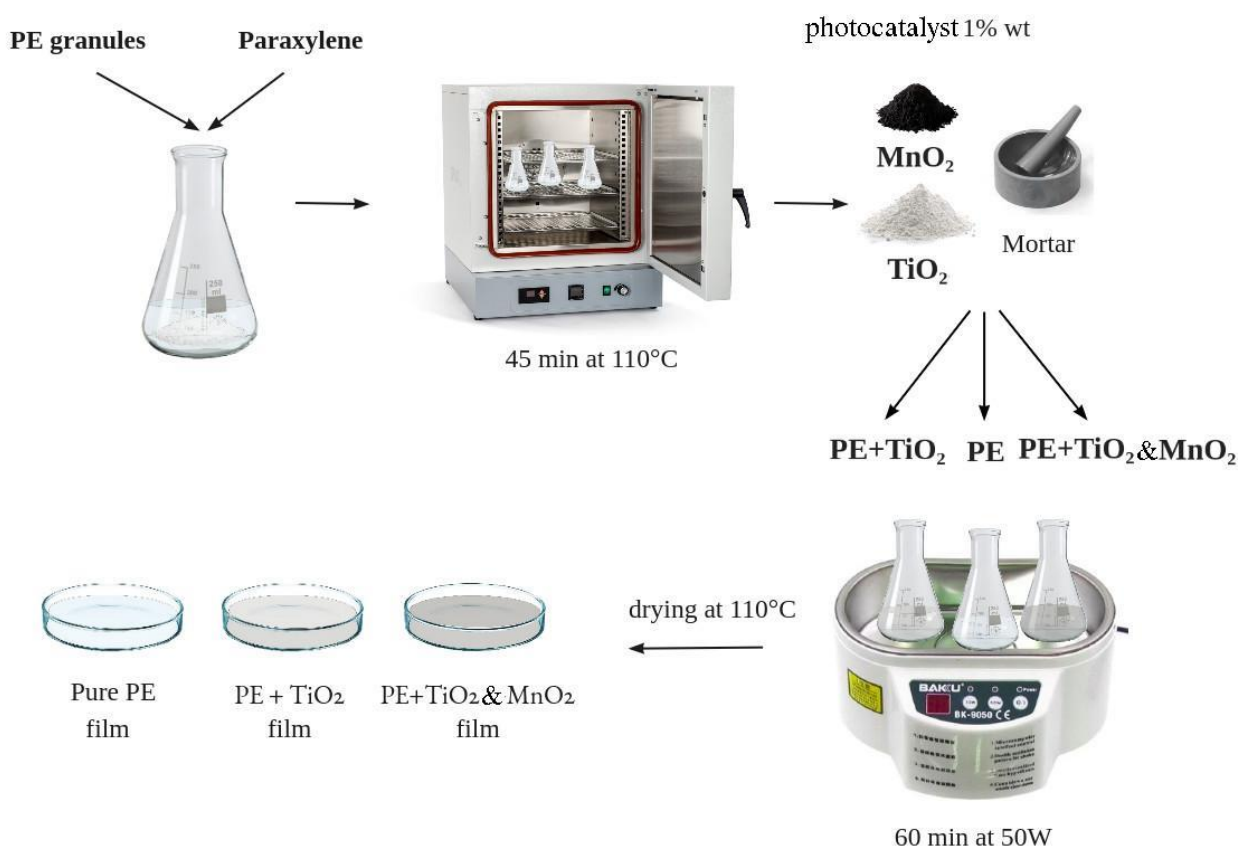


Figure 2.1. Schematic representation of the stages of film preparation.

2.2.4 Preparation of PE films decorated with HNTs

According to the literature data [85], cyclohexane was chosen as the solvent as the most suitable for PE treatment at relatively low temperatures. To achieve a uniform distribution of nanotubes in the solvent, mechanical stirring for 30 minutes, followed by ultrasonic stirring for 15 minutes, was applied before heating. Rectangular PE film samples of 12 cm² were immersed in suspension for various time intervals (60 sec. and 120 sec.) at 50 and 60 °C. The HNTs' mass content in the solvent was 3% by mass. Specific conditions of the preparation process are detailed in Table 2.3. Sample 0 was prepared under the same conditions without the addition of HNTs to compare properties.

Table 2.3. Preparation of PE film decorated with HNTs

Sample name	HNT / mass %	Temperature / °C	Immersion time / sec
0	0	50	60
1	3	50	60
2	3	50	120
3	3	60	60

2.2.5 Preparation of adhesive composition and its application for the decoration of PE films with photocatalyst

The adhesive composite was prepared by dissolving specific amount of Polyvinylpyrrolidone K90 (PVP K90) in ethanol. Following this, polyethylene glycol 300 (PEG 300) was added as a plasticizer in varying mass ratios relative to the PVP. The catalyst was incorporated in an amount equal to 1% by mass of the PE film to which the composite was applied. The optimal PVP to PEG ratio was found to be 1 to 7, while the amount of solvent varied depending on the application method. The preparation procedure included adding PVP to alcohol, after its complete dissolution the required amount of PEG and catalyst was added with constant mechanical stirring. The amount of

ethanol corresponded to 18 parts relative to the total mass of polymers. While for application with a sponge the amount of added ethanol was 15 parts. 1 g of adhesive composite, along with the corresponding quantity of catalysts, was applied to the surface of industrially produced PE films (10 cm by 10 cm in size, with an average thickness of 0.024 mm) using either the spray drying method or a sponge.

2.3 Physico-chemical research methods

2.3.1 Thermogravimetric Analysis

Thermogravimetric Analyzer Discovery TGA550 with TRIOS Software was applied for analysis of powder chemically synthesized samples. Measurements were carried out under the nitrogen and air flow of $60 \text{ cm}^3 \cdot \text{min}^{-1}$ for the sample and $40 \text{ cm}^3 \cdot \text{min}^{-1}$ for the balance. The temperature range was between 25 and 800°C . Each sample was placed in a platinum pan and heated with a heating ramp of $20^\circ\text{C min}^{-1}$ up to 800°C .

Analysis of PE film samples was performed with the same instrument under the nitrogen flow of $60 \text{ cm}^3 \cdot \text{min}^{-1}$ for the sample and $40 \text{ cm}^3 \cdot \text{min}^{-1}$ for the balance. The temperature range was between 25 and 600°C . Each sample was placed in a platinum pan and heated under the modulate temperature of 5°C min^{-1} for 200 s. Then, a heating ramp of 2°C min^{-1} was applied up to 600°C . The processed experimental data allowed us to determine the decomposition temperature (T_d) taken at the differential thermogravimetric curves and activation energy peak. The QtiPlot software was used to treat the TG data.

TG analysis combined with Differential Thermal Analysis of electrodeposited samples was performed using a Derivatograph Q1000 (MOM, Hungary) in airflow with a heating rate of 5°C min^{-1} up to 1005°C . The average mass of the sample analysed was $\sim 100 \text{ mg}$. After completing the experiment, the sample was maintained for an additional 5 min at 1005°C to ensure that the decomposition reaction was complete.

For composite PE/catalytic material, the impact of nanoparticles (TiO_2 and $\text{TiO}_2\&\text{MnO}_2$) on the thermal degradation kinetics of PE was investigated. In this context,

the findings from the e International Confederation for Thermal Analysis and Calorimetry (ICTAC) Kinetics Committee underscored the appropriateness of thermogravimetry as a method for assessing kinetic parameters, such as activation energy and pre-exponential factor, associated with the thermal degradation of both polymer and polymer/filler composites [86]. To calculate the time (t_α) required to achieve a certain conversion degree (α) of degradation at a fixed temperature (T_0) by using the following equation:

$$t_\alpha = \frac{g(\alpha)}{A \cdot \exp\left(\frac{-E}{RT_0}\right)}, \quad (2.2)$$

where $g(\alpha)$ – integral form of the reaction model, as concerns the A3 model, $g(\alpha)$ is expressed as $[-\ln(1-\alpha)]^{1/3}$.

Based on Equation (2.2), it is possible to calculate the t_a vs a functions under isothermal conditions at various temperatures. These patterns simulate the conversion degree of polyethylene films over time, enabling an examination of how the incorporation of nanofillers influences the polymer's thermal degradation. In this context, it is noted in the literature that the lifespan of polymeric materials can be predicted once a conversion degree of 0.05 is achieved [86], [87], [88]. Namely, ICTAC recommendations report that the limiting extent of decay beyond which the material becomes unusable can be defined when 5% mass loss is reached [89]. A more accurate estimation of the polymer lifetime needs to establish the correlation between degradation chemistry and materials performance, which is generally associated with mechanical properties (elasticity, toughness, adhesion, impact fracture resistance). Furthermore, changes in molecular mass and other attributes, such as transmissivity and discolouration, can be appropriate to predict the progressive material degradation of polymers.

The Ruetschi model was first proposed in 1984 for electrodeposited or chemically synthesized MnO_2 . It assumes the presence of two types of defects: substitution of Mn^{4+} with Mn^{3+} producing so-called Coleman protons and cation vacancies (Ruetschi protons). Ruetschi protons are located near Mn^{4+} vacancies, while Coleman protons – near Mn^{3+} in the tunnels.

This model proposes to accept that vacancies appears only on the manganese sublattice and all the oxygen sublattice is complete but some oxygens are replaced with OH⁻ ions for charge compensation [90], [91].

$$(Mn^{4+})_{1-x-y}(Mn^{3+})_y(\square)_x(O^{2-})_{2-4x-y}(OH^{-})_{4x+y}, \quad (2.3)$$

where \square represents cation vacancies. Typically, the parameter x fluctuates between 0.06 and 0.08, while y ranges from 0.04 to 0.12 and represents missing Mn⁴⁺ ions. Each vacancy is coordinated with four protons (OH⁻) for charge compensation. Some protons are replaced with O²⁻ ions. Since O²⁻ has approximately same diameter, lattice parameters are not influenced [92]. Ruetschi defects may contribute to the structural complexity of γ -MnO₂ by stabilising ramsdellite structures and introducing disorder into the material.

2.3.2 Thermogravimetric Analysis combined with Mass Spectrometry

The thermogravimetric analysis was performed on a NETZSCH STA 449C instrument in Al pan. The measurements were conducted from 30 to 1005°C with 10 K·min⁻¹ gradient, after which the samples were cooled down to room temperature. The mass of initial samples was about 3.0 – 7.0 mg, and the pyrolysis process was conducted under an argon gas flow of 30 mL·min⁻¹.

2.3.3 Fourier Transform Infrared Spectroscopy

Fourier transform infrared (FTIR) spectra of synthesized samples were determined using a Frontier FTIR spectrometer (PerkinElmer) at 25°C in the wavenumber range between 400 and 4000 cm⁻¹. KBr pellets were employed for FTIR analyses. An average of 15 scans per sample using a nominal resolution of 4 cm⁻¹ was registered.

For composite PE/catalysts samples the carbonyl index (CI) is a widely utilized metric for quantifying the extent of photooxidation in polyethylene, as referenced in [93]. This methodology is equally applicable to other functional groups formed as intermediates during degradation, such as hydroxyl groups (denoted as HI) or to the characteristic absorption bands of newly formed degradation products, such as the one at 1177 cm⁻¹ (denoted as NI), which is indicative of C — O stretching vibrations. The calculation of CI and HI for various PE films involves normalizing the intensity of the

specific absorption bands—namely, the C = O stretching vibration band at 1720 cm⁻¹ and the OH stretching vibration band at 3430 cm⁻¹ with respect to the intensity of the isolated PE band at 720 cm⁻¹, as detailed in literature sources [94], [95], [96], [97]. The NI was determined using a procedure similar to those used for calculating CI and HI.

2.3.4 X-ray diffraction and X-ray Fluorescence analyses

The phase composition of chemically synthesised samples was analyzed with X-ray diffractometer (Rigaku, MiniFlex600) with a CuK α radiation source. The wavelength of the X-ray beam was 0.15406 nm, the tube voltage 40 kV, tube current 15 mA. The diffractograms were recorded at a scanning angle between 7 to 70° using a scanning rate of 10 °/min and a step size of 0.02°. The instrument accuracy was $\pm 0.02^\circ$ (Palermo, Italy).

For qualitative and quantitative phase analysis and crystal structure determination of electrodeposited samples X-ray diffractometer (BRUKER AXS D4 ENDEAVOR) with a CuK α radiation source ($\lambda=0.15406$ nm) were used with the tube voltage 40 kV, tube current 30 mA. The diffractograms were recorded at a scanning angle between 5 to 60° using a step size of 0.04° (Ljubljana, Slovenia).

The calculation of the average crystallite size (D , nm) of the phases was carried out automatically according to the analysis data using Scherrer's formula:

$$D = \frac{K \cdot \lambda}{\beta \cdot \cos \theta}, \quad (2.4)$$

where K is the Scherrer's constant (0.89), λ is the wavelength of X-ray radiation, nm, β the width at half height of maximum peaks, rad, θ is a diffraction angle.

X-ray Fluorescence (XRF) Spectrometry was carried out by an Olympus Innov-X DS-2000 Delta (Palermo, Italy).

2.3.5 ζ -potential and Dynamic light scattering analysis (DLS)

ζ -potential and dynamic light scattering measurements were performed in 0.001 mass % aqueous dispersions by a Zetasizer NANO-ZS (Malvern Instruments) at $25 \pm 0.1^\circ\text{C}$. For ζ -Potential experiments, a disposable folded capillary cell was used. Analysis of the intensity of scattered light made it possible to obtain data on the

hydrodynamic diameter of the particles and their ζ -potential. These results provided a description of the particle sizes and surface charge properties.

2.3.6 UV-Vis spectroscopy

Absorption spectra of dye solutions were recorded using a Specord S600 spectrophotometer (Analytik, Jena, Germany) to investigate the degradation level. Distilled water served as both the solvent and the reference solution. Quartz cuvettes were used for the measurements. The spectra were recorded in the range of 200 – 800 nm with a step of 1 nm at ambient temperature. Photometric accuracy of the instrument is 0.001 at $A = 1$.

2.3.7 Diffuse reflectance spectroscopy. Band gap calculation

UV-Vis-NIR diffuse reflectance spectra were recorded on samples diluted in BaSO_4 using the ISR-3100 integrating sphere attachment mounted in the Shimadzu UV-3600 UV-VIS-NIR spectrophotometer. Diffuse reflectance spectra of the prepared samples were recorded in the range 200-2000 nm with sampling interval 1 nm and slit width 20 nm. Barium sulfate was used as a standard. 12 mg of each photocatalyst powder was well ground with 0.5 g of BaSO_4 , placed in the center of filled with BaSO_4 sampling plate and pressed with help of glass cylinder (Fig. 2.2). The background reflectance of BaSO_4 (reference) was measured before.



Figure 2.2. Diluted by BaSO_4 Sample in 12/500 ratio by mass (at the top) placed on BaSO_4 powder in a metallic holder for DRS measurements.

Determining the energy of the band gap according to the Kubelka-Munk theory [98] is performed by plotting a dependence $(h\nu \cdot F(R_\infty))^{1/n}$ on $h\nu$ (eV) and extrapolation of the linear part along the energy axis. The parameter n can take values from 0.5 to 3 depending on the nature of the transition. In our work, the parameters 0.5 for direct allowed and 2 for indirect allowed transition were used.

The energy of each photon is determined by the wavelength of the light, as given by formula:

$$E = \frac{hc}{\lambda}, \quad (2.5)$$

where h is a Planck constant (6.626×10^{-34} J/s), c is velocity of light (2.998×10^8 m s⁻¹), λ represents the wavelength of the light, nm.

The Kubelka-Munk function $F(R_\infty)$ was calculated as:

$$F(R_\infty) = \frac{K}{S} = \frac{(1-R_\infty)^2}{2R_\infty}, \quad (2.6)$$

$$K = (1 - R)^2, \quad (2.7)$$

$$S = 2R, \quad (2.8)$$

where R_∞ diffuse reflectance of the sample relative to the reflectance of a standard, K is the molar absorption coefficient, S is the scattering factor.

Another important parameters to be calculated were E_{CB} – energy of highest occupied electronic level and E_{CB} , which is a conduction band potential measure of the electron affinity of the compound. The values of these energies are related to each other and the width of the band gap energy by the following relation:

$$E_{CB} = E_{VB} + E_g, \quad (2.9)$$

According to Butler and Ginley [99] for a semiconductor the bulk electronegativity (χ) corresponds to the halfway between the bottom of the conduction band and the top of the valence band:

$$\chi = \frac{1}{2} \cdot (A_f + I), \quad (2.10)$$

where A_f is the atomic electron affinity and I is the first ionisation potential.

The electronegativity of a component (MaXb) can be considered as:

$$\chi = (\chi_M^a \cdot \chi_X^b)^{1/(a+b)}, \quad (2.11)$$

The Butler-Ginley relation for calculating the conduction band potential is defined as follows:

$$E_{VB} = E_0 - \chi - \frac{1}{2} \cdot E_g, \quad (2.12)$$

where E_0 is the energy of free electron on the hydrogen scale 4.5 eV.

2.3.8 Water Contact Angle Measurements

The measurement of contact angles was conducted utilizing an optical contact angle measuring device (OCA 20, Data Physics Instruments), which was outfitted with a high-resolution CCD camera. Data acquisition and analysis were facilitated by the SCA 20 software. Films of rectangular shape (7×20 mm) were affixed to a flat solid base using double-sided adhesive tape. The contact angle (θ) of water droplets in air was determined via the sessile drop technique, whereby a droplet of water (10.0 ± 0.5 μ l) was deposited on the film's surface. The experiments were conducted at a temperature of $25.0 \pm 0.1^\circ\text{C}$ for both the support and the syringe used for droplet injection. The capture of images was done at a frequency of 50 frames per second, and at least two droplets were analyzed for each film sample. Reported are the mean contact angle values along with their standard deviations for the initial water contact angles.

2.3.9 SEM and SEM combined with EDS analysis

The ethanol suspension of a sample was sonicated for 3 minutes in a sonication bath at 37 kHz and 100% power (ELMA, Elmasonic P). The drop of suspension was poured off by a micropipette onto a heated at 85°C disk to form small spot that immediately dries with good adhesion to the disk. The carbon coating of the disk with samples of up to 6 nm thickness was created by Gatan 682 precision etching system. Scanning Electron Microscope of ThermoScientific, Verios G4HP was used to take SEM images.

Scanning electron microscopy and energy-dispersive X-ray spectroscopy (SEM/EDS) were carried out with the aim of obtaining elemental composition of the samples. Measurements were done using Quanta 650 Thermo Scientific SEM Oxford equipped Ultim Max 40 detector. Sample preparation is depicted on Fig. 2.3 included the preparation of a compressed tablet from a sample powders with a diameter of 3 mm and a height of approximately 1 mm. The tablets were sprayed with a 6 nm carbon layer. The analyzed area was about $600 \times 500 \mu\text{m}$.



Figure 2.3. Electrodeposited Samples prepared for EDS analysis.

2.3.10. Dynamic mechanical analysis

Dynamic mechanical analysis was carried out utilizing the DMA Q800 system from TA Instruments. The procedure involved conducting tensile tests with an applied stress increase of 1 MPa per minute at a controlled temperature of $25.0 \pm 0.5 \text{ }^{\circ}\text{C}$. During these tests, key mechanical properties of the films were assessed, including the elastic modulus, tensile strength (identified as the stress level at which initial fracture occurs in the sample), percentage elongation at break, and the yield point.

2.3.11 BET analysis

Surface areas of the materials were determined using the Brunauer–Emmett–Teller (BET) method from N₂ adsorption and desorption isotherms which were measured on a Gemini II 2370 Micromertics analyzer (Ljubljana, Slovenia).

2.4. Methods for evaluation of photocatalytic activity

2.4.1. Photocatalytic degradation of PE films

Study of the degradation process under the influence of UV radiation included exposure of the films to light of a wavelength of 280 nm and monitoring of the mass loss of the films after every 10 hours of irradiation. For irradiation, an OUFK-01 lamp with a power of 6 W was used at ambient air and temperature in a lamp-housing box (50 cm × 40 cm × 30 cm). The distance between the source of light and film was maintained at 5 cm. The accuracy of analytical balance XAC 220/C used was of 0.0001 g.

2.4.2 Photocatalytic degradation and adsorption of organic dyes (Methylene Blue, Congo Red)

The degradation of dyes was studied under UV irradiation and compared with results obtained in dark conditions. For this experiment, 50 ml of a model dye solution with a concentration of 6 mg/L for Methylene Blue and 40 mg/L for Congo Red with the addition of 0.025 g of photocatalyst was irradiated using a UV-A lamp (Guangzhou Accurates) with a power of 40 W and a wavelength of 365 nm. The distance between lamp and surface of solution was 8 cm. After a certain period of irradiation, 3ml aliquots were taken and the light absorption intensity was measured at the wavelength of maximum absorption of the dye (λ_{max}), namely 664 nm for Methylene Blue and 498 nm for Congo Red. Furthermore, the concentrations in the liquor were determined using a standard curve. The change in absorption intensity gave us information about the degree of degradation of the dye solution and also allowed us to calculate the kinetic parameters of the degradation process.

Following equations were employed for estimation the degree of dye degradation:

$$Removal = \frac{A_0 - A_t}{A_0} \cdot 100\% , \quad (2.13)$$

where A_0 the initial absorbance of the dye solution, A_t the absorbance of the dye solution after UV-light irradiation at time t .

The photocatalytic reaction of dye degradation may be described by the first order kinetics model:

$$\ln C_t = k_1 t + \ln C_0 \quad (2.14)$$

or second order :

$$\frac{1}{C_t} = k_2 t + \frac{1}{C_0} , \quad (2.15)$$

C_0 is the initial concentration of the dye, mg/L, C_t is the concentration at time t , mg/L, k_1 degradation rate constant for the first-order, k_2 degradation rate constant for the second-order model.

To study the kinetics of photodegradation of dyes, curves of the parameters $\frac{1}{C_t}$ and $-\ln C_t$ depending on time were plotted. In case of the best fit of correlation coefficient R^2 (as close to 1 as possible) and chi-square χ^2 (as low as possible) the model will be considered suitable. The value of k was calculated using the slope of the plot.

Additionally adsorption experiments were conducted to evaluate adsorption capacities of pristine HNT [100]. A stock solution of 0.1 g/L Congo red and 0.03 g/L Methylene Blue was prepared in 50 ml of distilled water. The required concentrations of the dye solution were obtained by appropriate dilution of the stock solution. 0.01 g of HNT was added to 25 mL of Congo red solutions of 10, 20, 40, 50 and 60 mg/L at pH 6. In the same way 0.01g of HNTs were addad to 25 ml of Methylene Blue solutions of 1.5, 3, 6, 9, 12 mg/L. The mixture was stirred at ambient temperature for 2 h to ensure the adsorption-desorption equilibrium between theadsorbent and dye, and then centrifuged at 5000 rpm for 20 min to remove HNTs. All the experiments were carried out at an ambient temperature of (23 ± 2) °C. The concentration of the dye solutions before and after adsorption was measured using UV-visible spectrophotometer at 498 nm for CR and 664 nm for MB.

The adsorption percentage and the equilibrium adsorption capacity of the adsorbent (q_e) were calculated as follows:

$$\text{Adsorption} = \frac{(C_0 - C_e)}{C_0} \times 100 \% , \quad (2.16)$$

$$q_e = (C_0 - C_e) \times \frac{V}{m} , \quad (2.17)$$

where C_0 represents initial concentration of dye solution, mg/L, C_e is the equilibrium concentration of the adsorbate, mg/L, V is the volume of the dye solution, L, m is the mass of the adsorbent, g.

Adsorption capacity is affected by various factors, such as surface area of the adsorbent, the pore size distribution, the surface chemistry of the adsorbent, the temperature and pH of the solution.

Analysis of experimental data for compliance with first and second order models will allow determining kinetic parameters of the adsorption process. The first-order kinetics model assumes that mass transfer is the rate-limiting mechanism, whereas the second-order model attributes the rate limitation to chemical adsorption [101].

Equations for the first order in classical and integrated form:

$$q_t = q_e \cdot (1 - e^{-k_1 t}), \quad (2.18)$$

$$\ln(q_e - q_t) = -k_1 t + \ln q_e, \quad (2.19)$$

Equations for second order in classical and linearized form:

$$q_t = \frac{k_2 q_e^2 t}{1 + t k_2 q_e}, \quad (2.20)$$

$$\frac{t}{q_t} = \left(\frac{1}{q_e}\right) \cdot t + \frac{1}{k_2 q_e^2}, \quad (2.21)$$

For PSO model initial adsorption rate h_0 can be additionally calculated according to formula

$$h_0 = k_2 \cdot q_e^2, \quad (2.22)$$

where q_e is the amount adsorbed (mg/g) at equilibrium, t time, min, q_t amount adsorbed at time t , mg/g, k_1 rate constant for the first order model, min^{-1} , k_2 rate constant for the second order model, $\text{g} \cdot \text{mol}^{-1} \cdot \text{min}^{-1}$, h_0 initial adsorption rate, $\text{mol} \cdot \text{g}^{-1} \cdot \text{min}^{-1}$.

Adsorption isotherms were studied using Langmuir and Freundlich isotherm models [102]. Langmuir isotherm describes dynamic equilibrium between rate of the monolayer

adsorption and desorption. According to this model the amount of adsorbed substance is directly proportional on the uniform surface of the adsorbent available for adsorption. Desorption in turn depends on already occupied by pollutant molecules surface of adsorbent. It assumes the presence of dynamic equilibrium between adsorption and desorption.

$$\frac{C_e}{q_e} = \frac{1}{q_m \cdot K_L} + \frac{C_e}{q_m}, \quad (2.23)$$

where q_m maximum amount adsorbed, mg/g, C_e final concentration of dye in solution, mg/g, K_L Langmuir or equilibrium constant for adsorption, L/g.

In turn, the Freundlich model describes the behaviour of a multilayer of pollutant molecules on the non uniform surface [103]. Which results in exponential decrease in the energy distribution of the adsorbed sites.

$$\ln q_e = \ln K_F + \frac{1}{n} \ln C_e, \quad (2.24)$$

where K_F and n are Freundlich constants representing the adsorption capacity (L/mg) and adsorption intensity respectively, which indicates the degree of heterogeneity of the adsorbent surface and the distribution of active sites with different adsorption energies.

Conclusions to Section 2

The research methods used in the work are described, namely: TG, FTIR, XRD, DLS, EDS, Dynamic Mechanical analysis, Scanning Electron microscopy and Transmission electron microscopy, Water Contact Angle measurements, UV-Vis and Diffuse Reflectance spectroscopy as well as research methods of photocatalytic removal of dyes and UV degradation of polyethylene films. Methods for the chemical and electrochemical synthesis of composite materials of manganese oxides, both alone and with the addition of halloysite nanotubes, are described in detail.

The results of the research in this section are presented in the following publications:

Articles:

1. **I. Kovinchuk**, N. Haiuk, G. Lazzara, G. Cavallaro, and G. Sokolskyi, 'Enhanced photocatalytic degradation of PE film by anatase/ γ -MnO₂', *Polym. Degrad. Stab.*, vol.

210, p. 110295, Apr. 2023, doi: 10.1016/j.polymdegradstab.2023.110295. The journal is cited by the scientometric databases SCOPUS and Web of Science (Q1). *Personal contribution is analysis of literary sources, conducting experimental research, processing and formatting results, writing the article.*

2. **I. Kovinchuk**, G. Sokolsky, and G. Lazzara, ‘Single-stage and simple fabrication of PE films decorated with halloysite nanotubes’, *KPI Sci. News*, vol. 136, no. 1–4, Apr. 2024, doi: 10.20535/kpissn.2023.1-4.297046. Journal adopted by the Ministry of Education & Science of Ukraine as professional ones in specialty 161 Chemical technology and engineering. *Personal contribution is analysis of literary sources, conducting experimental research, processing and formatting results, writing and submitting the article.*

3. **I. V. Kovinchuk**, G. Lazzara, Ragulya, A.V., M. M. Kržmanc, and G. V. Sokolsky, ‘Evaluation of nanoparticles’ size characteristics of manganese oxide/hydroxide based photocatalysts’, *Visnyk Kherson Natl. Tech. Univ.*, vol. 4, no. 91, pp. 52–59, 2024.

Journal adopted by the Ministry of Education & Science of Ukraine as professional ones in specialty 161 Chemical technology and engineering. *Personal contribution is analysis of literary sources, conducting experimental research, processing and formatting results, writing and submitting the article.*

Conference materials:

4. **Kovinchuk I.**, Lazzara G., Cavallaro G., Sokolsky G. MnO₂/TiO₂ Nanopowders-Assisted Photocatalytic Degradation of Low-Density Polyethylene Films, 2022 *IEEE 12th International Conference Nanomaterials: Applications & Properties*, 2022 P. 10nee–27. <https://doi.org/10.1109/NAP55339.2022.9934707>. *Personal contribution is analysis of literary sources, conducting experimental research, processing and formatting results, writing and submitting the abstract.*

5. Sokolsky G.V., **Kovinchuk I.V.**, Ragulya A.V., Spreitzer M., Kržmanc M.M. Electrodeposition of nanodispersed α/δ - & γ/α -manganese dioxide composites for visible light photocatalytic applications, *10th Ukrainian Congress of Electrochemistry Achievements Problems and Prospects*, 2, 2024, P. 32-36. <https://doi.org/10.33609/elchimcongr.2024.09.1-210>. *Personal contribution is analysis*

of literary sources, conducting experimental research, processing and formatting results, writing.

Abstracts of conference presentations:

6. Haiuk N.V., Sokolsky H.V., Svyntsova A.V., **Kovinchuk I.V.** (2021) Fotokatalitychna destruktsiia polietylenovykh plivok dioksydamy tytanu i manhanu. [Photocatalytic destruction of polyethylene films by titanium and manganese dioxides] *Materialy XV mizhnarodnoi naukovo-tekhnichnoi konferentsii «AVIA-2021»*. m. Kyiv, (Ukraine). P. 19.1-19.4. *Personal contribution is analysis of literary sources, conducting experimental research, processing results.*

7. Haiuk N.V., Dmitriieva Y., **Kovinchuk I.V.**, Sokolsky H.V. (2021) Tverdofazna fotokatalitychna destruktsiia polietylenovykh plivok oksydnymy materialamy manhanu ta tytanu [Solid-phase photocatalytic destruction of polyethylene films by manganese and titanium oxide materials]. *Materialy I Mizhnarodnoi naukovo konferentsii «Aktualni problemy khimii, materialoznavstva ta ekologhii»*. m. Luts'k, (Ukraine). S. 119–122. *Personal contribution is analysis of literary sources, conducting experimental research, processing and formatting results.*

8. **Kovinchuk I.V.**, Sokolskyi H.V., Haiuk N.V. (2021) Vyznachennia serednoho diametru nanostryzheniv Manhan (IV) oksydu riznoho pokhodzhennia v prohramnomu seredovyshchi ImagJ ta SciDAVi [Determination of the average diameter of Manganese (IV) oxide nanorods of various origins in the ImagJ and SciDAVi software environments]. *Materialy shkoly-konferentsii molodykh vchenykh suchasne materialoznavstvo: fizyka, khimiia, tekhnolohii*. m. Uzhhorod, (Ukraine). P. 245–246. *Personal contribution is analysis of literary sources, conducting experimental research, processing and formatting results, writing and submitting the abstract.*

9. **Kovinchuk I.**, Haiuk N., Cavallaro G., Lazzara G., Sokolsky G. (2022) Thermogravimetric study of PE films containing TiO₂, MnO₂ photocatalysts, and their composites. *Book of abstracts of the 13 European Symposium on Thermal Analysis and Calorimetry*. Palermo, (Italy). P. 214. *Personal contribution is analysis of literary sources, conducting experimental research, processing and formatting results, writing and submitting the abstract.*

10. **Kovinchuk I.**, Sokolsky G., Lazzara G. (2023) Single stage and simple fabrication of PE films Impregnated with halloysite nanotubes. *Book of abstracts. International Conference on Chemistry, Chemical Technology and Ecology*. Kyiv, (Ukraine). P. 60–61. *Personal contribution is analysis of literary sources, conducting experimental research, processing and formatting results, writing and submitting the abstract.*
11. P. Hlukhova, **I.V. Kovinchuk**, Dzh. Lazzara, i H. V. Sokolskyi (2023) Fotokatalitychni vlastyivosti kompozytiv oksydiv-hidroksydiv manhanu z haluazytom, syntezovanykh hidrokhimichnym metodom [Photocatalytic properties of manganese oxide-hydroxide composites with halloysite synthesized by the hydrochemical method]. *Zbirka tez dopovidei. Mizhnarodna konferentsiia z khimii, khimichnoi tekhnolohii ta ekolohii, prysviachenii 125-richchii KPI im. Ihoria Sikorskoho*. m. Kyiv, (Ukraine). P. 14–16. *Personal contribution is analysis of literary sources, conducting experimental research, data curation.*
12. **Kovinchuk I.V.**, Hlukhova P.I., Telina M.M., Khrebtan D.R., Vechirko E.R., Lazzara G., Sokolsky G.V. (2024) Halloysite nanotubes as components of nanocomposites with mn oxides/hydroxides. *Book of abstracts. 12th International Conference "Nanotechnologies and Nanomaterials" NANO-2024*. Uzhgorod, (Ukraine). P. 77. *Personal contribution is analysis of literary sources, conducting experimental research, processing and formatting results, writing and submitting the abstract.*
13. **Kovinchuk I.**, Hlukhova P., Lazzara G., Sokolsky G. (2024) Enhanced Photocatalytic Methylene Blue Degradation by Mn_3O_4 /HNT-based composite material. *Book of abstracts. XXVIII Congresso Nazionale della Società Chimica Italiana*. Milan, (Italy). P. FIS-PO-005. *Personal contribution is analysis of literary sources, conducting experimental research, processing and formatting results, writing and submitting the abstract.*

SECTION 3. PHYSICOCHEMICAL AND MECHANICAL PROPERTIES OF STANDARD MATERIALS OF MnO_2 , TiO_2 , PRISTINE HNTs, AND COMPOSITE PE FILMS

3.1 Characterization of standard materials of TiO_2 , MnO_2 in this study, and pristine HNTs

TiO_2 (anatase) produced by the Institute for Problem of Material (IPM) Science of NASU. The powder consists of soft aggregates ranging in size from 50 nm to 500 nm, the average size of non-aggregated particles of which is 10 nm (Fig. 3.1 a). Average surface area determined by BET method is $53.67 \text{ m}^2\cdot\text{g}^{-1}$ with mesoporus volume around $0.2325 \text{ cm}^3\cdot\text{g}^{-1}$. The band gap calculated from absorption spectrums in waverange 190–400 nm was reported as equal to 2.75 eV [46]. This material showed high efficiency of the photoelectrocatalytic process for aminoazodyes and PE degradation in comparison with the widely known and used P25 Evonic [104].

MnO_2 of industrial production was provided by Prydniprovsky Chemical Plant (PCP), Kamyanske, Ukraine. The average size of nanoparticles was estimated as $40 \pm 5 \text{ nm}$ (Fig. 3.1 b) [105], the phase composition was determined in the previous study as a ramsdellite-type. MnO_2 NPs are formed by the aggregated needle-like crystallites with an average length of 200–1000 nm. The BET surface area is relatively low ($20\text{--}30 \text{ m}^2\cdot\text{g}^{-1}$) [106].

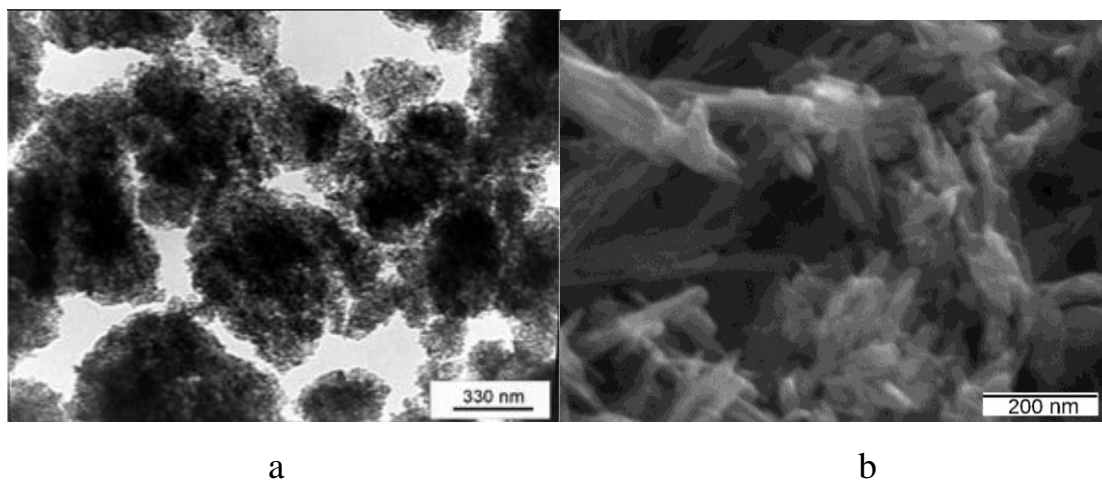


Figure 3.1 SEM image of TiO_2 from IPM NASU (Ukraine) (a) and MnO_2 from PCP (Ukraine) (b).

Halloysite from Sigma Aldrich was used in this study. A comprehensive analysis of the properties of the pure material was carried out. Figure 3.2. shows the Fourier Transform Infrared Spectroscopy curve of Halloysite used in this study.

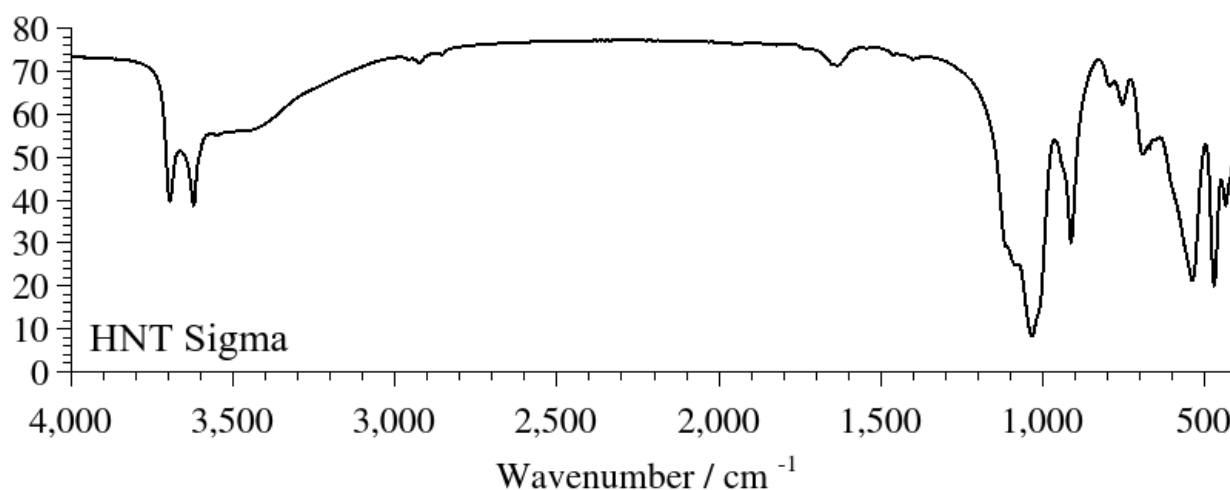


Figure 3.2. FTIR spectrum of Halloysite nanotubes (Sigma Aldrich).

According to the previous studies [107], [108], [109] characteristic bands for siloxane Si – O – Si, silanol (Si – OH), and aluminol (Al – OH) groups of HNTs were identified and listed in Table 3.1.

Table 3.1. FTIR wave numbers of functional groups vibrations of pristine HNTs.

Wavelength, cm ⁻¹	Assignment
3696	O – H stretching of inner-surface Al – OH
3622	O – H stretching of interface between Si–O tetrahedron and Al – O octahedron
1634	O – H bending vibration of the absorbed water molecules
1113	Si – O symmetrical stretching
1083	Si – O asymmetric stretching
1032	Si – O – Si in plane stretching
940	Al – OH deformation of inner surface hydroxyl groups
912	six coordinated Al – O stretching vibrations of inner

Wavelength, cm^{-1}	Assignment
	hydroxyl groups
792	Si – O – Si symmetric stretching
753	Si – O – Al stretching
690	Si – O – Al stretching
537	Si – O – Al bending vibration
470	Si – O in-plane bending vibration
434	Si – O deformation

The results of thermal analysis are well supported by previously obtained data for pure halloysite nanotubes. The raw HNT showed a mass loss between 30 °C and 200 °C (Fig 3.3), which, according to literature [110] corresponds to the moisture content and desorption of water molecules, whereas the typical interlayer water molecules removal or dehydroxylation of structural Al – OH groups can be observed between 400 and 600 °C with a peak at 505 °C. The mass loss was 13.1% in agreement with [111].

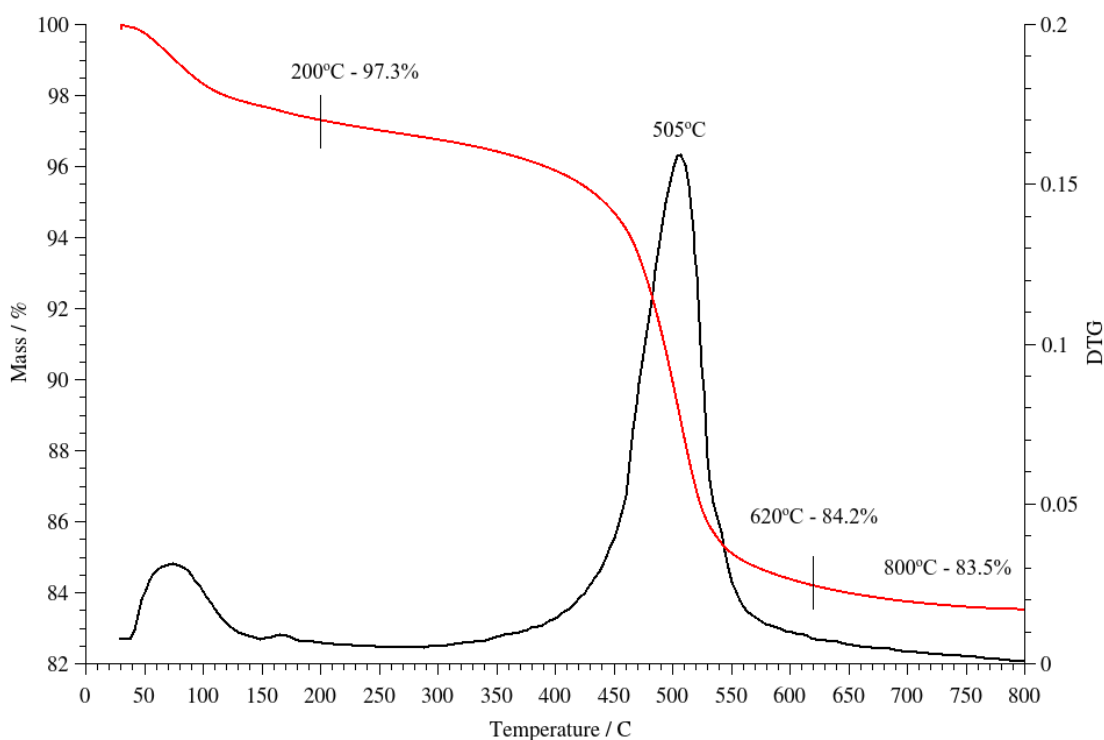


Figure 3.3. Typical thermal behaviour of halloysite nanotubes.

The study of X-ray diffraction patterns provides valuable information about the structural composition of the nanotubes that were used in the work. Characteristic reflections for dehydrated 7Å-form were registered at two theta (2θ) degrees of 12.2° corresponding to (001) basal distance of 0.73 nm, 20.0° (110/020) for basal spacing of 0.44 nm and 24.8° (002) basal spacing of 0.35 nm, 35.0° (110), 54.6° (210), and 62.5° (300) (Fig. 3.4), these data are in good agreement with data reported previously [107]. The absence of a sharp 2θ peak at 8.76° [112], suggests the absence of the 10Å form of hydrated HNTs.

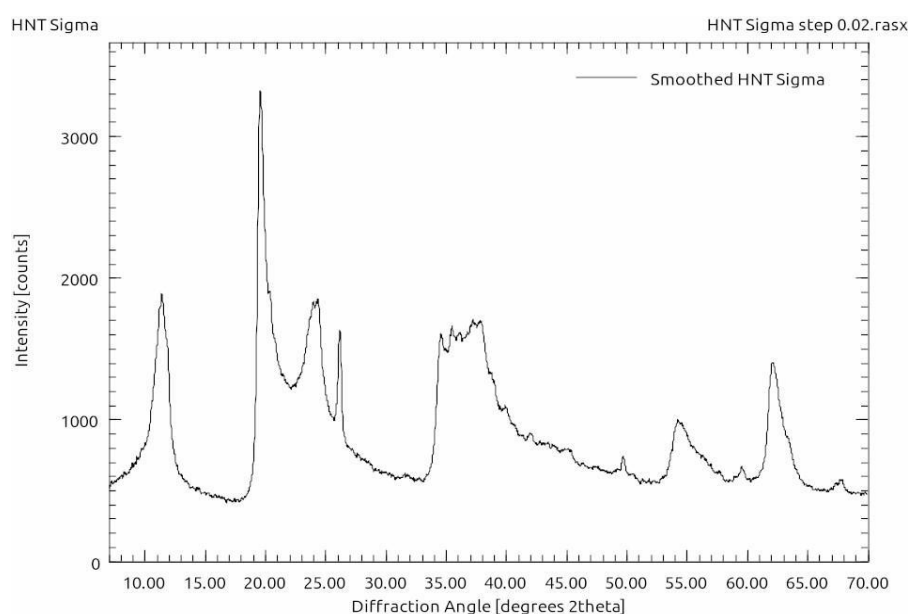


Figure 3.4. XRD pattern of Halloysite nanotubes (Sigma Aldrich).

3.2 Characterization of PE, PE/TiO₂, and PE/TiO₂&MnO₂ films: wettability and tensile performance

Figure 3.5 represents images of water droplets along with the measured contact angles just after placement on films of PE, PE/TiO₂, and PE/TiO₂&MnO₂. Generally, the contact angles are around 90 degrees, indicating the films' hydrophobic nature. It was noted that the addition of inorganic fillers does not significantly affect the wettability of PE, suggesting a slight increase in hydrophobicity, possibly due to enhanced surface roughness by the composite materials.



Figure 3.5. Images of water droplets and the corresponding contact angle values just after their deposition on the surface of (a) PE, (b) PE/TiO₂, (c) PE/TiO₂&MnO₂.

The impact of nanofiller incorporation on the mechanical strength of PE-based films was analyzed through DMA. The stress versus strain curves derived from this analysis are shown in Figure 3.6, and the corresponding mechanical properties are presented in Table 3.2.

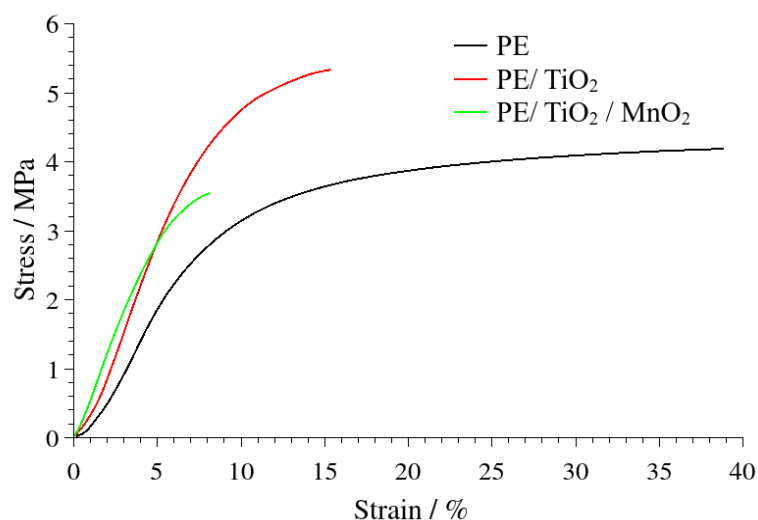


Figure 3.6. Tensile strength versus stress curves of PE composite films.

Table 3.2. Tensile properties of PE, PE/TiO₂, and PE/TiO₂&MnO₂ films.

	Elongation at break / %	Stress at break point / MPa	Elastic modulus / MPa	Yield point / %
PE	21.91	3.93	61.4	7.56
PE/TiO ₂	14.19	5.27	82.08	7.64
PE/TiO ₂ &MnO ₂	8.1	3.54	63.49	5.42

Referencing the literature [113], it was observed that nanoparticle addition leads to a reduction in ultimate elongation, a phenomenon that may be explained by the interaction between PE and nanofillers hindering the movement of polymer chains [114]. Contrarily, the PE filling with TiO_2 improved the elastic modulus and the stress at the breaking point, while the presence of TiO_2 and MnO_2 did not generate any significant variations in these parameters.

3.2 Characterization of PE films decorated with halloysite nanotubes

The TG curve of pure halloysite nanotubes shows one mass loss of 14.95 mass% [115] attributed to the removal of the interlayer water molecules from the HNT structure. Sample 0-3 showed a significant mass reduction of about 90-100 % from 400° to 520 °C as a consequence of the PE thermal degradation (Fig. 3.7).

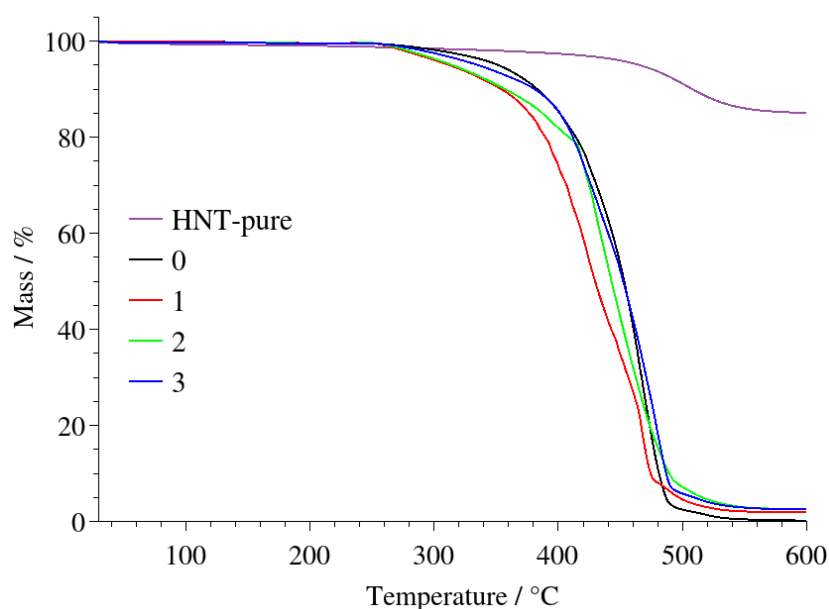


Figure 3.7 Mass loss of films under N_2 flow.

Moreover, thermogravimetric data provided the mass fraction of HNT in composite films. Sample 2, immersed in HNT suspension in cyclohexane at 50 °C for 120 seconds, showed the most considerable residual mass among all samples (Table.3.3). The calculated HNT content was equal to 2.83 mass% corrected on water loss. Sample 3 immersed at 60 °C for 60 sec, showed a slightly lower HNT content of 2.74 %. PE degradation temperature (T_d) was calculated from the maximum of the DTG peaks. It can be pointed out that T_d for Sample 2 is shifted towards lower temperatures 37° compared

with pure PE, while for Sample III the main degradation peak is shifted towards higher temperature for 14° compared with pure PE.

At the same time, Sample 2 showed the highest hydrophilicity with a contact angle 77.11° while Sample 0 demonstrated a contact angle of 99.24° (Fig. 3.8 a). It can be explained by the presence of hydrophilic HNTs on the film's surface. Which is in good agreement with TGA analysis. Sample 3, in turn, remains hydrophobic despite the almost equal content of nanotubes (Fig. 3.8 d). Possibly due to the higher treatment temperature, nanotubes were included into a deeper layer of a film.

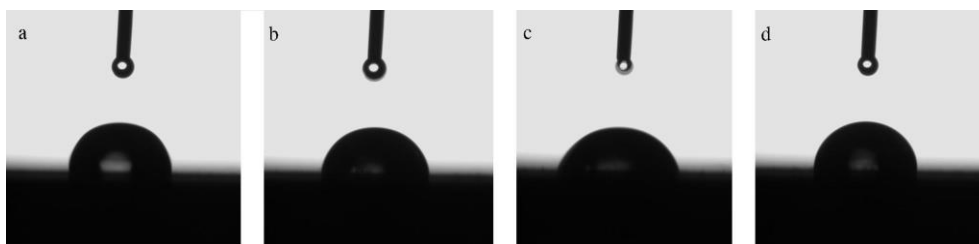


Figure 3.8 Images of droplets just after their deposition onto the surface of (a) Sample 0, (b) Sample 1, (c) Sample 2, (d) Sample 3.

Table 3.3. Thermogravimetric and wetting properties of treated samples

Sample name	RM ₆₀₀ , %	Contact angle, °
0	0.18	99.24 ± 0.76
1	1.93	85.21 ± 8.81
2	2.59	77.11 ± 4.71
3	2.51	89.18 ± 4.03

Dynamic mechanical analysis (Fig. 3.9) showed that samples are elastic since the strain grows linearly with stress. After reaching the yielding point deformation becomes irreversible. As a result of mechanical tests, it can be concluded that the duration of treatment is of key importance. Processed for the longest time of 120 sec Sample II, has the lowest mechanical characteristics. An increase in elasticity can be noted for samples treated for 60 sec. (Sample 1 and 3) in a Halloysite suspension, while the strength characteristics remained almost constant compared to reference Sample 0, prepared without HNTs (Table 3.4.).

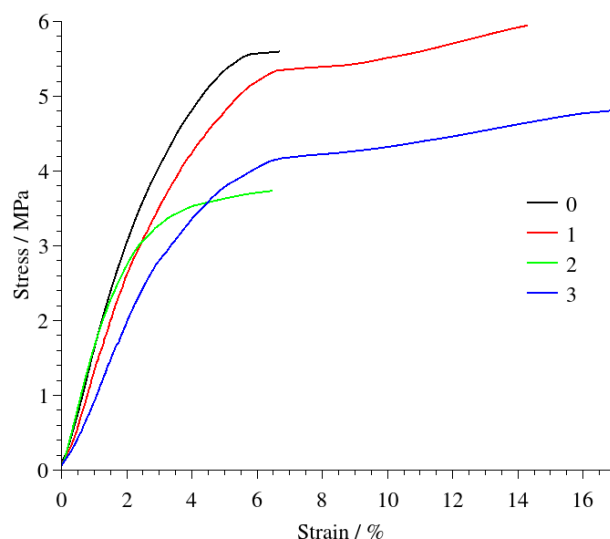


Figure 3.9. Stress vs. strain curves of treated samples.

It is worth notifying the values of Elastic Modulus, also known as Young's modulus, as a property of materials that measures their stiffness or resistance to elastic deformation for the synthesized samples, are higher than those of pristine PE. The reinforcing effect of HNT in polymers is often explained as a result of agglomerates of nanoparticles and the formation of the interface region between matrix/nanoparticles, which restricts the mobility and deformability of PE [116], [117].

Table 3.4. Tensile strength properties of films

Sample name	Elongation at break / %	Stress at break point / MPa	Elastic modulus / MPa	Yield point / %
PE non-treated	>150	>12	80.4	11.9
0	6.68	5.60	168.9	3.48
1	14.27	5.64	135.2	5.69
2	6.45	3.74	164.8	2.44
3	16.82	4.81	103.3	5.39

Based on the analysis of optical images, we can assert that treatment of films at a temperature of 50°C allows us to obtain a uniform deposition of nanomaterial on the surface while raising the temperature to 60°C leads to the formation of areas with aggregated particles (Fig. 3.10).

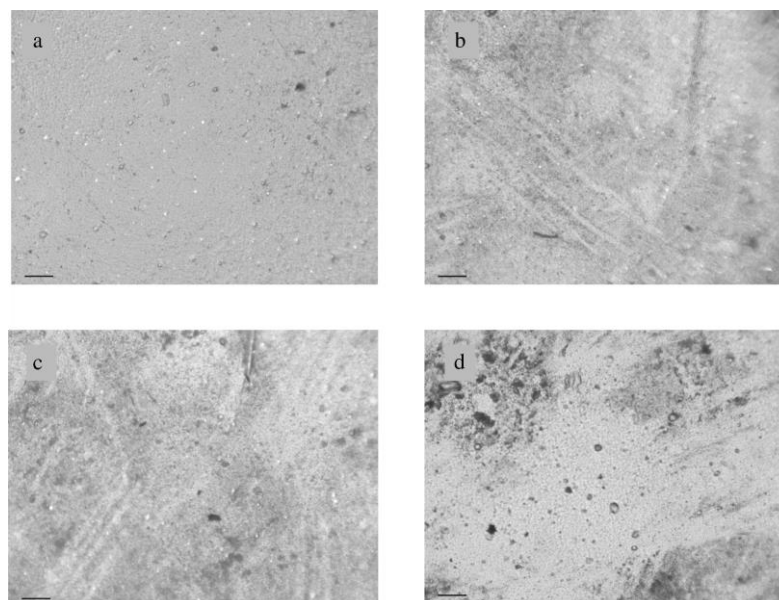


Figure 3.10. Optical images of PE films treated in HNT/cyclohexane suspension under different conditions: (a) Sample 0, (b) Sample 1, (c) Sample 2, (d) Sample 3. The scale bar is equal to 0.1 mm.

3.3 Characterization of PE films decorated with photocatalysis series CS1-9.

Optical microscope investigation

To avoid the use of toxic solvents when applying nanomaterials to the surface of polyethylene film, as well as the use of heating, which greatly worsens the mechanical characteristics of the pristine polyethylene, a series of adhesive compositions was developed. PVP was used as a polymer base, PEG was introduced as a plasticizer to prevent cracking of the coating and give it flexibility. Since the polyethylene surface is hydrophobic, ethyl alcohol was chosen as a solvent. In addition, it has the advantage that the composition based on it dries quickly in the open air at room temperature. Two main application methods were considered: spraying a nanomaterial suspension in an adhesive composition using a spray and layering using a sponge or brush. Based on previous work, the content of photocatalyst was taken as 1% by mass of the mass of polyethylene [105].

To check the uniformity of the catalyst distribution, studies were carried out using an optical microscope (Fig. 3.11)

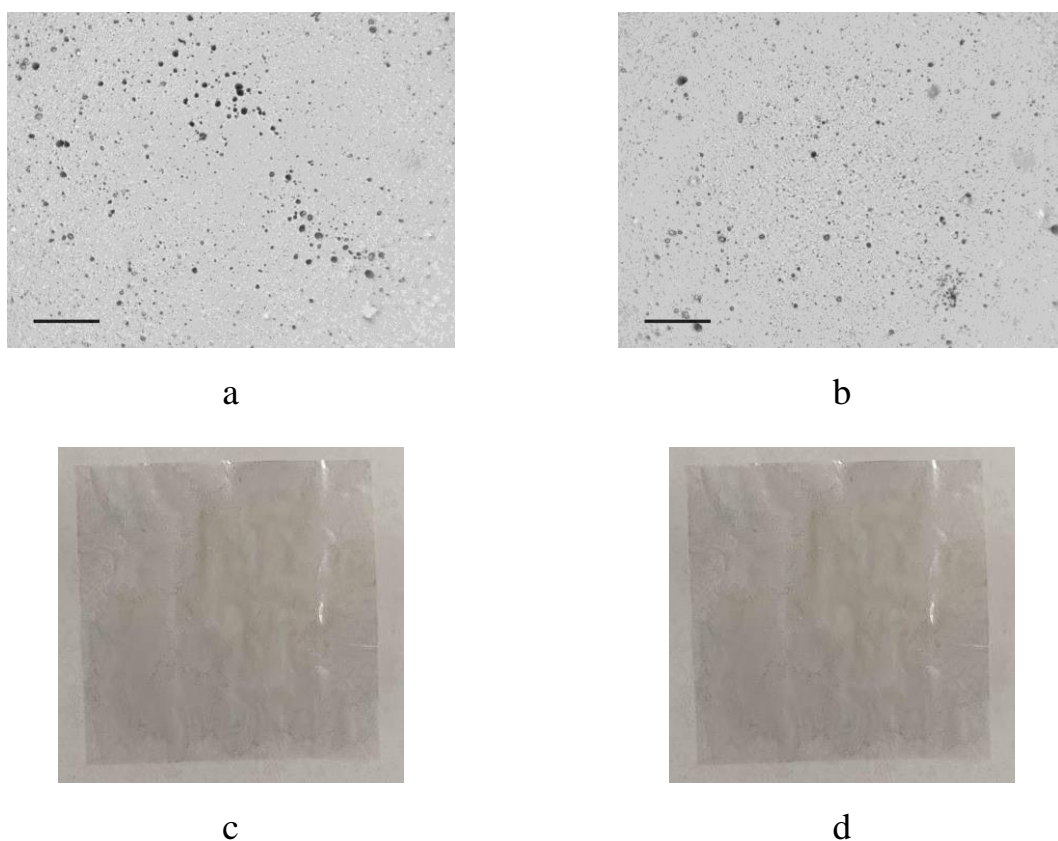


Figure 3.11. Images obtained with an optical microscope and photos of films with applied catalyst by spraying (a, c) and layering (b, d). The scale bar is equal to 0.2 mm.

After complete drying the films remained transparent, the surface was not sticky. From the images (Fig. 3.11) it can be concluded that the material is distributed evenly both when spraying and when applied with a sponge.

Conclusions to Section 3

Before the study of complex composite systems the properties of individual components were considered in this Section. Manganese dioxide and titanium dioxide were taken as standards for comparison purposes. HNTs were studied as pristine materials that are planned to be introduced into reaction synthesis medium for composites preparation.

The characterisation of TiO_2 IPM NASU and MnO_2 PCP (Kamyanske, Ukraine) was made. Wettability, thermal and mechanical behaviour of the PE films with these oxides were studied. A methods for depositing nanomaterials on the surface of PE films by partial surface dissolution and using an adhesive composition was also developed. The

prepared films were characterized by optical microscopy, contact angle measurements, and thermogravimetry.

The results of experimental studies of this section are presented in the following publications:

Articles:

1. **I. Kovinchuk**, N. Haiuk, G. Lazzara, G. Cavallaro, and G. Sokolskyi, ‘Enhanced photocatalytic degradation of PE film by anatase/ γ -MnO₂’, *Polym. Degrad. Stab.*, vol. 210, p. 110295, Apr. 2023, doi: 10.1016/j.polymdegradstab.2023.110295. The journal is cited by the scientometric databases SCOPUS and Web of Science (Q1). *Personal contribution is analysis of literary sources, conducting experimental research, processing and formatting results, writing and submitting the article.*

2. **I. Kovinchuk**, G. Sokolsky, and G. Lazzara, ‘Single-stage and simple fabrication of PE films decorated with halloysite nanotubes’, *KPI Sci. News*, vol. 136, no. 1–4, Apr. 2024, doi: 10.20535/kpissn.2023.1-4.297046. Journal adopted by the Ministry of Education & Science of Ukraine as professional ones in specialty 161 Chemical technology and engineering. *Personal contribution is analysis of literary sources, conducting experimental research, processing and formatting results, writing and submitting the article.*

Conference materials:

3. **Kovinchuk I.**, Lazzara G., Cavallaro G., Sokolsky G. MnO₂/TiO₂ Nanopowders-Assisted Photocatalytic Degradation of Low-Density Polyethylene Films, 2022 *IEEE 12th International Conference Nanomaterials: Applications & Properties*, 2022 P. 10nee–27. <https://doi.org/10.1109/NAP55339.2022.9934707>. *Personal contribution is analysis of literary sources, conducting experimental research, processing and formatting results, writing and submitting the abstract.*

Abstracts of conference presentations:

4. Haiuk N.V., Sokolsky H.V., Svyntsova A.V., **Kovinchuk I.V.** (2021) Fotokatalitychna destruktsiia polietylenovykh plivok dioksydamy tytanu i manhanu. [Photocatalytic destruction of polyethylene films by titanium and manganese dioxides] *Materialy XV*

mizhnarodnoi naukovo-tekhnichnoi konferentsii «AVIA-2021». m. Kyiv, (Ukraine). P. 19.1-19.4. *Personal contribution is analysis of literary sources, conducting experimental research, processing results.*

5. Haiuk N.V., Dmitriieva Y., **Kovinchuk I.V.**, Sokolsky H.V. (2021) Tverdofazna fotokatalitychna destruktsiia polietylenovykh plivok oksydnymy materialamy manhanu ta tytanu [Solid-phase photocatalytic destruction of polyethylene films by manganese and titanium oxide materials]. *Materialy I Mizhnarodnoi naukovoï konferentsii «Aktualni problemy khimii, materialoznavstva ta ekolohii»*. m. Luts'k, (Ukraine). S. 119–122. *Personal contribution is analysis of literary sources, conducting experimental research, processing and formatting results.*

6. **Kovinchuk I.**, Haiuk N., Cavallaro G., Lazzara G., Sokolsky G. (2022) Thermogravimetric study of PE films containing TiO₂, MnO₂ photocatalysts, and their composites. *Book of abstracts of the 13 European Symposium on Thermal Analysis and Calorimetry*. Palermo, (Italy). P. 214. *Personal contribution is analysis of literary sources, conducting experimental research, processing and formatting results, writing and submitting the abstract.*

7. **Kovinchuk I.**, Sokolsky G., Lazzara G. (2023) Single stage and simple fabrication of PE films Impregnated with halloysite nanotubes. *Book of abstracts. International Conference on Chemistry, Chemical Technology and Ecology*. Kyiv, (Ukraine). P. 60–61. *Personal contribution is analysis of literary sources, conducting experimental research, processing and formatting results, writing and submitting the abstract.*

SECTION 4. PROPERTIES OF CHEMICALLY SYNTHESIZED MANGANESE OXIDES AND OXIDEHYDROXIDES COMPOSITES WITH HNTs

4.1 Characterization of manganese oxides and oxidehydroxides composites with HNTs

4.1.1 Characterization of manganese oxides and oxidehydroxides with HNTs composites aqueous dispersions: ζ potential, size distribution (DLS, TEM)

We explored the surface charge and the aqueous dynamic behaviour of manganese oxides and oxidehydroxides with halloysite nanocomposites. As expected, the surface charge of the composites is negative within the whole set of samples. In particular, the ζ potential ranges between 15.8 and 21.63 mV (Table 4.1). According to literature ζ potential of pure HNT is -24.9 ± 0.3 mV [118]. With this in mind, it can be concluded that, after the interactions between the Mn oxides and the nonclay, the ζ potential shifts towards more positive values. This effect can be related to the effective decoration of HNTs' outer surface, which neutralizes the negative external charges of the silica surface of the tube, leading to a lower net negative charge for the system.

The colloidal and structural characteristics of the Mn oxides/oxidehydroxides with HNT nanocomposites were determined by DLS measurements. Sample CS-4, showed the smallest average particle size of 78 nm, while sample CS-5 has the biggest size of particle 175 nm.

Table 4.1. Average size and ζ potential obtained by DLS analysis

Sample name	Average size / nm	ζ -potential / mV
CS-1. Mn-HNT-pH10-H ₂ O ₂	119 \pm 49	-18.10 \pm 0.56
CS-2. Mn-NH ₄ ⁺ -HNT-pH10-H ₂ O ₂	141 \pm 43	-16.13 \pm 0.90
CS-3. Mn-NH ₄ ⁺ -pH10-air	125 \pm 52	-19.53 \pm 1.27
CS-4. Mn-NH ₄ ⁺ -pH5-6-H ₂ O ₂	78 \pm 35	-21.63 \pm 1.01
CS-5. Mn-pH5-6-H ₂ O ₂	175 \pm 86	-19.2 \pm 1.11
CS-6. Mn-NH ₄ ⁺ -HNT-pH5-7.5-H ₂ O ₂	143 \pm 52	-19.4 \pm 1.7
CS-7. Mn-HNT-pH5-6-H ₂ O ₂	118 \pm 36	-15.8 \pm 0.75
CS-8. Mn-NH ₄ ⁺ -pH5-7.5-H ₂ O ₂ slow	129 \pm 53	-19.0 \pm 0.2
CS-9. Mn-NH ₄ ⁺ -pH5-8-H ₂ O ₂ express	118 \pm 38	-20.0 \pm 1.18

Additionally, the size distribution was assessed from TEM images using ImageJ software. The typical procedure involved measuring the linear dimensions of all visible particles in the images. TEM images containing the maximum number of well-defined individual aggregates were selected for analysis. Subsequent statistical processing of the data enabled the determination of the particle size distribution for each sample. The normal distribution and Gauss fitting by size for each sample is shown in the Figure 4.1. As indicated by the data in Figure 4.1, the average size analysis conducted via DLS revealed the sizes of particle aggregates rather than individual particles.

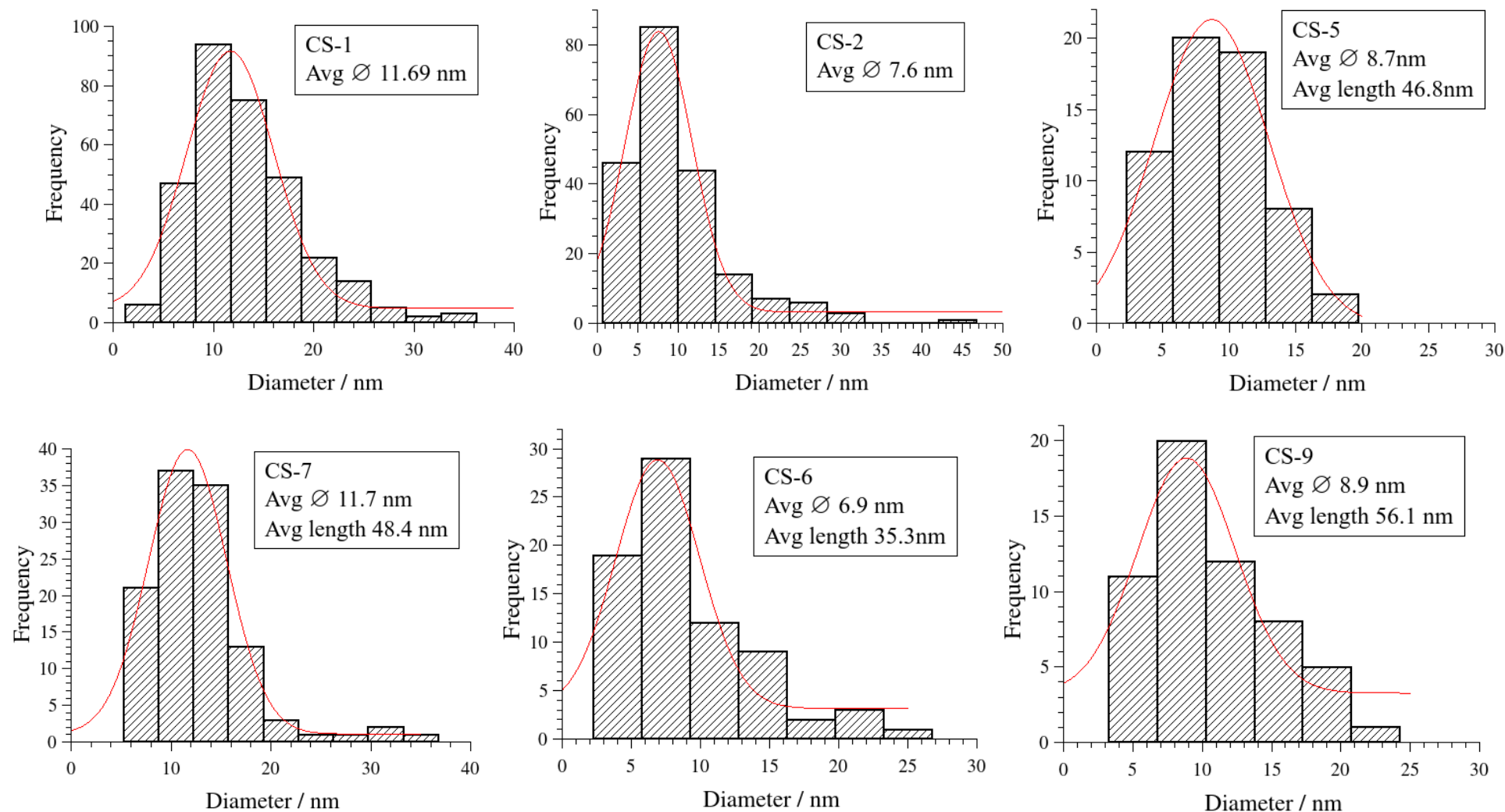


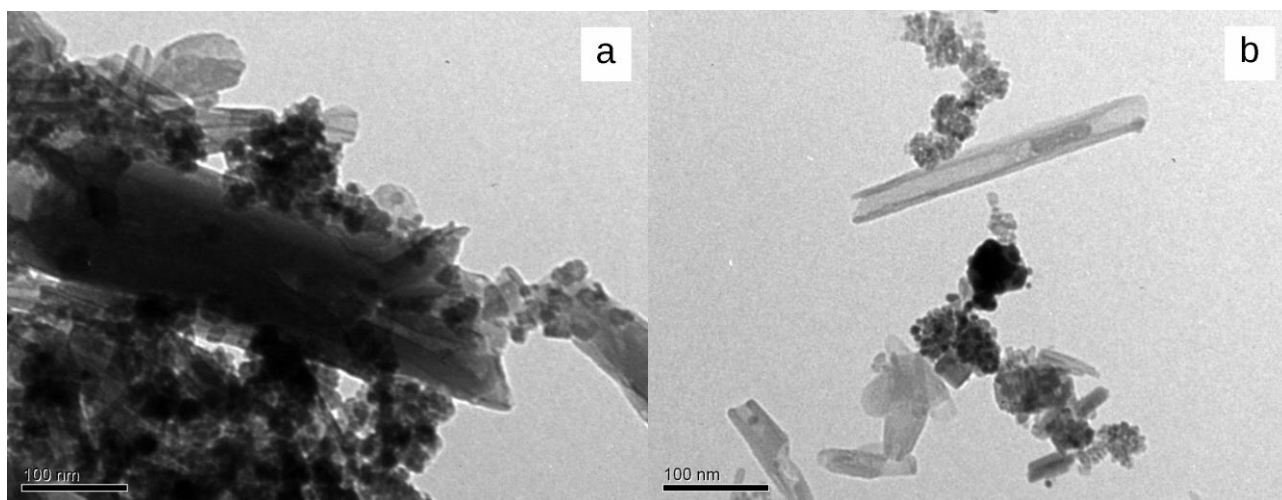
Figure 4.1. Particle size distribution calculated by ImageJ software of manganese oxides and oxidehydroxides with halloysite composites in the series CS-1– CS-9.

Samples CS-1 and CS-2 contain round-shaped Mn oxide particles typical for Mn_3O_4 with average diameter of 11.7 and 7.6 nm respectively. It is clear that samples CS-5 – CS-9 synthesized at lower pH = 5-6 have similar diameters of anisotropic needles that are larger in size (35-56 nm) comparing with round-shaped Mn_3O_4 NPs. All samples demonstrate approximately identical size distribution to within 20-30 nm.

Table 4.2. Average size of NPs evaluated by ImageJ from TEM study

Sample	Avg size / nm	SD	R ²
CS-1	11.69	0.39	0.96
CS-2	7.6	0.2	0.99
CS-5	8.7	0.19	1
CS-6	6.9	0.45	0.95
CS-7	11.7	0.12	1
CS-9	8.9	0.73	0.92

Based on the TEM images (Fig. 4.2), an analysis of the behavior of manganese towards the surface of aluminosilicate tubes was also carried out.



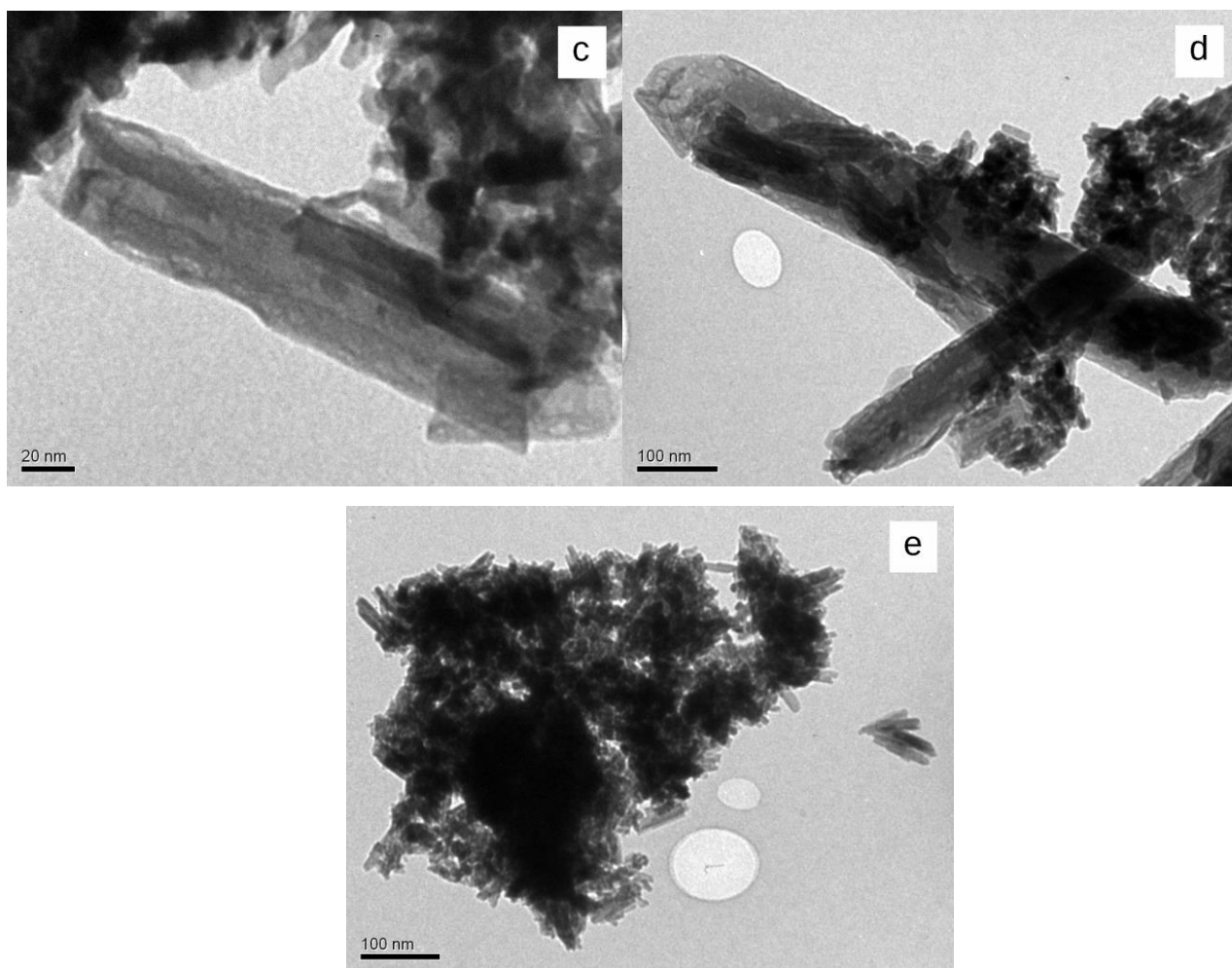


Figure 4.2. TEM images of Samles CS-1 (a), CS-2 (b), CS-6 (c), CS-7 (d), CS-5 (e).

In Samples CS-1 and CS-7, synthesized without NH_4^+ oxides behave in a similar way with respect to the surface of nanotubes: oxide particles predominantly decorate the outer surface of the nanotube. It is interesting to note that larger tubes (50-100 nm in diameter) are decorated better than tubes with a smaller diameter. At the same time, the lumens mostly remain clean with smooth, clearly visible walls. Oxide particles aggregate among themselves, forming aggregates of 100-400 nm. For samples synthesized in the presence of NH_4^+ ions excess (samples CS-2, CS-6) oxide particles are characterized by the opposite behavior - the outer surface of the tubes remains clean in most cases, while in the inner lumen one can observe particles (Fig. 4.2 c), or in some cases the lumen itself looks darker, heterogeneous. The absence of a lumen in the nanotubes in some images can be explained by the complete or partial filling of the cavity with the Mn^{2+} solution and subsequent crystallization of this solution inside. Damage to the structure of the tube

during the analysis, namely the direction of a concentrated beam with high energy on the tube, can also be a factor affecting the structure of the material.

Based on the obtained data, it is possible to conclude about the influence of an excess of NH_4^+ ions in the reaction mixture on the preferred positions/locations of nucleation. Positively charged ammonium ions form a double electric layer with the negatively charged outer surface of halloysite nanotubes formed by silanol groups, while the positively charged inner surface of nanotubes interacts with negatively charged particle $[\text{Mn}_2(\text{SO}_4)_3]^{2-}$ and $[\text{Mn}(\text{SO}_4)_2]^{2-}$ of the Tutton salt stable at the conditions of excess NH_4^+ ions [119].

Analysis of images of TEM samples without halloysite nanotubes (CS-5 and CS-9) despite the difference in presence of NH_4^+ ions showed similar picture – both phases are present – elongated particles of Manganite and rounded Hausmannite. Which tend to create the aggregates of size 100-400 nm.

These data are in the good agreement with values of grain size distribution. The biggest size is recorded for samples CS-1 and CS-7 with HNT and excess of NH_4^+ ions (11.7 nm), the smallest - for samples CS-2 and CS-6 with HNT and without NH_4^+ ions (7.6 and 6.9 nm respectively).

4.1.2 BET analysis

BET surface area values were measured for available for us Samples CS5-9 and pure HNTs (Table 4.3). Surface area of HNTs and Mn oxides/oxidehydroxide compounds are compatible It can be suggested that slight decrease of S_{BET} for CS-6 Sample versus CS-8, CS-9 is the response of decoration effects of Mn oxides/oxidehydroxides on HNTs surface.

Table 4.3. Data of surface area of some chemically deposited Mn oxide composite samples

Sample name	BET Multipoint Surface Area, m ² /g
CS-5	55.27
CS-6	59.24
CS-7	54.98
CS-8	65.20
CS-9	65.96
HNT Sigma	65.94

4.1.3 Phase and elemental composition of synthesized composites of manganese oxides and oxidehydroxides with halloysite

Standard procedure for processing diffractograms consists in their smoothing, removing the background, finding and selection of peaks and searching for correspondences in database according to the specified criteria.

Materials of the manganese oxide system have individual features of their structural behaviour: localized Mn⁴⁺/Mn³⁺ defects, ramsdellite/pyrolusite de Wolff's intergrowth defects, P. Ruetschi's cation vacancies [120].

Structure refinement was performed using the Rietveld method via PowderCell and the Profex software [121] to evaluate the percentages of the phases present. This technique aligns the theoretical and observed diffractograms as closely as possible to recalibrate the crystalline structure towards an approximation of its observed form (employing a best-fitting approach). Additionally, Crystallography Information Framework (CIF) files from the Crystallography Open Database served as control files for the refinement process.

All synthesized samples showed a low degree of crystallinity, defectiveness, nanocrystallinity.

The XRD patterns of samples CS-1, 2, 6, 7 synthesized with the addition of HNTs clearly show the presence of characteristic 7 Å-HNT peaks at 2θ of 12.2° (001), 20.0° (100), 24.8° (002), 35.0° (110), 54.6° (210), and 62.5° (300).

A more detailed examination allows us to make conclusions about the difference in the phase composition of the samples depending on the synthesis conditions (Table 4.4). In our previous works, for electrochemically synthesized products the formation of predominantly ramsdellite manganese dioxide phases in the absence of ammonium ions and the hollandite phase in the case of excess ammonium cations was detected.

Table 4.4. Rietveld refinement results of XRD patterns of CS 1-9 series of samples

	MnO	Mn ₃ O ₄	α -Mn ₂ O ₃	Mn ₅ O ₈	α -MnOOH	γ -MnOOH	α -MnO ₂	β -MnO ₂	γ -MnO ₂	MnO ₂ romanchite	MnO ₂ todorkite	HNT
CS-1	-	30.14	46.88	6.59	-	-	-	-	-	-	-	16.39
CS-2	-	47.7	13.10	-	0.70	-	2.4	-	2.00	6.50	-	27.60
CS-3	-	63.23	25.28	-	3.93	-	-	2.65	-	4.17	0.72	-
CS-5	-	-	-	-	46.2	23.55	-	6.16	24.09	-	-	-
CS-6	-	-	-	-	21.4	39.3	-	-	3.1	-	-	36.2
CS-7	-	-	-	-	13.8	57.9	-	-	-	-	-	28.3
CS-8	1.3	-	-	-	55.46	-	-	11.08	32.03	-	-	-
CS-9	-	0.61	4.58	-	48.37	-	-	30.40	16.04	-	-	-

The peculiarity of composites obtained with pH close to 10 (CS-1–CS-4) includes formation of lower valenced phases of Mn₃O₄, Mn₂O₃. In contrast, composites synthesized in a neutral medium (pH ~ 5–7) have MnOOH phases with integration of small amounts of ramsdellite and pyrolusite polymorphs. Open structure polymorphs of MnO₂ were present only in CS-2 and CS-3 with low content.

As we know, XRD signal broadening shows the sizes of coherent scattering regions or crystallites that are generally less and not equal to the actual sizes of NPs that can be seen in SEM/TEM images. On the contrary, average sizes of NPs received from the DLS method are usually larger than true sizes since NPs' agglomeration occurs. It can be concluded from performed analysis of NPs sizes data of studied Samples that the exact method of Rietveld refinement resulted in good agreement with IMAGJ software for particular cases of Samples CS-1 – CS-9 taken for analysis. It is also clear that all information from characterisation of Samples is valuable for further nanoapplications.

The elemental composition of the composite materials was determined by the EDS method (Table 4.5). In the samples with halloysite, Si and Al was found in a ratio of 1:1 as in the pristine material, which indicates that the synthesis procedure did not affect the structure of nanoclay.

Table 4.5. Chemical composition of some CS composites in atomic % defined with EDS.

Sample name	Mn	O	Al	Si	S
CS-5	36.76	60.53	-	-	2.69
CS-6	22.6	62.84	6.05	5.6	2.91
CS-7	22.10	65.14	5.68	5.14	1.93
CS-8	36.70	59.18	-	-	4.12
CS-9	38.78	58.92	-	-	2.31

4.1.4 FTIR study

The examination of the FTIR spectra yielded valuable information regarding the composition of the samples under investigation. As depicted in Fig. 4.3 a, a notable broad peak is observed in all the samples, centred at approximately 3400 cm^{-1} , which covers the wavelength range from 4000 to 2700 cm^{-1} . This peak is indicative of the OH stretching

vibration of H₂O. The OH groups located between tetrahedral and octahedral sheets are characterised by absorption at 3696 cm⁻¹ in all clay minerals.

By studying the FTIR spectra in the so-called “fingerprint” range of 400-1100 cm⁻¹ (Fig. 4.3a), the positions of the characteristic peaks of halloysite nanotubes were analyzed, as well as the changes that occur as a result of interaction with manganese oxides in samples CS-1, CS-2, CS-6 and CS-7. As described in Section 3.1.1, wavenumbers of 912 and 940 cm⁻¹ are attributed to Al—O stretching and deformation vibrations remain unchanged for all composite samples. As for the peaks associated with manganese oxides, their isolation and description is associated with some difficulties due to overlaps.

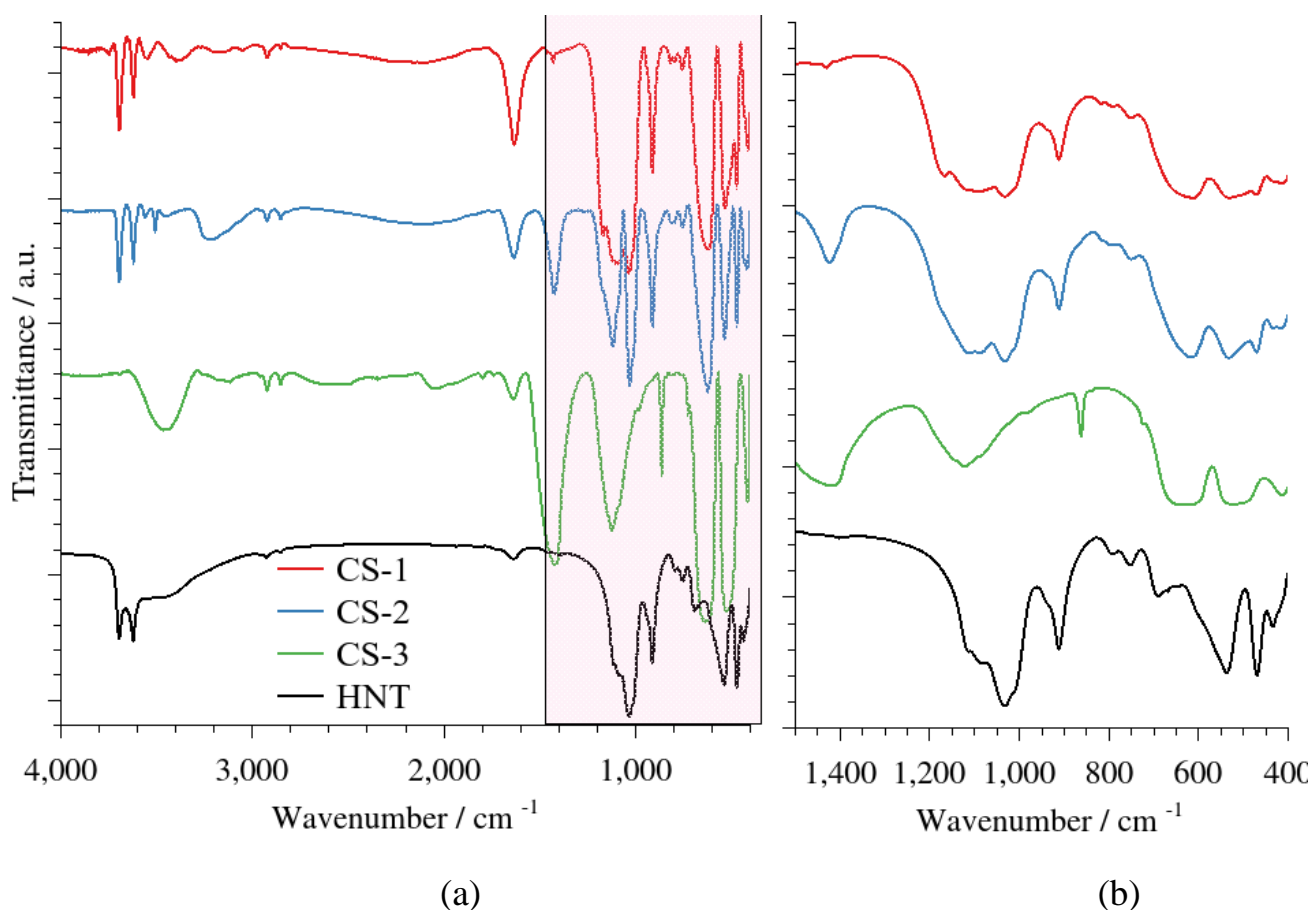


Figure 4.3. IR spectra of synthesised at pH 10 composites (a) and fingerprint region for these samples (b).

Figure 4.3b shows the FTIR spectral analysis of Sample CS-3, which, according to XRD, consists of mainly Mn₃O₄ NPs and composite materials CS-1, CS-2 with the main phase of Mn₃O₄ and HNTs. According to literature, Mn₃O₄ nanoparticles have three standard

significant bands around 418, 480 and 609 cm^{-1} , corresponding to the Mn^{3+} ions vibration in an octahedral site [122], [123]. The broad and sharp peaks at 3410 cm^{-1} indicate the stretching vibration of the surface water molecules and hydroxyl groups [124]. The strong characteristic of Mn–O has both stretching modes at 632 cm^{-1} in tetrahedral sites and distortion vibration at 523 cm^{-1} in an octahedral environment, weak peak at 412 cm^{-1} can be attributed to the vibration of manganese species (Mn^{3+}) in an octahedral site.

The sample CS-5, CS-6 and CS-7 series is characterized by similar IR spectra with some differences (Fig. 4.4).

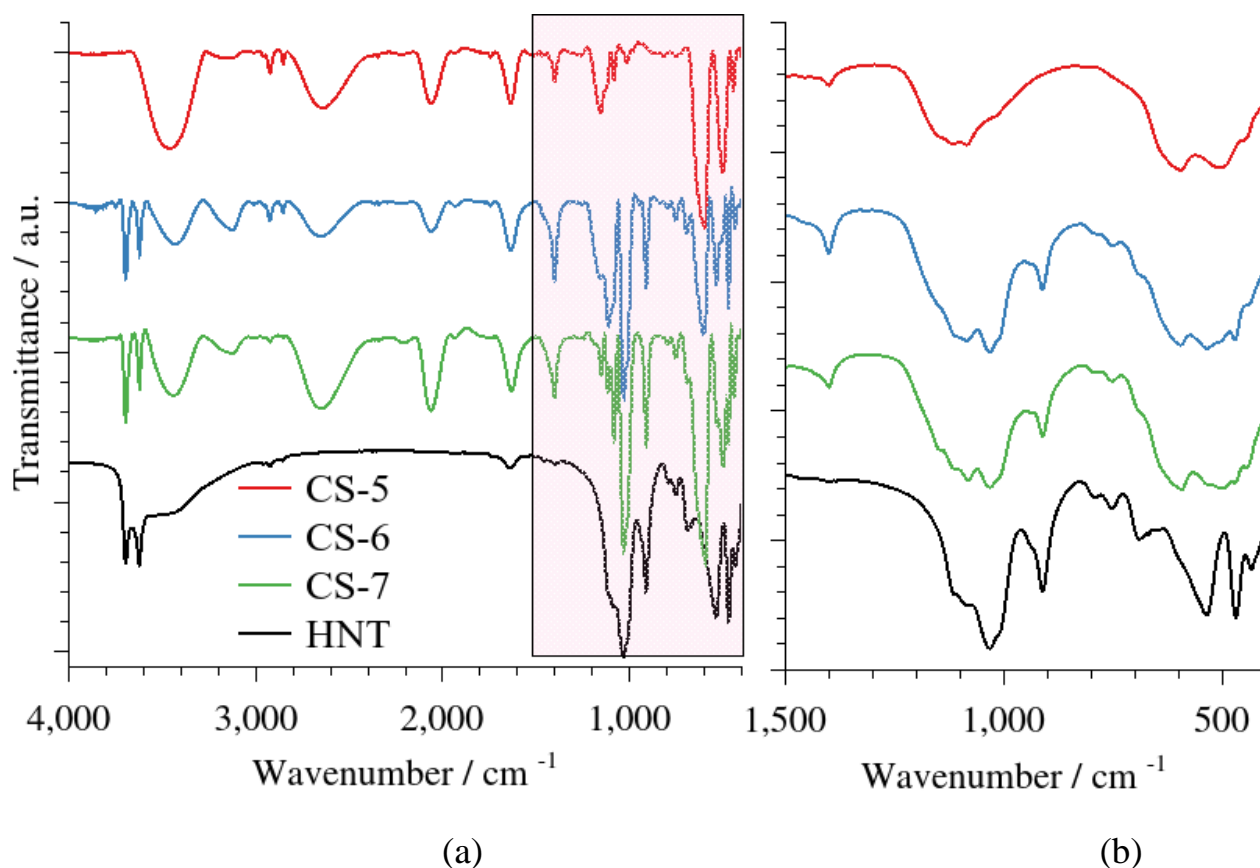


Figure 4.4. IR spectra of synthesised at pH 5-7 composites (a) and fingerprint region for these samples (b).

They show peaks characteristic of MnOOH . As reported by T. Kohler [125] the broad band at 2687 cm^{-1} is the O–H stretching mode belonging to a hydrogen bond with an O–H...O length of ~ 2.60 Å. Another peak at 2043 cm^{-1} was considered to be a combination band of the OH-stretching mode at 2667 cm^{-1} and the excited lattice mode at 595 cm^{-1} . Vibrations at 507 cm^{-1} , 448 cm^{-1} are responsible for Mn–O stretching, whereas

the bending of Mn–OH was visible at 1632cm^{-1} [59], [125]. The absorption peaks at 1086 cm^{-1} are due to out of plane bending vibration, while 1116 cm^{-1} and 1152 cm^{-1} assigned to in-plane bending mode of OH of MnOOH.

4.1.5 Thermal properties of samples in air and nitrogen atmosphere

To evaluate the samples' phase content, influence of HNT and thermal behaviour, thermogravimetric analysis was employed alongside differential thermogravimetry as a TGA derivative technique that measures the weight change rate as a function of temperature.

The occurrence of phase changes in manganese oxides as a function of temperature variation is influenced by several factors, including the precursors employed, the stoichiometry, particle size, and the morphology of the synthesized materials. Thermal analysis conditions, namely atmosphere and heat flow, can also influence the dynamics of phase transitions [126].

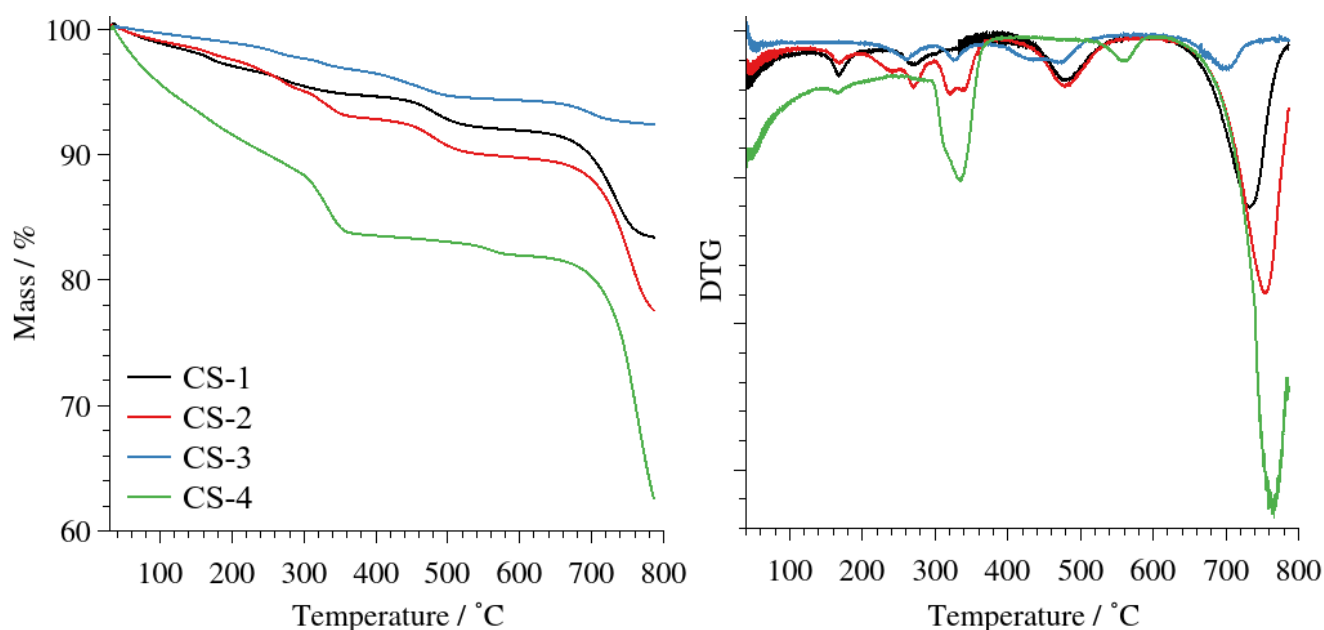


Figure 4.5. Thermogravimetric DTG and TG curves for Samples CS-1 – CS-4

The thermograms of Samples CS-1 and CS-2 synthesized at pH = 10 using hydrogen peroxide as an oxidizing agent with the addition of halloysite nanotubes are presented on Fig 4.5. Sample CS-1 was obtained without the excess of ammonium ions in the reaction mixture, whereas sample CS-2 was synthesized in their presence. In the temperature range

of 20-200°C, both samples exhibit the loss of surface and crystallization water, amounting to 3.24% for sample CS-1 and 2.36% for CS-2. The following slight mass loss is characteristic of both samples with a peak in the DTG curve at temperature 267°C can be attributed to loss of one molecule of water. The primary difference between two samples can be observed in the range from 295 to 390°C. The DTG curve shows a wide peak consisting of two merged together (at 319°C and 340°C). According to [127] the possible explanation is loss of $(\text{NH}_4)_2\text{SO}_4$ in double salts of Manganese. At the same time, for CS-1 such an effect is not observed. Farther behaviour for both of samples is similar: the typical dehydroxylation of structural Al-OH groups of halloysite can be observed at 478°C. Mass loss of 2.78 and 3.25% corresponds to that calculated for a given content of HNTs in the composite. Later, at 585-800 °C significant mass reduction up to 8.5% for sample without excess of ammonia ions and 12.3% for sample with it was observed. Typically, at this range loss of one molecule of O_2 by Mn_2O_3 is expected with formation of Mn_3O_4 . But the actual observed mass loss significantly exceeds the theoretical 3.4%.

TGA and DTG curves of Sample CS-3, synthesised without hydrogen peroxide in presence of excess ammonia ions are shown in Fig. 4.6 c. Its thermal behaviour is typical for Mn_3O_4 . The initial mass loss of 0.7% in the range of 30–220°C corresponds to the evaporation of adsorbed water content on the surface, the total mass loss of 7.61% were recorded.

The thermogram of Sample CS-4 significantly differs from the TG curves of all other samples, suggesting a cardinal difference in the phase composition. The largest total mass loss was registered, which amounted to 37.39%. The gradual loss of mass at the first stage in the temperature range from 25 to 280°C corresponds to the loss of surface water, in the range of 250 - 600°C with a peak at 330°C 6.59% probably observed decomposition of double manganese salts with loss of ammonium groups. The most active peak at 765°C with a loss of 19.4%.

The thermograms of the following samples are considered, taking into account two different modes of thermal decomposition: in an inert nitrogen atmosphere and in an air atmosphere. Comparing the behaviour of the samples under the influence of elevated temperatures in the presence of oxygen will provide additional information on their

composition. In general, a shift of some release of O_2 peaks towards higher temperatures was registered and vice versa for OH groups of $MnOOH$, for instance, for CS-5 Sample.

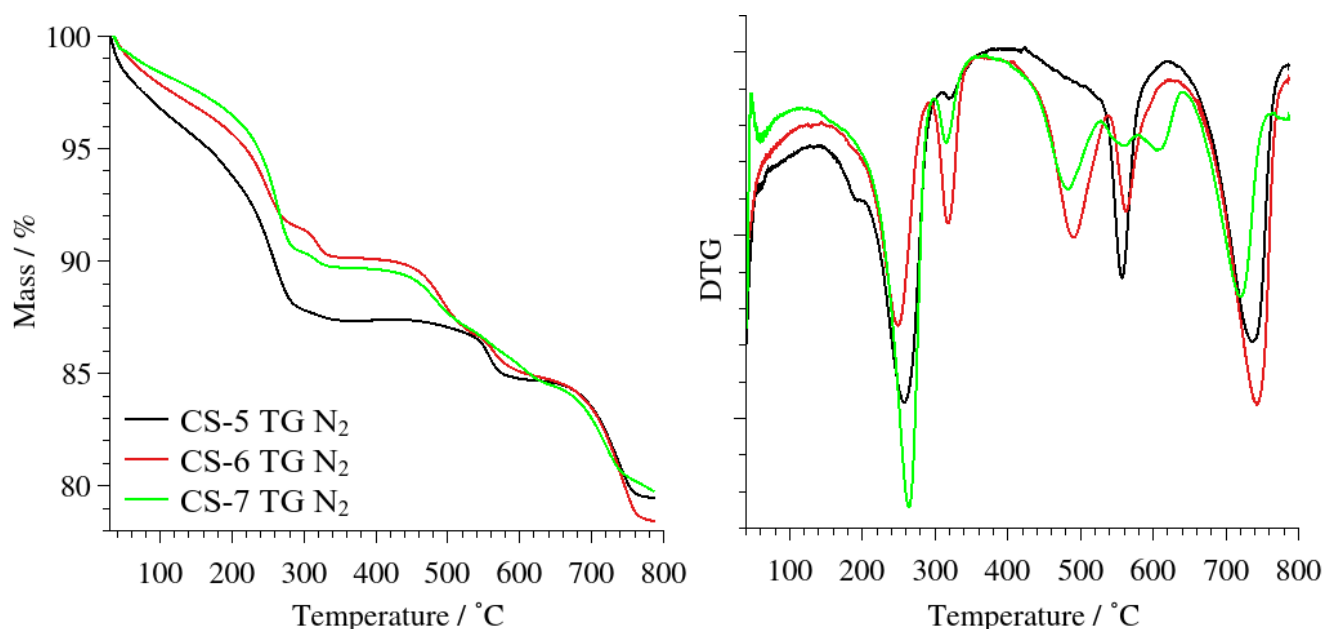


Figure 4.6. Thermogravimetric DTG and TG curves for Samples CS-5 – CS-7.

For CS-5 Sample initial mass loss of 4.48% in N_2 and 3.56 % in Air atmosphere up to 150 °C is attributed to physically adsorbed water loss. Next mass loss occurs between 150 and 200 °C as a surface hydroxide groups. DTG effect between 200 and 300°C is expected from hydroxide groups of crystal lattice of manganite and groutite detected by the Rietveld refinement in this Sample. Probably, some energetically non-equivalent positions of OH groups exist in both structures that are approximately equal in content in the Sample CS-5 (groutite unit cell contains layers of OH-groups with H atoms inside the cell unlike manganite unite cell where H atoms forming apices of the unit cell) contribute in small so-called satellites of main peak of DTG at about 240 oC.

The observed mass increase of 0.68% in Air atmosphere in the range of 342 °C to 526 °C can be attributed to the weak oxidation process of Mn^{3+} oxide formed in air atmosphere, notably in the transition from Mn_2O_3 to MnO_2 . The positive difference of mass losses of oxygen release between 540 and 580 °C in air and nitrogen atmospheres is in agreement with this hypothesis. Then, between 580 °C and 715 °C, the reactions indicate the conversion of Mn_2O_3 phase to Mn_3O_4 (peak at 657 °C) and O_2 release, resulting in a considerable mass loss, around 2.08%.

Sample CS-6 derivatogram is shown in Fig. 4.6. The additional effects can be seen comparing with thermograms of CS-5 Sample. They can be attributed to HNTs water loss and etc. (see Fig. 3.3 above). Nevertheless, temperatures of them are different and their shift to higher temperatures region could be the result of some kind of interaction of HNTs with Mn oxide/hydroxide compounds.

The behavior of the thermogram of Sample CS-7 is similar to Sample CS-6.

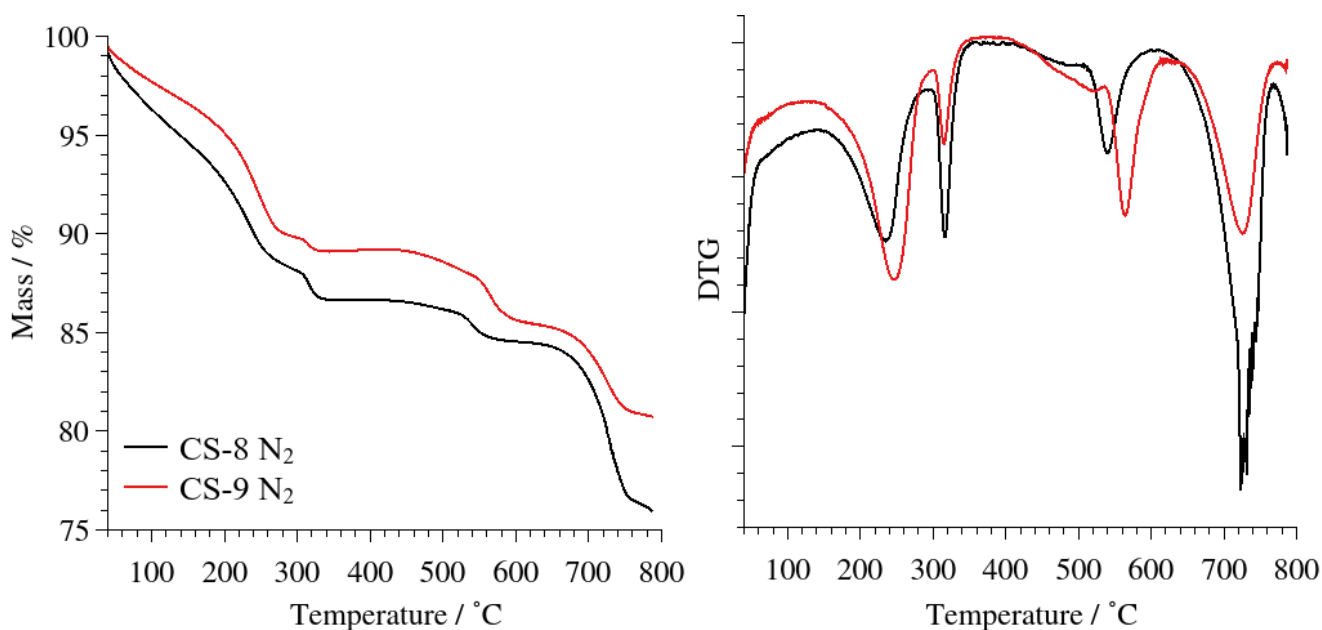


Figure 4.7. Thermogravimetric DTG and TG curves for Samples CS-8 and CS-9.

Samples CS-8 and CS-9 synthesized without halloysite nanotubes in the presence of excess ammonium ions according to X-ray diffraction analysis consist mainly of MnOOH and MnO₂. Thermograms demonstrate quite high mass loss in the range of release of physically sorbed water and transition of MnOOH to MnO₂ up to 350°C. Which is followed sequentially by stages of oxygen loss with a peak at temperature 539°C and 564°C for CS-8 and CS-9, respectively, which corresponds to the transition of Mn⁴⁺ to Mn³⁺ and a peak at 728°C, which is characteristic of the transition of Mn₂O₃ to Mn₃O₄. The summarized data on the thermal analysis are given Tables 4.6 and 4.7.

Table 4.6. Thermogravimetric analysis data of CS Manganese composite oxide samples in N₂ atmosphere

		CS-1	CS-2	CS-3	CS-4	CS-5	CS-6	CS-7	CS-8	CS-9
H ₂ O _{f.s.} , up to 150°C	Δm/%	1.89	1.56	0.7	6.47	4.48	3.19	2.42	5.36	3.41
H ₂ O _{c.s.} +OH groups	Δm/%	3.4	5.57	2.57	10.59	8.1	6.77	7.95	7.99	7.38
HNTs' H ₂ O loss	T/ °C	478	478	430			490	481		
	Δm/%	2.78	3.25	2.38			3.34	2.62		
MnO ₂ to Mn ₂ O ₃	T/ °C				559	557	562	559	539	564
	Δm/%				1.18	2.73	1.89	2.53	2.2	3.82
Mn ₂ O ₃ to Mn ₃ O ₄	T/ °C	733	754	702	765	736	744	720	728	727
	Δm/%	8.51	12.03	1.96	19.14	5.23	6.39	4.68	8.46	4.67
Residual mass at 800°C		83.42	77.59	92.39	62.61	79.46	78.42	79.81	75.99	80.75

Table 4.7. Thermogravimetric analysis data of CS Manganese composites in Air atmosphere

		CS-5	CS-6	CS-7	CS-8	CS-9
H ₂ O _{f.s.} , up to 150°C	Δm/%	3.56	3.06	2.08	4.31	3.01
H ₂ O _{c.s.} + OH groups	Δm/%	7.05	5.75	6.15	7.1	7.1
Mass growth	T/ °C	344-526	347-445	342-458	347-490	343-516

		CS-5	CS-6	CS-7	CS-8	CS-9
Oxidation of Mn ₂ O ₃ to MnO ₂	$\Delta m/\%$	↑ 0.68	↑ 0.19	↑ 0.28	↑ 0.39	↑ 0.73
HNTs' H ₂ O loss	T/ °C		488	487		
	$\Delta m/\%$		3.33	2.38		
MnO ₂ to Mn ₂ O ₃	T/ °C	569	577	574	559	577
	$\Delta m/\%$	3.53	2.46	3.11	2.99	4.28
Mn ₂ O ₃ to Mn ₃ O ₄	T/ °C	731	745	737	743	726
	$\Delta m/\%$	5.02	6.46	4.48	7.76	4.71
Residual mass at 800°C		80.74	78.94	81.8	77.84	80.9

4.1.6 DRS and band gap calculation

Semiconductor properties of CS series of samples were studied. DRS spectra were recorded (Fig. 4.8) and recalculated into absorption spectra by applying the Kubelka-Munk function, $F(R_\infty)$. The parameter $(F(R_\infty)h\nu)^{1/n}$ with $n = 1/2$ for direct allowed transition was further taken into account for calculations. The Tauc plots that include the Kubelka-Munk function plotted against photon energy for the CS series of all samples are shown in Appendix A and calculated band gaps and CB and VB edge potentials according to Mulliken electronegativity are shown in Table 4.8.

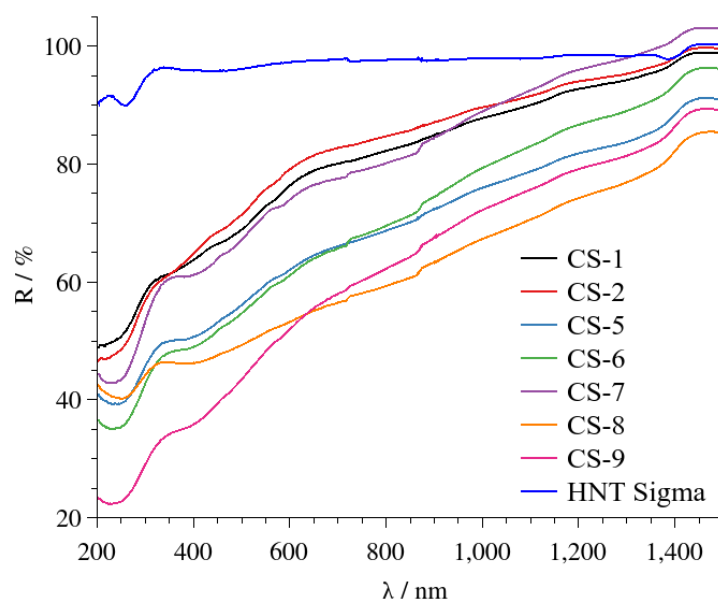


Fig. 4.8. DRS of some samples of the CS series and Halloysite Sigma

Table 4.8. Band gap energies obtained from Kubelka Munk plot.

Sample name	E_g , eV	E_{CB} , eV	E_{VB} , eV
CS-1	2.52	-0.33	2.19
CS-2	2.7	-0.41	2.29
CS-5	2.28	0.47	2.75
CS-6	2.29	0.49	2.78
CS-7	2.28	0.49	2.78
CS-8	1.99	0.61	2.60
CS-9	2.38	0.40	2.78
HNT Sigma	4.25	-0.24	4.01
MnO ₂ PCP	1.98	0.32	2.3

From the obtained data, it can be concluded that all samples with a band gap width of less than 3 eV are semiconductor materials and can potentially be used as photocatalysts in the visible light range. The introduction of halloysite nanotubes into the composite, which are insulators by their nature with a band gap width of 4.25eV for Samples CS-6 and CS-7, did not lead to a significant change in the band gap width in

comparison with sample CS-5, which does not contain HNTs. While samples CS-1 and CS-2, consisting mainly of low-valent manganese (Mn_2O_3 and Mn_3O_4) demonstrated a band gap width significantly wider than that of the sample consisting mainly of MnOOH .

Conclusions to Section 4

The physicochemical properties of chemically deposited compounds of manganese and their composites with HNTs were described in this Section. The choice of alkaline and neutral pH was successful from the point of view of significant differences in the nature of products in both cases and in comparison with the electrodeposition method described below. The lower valenced hausmannite phase and Mn_2O_3 were the main phase states at the basic pH in this study. The higher valenced MnOOH and MnO_2 were refined by the Rietveld method in CS5-CS9 at the neutral medium.

The incorporation of HNTs was accomplished by a simple chemical precipitation procedure from aqueous suspensions of aluminosilicate nanotubes with the importance of a preliminary evacuation step to ensure the filling of the lumen. An important positive effect of this approach was detecting the effect of nanotube decoration and loading of their lumens with chemical precipitation products. DRS measurements were used to evaluate the semiconducting properties of the CS samples. It can be noted that all samples are photocatalysts that can be excited by visible light photons, including the HNTs composites with band gap values in the range of 1.99 - 2.7 eV. At the same time, CS-1 and CS-2 samples demonstrate maximum E_g values of 2.52 and 2.7 eV, respectively, in contrast to other HNTs-containing composites (CS-6, CS-7).

The results of experimental studies of this section are presented in the following publications:

Articles:

1. **I. V. Kovinchuk**, G. Lazzara, Ragulya, A.V., M. M. Kržmanc, and G. V. Sokolsky, ‘Evaluation of nanoparticles’ size characteristics of manganese oxide/hydroxide based photocatalysts’, *Visnyk Kherson Natl. Tech. Univ.*, vol. 4, no. 91, pp. 52–59, 2024. Journal adopted by the Ministry of Education & Science of Ukraine as professional ones in

specialty 161 Chemical technology and engineering. *Personal contribution is analysis of literary sources, conducting experimental research, processing and formatting results, writing and submitting the article.*

Abstracts of conference presentations:

2. P. Hlukhova, **I.V. Kovinchuk**, Dzh. Lazzara, i H. V. Sokolskyi (2023) Fotokatalitychni vlastyvoli kompozytiv oksydiv-hidroksydiv manhanu z haluazytom, syntezyovanykh hidrokhimichnym metodom [Photocatalytic properties of manganese oxide-hydroxide composites with halloysite synthesized by the hydrochemical method]. *Zbirka tez dopovidei. Mizhnarodna konferentsiia z khimii, khimichnoi tekhnolohii ta ekolohii, prysviachenii 125-richchii KPI im. Ihoria Sikorskoho*. m. Kyiv, (Ukraine). P. 14–16. *Personal contribution is analysis of literary sources, conducting experimental research, data curation.*

3. Sokolsky G., **Kovinchuk I.**, Lazzara G., Zudina L., Hlukhova P., Andriiko O. (2023) Comparison of chemical and electrodeposition pathways of manganese dioxide from NH_4^+ -containing electrolytes. *Book of abstracts. International Conference on Chemistry, Chemical Technology and Ecology*. Kyiv, (Ukraine). P. 87–88. *Personal contribution is analysis of literary sources, conducting experimental research, processing and formatting results.*

4. **Kovinchuk I.V.**, Hlukhova P.I., Telina M.M., Khrebtan D.R., Vechirko E.R., Lazzara G., Sokolsky G.V. (2024) Halloysite nanotubes as components of nanocomposites with mn oxides/hydroxides. *Book of abstracts. 12th International Conference "Nanotechnologies and Nanomaterials" NANO-2024*. Uzhgorod, (Ukraine). P. 77. *Personal contribution is analysis of literary sources, conducting experimental research, processing and formatting results, writing and submitting the abstract.*

5. **Kovinchuk I.**, Hlukhova P., Lazzara G., Sokolsky G. (2024) Enhanced Photocatalytic Methylene Blue Degradation by Mn_3O_4 /HNT-based composite material. *Book of abstracts. XXVIII Congresso Nazionale della Società Chimica Italiana*. Milan, (Italy). P. FIS-PO-005. *Personal contribution is analysis of literary sources, conducting experimental research, processing and formatting results, writing and submitting the abstract.*

SECTION 5. PROPERTIES OF ELECTROCHEMICALLY SYNTHESIZED MANGANESE DIOXIDE MATERIALS

Chemical synthesis and electrodeposition are among the traditional methods for preparing manganese dioxide, both of which involve multistep mechanisms with peculiar kinetic and thermodynamic characteristics, making precise functionality control challenging. The electrolytic doping approach developed by our group previously [83] involves introducing cations into the reaction medium as an additional tool, offering a wide range of thermodynamic possibilities for stabilizing defined phase compositions, including entropic factor influence, or for introducing various defect states at different concentrations.

5.1 Characterization of electrodeposited manganese dioxide materials

The polymorphism of manganese (IV) oxide system is a well known structure behavior complexity problem that needs special attention. For the purposes of this study, derived from the very close similarity of tunnel Mn(IV) oxide polymorphs, structure complexity opens opportunities towards better photocatalytic performance. Stacking faults, intergrowth, and point defects in the oxide matrix could stop, or at least slow down, the recombination of electron-hole pairs and be responsible for other effects. The idea to obtain manganese (IV) oxide nanophotocatalysts by electrodeposition methods had the following roots:

- the recent growth of interest towards photocatalytic behaviour of manganese oxide/hydroxide compounds as daylight photocatalysts;
- the finding that Mn_4O_4 cubane photocatalyst is responsible for oxidation of water during natural photosynthesis in plants [128];
- electrodeposition provides unique characteristics of its product manganese dioxide that can be further optimised as a nanomaterial.

Taking these work goals into account, the conditions of electrodeposition were modified as follows: hydrofluoric acid was replaced by sulfuric acid. The diffusion

control was also considered as a mechanism favouring the nano-dimensional state of the product. It was applied by means of a low Mn^{2+} concentration in an electrolyte and high current density. Manganese(II) sulfate concentration was decreased by 3.5 times at the same high current densities.

The series of Mn oxide samples were prepared using the electrodeposition method, with variations in the following parameters (Table 5.1).

Table 5.1. Parameters of concentration of components ($\text{mol} \times \text{L}^{-1}$) varied in this study

[H ⁺] (added)			[Mn ²⁺]		[NH ₄ ⁺]		[Cr ³⁺]	
0	0.031	2	0.05	0.1	0	1.5	0	0.01

Current density was standard for high rate electrodeposition used before for fluorinecontaining electrolytes [129] ($10 \text{ A} \times \text{dm}^2$). Pt electrodes were used as cathode and anode where the cathode area was about 3-5 times larger. Namely, the anode area was 8.5 cm^2 . The synthesis voltage ranged from 3.4 to 3.9 V for samples with $[\text{NH}_4^+]$, and was slightly higher for samples without it. All obtained samples and compositions of electrolytes are shown in Table 2.2.

The difference with conventional electrochemical MnO_2 synthesis was observed as a pink colour of an electrolyte from the beginning of electrodeposition (Fig. 5.1). We suppose that it was one of the evidences of simultaneous diffuse control and many-electron electrode process with permanganate-ions formation.

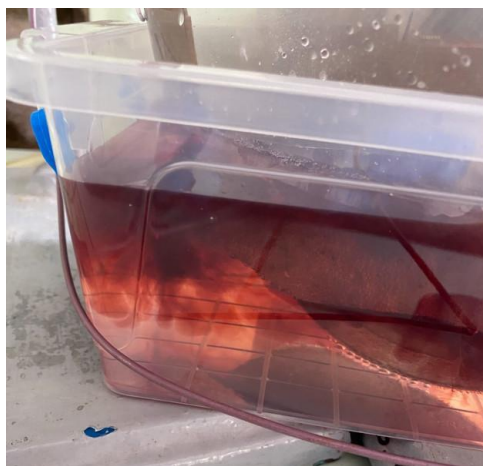
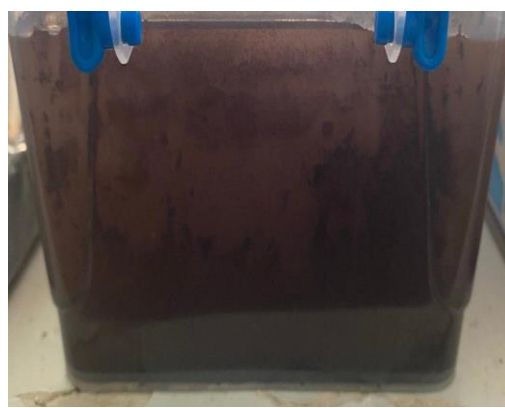


Figure 5.1. Photograph of sample ED-7 during the first minutes of synthesis.

Some fraction of these deposits existed as a relatively stable colloidal solution. The deposits in the latter electrolytes were dispersed with the maximal degree of comminution (Fig.5.2 b). Probably, the reason of larger size of aggregates at the presence of ammonium-ions is more active coagulation at the highest in this study total salt concentration (Fig. 5.2 a).



a



b

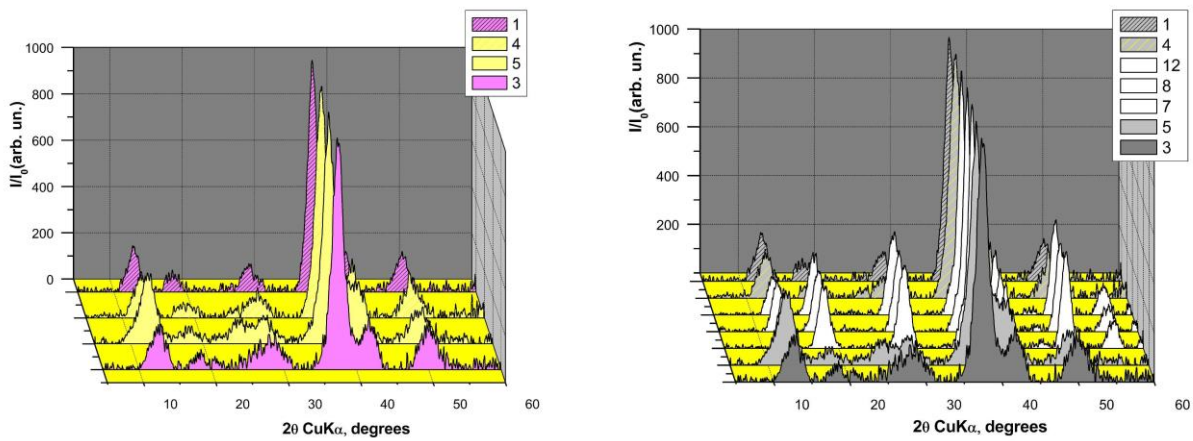
Figure 5.2. Photographs of electrolyte with sediment of samples ED-3 (a) and ED-2 (b) after synthesis and 24 hours of maturation.

5.1.1 XRD study

XRD patterns of ED series of samples are shown in Fig 5.3. The Rietveld refinement method was applied to simulate XRD patterns of electrodeposited samples ED1-13 by means of Powder Cell v. 2.3 Software. The method of trial and error was applied to

minimize R_p , R_{wp} , R_{exp} parameters. Refinement was performed step by step with single parameter change per iteration. Parameters were related to individual component: scale factor, crystal lattice unit cell (a , b , c , α , β , γ), profile of XRD peak FWHM (U , V , W), phase content, concentration, site occupancy, atomic coordinates etc. or common for all phases-candidates (zero shift).

Multiphase composition of samples was taken into account. The main phase component was simulated first. Then, gradually, the next by significance and content phase was involved in analysis. An example of such treatment can be seen below (Fig. 5.4). The preferred crystallographic orientation (predominately, March-Dollase [130]) was the mechanism to achieve better fitting of some XRD peaks choosing corresponding to this peak crystallographic plane. This method works especially well when one peak modelling results demonstrate significant deviations with experiment.



a

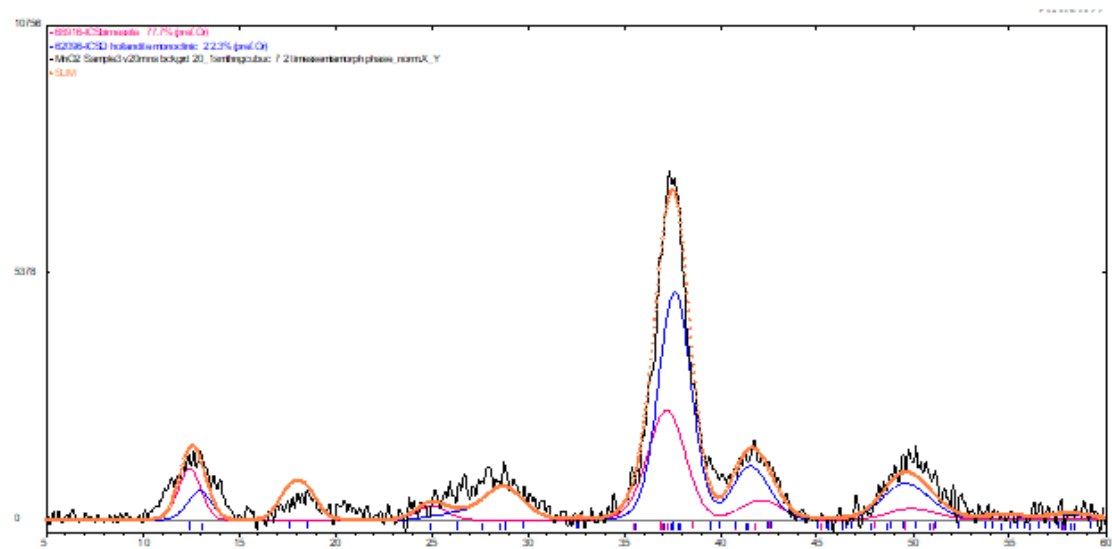
b

Figure 5.3. XRD Patterns of samples with main ramsdellite phase component (a) and α - MnO_2 phase component (b). Sample numbers are shown in legend.

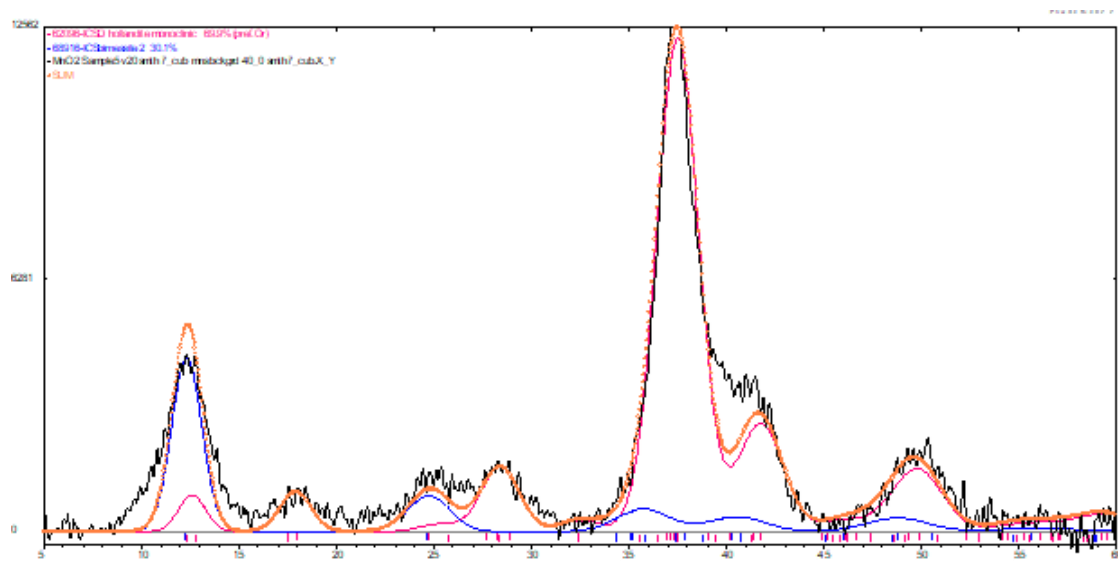
The result of modelling phase composition of samples by the Rietveld refinement is shown in Table 5.2, Fig. 5.4.

Table 5.2. XRD analysis of phase composition of electrodeposited samples.

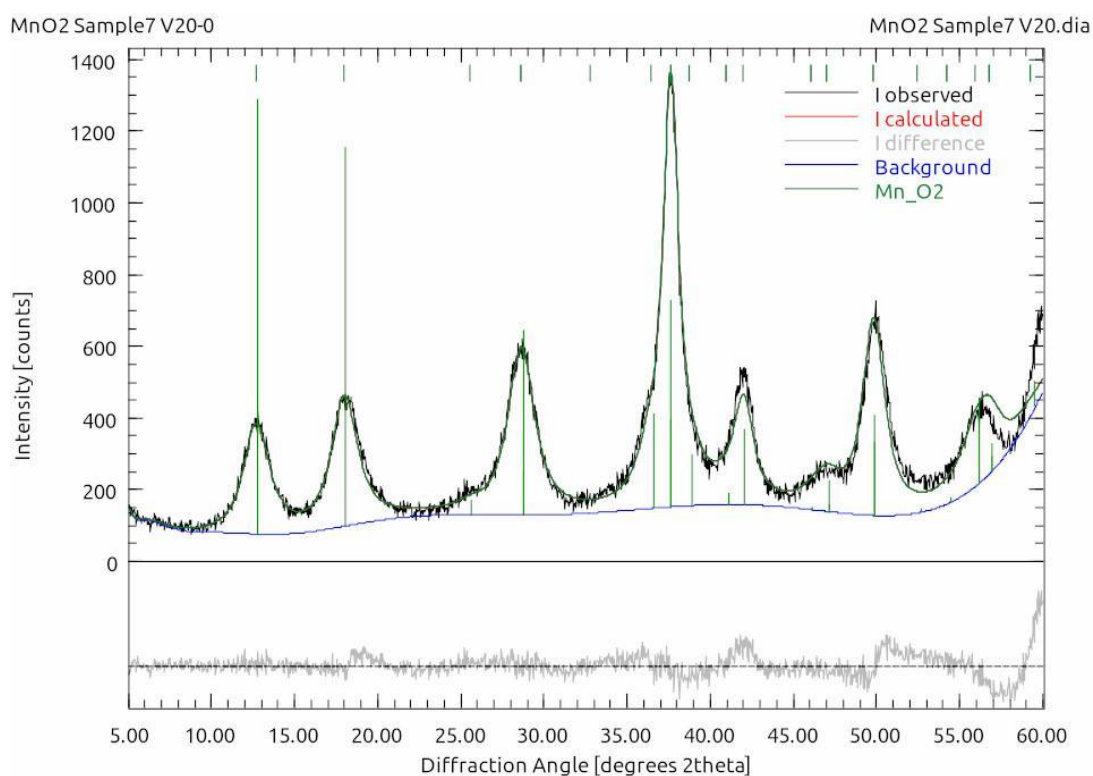
	Electrolyte composition, mol·L ⁻¹				Phase composition				
	[NH ₄ ⁺]	[H ⁺]	[Mn ²⁺]	[Cr ³⁺]	α -MnO ₂	γ -MnO ₂	δ -MnO ₂	ϵ -MnO ₂	Pt
1	1.5	0.031	0.05	0	85.4	0	14.6	0	
2	0	0.031	0.05	0	0	16.42	0	83.58	
3	1.5	0.031	0.1	0	22.30	0	77.7	0	
4	1.5	0	0.1	0	85.59	0	14.41	0	
5	1.5	0	0.05	0	69.89	0	30.11	0	
6	0	0.031	0.1	0	0	20.71	0	79.21	0.08
7	1.5	2	0.1	0	100	0	0	0	
8	1.5	2	0.05	0	100	0	0	0	
9	0	2	0.1	0	3.01	23.88	0	73.11	
10	0	2	0.05	0.01	19.94	11.95	0	68.11	
11	0	2	0.1	0.01	2.34	8.11	0	89.54	
12	1.5	2	0.1	0.01	100	0	0	0	
13	0	0.031	0.1	0.01	0	21.4	0	78.5	0.07



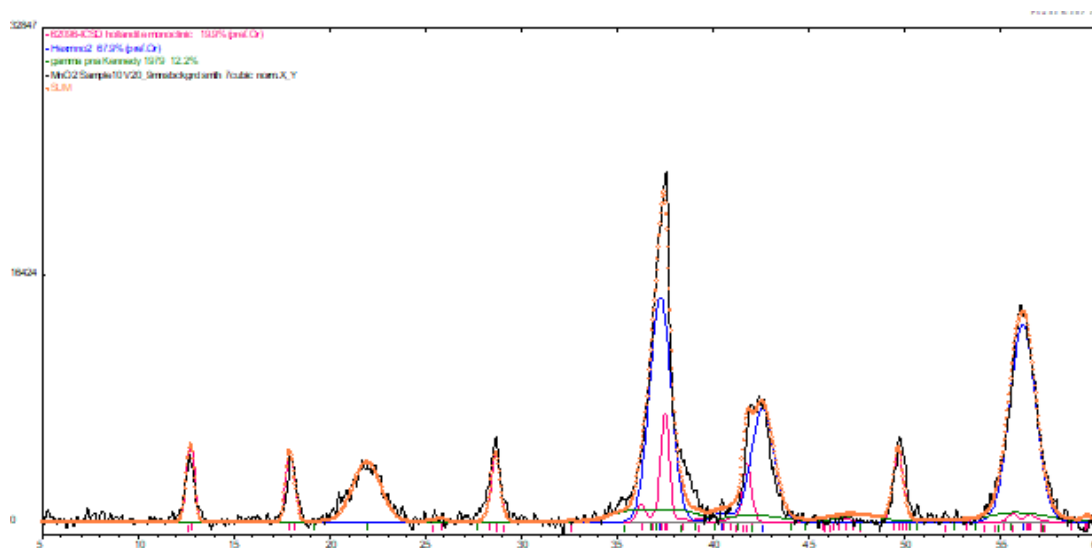
a



b



c



d

Fig. 5.4. Refinement by Powder Cell v.2.3 software XRD patterns of Samples ED-3 (a), ED-5 (b), ED-7 (c), ED-10 (d).

XRD patterns refinement was applied to evaluate phase composition, unit cell parameters and some more particular structural information of electrodeposited samples. It was found that an open structure polymorph of hollandite, psylomelane, etc. depending on stabilizing structure cavities cations) is observed at the presence of

NH_4^+ -ions. Electrolytes with 2M H_2SO_4 demonstrate maximal NH_4^+ influence with 100% content of $\alpha\text{-MnO}_2$ polymorph in the product (Fig. 5.4 c). Products electrodeposited from 1.5 M $[\text{NH}_4^+]$ electrolytes without H_2SO_4 also contain minor 15 – 30% of layered $\delta\text{-MnO}_2$ birnessite polymorph .

The stabilisation of γ -type group of products (γ - and $\varepsilon\text{-MnO}_2$ phases) takes place in an electrolyte without NH_4^+ -ions. Typical cases have intermediate acidity of electrolyte in this study (0.031 M) with γ/ε -phases ratio 20/80. Surprisingly, electrolytes with 2M H_2SO_4 and with no $[\text{NH}_4^+]$ contained totally three components with minor content of up to 20% of $\alpha\text{-MnO}_2$ polymorph (Fig. 5.4 d). These samples are prospective candidates of future heterojunction due to their multiple heterophase contacts. It can be suggested that the disproportion chemical stage becomes faster and possibly is responsible for $\alpha\text{-MnO}_2$ content growth.

It is interesting to compare the evidences of permanganate-ion formation with the phase composition. It can be shown that electrolytes with 2M H_2SO_4 with no $[\text{NH}_4^+]$ had pink colour during the first stage of electrodeposition attended by appearance of opalescent solution with a precipitate of predominantly γ -type product.

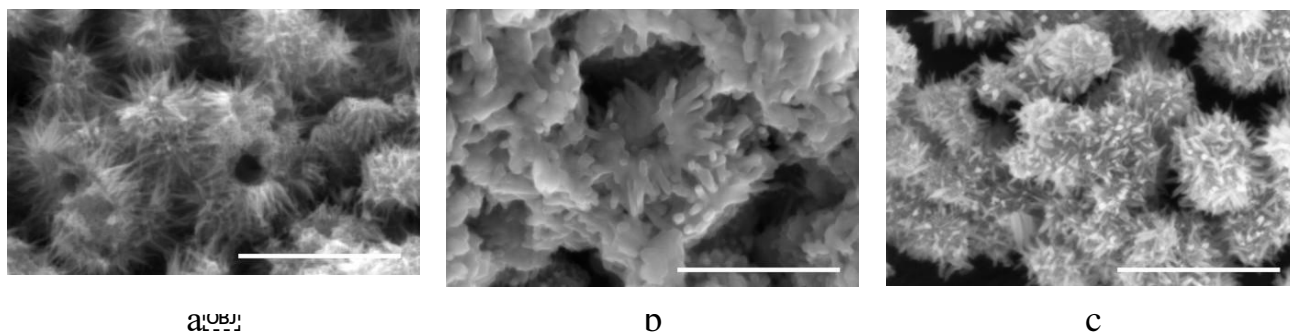
Coherent scattering regions. We used generated by Powder Cell software sizes and strains for comparison purposes. As shown by our previous observations with more sensitive $\text{MoK}\alpha$ - irradiation these data of sizes on $\text{CuK}\alpha$ are overestimated. There is always some fraction of particles between 2 and 5 nm and X-Ray amorphous state due to lower size or other reasons. Generally, these data agree with the smallest dimensions of nanoparticles from SEM/TEM observations.

The sizes of $\alpha\text{-MnO}_2$ crystallites in electrodeposition products increase in a 2M H_2SO_4 solution environment by up to 3 times. As shown by our previous SEM-studies of $\alpha\text{-MnO}_2$ nanoneedles, their thickness is to within 13-20 nm and XRD crystallites are generally close to the sizes of particles of $\alpha\text{-MnO}_2$ visible in SEM. Ramsdellite phase sizes have the same order of magnitude as $\alpha\text{-MnO}_2$. Well-crystallised close-packing of oxygens in ε -polymorph has one of the largest sizes of crystallites (8-17 nm) in this study.

The lowest strains in α -MnO₂ crystallites demonstrate electrolytes with maximal acid concentration (2M). Maximal strains for them are typical for lowest acidity of electrolytes (no acid). Ramsdellite polymorph crystallites have maximal strains in 2M acid electrolytes.

5.1.2 SEM, EDS and size distribution

Morphology of Samples is varied significantly (Fig. 5.5). Needle-like morphology is typical for Samples ED-7 and ED-10 (Fig 5.5, a,d and c,f). As follows from the phase analysis, needle-like morphology is typical for both ramsdellite and hollandite monophase samples. Nevertheless, this shape is practically absent for mixtures of these phases. It can be suggested the influence of intergrowth defects as the reason of this phenomenon. Samples synthesised in the presence of 0.031M H₂SO₄ without [NH₄⁺] have a particular structure of nanoplate-like growths with an average length of 65 nm and a thickness of 20 nm. This morphology probably corresponds to the presence of both γ - and ε -phases. In contrast, samples with aggregates of needle-like NPs of α -MnO₂ together with δ -phase form medium-sized (120-150 nm) aggregates entangled in a dense network of thin threads. For the pure hollandite phase observed after electrodeposition in electrolytes with 2M H₂SO₄ the formation of large aggregates with an average size of 650 nm is characteristic.



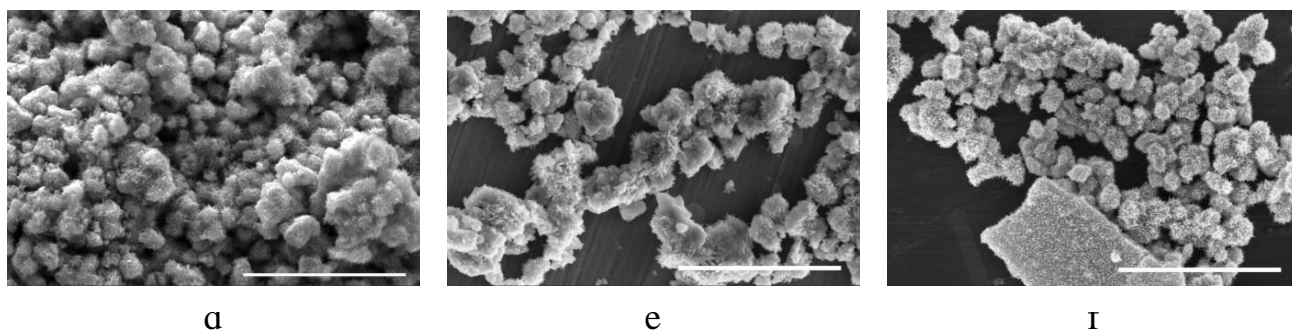
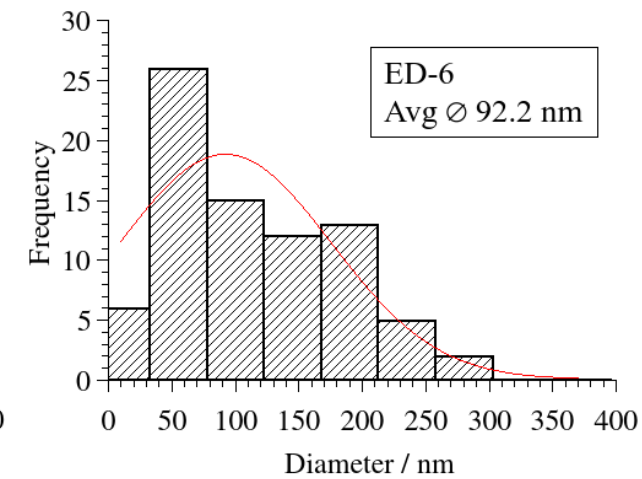
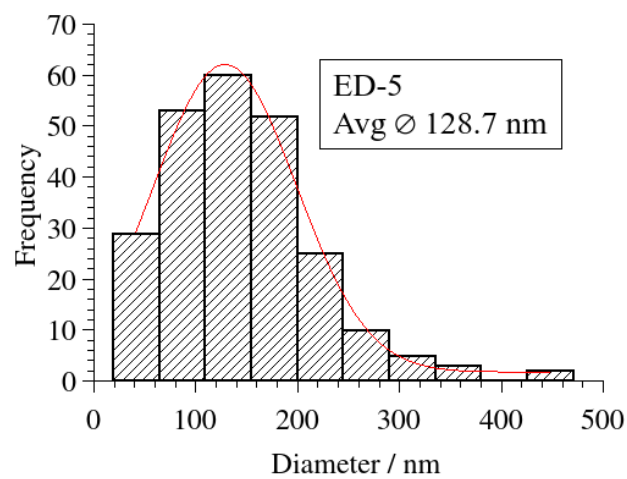
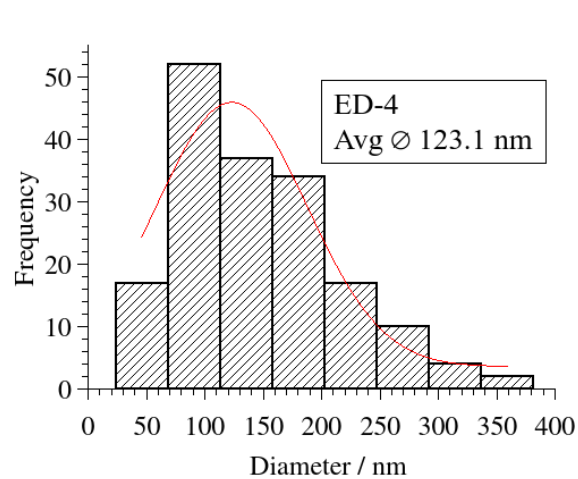
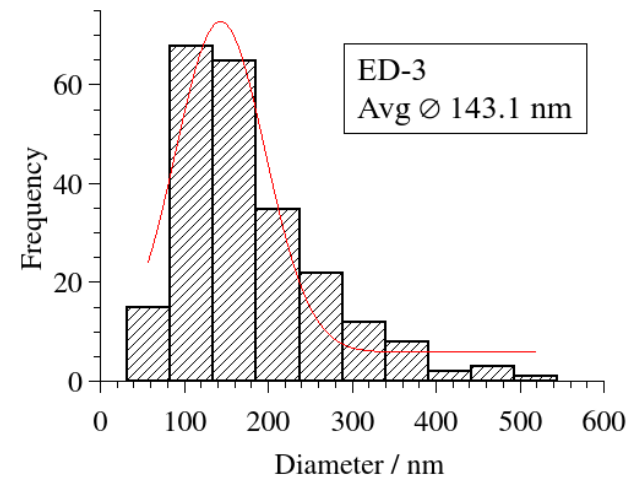
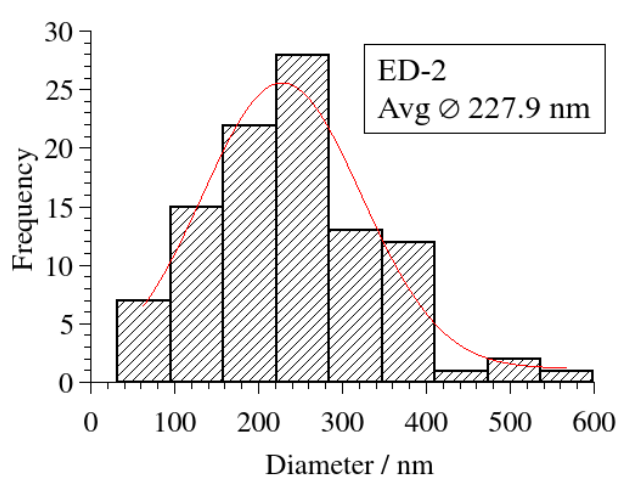
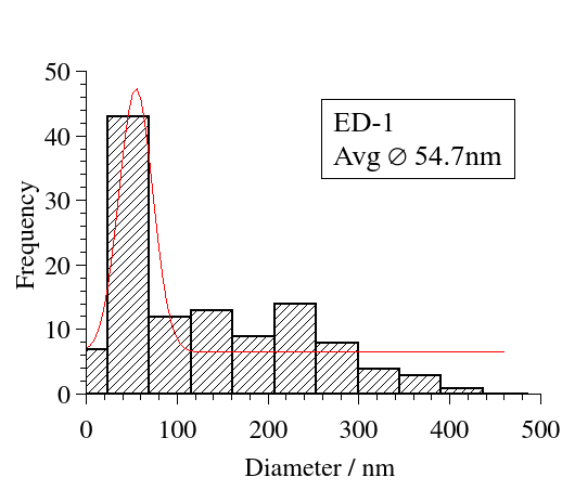


Fig. 5.5. SEM images of Samples ED 7 (a, d), 8 (b, e) 10 (c) with different magnification, Scale bar is 1 μm for images a, b,c and 5 μm for d, e, f.

Change of dispersity and morphology. Particle size, as a fundamental characteristic of a material, influences many properties and is an important indicator of the quality and performance of particles. To evaluate the average aggregate size distribution, the ImageJ software was used. A typical procedure involved measuring the linear dimensions of all particles in the visible region of the SEM image. SEM images with the maximum number of well-defined individual aggregates were selected for analysis. Further statistical processing of the data allowed us to determine the particle size distribution for each sample. The results were compared with those obtained using X-ray structural analysis.

It can be seen that ramsdellite-like samples possess maximal dispersity of aggregates starting with 50 nm till 150 nm. Sample ED-1 has minimal size of aggregates of NPs (50 nm). The maximum size of 300-600 nm in this series was found after electrodeposition in electrolytes with 2M H_2SO_4 (Fig.5.6).



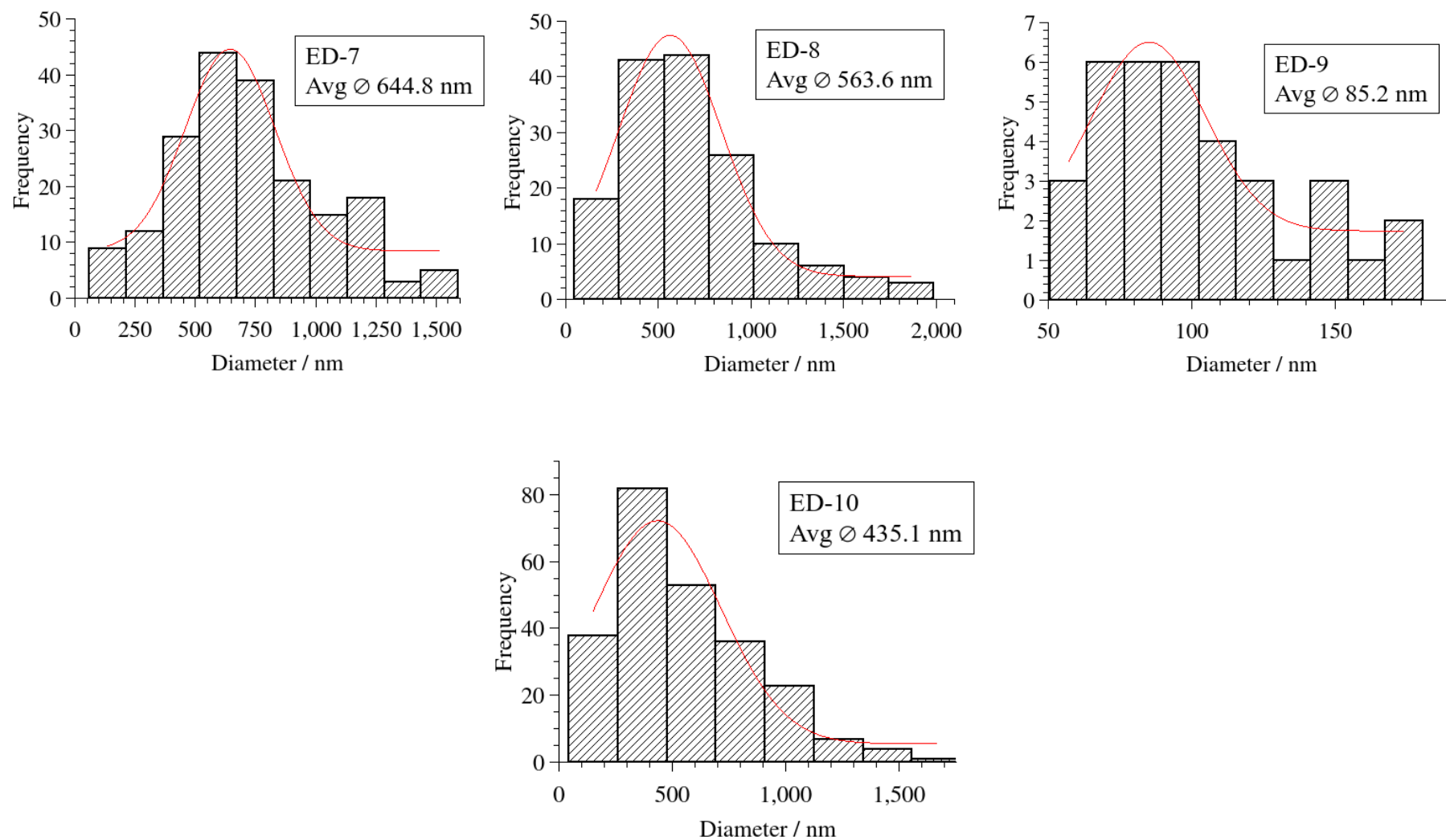


Figure 5.6. Aggregate size distribution calculated using ImageJ software of electrodeposited MnO_2 particles

To expand the understanding of the nature of composite materials and further calculation of formulas, an EDS analysis was carried out, the results of which are presented in the Table 5.3.

Table 5.3. Chemical composition of ED composites in atomic %.

Sample name	Mn	O	Cr	S
ED-1	43.2	56.8		
ED-2	43.1	56.9		
ED-3	43.4	56.6		
ED-4	43.1	56.9		
ED-5	43.1	56.9		
ED-6	41.4	58.6		
ED-7	43.7	56.3		
ED-8	43.6	56.4		
ED-9	41.5	58.5		
ED-10	40.8	59.2	-	
ED-11	45.7	54.2	0.15	
ED-12	48.8	50.4	0.35	0.21
ED-13	48.1	50.6	0.49	

EDS analysis showed the Mn to O ratio characteristic of manganese dioxides. Samples ED11-13 contained Chromium, which was introduced into the electrolyte as a dopant.

5.1.3 BET analysis

The results of surface area measurements are shown in Table 5.4. The data received are sometimes by several times larger than the surface area of CS1-CS9 series of samples. SEM and TEM data of both series of samples demonstrate in contrary smaller size of NPs of CS series of samples. Therefore, the tendency to aggregation for CS series NPs is larger irrespectively the composite with HNTs or pure Mn oxides/oxidehydroxides. The

probable reasons of distinguishing behaviour of ED series are in the difference of chemical composition since the latter consists mostly of MnO₂ polymorphs. Moreover, ramsdellite based samples ED-2, ED-13 have surface area below 100 m²/g that is in agreement with the existence in birnessite, hollandite polymorphs usually some additional contribution of micropores of structure tunnels of 0.5 nm in diameter.

Table 5.4. Data on surface area of electrodeposited MnO₂ samples

Sample name	BET Multipoint Surface Area, m ² /g
ED-1	166.34
ED-2	82.88
ED-3	212.29
ED-4	210.26
ED-7	209.15
ED-10	146.09
ED-12	215.16
ED-13	65.65

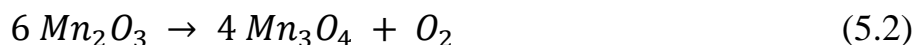
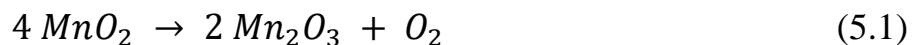
Therefore, it can be seen that the surface area of ED samples obtained with NH₄⁺ have maximal values to within 200 m²/g. Probably, the highest acid concentration in this study (2M) acts independently of NH₄⁺-ions as a parameter of surface area enlargement (Samples ED -7,10, 12).

5.1.4 TGA/DTA/MS analysis

Thermal analysis provides important data on the thermal stability, phase composition, and content of different types of water in synthesised samples. MnO₂.

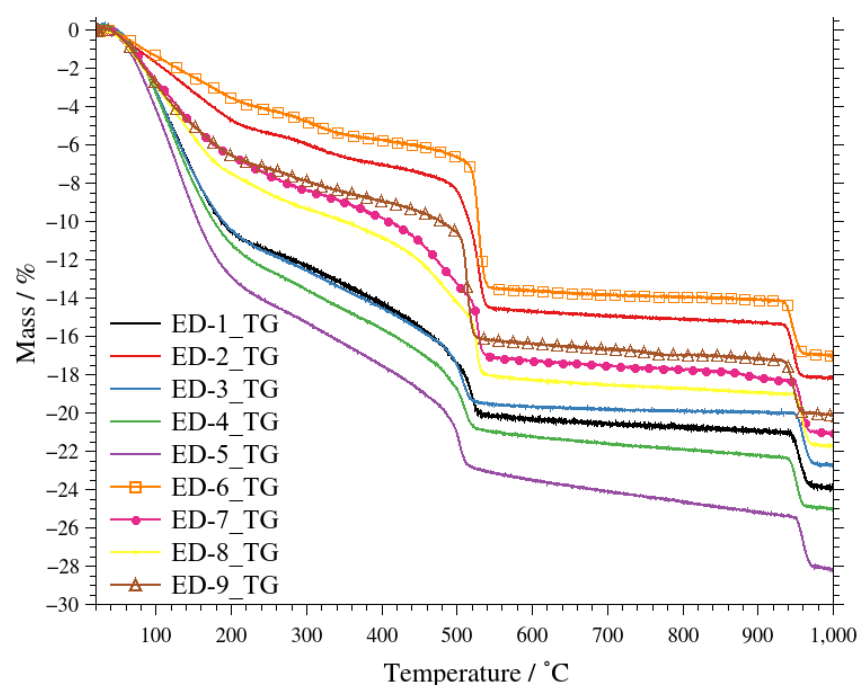
Upon heating MnO₂ undergoes a series of transformations into more thermally stable forms. At temperature in the range of 310-390°C degrees, a weak exothermic may be present indicating dehydration of γ - MnO₂ and its phase transition to tetragonal pyrolusite β -MnO₂. A subsequent increase in temperature leads to the loss of O₂ and the formation

of trivalent manganese oxide Mn_2O_3 with trigonal crystal structure. Typically, the process occurs at a temperature of 450-550°C and is accompanied by a sharp peak on the DTG curve. At a temperature of 950-1000°C losing oxygen Mn^{3+} partially reduces to Mn^{2+} transforming into tetragonal hausmannite Mn_3O_4 . The final stage of thermal transformations of MnO_2 is the complete reduction of all manganese atoms to Mn^{2+} with formation of cubic MnO [49] occurs at 1460°C in N_2 atmosphere [131]. The corresponding sequence of chemical reactions is given below (5.1 – 5.3).

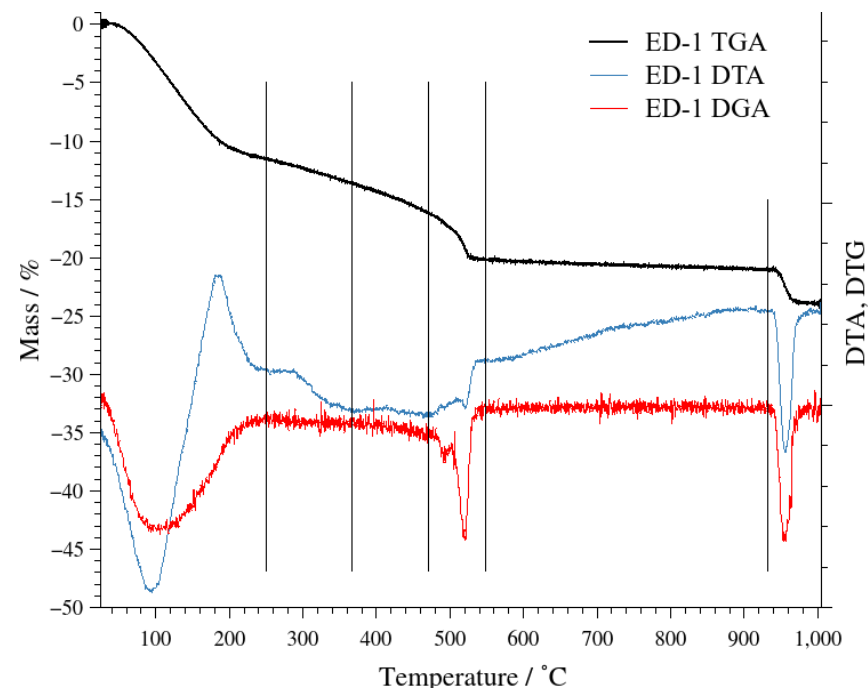


Particular attention should be paid to the behaviour of water associated with the manganese crystal lattice, including surface and bulk OH groups [132]. These data can be useful for calculating the phase composition and assessing defects.

Initially physisorbed molecular water is removed in range from room temperature to 130-150°C. Next, structural water is released in two steps: chemically bonded from 150 to 250°C and OH-water at 250-490°C attributed to removal of lattice OH groups from volume. The loss of structural water is closely associated with the presence of vacancies in the crystal structure. The loss of chemically adsorbed oxygen from the crystalline manganese dioxide lattice occurs 50° before the start of the main O_2 loss during the transition to Mn^{3+} oxide. Figure 5.5a shows thermogravimetric curves of electrodeposited samples as well as an example of analysis of the TG curve for ED-1 (Fig. 5.5b).



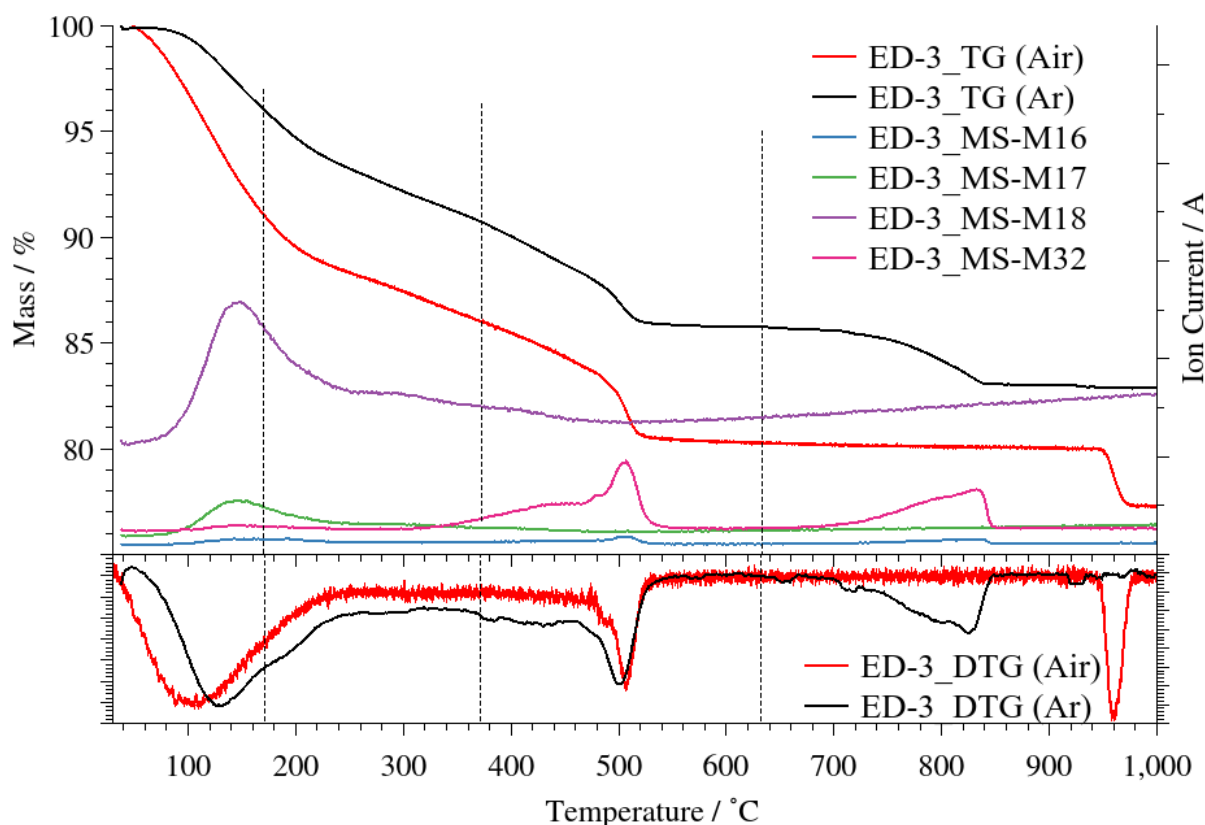
a



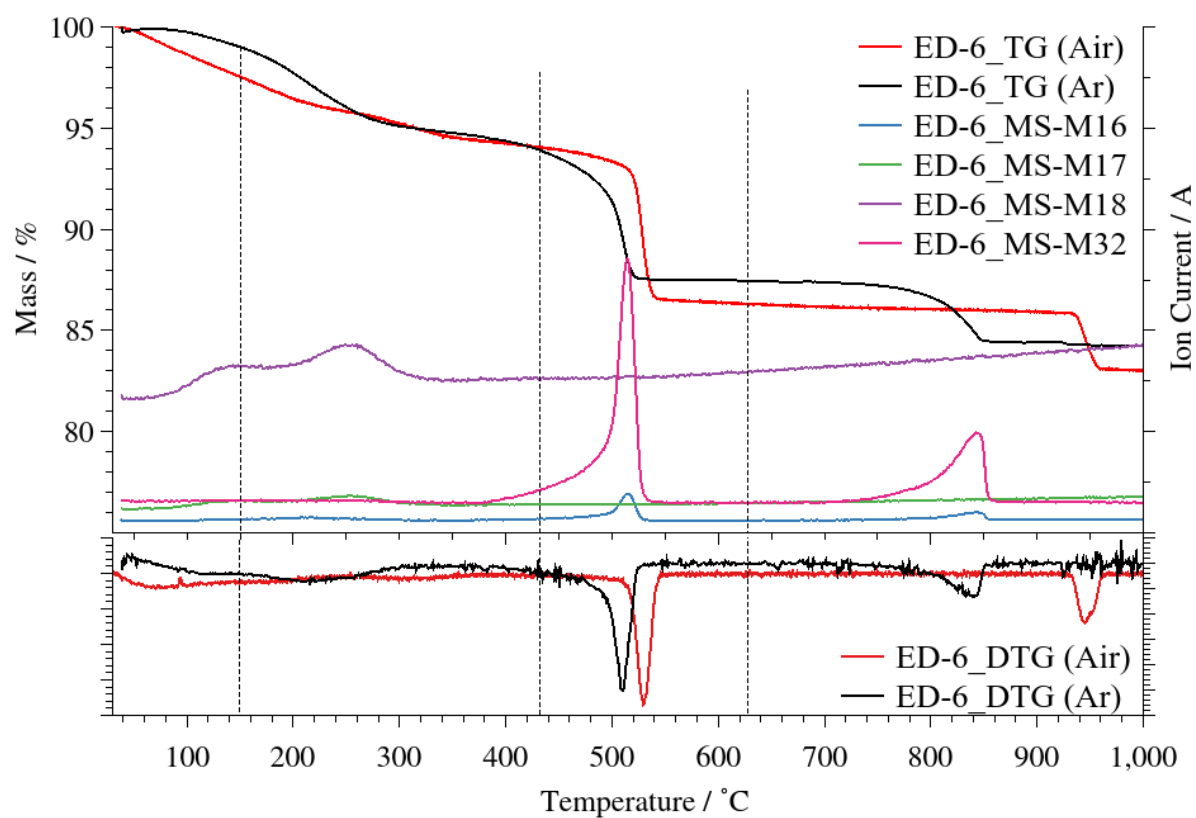
b

Figure 5.5 – TGA curves of electrodeposited MnO₂ samples in Air flow (a) and example of mass loss analysis for sample ED-1 (b)

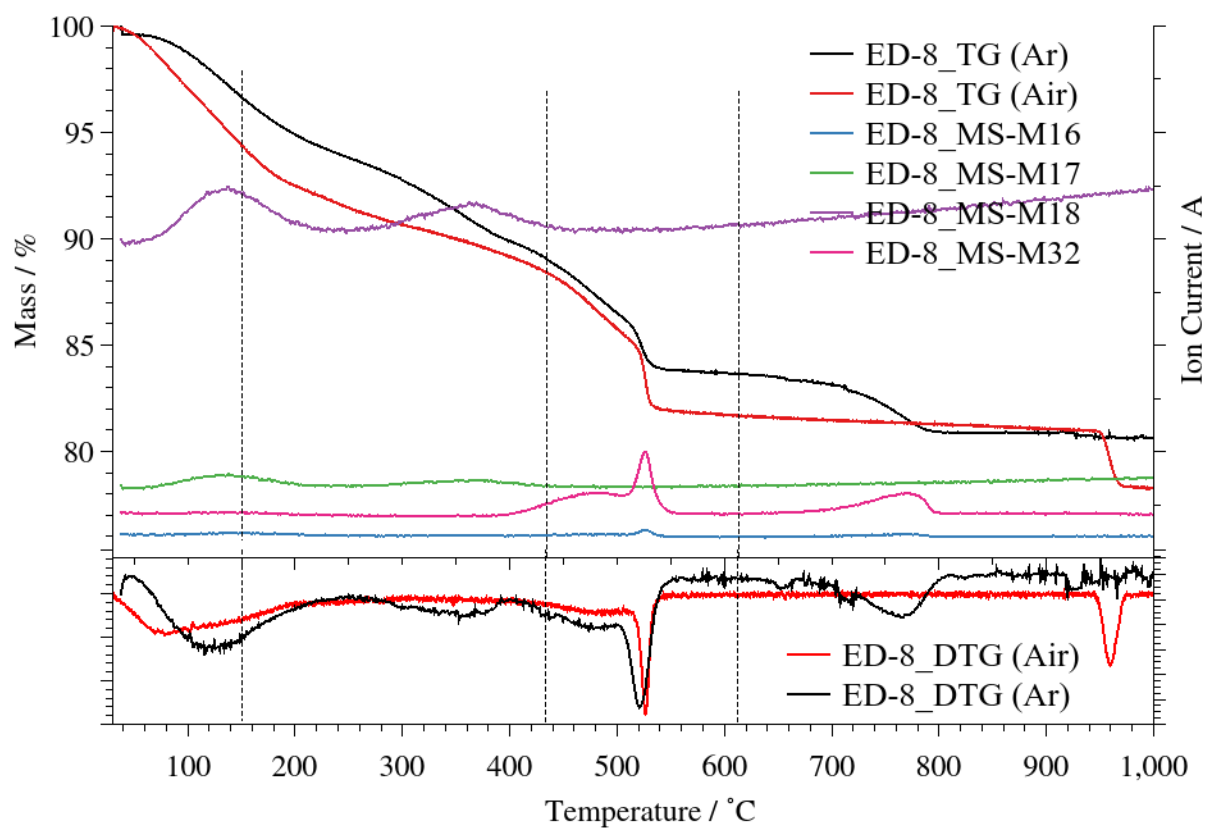
For a more detailed analysis of mass losses, we carried out the TG analysis coupled with mass spectroscopy in an inert atmosphere of Argon for samples ED-3, ED-6, and ED-8 (Fig 5.6). These samples were chosen as representatives for series with main δ -, ϵ - and α - phases of MnO_2 , respectively. Obtained data are the key to precise determination of products released during TG analysis for further evaluation of the content of defects in the material.



(a)



(b)



(c)

Figure 5.6. TG-MS and DTG curves of (a) Sample ED-3, (b) Sample ED-6, (c) Sample ED-8 main δ -, ϵ - and α - phases of MnO_2 , respectively.

Mass spectra give direct evidence and proof of the temperature range of evolving gasses. For instance, the analysis of water release demonstrates two effects for all three samples. The first one is the physically sorbed water ($H_2O_{f.s.}$), which is typical for all samples, but the second one's behaviour is different. Birnessite derived Sample ED-3 and γ -polymorph based Sample ED-6 have broadened maximum below 300°C, whereas α -derived Sample ED-8 has its edge above 400 °C. We can suggest eliminating water ($H_2O_{c.s.}$) from micropores of hollandite structure tunnels here. This temperature is 100°C higher than the data of porometry analysis obtained in our group for hollandite samples earlier [133]. The latter effect overlaps slightly with the effect of oxygen-evolving in Sample ED-8, which occurs again differently for all samples.

Hollandite displays the first broadened peak of oxygen release ($M = 32$ a.m.u.) with a distinct maximum at 470 °C. Birnessite (Sample ED-3) has its more broadened shoulder at lower temperature (340 vs 400 °C in hollandite). Ramsdellite-like structure (Sample ED-6) demonstrates an intensive asymmetric peak of one process with maximum at 510 °C. It can be suggested by comparison with BET data available now and received previously in our group that Sample ED-8 and Sample ED-6 have significant contributions to the interface states, unlike ramsdellite samples, which usually have lower surface area (below 100 m²/g). The presence of a maximum of this peak for hollandite can be due to the very distinct needle-like shape of its NPs, unlike birnessite Sample ED-3. The summarized data of TG analysis combined with mass spectroscopy for selected samples are presented in the Table 5.5.

Table 5.5. Summary on the thermal behaviour of samples ED-3, ED-6, ED-8 in Air and Argon atmosphere coupled with MS data

		ED-3		ED-6		ED-8	
		Air	Ar	Air	Ar	Air	Ar
$H_2O_{f.s.}$	T, °C	20 - 170	20-170	20-150	20-150	20-150	20-150
	Δm , %	8.93	3.93	2.47	1.00	5.61	3.32

		ED-3		ED-6		ED-8	
		Air	Ar	Air	Ar	Air	Ar
H ₂ O _{c,s} + OH groups	T, °C	170-372	170-372	150-432	150-432	150-343	150-434
	Δm, %	5.05	5.32	3.49	5.09	5.97	7.59
O ₂ release (1)	T, °C	507	502	529	510	526	520
	Δm, %	5.75	4.98	7.74	6.45	6.74	5.45
O ₂ release (2)	T, °C	961	825	944	839	956	766
	Δm, %	3.03	2.94	3.35	3.31	3.45	3.09

The chemical formula of the composites was calculated based on the Ruetschi model using thermal analysis data applying formula 2.3 as outlined in Section 2.3.1 (Table 5.6).

Table 5.6. Calculated formula of some ED samples by the Ruetschi model

Sample name	Calculated formula
ED-6	$Mn_{0.81}^{4+} Mn_{0.15}^{3+} \square_{0.04} O_{1.69}^{2-} OH_{0.3}$
ED-8	$Mn_{0.68}^{4+} Mn_{0.28}^{3+} \square_{0.04} O_{1.55}^{2-} OH_{0.45}$

5.1.5 DRS analysis and calculation of band gap width, determination of energy level positions

Semiconductor properties of electrodeposited series of samples were determined using Diffuse Reflectance Spectroscopy. The DRS spectra of some ED samples are shown in Fig. 5.7. Spectra are grouped in accordance with the main phase component. For instance, the group of Samples (ED-2, ED-10, ED-13) has common in behaviour, probably, due to the same main γ -MnO₂ component. Samples ED-7, 8, 12, in turn, form the group of spectra with α -MnO₂ component.

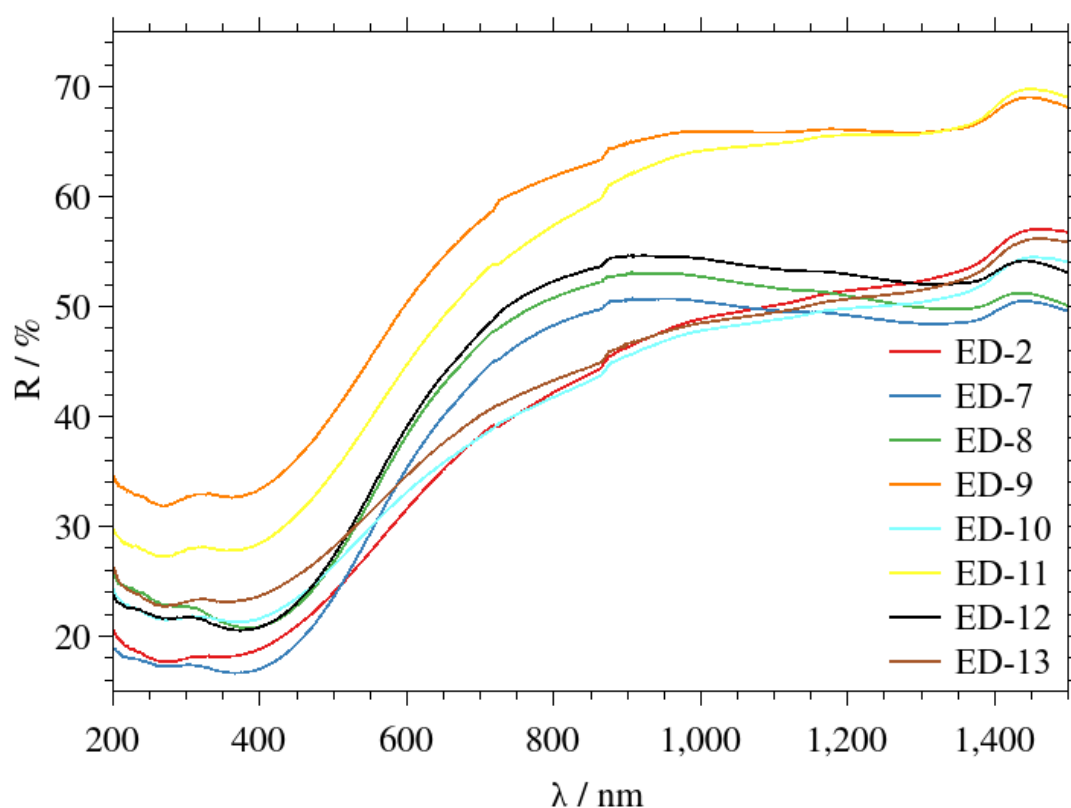


Fig. 5.7. DRS of some samples of the ED series

The reflectance spectra of these samples were transformed into absorption spectra by applying the corresponding Kubelka-Munk function, $F(R_\infty)$. The parameter $(F(R_\infty)h\nu)^{1/n}$ with $n = 1/2$ for direct allowed transition was further taken into account for calculations. The Tauc plots that include the Kubelka-Munk function plotted against photon energy for the ED series of samples are shown in Appendix B. The x-axis

intersection point of the linear fit of the Tauc plot gives an estimate of the band gap energy.

The range of band gap values is varied to within 2 - 2.4 eV that confirm visible light photoactivity of the composite materials of ED-series. Analysis of band gap results of some previously obtained samples of γ - and α -polymorphs in [50], [83] study confirmed their prospectives as photocatalysts of water splitting.

According to formulas 2.8-2.11 given in Section 2.3.7, the absolute electronegativity of Mn and O atoms, the Mulliken electronegativity of MnO_2 and positions of the conduction band and the valence band were calculated for the electrodeposited MnO_2 samples. Based on literary data, electron affinity is a neutral atom's energy change when an electron is added to the atom to form a negative ion. First ionization energy is the energy necessary to remove an electron from the neutral atom. For Manganese, it is -0.52 eV and 7.434 eV, respectively. In turn, the parameters for oxygen electron affinity is 1.46 eV, first ionization energy is 13.62 eV. Calculated according to formula 2.11 Mulliken electronegativity of MnO_2 was 5.81 eV. For further calculations, the data of the band gap energy obtained with the help of the Kubelka Munk function were used. The calculations details according to Mulliken electronegativity are presented in Table 5.7.

Table 5.7. Calculated CB and VB edge potentials for MnO_2 samples.

Sample name	E_g , eV	E_{CB} , eV	E_{VB} , eV
ED-1	2.29	0.17	2.46
ED-2	2.24	0.19	2.43
ED-3	2.25	0.19	2.44
ED-4	2.23	0.20	2.43
ED-5	2.34	0.14	2.48
ED-6	2.36	0.13	2.49
ED-7	2.32	0.15	2.47
ED-8	2.25	0.19	2.44

Sample name	E _g , eV	E _{CB} , eV	E _{VB} , eV
ED-9	2.28	0.17	2.45
ED-10	2.21	0.21	2.42
ED-11	2.26	0.18	2.44
ED-12	2.28	0.17	2.45
ED-13	2.16	0.23	2.39
MnO ₂ PCP	1.98	0.32	2.30

For a theoretical assessment of the sample efficiency, it is essential to compare the calculated energy levels of the conduction and valence bands, expressed on the SHE scale, with the electrode potentials of the processes responsible for the formation of reactive species potentially involved in photocatalytic degradation, which are presented below (5.4-5.10) [134]:



It is worth noting that, unlike the CS series, the samples of the ED series are not responsible for processes (5.4, 5.5) but can be active in the generation of active oxygen species (5.6-5.10).

5.2 Comparison of chemical and electrodeposition pathways of manganese dioxide from NH_4^+ -containing electrolytes

This study is focused on products of oxidation of Mn^{2+} obtained by chemical and electrodeposition methods. Nonspontaneous electrodeposition of manganese dioxide was the starting point of selection of conditions of spontaneous chemical deposition, keeping in mind the electrolytic doping technique applied earlier to electrodeposition to control phase composition and defect states of interface and in bulk as active sites for solid state electroreduction in batteries or (photo/electro)catalytic processes [83], [135].

Electrodeposition mechanism of manganese dioxide is complex. It includes chemical stages of disproportionation, hydrolysis and some more special stages can be observed depending on cationic electrolyte composition [83]. The latter stages are practically omitted for study in scientific literature. However, the opportunity to control the polymorphic composition of MnO_2 by the addition of cations of various natures opens new perspectives on the development of new functional materials.

The influence of cations as templates of stabilisation of open structure polymorphs of manganese dioxide system is shown earlier for particular conditions of hydrothermal synthesis [136]. Entropic factor predominates in this stabilisation since cations have dynamic positions in structure tunnels together with molecules of water. We observed the stabilisation of hollandite structure polymorph with alkali metal and ammonium ions at electrodeposition from sulfate and fluorine-containing electrolytes [83]. Nevertheless, the complexity of the electrodeposition mechanism makes problematic reliable analysis of the mechanism of open structures of manganese dioxide frameworks formation at the presence of NH_4^+ ions.

The formation of open structure polymorph of hollandite at the presence of alkali metal ions and NH_4^+ at electrodeposition could be the signature of one of the chemical stages. In this case, the appearance of hollandite among chemical deposition products should be one of the confirmations of this hypothesis. That is why, conditions of chemical synthesis in the CS series of samples were chosen as close to electrodeposition conditions as possible. Let us note that the chemical deposition

requires substantially different synthesis conditions regarding medium acidity. pH must be larger than 5-6. The Pourbaux diagram indicates increased stability of lower valenced states of $\text{Mn}^{2+/3+}$ oxides in alkaline medium conditions. This means that the narrow region of close to neutral medium conditions is the most suitable for this analysis.

Our phase analysis of 2 groups of samples (from CS-1 to CS-4, and from CS-5 to CS-9) with pH=10 and 5-7 respectively demonstrated results without the direct answer to the issue above. CS-5 Sample without ammonium ions and Samples CS6-9 synthesized at pH below 7 had no hollandite or any other open polymorph in composition. To be accurate, XRD patterns of CS-6-9 contain very broad amorphous structure waves with maximum at $d=0.7$ nm, i.e. of birnessite maximal intensity peak where other open structure states can be present. It signifies that coherent scattering regions of open structures here are below 2-5 nm, i.e. the distinct template effect visible in acid medium for electrodeposition products is not working for chemical deposition. Nevertheless, deposited in alkaline medium (pH=10) Samples CS2-3 with ammonium ions contained traces of open structure polymorphs of romanechite etc. that are not amorphous states.

Thus, we can conclude that additional proofs of the chemical stage hypothesis of hollandite formation were not added. The absence in neutral and traces of open structure polymorphs in alkaline mediums signify some complex phenomena in the roots that need further study. For instance, the role and stability of the Tutton salt should be analysed depending on pH. Otherwise, hypotheses about the electrochemical nature of hollandite formation at electrodeposition should be considered.

Conclusions to Section 5

The electrodeposition method is traditionally applied to obtain manganese dioxide. Our approach included the lowest Mn^{2+} concentrations in combination with the high current density that together supported diffusion control and, as a result, the highest possible dispersity of particles in the product. Different acidity of the electrolyte was applied. The maximal acidity (2M H_2SO_4) favours disproportionation of Mn^{3+} and various morphology. The absence of acid addition

corresponded to pH close to 3.5 – 4.0. This range of samples can be distinguished by δ/α -MnO₂ polymorphs intergrowth.

The additive of ammonium ions was used as a template for the hollandite phase. Some samples have natural combinations of 2-4 polymorphs. SEM data demonstrate micro fragments of plate-like aggregates of δ -MnO₂ and γ -, α -MnO₂ needles at the surface.

Analysis of band gap results of some conventional electrodeposited samples of γ - and α -polymorphs obtained in [50], [83] study confirmed their prospectives as photocatalysts of water splitting. Nevertheless, the important drawback some of them for hydrogen evolving reaction (HER) is up to 0.5 V (SHE) difference of E_c with $E^0H^+/H_2 = 0.0$ V (SHE). As can be seen in the formula below, the following factors of influence could help to overcome this problem: increase of band gap together with decrease of electronegativity of the photocatalyst:

$$E(\text{SHE}) = \chi - 0.5 E_g - 4.5 = 5.814 - 0.5E_g - 4.5 \quad (5.11)$$

where $E(\text{SHE})$ is conductivity band energy value expressed in hydrogen scale of potentials (SHE); χ is the Mulliken electronegativity of MnO₂; E_g is a band gap. Nevertheless, some manganese oxides [64] have excellent E_g values and E_{CB} positions towards HER that can be taken into account for our further studies.

It is suggested that the following directions of adjustment of electrodeposited MnO₂ to HER photocatalysis exist. The growth of Mn^{2+,3+} contribution will reduce electronegativity of a product. The heterojunctions with low valence oxides of manganese, titanium dioxide can be used. The addition of dopants like Fe³⁺ or Cr³⁺ [50] could cause a positive effect on E_c .

The results of experimental studies of this section are presented in the following publications:

Conference materials:

1. Sokolsky G.V., **Kovinchuk I.V.**, Ragulya A.V., Spreitzer M., Kržmanc M.M. Electrodeposition of nanodispersed α/δ - & γ/α -manganese dioxide composites for

visible light photocatalytic applications, *10th Ukrainian Congress of Electrochemistry Achievements Problems and Prospects*, 2, 2024, P. 32-36. <https://doi.org/10.33609/elchimcongr.2024.09.1-210>. *Personal contribution is analysis of literary sources, conducting experimental research, processing and formatting results, writing.*

Abstracts of conference presentations:

2. Sokolsky G., **Kovinchuk I.**, Lazzara G., ZudinaL., Hluhova P., Andriiko O. (2023) Comparison of chemical and electrodeposition pathways of manganese dioxide from NH_4^+ -containing electrolytes. *Book of abstracts. International Conference on Chemistry, Chemical Technology and Ecology*. Kyiv, (Ukraine). P. 87–88. *Personal contribution is analysis of literary sources, conducting experimental research, processing and formatting results.*

CHAPTER 6. FUNCTIONALIZATION OF SAMPLES OF MANGANESE SYSTEM (III, IV)

6.1 Photocatalytic degradation of composite films: mass loss measurements, lifetime prediction and carbonyl index

Figure 6.1 shows the photos of the films, preparation procedure and characterization if which is reported in Sections 2.2.3 and 3.1 respectively after UV-irradiation. They are clearly demonstrating that the combined use of TiO_2 and MnO_2 as a photocatalyst exhibits enhanced effect over the use of only TiO_2 . After a total of 90 hours of UV irradiation, the films made with addition of 1:1 blend of TiO_2 and MnO_2 demonstrated a notable synergistic increase in mass loss, reaching 21.2% by mass. In comparison, films that used only TiO_2 as a photocatalyst exhibited a mass loss of 14.6%, as shown in Figure 6.2.

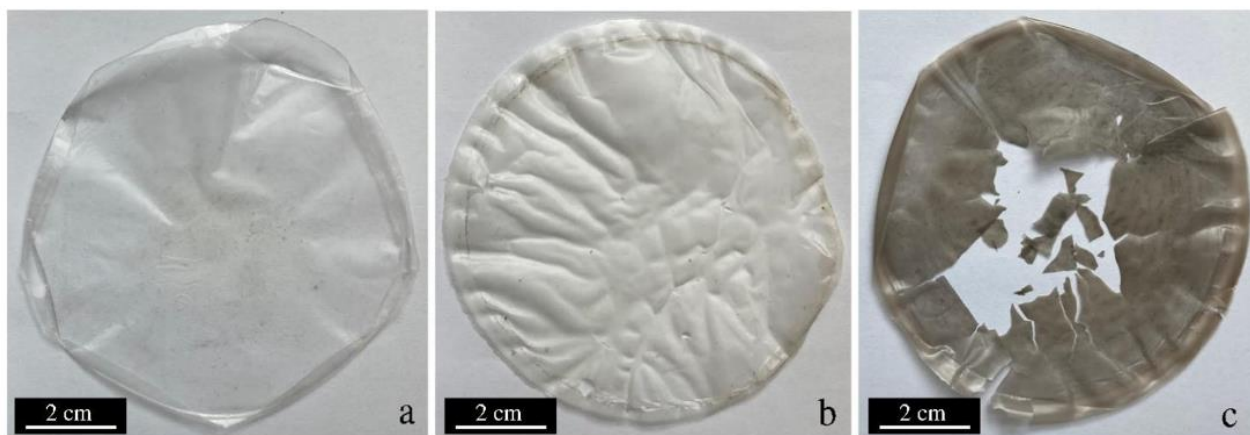


Figure 6.1. Photos of pristine (a) and composite films PE/TiO_2 (b), $\text{PE/TiO}_2/\text{MnO}_2$ after 90h of irradiation.

The coupling effect of TiO_2 with MnO_2 probably explains the synergism of the simultaneous action of both oxides. Thus, the increase in mass loss may be due to the improved separation of photoinitiated charge carriers in the presence of manganese dioxide. Therefore, using nanosized TiO_2 with MnO_2 leads to a significant increase in photocatalytic activity. Fig. 6.2 b illustrates the mass loss of films under dark conditions. Rutile polymorph of titanium dioxide was used in this experiment.

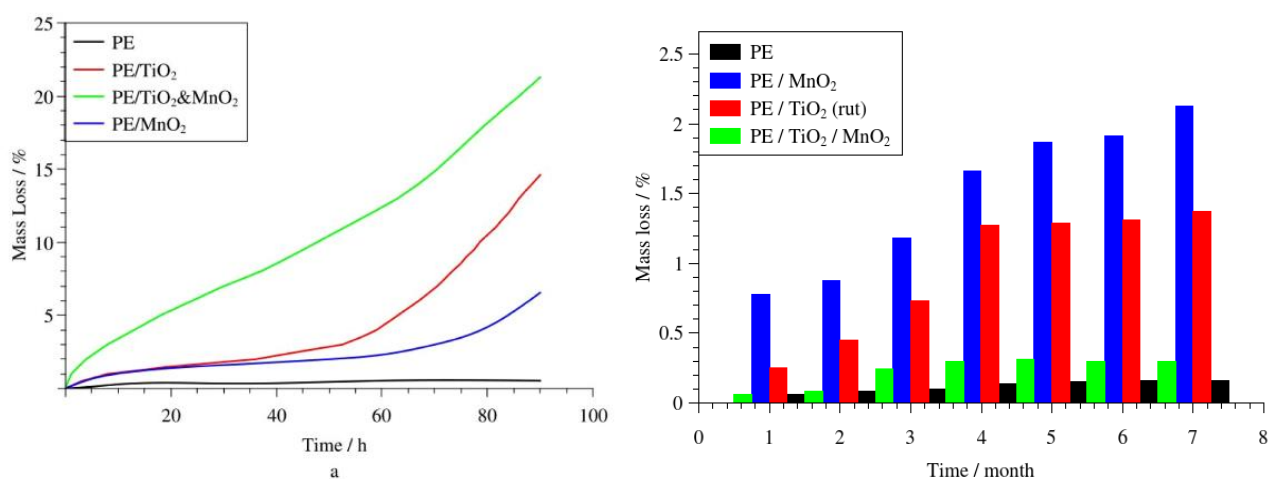


Figure 6.2. Dependence of film mass loss on time under UV irradiation (a) and in dark conditions (b).

Notably, neither anatase nor rutile forms of TiO₂ show any oxidizing or photocatalytic abilities under these conditions. As a photocatalyst, titanium dioxide performed worse than manganese dioxide when light was absent. This result is consistent with expectations, as manganese dioxide's oxidizing properties contribute to its better performance in the dark. The significant reduction in efficiency of the TiO₂&MnO₂ mixture can be attributed to the reduction products of manganese dioxide interfering with the polymer degradation process.

The mass loss of composite films as a function of irradiation time was analyzed graphically, showing a notably high correlation coefficient for both zero and first-order kinetics in the PE/TiO₂&MnO₂ samples. Similar kinetic behaviour is observed in samples containing only TiO₂ during the initial stages of degradation. This allows us to conclude that the composite catalyst stabilizes a definite degradation mechanism. Theoretical models of chemical solid-phase reactions were evaluated by applying Yander's, Anti-Yander's, and Wagner's equations. According to the Erofeev-Avrami equation, the nuclear model demonstrated the best correspondence for sections of curves where the zero and first-order kinetic dependencies are fulfilled. Thus, the nuclei of oxidation products are grains rather than flat ($n = 2, 3$). Such a reaction predominantly occurs within a heterogeneous region, aligning with characteristics typical of a zero order reaction.

The Fourier Transform Infrared spectrum of the pristine film exhibits characteristic absorption bands at 2920 cm^{-1} and 2850 cm^{-1} , which are attributed to the stretching vibrations of the asymmetric and symmetric -CH_2 groups, respectively, as shown in Fig. 6.3. The intense band at 1467 cm^{-1} is identified as the deformation vibration of the -CH_2 group. The absorption band at 727 cm^{-1} is associated with the γ -fluctuations of the -CH_2 group. The positions of these bands remain unchanged throughout the degradation process.

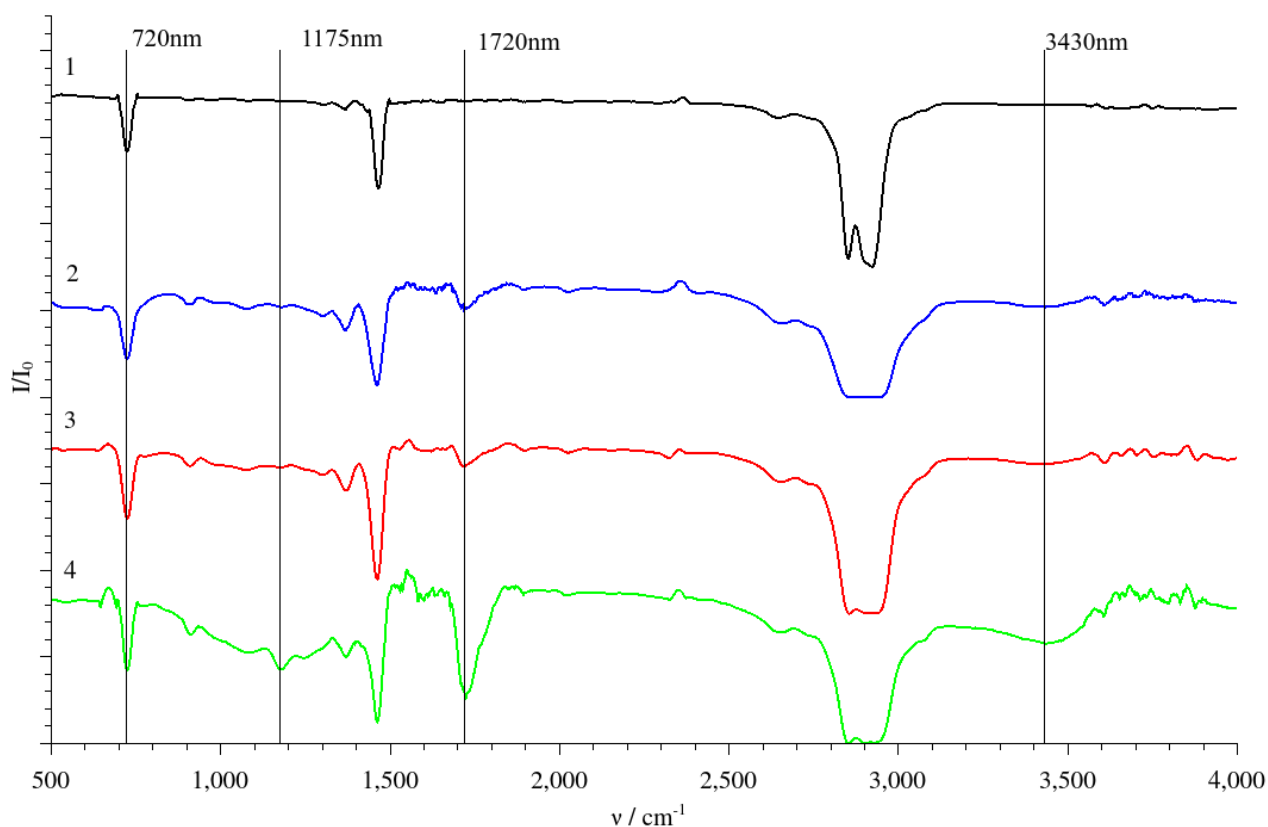


Figure 6.3. FTIR spectrum of PE films: 1 - PE before irradiation; 2 - PE after 40 h of UV; 3 - PE/TiO₂ after 40 h of UV; 4 - PE/TiO₂&MnO₂ after 40 h of UV.

After irradiation, the films exhibit novel absorption bands, with the PE/TiO₂&MnO₂ sample displaying particularly pronounced intensities. A broad band at 3400 cm^{-1} , a sharp band at 1720 cm^{-1} , and a complex, wide area ranging from 800 to 1400 cm^{-1} are observed at maximum intensity. Several of these newly appearing absorption bands are indicative of alcohol groups: vibrations of the bound OH-group manifest as a broad infrared band above 3400 cm^{-1} , in-plane bending or deformation of

the OH-group is noted between 1200 and 1450 cm^{-1} , and the stretching vibrations of the C – O group are found in the range of 970 to 1260 cm^{-1} . The positions of these frequencies typically vary as follows: for – CH₂ – OH between 1075 and 1000 cm^{-1} ; CH – OH from 1125 to 1000 cm^{-1} ; and C – OH, within 1210 to 1100 cm^{-1} [88]. The strong absorption band observed at 1720 cm^{-1} is attributed to the stretching vibrations of the C = O functional group, with the evidence more strongly supporting the presence of a ketone carbonyl rather than a carboxyl group. This conclusion is drawn from two key observations: firstly, the bonded OH-group is present at 3200–3300 cm^{-1} , yet there is an absence of a narrow band characteristic of the free OH group of carboxylic acids, which typically appears at 3500–3550 cm^{-1} . Secondly, the out-of-phase bending vibration of OC – OH, usually found within 880–960 cm^{-1} , cannot be distinctly identified.

Nature of the effects on the FTIR spectra of oxide-modified films is complex. Esters are also possible products with two strong bands of symmetric and asymmetric stretching vibrations of C – O located within the 1050 - 1300 cm^{-1} range. Additionally, specific compounds such as formates and propionates, evident at 1185 cm^{-1} , acetates at 1240 cm^{-1} , along with γ - and δ -lactones, also at 1180 cm^{-1} , are possible candidates for asymmetric stretching vibration. According to findings documented in other studies [137], the prominent absorption band observed in the range of 3150 to 3550 cm^{-1} can be attributed to the formation of hydroperoxide groups [137].

The formation of oxygen-containing groups during the degradation of PE films is expected to increase the mass of the sample. However, the observed kinetic curves distinctly show a reduction in mass, suggesting the likely generation of intermediates catalyzed in the near-interface region. These intermediates are thought to initially form alcoholic OH-groups, which oxidize into ketone carbonyls. These ketone carbonyls can then further react, leading to the formation of esters when the C – C bonds are broken. The final stages of this process involve the cleavage of CO₂ and the decomposition of formates and acetates. This indicates that the identified compounds represent only a partial listing of the degradation products, highlighting the complexity of the chemical transformations occurring during the photocatalytic degradation of PE films. The

degradation of a PE film modified with TiO₂ involves not only the photolytic reaction of PE but also the photocatalytic reactions occurring on the surface of the photocatalyst. Literature sources [137], [138], [139], [140] detail a potential mechanism for this process, which starts with generating holes and electrons on the TiO₂ surface. These charge carriers engage with LDPE, forming macromolecular radicals producing superoxide anion and hydroxyl radical, both of which are highly reactive oxygen species known for their efficacy in degrading PE. As reported in [141], new absorption peaks were identified at 1713 cm⁻¹ and 1177 cm⁻¹ after 288 hours of UV irradiation of PE films incorporating α -MnO₂ (cryptomelane-type), indicative of the C = O and C – O stretching vibrations, respectively. These peaks were also detected in the spectra of PE films modified with TiO₂ and MnO₂ (ramsdellite-type) composite film. This observation for PE/ α -MnO₂ and PE/TiO₂& γ -MnO₂ could refer to the same degradation mechanism for different α -MnO₂-polymorph-containing PE films.

The calculated indexes CI, NI and HI according to the methodology described in the Section 2.3.3 for samples are summarised in Table 6.1, highlighting the impact of incorporating TiO₂/MnO₂ on the CI, HI, and NI values. The slight deviations of indexes for PE/TiO₂ film vs pure PE film after UV-exposition, as well as PE/TiO₂&MnO₂ film behaviour, are the signatures of the different photo-oxidation mechanisms. The identical indexes of PE/TiO₂ and PE after UV with a simultaneous significant difference in the mass loss demonstrate the nature of the limiting stage in the process. Anatase TiO₂ is probably a photocatalyst of the last CO₂ cleavage stage attended by the C – C bond breakage. A conceivable explanation for the observed synergistic effect of TiO₂&MnO₂ coupling, as inferred from FTIR and photodegradation mass loss data, could be that the γ -MnO₂ nanoparticles, when combined with TiO₂, exhibit heightened activity in the intermediate stages of PE oxidation. This enhanced activity leads to a more significant accumulation of intermediates' functional groups than films containing only TiO₂.

Table 6.1. Functional groups indexes (CI, HI, NI) related to degradation products

	CI /arb.units (1720/720)	HI /arb. units (3430/720)	NI /arb. units (1175/720)
PE before UV	0.13	0.19	0.14
PE after UV	0.36	0.31	0.32
PE/TiO ₂	0.34	0.31	0.36
PE/ TiO ₂ &MnO ₂	1.27	0.73	0.99

The thermal behaviour of both unmodified polyethylene (PE) and its nanocomposites (PE/TiO₂ and PE/TiO₂&MnO₂) was examined through a thermogravimetric analysis conducted in an atmosphere of nitrogen. Within this, it should be noted that thermogravimetry under inert gas flows is suitable to explore the thermal characteristics of nanocomposite films obtained by the filling of polyethylene matrix with nanoparticles [142], [143]. Figure 6.4 represents the thermogravimetric and differential thermogravimetric curves associated with films based on polyethene.

As shown in Table 6.2, we detected that the residual masses at 575°C (RM₅₇₅) are higher in the composites with respect to that of pristine PE. These results are consistent with the incorporation of the inorganic nanofillers within the polymeric matrix.

As a general result, the TG curves show a significant decrease in the temperature range between 250 and 500°C that reflects the thermal degradation of the polymer. The PE degradation temperature (T_d) was calculated from the minimum of the DTG peaks (see insets in Fig. 6.4). We observed that the degradation temperature values of PE and PE/TiO₂&MnO₂ are similar (442 and 444°C, respectively), whereas the addition of TiO₂ reduces the temperature of polymer degradation up to 434°C for sample PE/TiO₂.

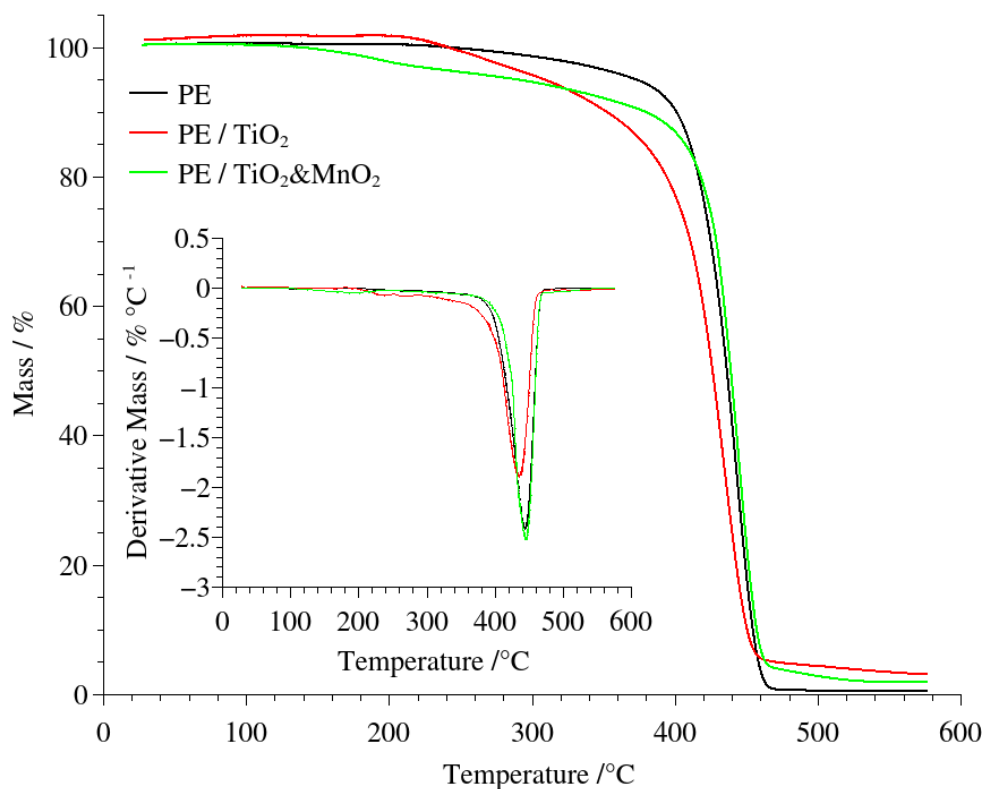


Figure 6.4. Thermal behaviour under N₂ flow and corresponding DTG curves for composite PE films.

Following the method given in the Section 2.3.1, we estimated the activation energy (E) and the pre-exponential factor (A) in the interval 250–500°C to explore the influence of the nanofillers on the kinetics of PE degradation. Table 6.2 reports the average values for both kinetic parameters.

Table 6.2. Thermal parameters of PE, PE/TiO₂, and PE/TiO₂&MnO₂ films.

	RM₅₇₅/%	T_d / °C	Activation energy / kJ·mol⁻¹	Pre-exponential factor / s⁻¹
PE	0.62	442	213±21	(468 ± 10) · 10 ¹⁰
PE/TiO ₂	3.18	434	201±15	(936 ± 12) · 10 ⁹
PE/TiO ₂ &MnO ₂	1.94	444	203±14	(605 ± 9) · 10 ⁹

We observed that the presence of the nanofillers slightly reduces the activation energy of the PE degradation indicating for all samples. As reported in various research

articles [86], [87], [89], the identification of the kinetic triplet-activation energy, pre-exponential factor, and the reaction model, facilitates the prediction of the temporal behaviour for the thermal degradation of organic macromolecules, polymers included. Using the method described in the Section 2.3.1, an assessment was made of the expected lifetime of composite films at different temperature. Fig. 6.5. shows the simulated t_α vs curves for pristine PE and the nanocomposites at four different temperatures (250, 300, 400 and 500°C) within the interval of the polymer degradation.

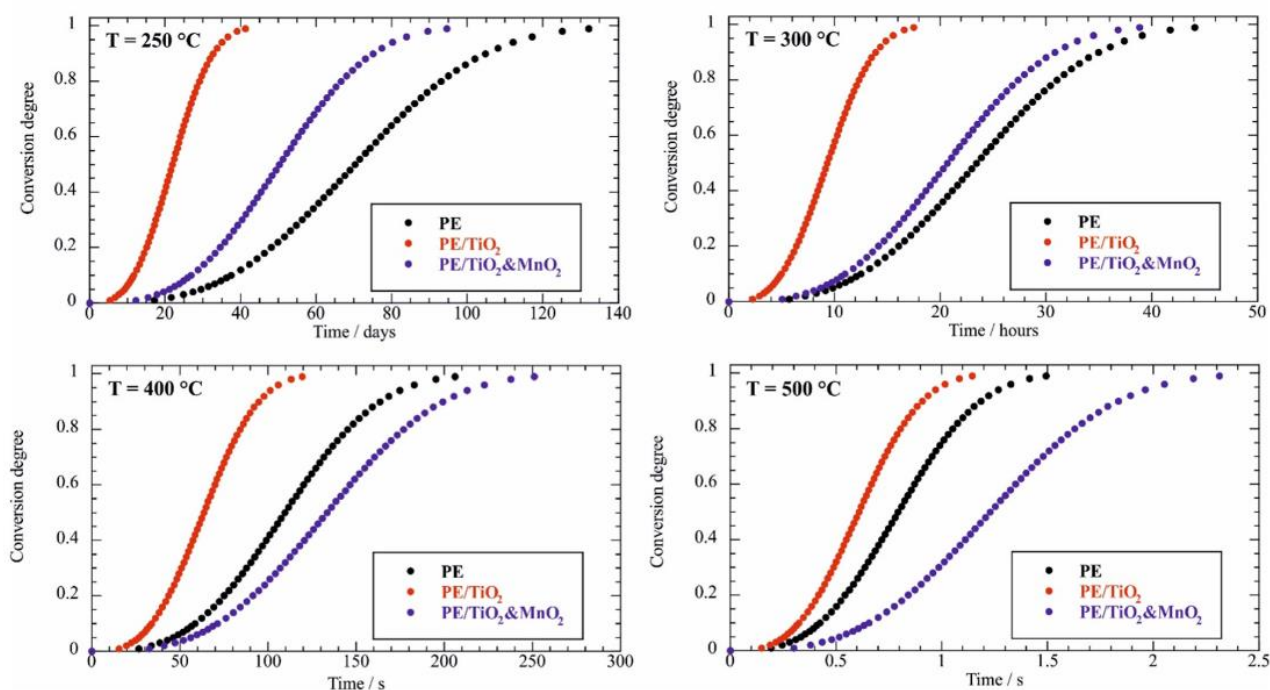


Figure 6.5. Lifetime prediction for composite films under different temperature conditions.

Based on the quantitative analysis of these curves, we determined t_α required to achieve conversion degree 0.05 (Table 6.3).

Table 6.3. Time required to achieve a 0.05 conversion degree for thermal degradation of PE, PE/TiO₂ and PE/TiO₂&MnO₂ under inert atmosphere at 250, 300, 400 and 500°C

	t_{α} at 250 °C	t_{α} at 300 °C	t_{α} at 400 °C	t_{α} at 500 °C
PE	29.5 days	9.84 h	42.03 s	0.336 s
PE/TiO ₂	8.53 days	3.91 h	24.71 s	0.255 s
PE/TiO ₂ &MnO ₂	21.13 days	8.67 h	56.06 s	0.516 s

These values are related to the thermal resistance of PE under inert atmosphere ruling out any potential effects (such as polymer embrittlement) due to oxidative and hydrolytic reactions. As a general result, PE/TiO₂ nanocomposite exhibited the lowest t_{α} ($\alpha = 0.05$) value highlighting that the presence of TiO₂ nanoparticles favors the thermal decomposition of the polymer. On the other hand, the influence of TiO₂&MnO₂ on the PE thermal stability depends on the temperature. Compared to the pristine polymer, we determined that the PE filling with TiO₂&MnO₂ reduces the t_{α} ($\alpha = 0.05$) value at 250 and 300°C. Oppositely, PE/TiO₂&MnO₂ showed the largest t_{α} ($\alpha = 0.05$) values at higher temperatures (400 and 500°C), evidencing that the addition of the mixed nanofillers (TiO₂&MnO₂) increased the thermal stability of the polymer.

As a summary we can conclude that PE filling with TiO₂&MnO₂ generates a slight hydrophobization of the polymeric film, while the highest improvements of the tensile performances were achieved by adding pristine TiO₂ nanoparticles. Thermogravimetric experiments under an inert atmosphere showed that the TiO₂ nanoparticles enhance the kinetics of the PE thermal decomposition for any temperature within the interval ranging between 250 and 500°C. On the other hand, the influence of the TiO₂&MnO₂ composite nanofiller depends on the specific temperature. We observed a stabilization effect on the PE thermal resistance at 400–500°C, while opposite results were estimated for lower temperatures (250–300°C). We investigated the photocatalytic degradation of PE films containing nanoparticles of titanium and manganese dioxides. The photodegradation results evidenced the coupling effects

between TiO_2 and MnO_2 semiconductors. The most intensive and distinctive view of absorbance of oxygen-containing species of alcohols, ketones, and esters on FTIR spectra is inherent to $\text{PE/TiO}_2\&\text{MnO}_2$ film. In addition, the mass loss features of studied films are in favour of additional mechanisms that facilitate the complete degradation process for $\text{PE/TiO}_2\&\text{MnO}_2$ film. The latter exhibits the best degradation result with a mass loss of about 21.3% after 90 h of UV irradiation. We observed that the presence of $\gamma\text{-MnO}_2$ photocatalyst generates an identical PE degradation mechanism with respect to that detected for $\text{PE}/\gamma\text{-MnO}_2$ nanocomposite. CI, HI, and NI data demonstrate that anatase TiO_2 is a photocatalyst of the last CO_2 cleavage stage. Interestingly, the PE photodegradation was enhanced by adding the composite filler ($\text{TiO}_2\&\text{MnO}_2$) within the polymeric matrix. This coupling effect could be explained by considering that the combination with TiO_2 renders the MnO_2 nanoparticles more active in the first intermediate steps of PE oxidation. Consequently, the accumulation of the in intermediates functional groups is higher compared to the PE/TiO_2 film.

6.2 Study of adsorption of Congo Red and Methylene blue on HNT's surface

Congo Red and Methylene Blue were chosen as representatives of cationic and anionic dyes to investigate adsorption on the surface of Halloysite. Since the outer and inner surfaces of Halloysite are oppositely charged, it is important to evaluate the impact of adsorption on the removal efficiency of synthesised composite materials.

Absorption spectra of dye solutions were recorded to plot a calibration graph. The corresponding linearized curves are shown in Figure 6.4. The graph itself was used to determine the change in dye concentration during degradation throughout the experiment.

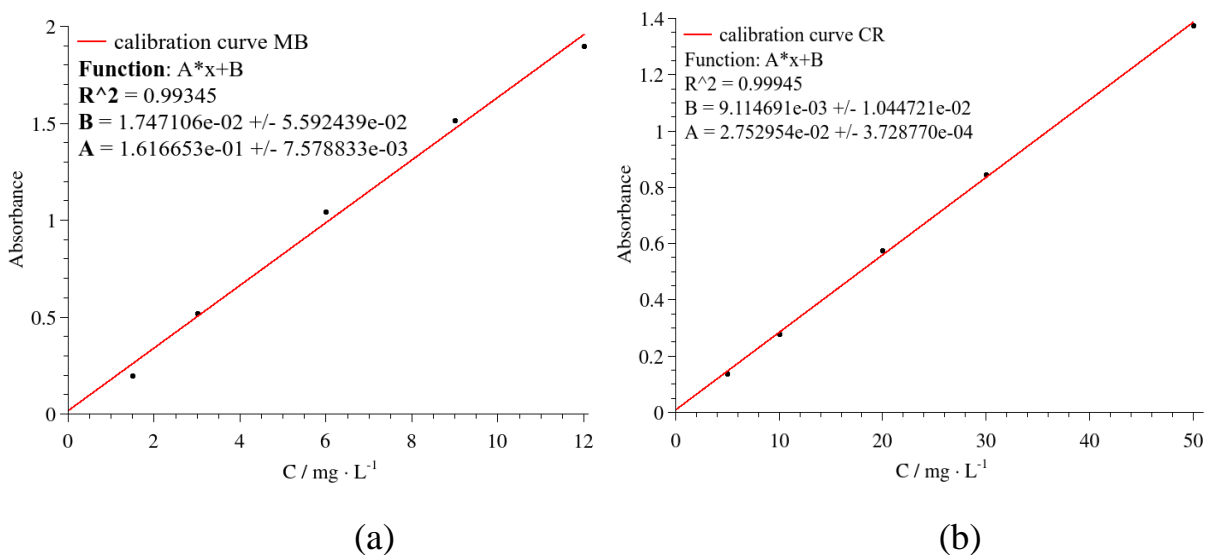


Figure 6.4. Dependences of absorbance on the concentration of the investigated dyes with a known concentration (calibration curves): MB (a); CR(b).

The dyes MB and CR were separately adsorbed onto HNTs and allowed to equilibrate under different concentrations. Two typical adsorption models (the Langmuir and Freundlich models) were used to fit the experimental adsorption data. According to the method described in Sections 2.4.2, the amount of adsorbed dye (q_e , mg·g⁻¹) was calculated according to equation 2.17. Adsorption isotherms were constructed and according to Langmuir and Freundlich fittings are shown in Fig.6.5 and 6.6.

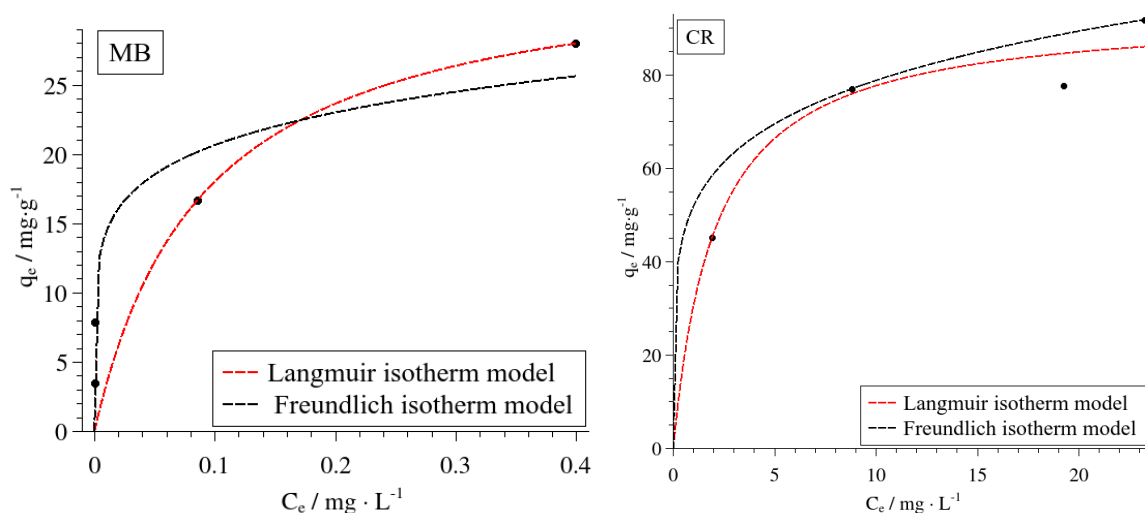


Figure 6.5. Adsorption isotherms of HNTs for MB and CR.

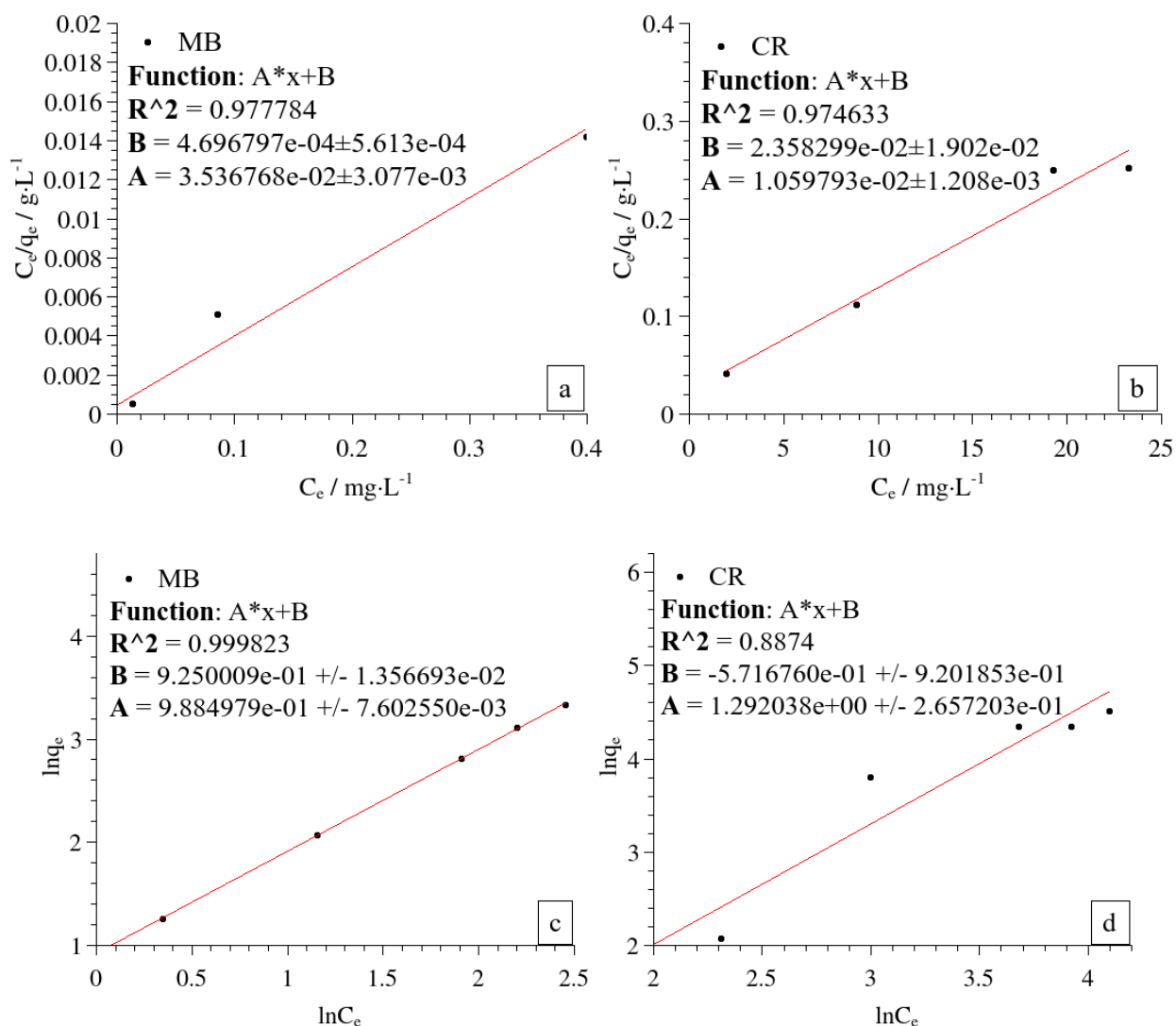


Figure 6.6 Linear fitting curves of Langmuir plot (a, b) and Freundlich isotherm (c, d) for equilibrium after 2 h of contact HNTs with MB and CR. R^2 represents the square of correlation coefficient.

Based on the calculated Langmuir and Freundlich parameters, as well as the determination coefficient, it was found that the Langmuir model fits the linearized experimental data of adsorption isotherms better than the Freundlich model. The corresponding coefficients are given in the Table 6.4. This indicates that the adsorption process leads to the formation of a single-layer adsorption of the dye on the surface of the nanotubes. Thus, the adsorption capacity of the material is limited.

Table 6.4. Langmuir parameters of MB and CR adsorption on HNT

	Langmuir model		
Dye	$q_m, \text{mg} \cdot \text{g}^{-1}$	$K_L, \text{L} \cdot \text{g}^{-1}$	R^2
MB	28.27	75.31	0.978
CR	94.36	0.449	0.974

Congo Red has a maximum capacity of about 3 times larger than MB by mass. Generally, these maximum adsorption capacity values are moderate in comparison with published data on other adsorbents. For instance, q_m achieves about 500 mg/g values for adsorption of MB and CR on the best adsorbents of activated charcoal. Nevertheless, these adsorbents possess by the order of magnitude larger surface area [144]. Comparison in mmol/g demonstrates compatible values of 0.0884 (MB) vs 0.1354 (CR). Considering surface charges, inner lumen positively charged aluminate groups in HNTs are more suitable sites for the adsorption of CR. CR adsorption into lumens is more favorable by 35% of molar maximum adsorption capacity. Any photocatalytic process begins with adsorption. Maximum adsorption capacity is a suitable parameter for planning further photocatalytic experiments.

MB and CR molecules surface areas were evaluated. These parameters were calculated by the division of HNTs surface area $65.9 \text{ m}^2/\text{g}$ onto maximum adsorption capacity (q_m) and the Avogadro constant $N_A 6.02 \cdot 10^{23} \text{ mol}^{-1}$. Calculated values were $12.4 \cdot 10^{-19} \text{ m}^2$ for MB and $8.01 \cdot 10^{-19} \text{ m}^2$ for CR.

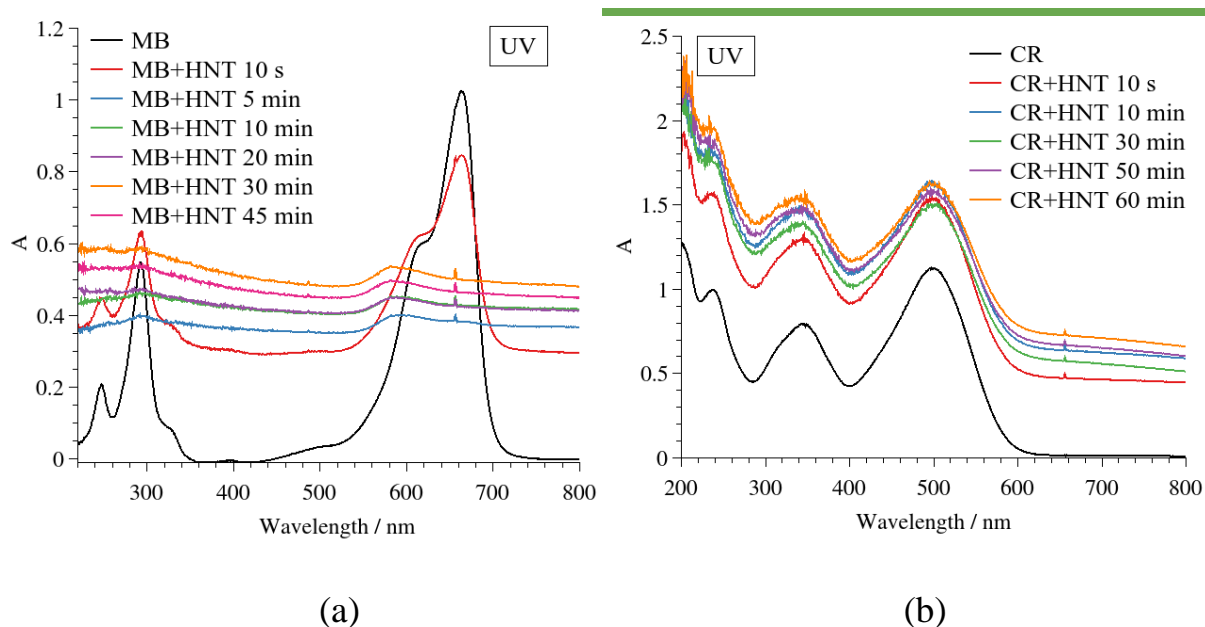


Figure 6.7 Curves showing the change in adsorption over time of (a) 6 mg/l solution of MB and (b) 40 mg/l solution of CR with addition of 0.025g HNTs, the investigated volume was 50 ml.

Fig. 6.7, a demonstrates the blue shift of main peaks of absorption near 600 nm to a single peak at 585 nm and decrease of their intensity as a result of adsorption of MB dye onto HNT's surface. The background growth is a consequence of scattering effects of distributed in a solution NPs of HNT's. In contrast, for Congo Red no shifts of the main peaks were observed during adsorption, while an increase in background was present in the same way as for Methylene Blue (Fig. 6.7, b). In our opinion, the non-uniform change of the background value during the experiment is the evidence of an adsorption kinetics mechanism. It is suggested that the background growth during the experiment signifies that adsorption of dyes favours the HNTs dispersity increase. The stronger adsorption by negatively charged silanol HNTs surface groups explains the blue shift of cationic MB dye absorbance in the experiment comparing with CR dye and even manganese oxides and oxidehydroxides used in this study..

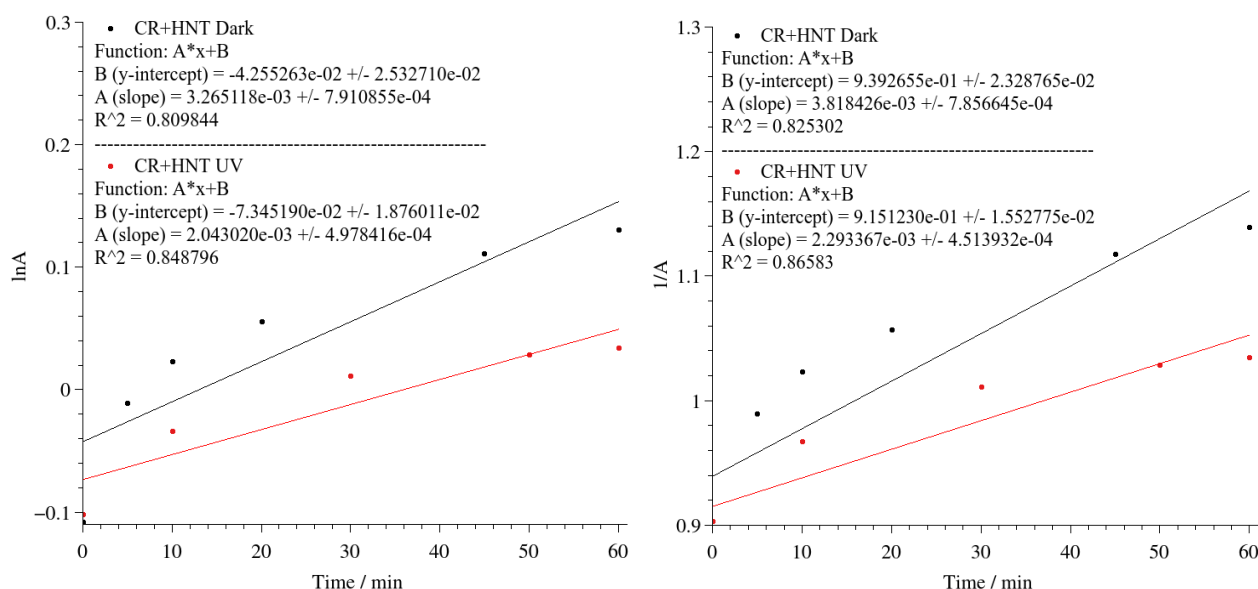


Figure 6.8 Kinetic curves of isothermal adsorption of CR on HNTs. The concentration of CR was 40 mg/l, amount of HNT 0.025g, volume of investigated solution 50 ml.

6.3 Study of photocatalytic activity manganese oxides and oxidehydroxides with halloysite for degradation of dyes in aqueous solutions (Methylene Blue and Congo Red)

The discoloration of dye solutions is one of the main methods of studying adsorption and photocatalytic degradation. MB and CR dyes are widely used test materials for these reactions.

The stability of dye solutions was inspected to exclude effects associated with spontaneous dye decomposition during the experiment. Both MB and CR did not demonstrate any change in concentration either in daylight or when exposed to UV-light for an experiment time (Fig 6.7).

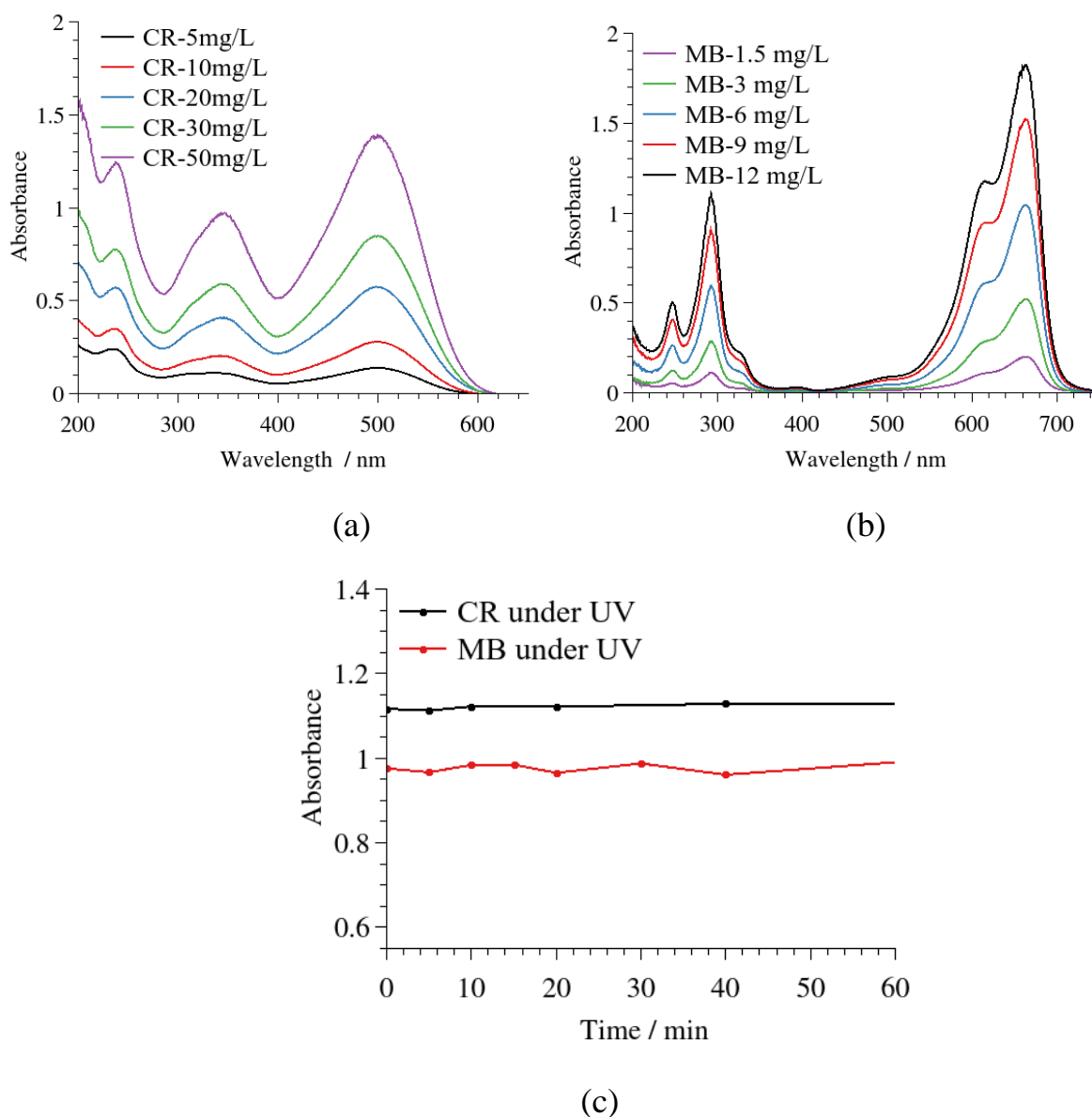


Figure 6.9. Absorption spectrum of solutions of CR (a) and MB (b) of different concentrations and also a test for dye stability under UV irradiation (c).

The absorption spectrum of an aqueous solution of Congo red is shown in Fig. 6.9a. The absorption band at 343 nm is associated with the $p-p^*$ transition of the aromatic ring, and the band at 496 nm can be attributed to the $n-p^*$ transition of the ion pair present in the N atom of the chromophore $-N=N-$ azo group. CR is considered an anionic dye, but its molecule contains functional groups of both basic ($-NH_2$, $pK_a = 10.7$) and acidic ($-SO_3$, $pK_a = -2.3$) nature. The degradation of the dye by photocatalysis can be followed by monitoring the decrease in the intensity of the absorption band at 497 nm, indicating cleavage of the $-N=N-$ bond [145].

Methylene blue as a cationic dye exhibits two major absorption bands at 293 (π - π^*) and 664 (n - π^*) nm in dilute aqueous solutions (Fig. 6.9 (b)), the latter having a shoulder at 610 nm corresponding to the 0-1 vibronic transition [146]. It is well known that the aggregation of MB significantly affects its optical properties. The self-organization of MB molecules is facilitated by electrostatic and dispersion forces, as well as hydrophobic effects. The sandwich-type (H-type) associations of this cationic dye show the blue shift of the spectral band of the π - π^* transition, while the head-to-tail (J-type) arrangement shows the redshift. The H-type aggregates are typically observed in aqueous solutions. While the \sim 664 nm band is assigned to an isolated molecule (monomer), a shift to 605 nm, accompanied by a second maximum at 697 nm, is observed when dimer forms and an additional blue shift to 575 nm appears when trimer forms. The degradation of methylene blue can be assessed by changing the intensity of the peak at 664 nm.

The analysis of MB (CS) degradation kinetics and mechanism by UV-, Vis-spectra was made (see Appendix C). The spectral characteristics of aqueous dispersion of nanosized particles of a photocatalyst have unique features that can be attributed to light scattering. These features can be varied during the degradation process due to a change of NP tendency to aggregation when the adsorbed MB(CR) or their degradation products layer prevents direct contact between particles of a photocatalyst. The more scattering the more intensive is non-specific background absorption that is typical for spectra at the end of degradation as Tyndall effect of scattering by particles comparable in size with the wavelength. The dependence of scattering (absorption) on the wavelength as the Rayleigh effect is typical for NPs less than 40 nm in [147], [148]. It can be seen from the Appendix C spectra that the degradation of CS-1 – CS-2 demonstrates the Rayleigh effect and the Tyndall effect, unlike CS5-9. It confirms the different kinetics and probably the different mechanisms of photocatalysis of low-valenced $\text{Mn}_3\text{O}_4/\text{Mn}_2\text{O}_3$ CS1-2 Samples and higher-valenced $\text{MnOOH}/\text{MnO}_2$ Samples CS-5 – CS-9.

For MB degradation, a considerable difference in absorbance tendencies exists for composites and pure oxides. Thus, CS-2, 6, 7 demonstrate increase of Tyndall effect

and existence of compatible with the wavelength in size NPs. On the contrary, the CS-1 Sample returns to practically the initial background of the absorption spectrum and low dispersity conditions. Pure Mn compounds show a negligible change in spectral view, but different background changes demonstrate scattering effects because of variations of dispersity.

From the point of view of kinetics, spectra of MB and CR photocatalytic degradation demonstrate the following effects: intensity of the main absorption bands drops, and the relative intensity of other peaks has the same tendency to decrease during photocatalytic degradation. The most interesting task is to compare the spectra of the most active and the least active MB (CR) photocatalytic degradation processes. Their analysis demonstrates differences for the most active samples. Sample CS-8, having the highest activity of CR degradation, demonstrates a well-resolved peak of additional absorption band at 320 nm after 60 min of degradation. Samples CS-6,7, 9 contain it too, but only a very broad one. This band can be attributed to amino group oxidation to nitrosyl in CR molecule as follows from E. Pretsch's book with Tables of spectral data [149]. It can also be seen that this spectral effect is absent for this Sample under dark conditions, and consequently, it has a photocatalytic nature (see Appendix C, D).

It is very important that different spectral behaviour and, consequently, a mechanism for MB degradation can be revealed for composites with HNTs (CS-1, 2,6,7) and pure Mn compounds (CS-3, 4, 5, 8, 9) (see the 500 - 750 nm range in Appendix E). Composites with HNTs have no absorption band at 664 nm after 60 min of UV irradiation.

Degradation tests were performed in the darkness and under UV-A irradiation at 365 nm during 1 hour. The volume of the dye solution being tested was 50 ml, the amount of photocatalysts added was 0.025 g. After a certain period, samples were taken and the intensity of light absorption at 664 nm for MB and 498 nm for CR was measured. Degradation rates were calculated according to formula 2.13 given in chapter 2.4.1. The kinetic curves of CR and photocatalytic degradation in different coordinates under UV and in the Darkness are shown in Fig. 6.10-6.11.

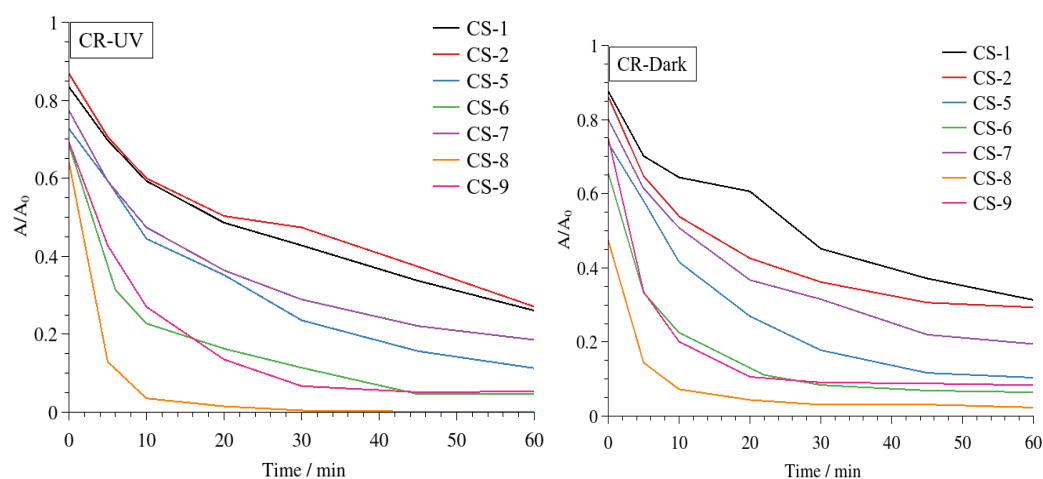


Figure 6.10. Change in absorption of CR solution in the presence of photocatalysts under UV irradiation and in the dark.

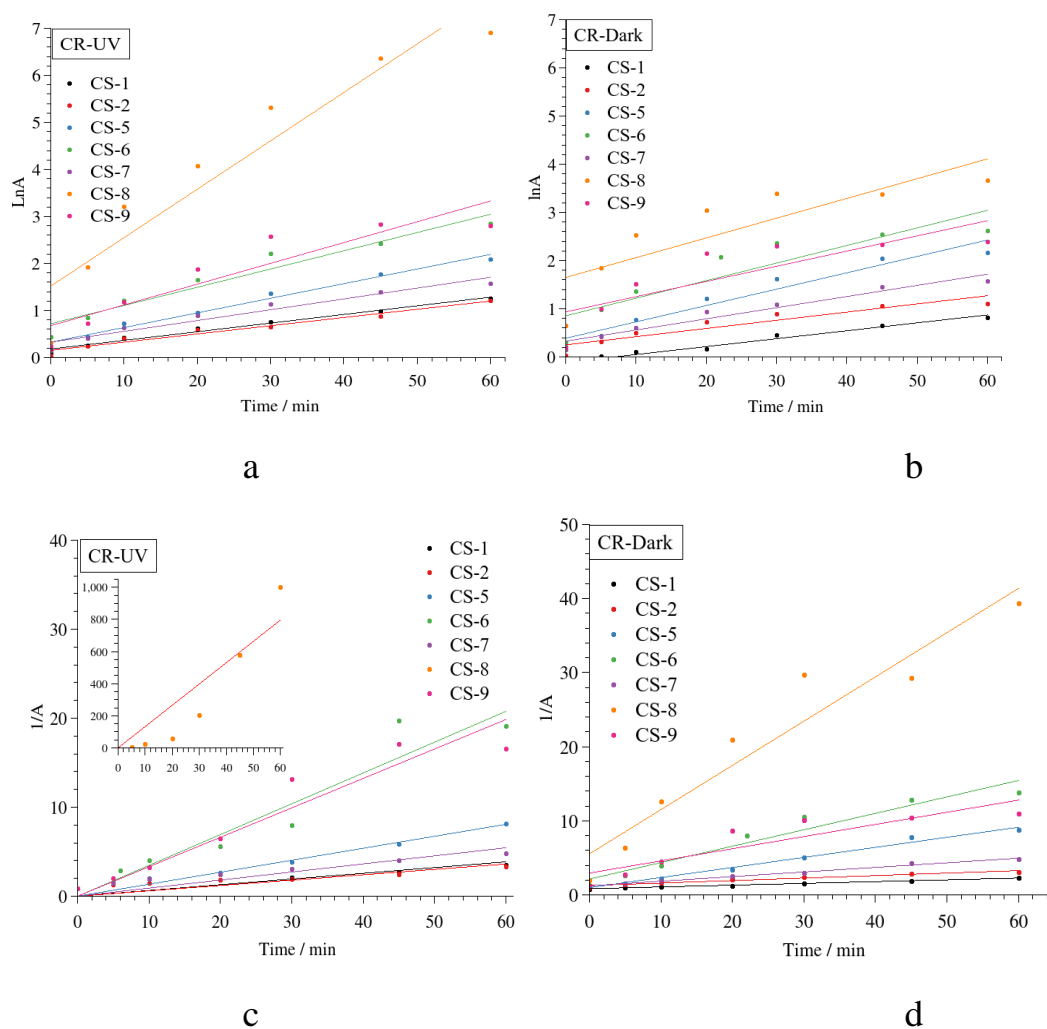


Figure 6.11. Linear approximation of kinetic dependences for Congo Red under ultraviolet irradiation and in the dark for first (a, b) and second (c, d) order reactions.

The value of k and the linear regression factors for the dye were determined graphically and are given in Table 6.5.

Table 6.5. Kinetic constants of first and second order models with correlation coefficient for CR degradation.

First order				
	UV		Dark	
	k / min^{-1}	R^2	k / min^{-1}	R^2
CS-1	0.0183	0.9796	0.0164	0.9687
CS-2	0.0175	0.9668	0.0169	0.8717
CS-5	0.0311	0.9864	0.0339	0.9432
CS-6	0.0388	0.9413	0.0365	0.8191
CS-7	0.0229	0.9479	0.0232	0.9481
CS-8	0.1028	0.9036	0.0410	0.7098
CS-9	0.0442	0.8568	0.0316	0.6843

Second order				
	UV		Dark	
	$k / \text{L} \cdot \text{mg}^{-1} \cdot \text{min}^{-1}$	R^2	$k / \text{L} \cdot \text{mg}^{-1} \cdot \text{min}^{-1}$	R^2
CS-1	0.0381	0.9896	0.0239	0.9853
CS-2	0.0347	0.9635	0.0336	0.9442
CS-5	0.1141	0.9785	0.1357	0.9850
CS-6	0.3332	0.9171	0.2217	0.9441
CS-7	0.0612	0.9973	0.0622	0.9911

Second order				
UV		Dark		
	$k / \text{L} \cdot \text{mg}^{-1} \cdot \text{min}^{-1}$	R^2	$k / \text{L} \cdot \text{mg}^{-1} \cdot \text{min}^{-1}$	R^2
CS-8	16.444	0.9003	0.5974	0.9251
CS-9	0.3000	0.9190	0.1641	0.8139

From this data, it can be seen that the photocatalytic degradation of the organic dye CR follows second-order kinetics, which has a linear relationship between $1/A$ and t , and the correlation coefficient tends to 1. The kinetic parameters of dye degradation indicate predominately a more active degradation process under UV irradiation compared to dark conditions. The distinctive feature of Mn-containing (oxide)hydroxide catalysts compared with TiO_2 is their high activity without irradiation or in darkness. Unfortunately, Vis-range irradiation photocatalysis was not available for all samples. MB degradation data under Vis-range irradiation demonstrate the most active photocatalytic process (Table 6.2).

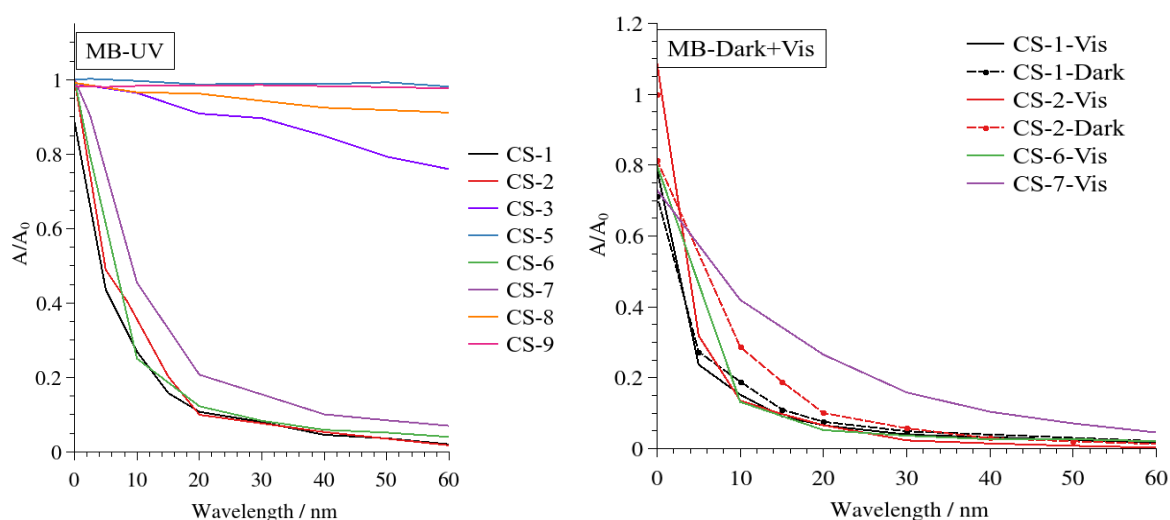
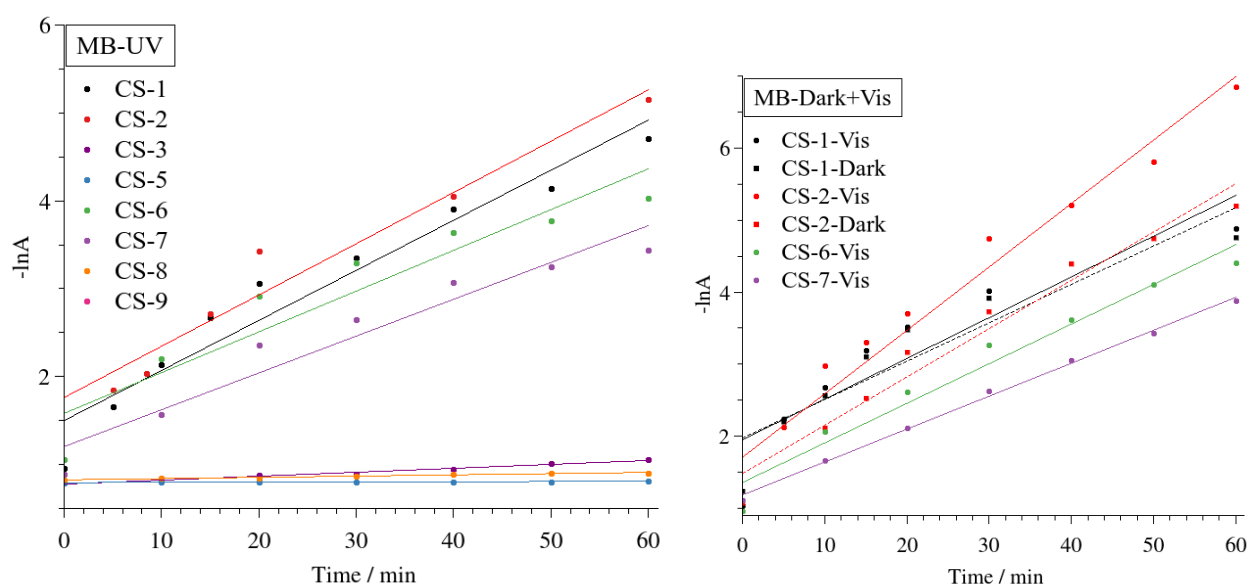
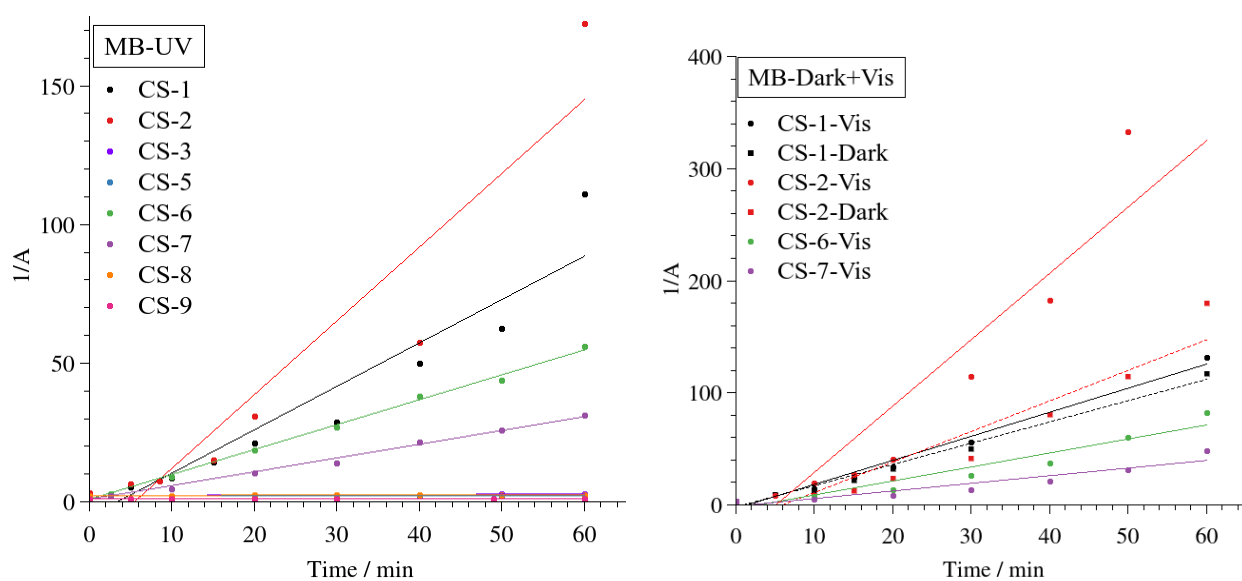


Figure 6.12. - Change in absorption of MB solution in the presence of photocatalysts under UV irradiation and in the dark



ab



cd

Figure 6.13. Linear approximation of kinetic dependences for MB under UV-, Vis-, and Dark conditions for the first (a, b) and the second (c, d) order reaction.

Table 6.6. Kinetic constants of first and second order models with correlation coefficient for MB degradation.

First order						
	UV		Visible		Dark	
	k / min^{-1}	R^2	k / min^{-1}	R^2	k / min^{-1}	R^2
CS-1	0.0607	0.9334	0.0565	0.8337	0.0532	0.8593
CS-2	0.0632	0.9448	0.0880	0.9553	0.0671	0.9605
CS-3	0.0045	0.9842				
CS-5	0.0003	0.6673				
CS-6	0.0522	0.8809	0.0549	0.9624		
CS-7	0.0456	0.9315	0.0457	0.9857		
CS-8	0.0015	0.9608				
CS-9	0.0002	0.3184				
Second order						
	UV		Visible		Dark	
	$k / \text{L} \cdot \text{mg}^{-1} \cdot \text{min}^{-1}$	R^2	$k / \text{L} \cdot \text{mg}^{-1} \cdot \text{min}^{-1}$	R^2	$k / \text{L} \cdot \text{mg}^{-1} \cdot \text{min}^{-1}$	R^2
CS-1	1.5643	0.9079	2.1457	0.9839	1.8965	0.9861
CS-2	2.6579	0.8889	5.9242	0.8830	2.7249	0.9049
CS-3	0.0111	0.9768				
CS-5	0.0006	0.6671				
CS-6	0.8975	0.9959	1.2513	0.9331		
CS-7	0.4964	0.9923	0.6803	0.9033		
CS-8	0.0036	0.9443				

Second order						
	UV		Visible		Dark	
	$k / \text{L} \cdot \text{mg}^{-1} \cdot \text{min}^{-1}$	R^2	$k / \text{L} \cdot \text{mg}^{-1} \cdot \text{min}^{-1}$	R^2	$k / \text{L} \cdot \text{mg}^{-1} \cdot \text{min}^{-1}$	R^2
CS-9	0.0002	0.3201				

The general analysis and comparison of MB and CR degradation mechanisms can be made depending on conditions under UV-, vis- light or without irradiation (Tables 6.5, 6.6). Generally, if to take a composite with halloysite, there is the 1st order for CS-1, 2 with low valenced Mn_3O_4 and the 2nd order for CS-6,7 with MnOOH -based phases in case of cationic dye MB under UV-light. There is another tendency to the CS-1 (2nd), CS-2 (1st) and CS-6 (2nd), CS-7 (2nd) under the visible light irradiation. In the dark place, CS-1 displays a better determination coefficient R^2 for the second order, and CS-2 demonstrates the first one.

Taking into account, that limiting stages of diffusion (1st order) and adsorption (2nd order) are possible in this kinetic experiment, the best sample CS-2 always demonstrate the limiting stage of diffusion (1st order) but CS-1 demonstrate the limiting stage of diffusion under the UV-light, and at visible light and in the darkness shows the limiting 2nd order reaction. It is also probable that the first order in case of CS-2 is a signature of MB dye decomposition process.

It can be seen that CS-1, 2, 6, 7 with HNTs display faster kinetics of MB degradation vs Mn containing samples only (CS-3, 5, 8, 9). From the point of view of phase composition $\text{Mn}_3\text{O}_4/\text{Mn}_2\text{O}_3$ ratio is maximal in CS-2 vs CS-1. On the other hand, CS-3 contains the larger content of Mn_3O_4 . Therefore, the HNTs + Mn_3O_4 (not HNTs+ Mn_2O_3) have to be together in the sample. Taking into account that CS-6,7 are better than CS-3,4,8,9 we arrive to a conclusion that Mn^{2+} content as lowest oxidation state of Mn in the series in heterojunctions with HNTs plays an important role. CR as an anionic dye displays the other tendency with dominance of 2nd order reaction under UV-light.

The further insight was made by analysis of the band gap potential diagrams of CS-series of samples and MO-diagram with HOMO and LUMO of a dye. Considering the data on the position of the valence band and conduction band of chemically synthesized samples (Fig. 6.14), given in Section 4.1.6, we can make some assumptions about why some samples have higher activity than others.

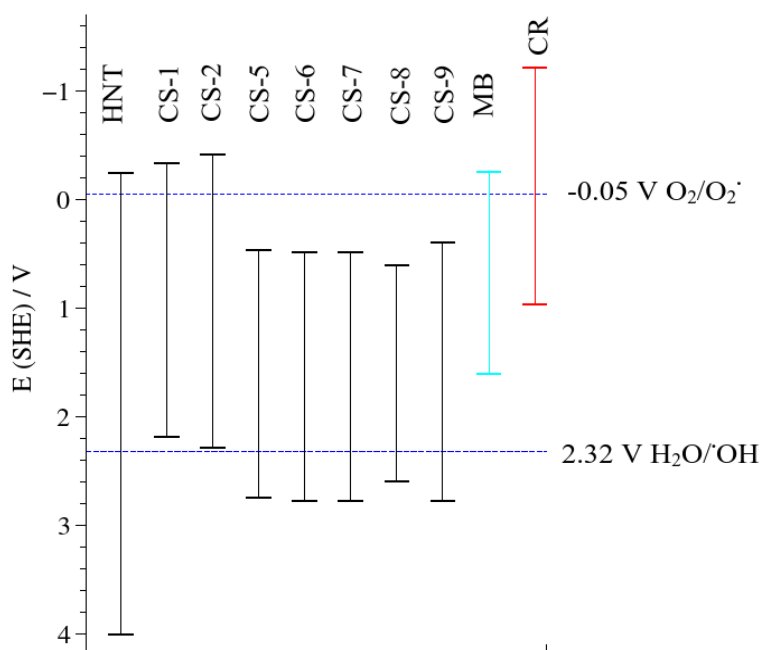


Figure 6.14. Calculated CB and VB edge potentials for CS samples (from DRS analysis) along with potentials of some redox reactions.

Fig. 6.14 explains the advantages of a heterojunction between Mn_xO_y and HNTs in CS-1(CS-2). Despite the insulator behaviour of HNTs, the edges of the conduction band of these materials are very close to one another, facilitating the electron/hole pair separation. In turn, this Figure clearly shows the close position of LUMO of MB with E_C of HNTs -CS-1(CS-2). It means that the direct transfer of photoelectrons to LUMO of MB is energetically favourable. The other direction of charge transfer is suggested from E_C of HNTs to MB LUMO level due to HNT/ Mn_xO_y heterojunction. It signifies that MB reduction could take place even at the interface of decorated by manganese oxides HNTs.

It can be suggested that aforementioned feature is responsible for the positive influence of HNT's surface decoration by Mn_xO_y on photocatalytic activity of MB

degradation due to the new option of direct electron transfer of photoelectron from E_C of both HNTs & Mn_xO_y and following MB dye reduction (Fig. 6.15, a). It is also evident from this diagram for CR dye that only CS-8 Sample has favorably aligned E_V to HOMO level of CR dye and, probably, this feature can be responsible for the faster direct oxidation of CR by holes from the valence band of CS-8 as a photocatalyst (Fig. 6.15, b). Thus, distinctly active behavior of CS-1&CS-2 photocatalysts toward MB degradation as well as CS-8 Sample high activity toward CR destruction can be explained by the semiconducting properties of these photocatalysts.

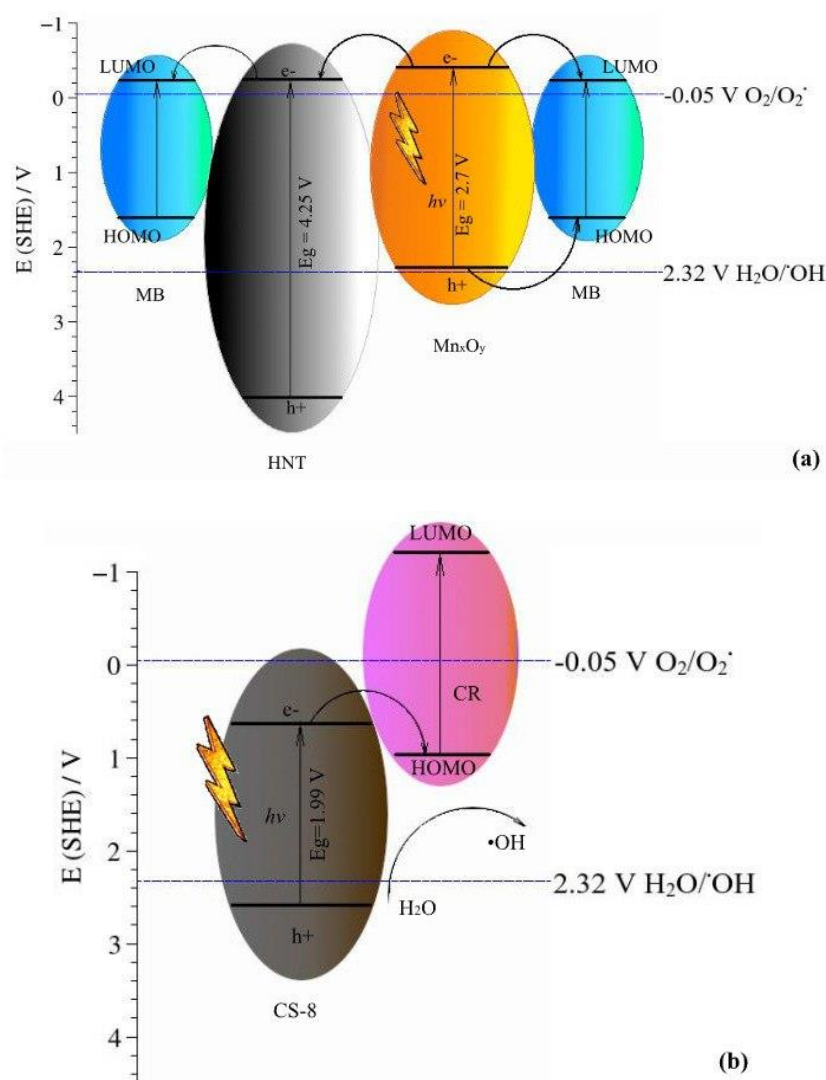


Fig. 6.15. Band gap potential diagram of: CS-1,2 Samples' photocatalytic degradation of MB dye (a); CS-8 distinct direct interaction with CR dye (b).

Conclusions to Section 6

Functional properties obtained in this study composites and some standard materials were studied. The coupling effect was established for PE film degradation containing mechanical mixture of TiO_2 and MnO_2 . The total ability of MnO_2 and other manganese compounds to be a catalyst of degradation process regardless the presence of light was established for PE film, MB, and CR dyes degradation.

The adsorption of MB and CR dyes on HNTs Aldrich Sigma was studied and such parameters as maximum molar capacity, molecule surface area were determined from Langmuir isotherm processing.

The kinetics of degradation of organic dyes of MB and CR under UV-irradiation was investigated. CS-1, 2 demonstrate the 1st order reaction and the fastest rate of MB dye degradation with $k_{\text{CS-2}} = 0.063 \text{ min}^{-1}$. CS-8 is the most active photocatalyst of CR dye degradation which demonstrates identical R^2 coefficient for the first and the second orders (0.90) and by several times higher activity ($k_{\text{CS-2}} = 0.1028 \text{ min}^{-1}$) compared with other samples obtained. The enhanced photocatalytic activity of MB degradation is attributed to the surface decoration of HNTs with Mn_xO_y , enabling direct electron transfer and MB reduction. For CR dye, the superior performance of the CS-8 sample is likely due to its favorable energy level alignment, facilitating direct oxidation by valence band holes. Overall, the semiconducting properties of CS-1 and CS-2 explain their efficiency in MB degradation, while CS-8 exhibits high activity in CR degradation.

The results of experimental studies of this section are presented in the following publications:

Articles:

1. **Kovinchuk, I.**, Haiuk, N., Lazzara, G., Cavallaro, G., Sokolsky, G. (2023). Enhanced photocatalytic degradation of PE film by anatase/ γ - MnO_2 . Polymer Degradation and Stability, 210, 110295. <https://doi.org/10.1016/j.polymdegradstab.2023.110295>. The journal is cited by the scientometric databases SCOPUS and Web of Science (Q1). *Personal contribution is*

analysis of literary sources, conducting experimental research, processing and formatting results, writing and submitting the article.

Conference materials:

2. **Kovinchuk I.**, Lazzara G., Cavallaro G., Sokolsky G. MnO₂/TiO₂ Nanopowders-Assisted Photocatalytic Degradation of Low-Density Polyethylene Films, 2022 *IEEE 12th International Conference Nanomaterials: Applications & Properties*, 2022 P. 10nee–27. <https://doi.org/10.1109/NAP55339.2022.9934707>. *Personal contribution is analysis of literary sources, conducting experimental research, processing and formatting results, writing and submitting the abstract.*

3. Sokolsky G.V., **Kovinchuk I.V.**, Ragulya A.V., Spreitzer M., Kržmanc M.M. Electrodeposition of nanodispersed α/δ - & γ/α -manganese dioxide composites for visible light photocatalytic applications, *10th Ukrainian Congress of Electrochemistry Achievements Problems and Prospects*, 2, 2024, P. 32-36. <https://doi.org/10.33609/elchimcongr.2024.09.1-210>. *Personal contribution is analysis of literary sources, conducting experimental research, processing and formatting results, writing.*

Abstracts of conference presentations:

4. Haiuk N.V., Sokolsky H.V., Svyntsova A.V., **Kovinchuk I.V.** (2021) Fotokatalitychna destruktsiia polietylenovykh plivok dioksydamy tytanu i manhanu. [Photocatalytic destruction of polyethylene films by titanium and manganese dioxides] *Materialy XV mizhnarodnoi naukovo-tekhnichnoi konferentsii «AVIA-2021»*. m. Kyiv, (Ukraine). P. 19.1-19.4. *Personal contribution is analysis of literary sources, conducting experimental research, processing results.*

5. Haiuk N.V., Dmitriieva Y., **Kovinchuk I.V.**, Sokolsky H.V. (2021) Tverdogazna fotokatalitychna destruktsiia polietylenovykh plivok oksydnymy materialamy manhanu ta tytanu [Solid-phase photocatalytic destruction of polyethylene films by manganese and titanium oxide materials]. *Materialy I Mizhnarodnoi naukovo konferentsii «Aktualni problemy khimii, materialoznavstva ta ekologhii»*. m. Lutsk, (Ukraine). S. 119–122. *Personal contribution is analysis of literary sources, conducting experimental research, processing and formatting results.*

6. **Kovinchuk I.V.**, Sokolskyi H.V., Haiuk N.V. (2021) Vyznachennia serednoho diametru nanostryzheniv Manhan (IV) oksydu riznoho pokhodzhennia v prohrannomu seredovyschi ImagJ ta SciDAVi [Determination of the average diameter of Manganese (IV) oxide nanorods of various origins in the ImagJ and SciDAVi software environments]. *Materialy shkoly-konferentsii molodykh vchenykh suchasne materialoznavstvo: fizyka, khimiia, tekhnolohii*. m. Uzhhorod, (Ukraine). P. 245–246. *Personal contribution is analysis of literary sources, conducting experimental research, processing and formatting results, writing and submitting the abstract.*
7. **Kovinchuk I.**, Haiuk N., Cavallaro G., Lazzara G., Sokolsky G. (2022) Thermogravimetric study of PE films containing TiO_2 , MnO_2 photocatalysts, and their composites. *Book of abstracts of the 13 European Symposium on Thermal Analysis and Calorimetry*. Palermo, (Italy). P. 214. *Personal contribution is analysis of literary sources, conducting experimental research, processing and formatting results, writing and submitting the abstract.*
8. P. Hlukhova, **I.V. Kovinchuk**, Dzh. Lazzara, i H. V. Sokolskyi (2023) Fotokatalitychni vlastyvoli kompozytiv oksydiv-hidroksydiv manhanu z haluazytom, syntezyvanykh hidrokhimichnym metodom [Photocatalytic properties of manganese oxide-hydroxide composites with halloysite synthesized by the hydrochemical method]. *Zbirka tez dopovidei. Mizhnarodna konferentsiia z khimii, khimichnoi tekhnolohii ta ekolohii, prysviachenii 125-richchii KPI im. Ihoria Sikorskoho*. m. Kyiv, (Ukraine). P. 14–16. *Personal contribution is analysis of literary sources, conducting experimental research, data curation.*
9. **Kovinchuk I.V.**, Hlukhova P.I., Telina M.M., Khrebtan D.R., Vechirko E.R., Lazzara G., Sokolsky G.V. (2024) Halloysite nanotubes as components of nanocomposites with mn oxides/hydroxides. *Book of abstracts. 12th International Conference "Nanotechnologies and Nanomaterials" NANO-2024*. Uzhgorod, (Ukraine). P. 77. *Personal contribution is analysis of literary sources, conducting experimental research, processing and formatting results, writing and submitting the abstract.*
10. **Kovinchuk I.**, Hlukhova P., Lazzara G., Sokolsky G. (2024) Enhanced Photocatalytic Methylene Blue Degradation by $\text{Mn}_3\text{O}_4/\text{HNT}$ -based composite

material. *Book of abstracts. XXVIII Congresso Nazionale della Società Chimica Italiana.* Milan, (Italy). P. FIS-PO-005. *Personal contribution is analysis of literary sources, conducting experimental research, processing and formatting results, writing and submitting the abstract.*

CHAPTER 7. CHEMICAL PROCESS TECHNOLOGY FOR SYNTHESIS OF COMPOSITE PHOTOCATALYST

Among the proposed materials, CS-2 proved to be the best for degrading the dye methylene blue, so it was chosen as the basis for developing a technology for synthesizing the material for use for water purification.

7.1 Block diagram for synthesis of photocatalytic material with halloysite nanotubes

Taking into account the data of sections 2.2.1 where synthesis methods are given, 3 where physicochemical properties are described and 6.3 where the photocatalytic activity of the synthesized samples is estimated, and based on these data, it is proposed to choose the CS-2 sample, consisting of the main phase of hausmannite with the addition of halloysite nanotubes, to develop a block diagram of the synthesis of this material. Figure 7.1 shows the proposed block flow diagram for synthesis of manganese oxide/oxidehydroxides with HNTs composite material, operating in a periodic mode.

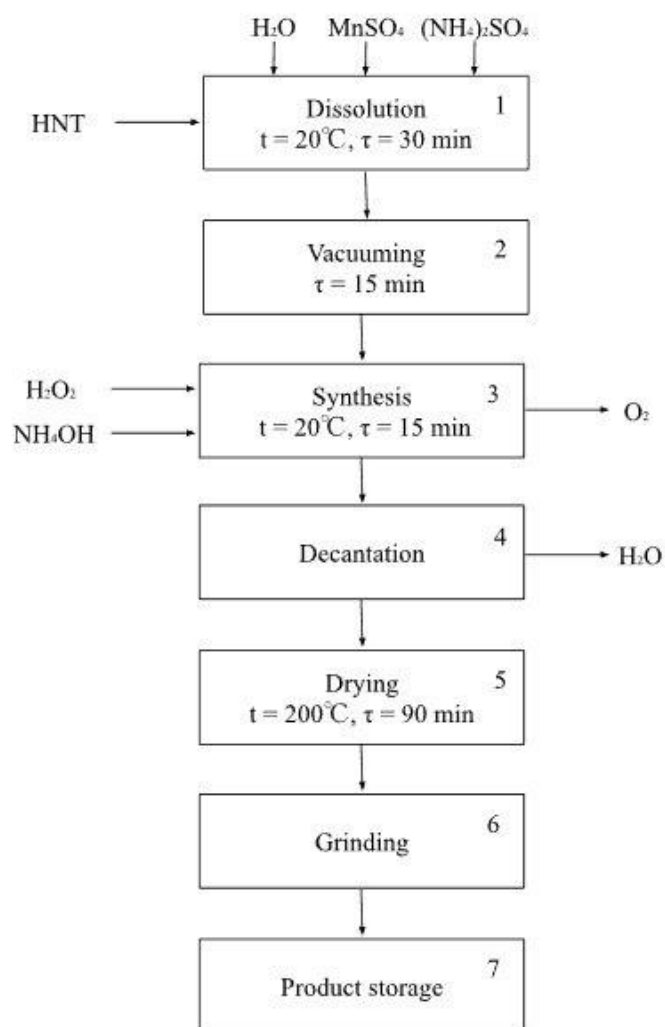


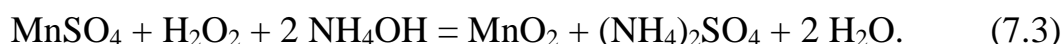
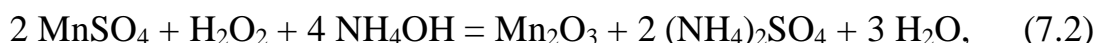
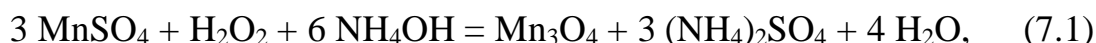
Figure 7.1. Block flow diagram of balanced processes for CS-2 composite material

At the preparatory stage of the synthesis, solutions of MnSO_4 and $(\text{NH}_4)_2\text{SO}_4$ in distilled water with a concentration of 0.5 M are prepared. The process takes place at room temperature in tank 1 with constant stirring. After complete dissolution, halloysite nanotubes are added and the resulting suspension is fed to a vacuum apparatus 2 to remove air from the lumen of the nanotubes and fill it with the reaction solution. Evacuation is carried out in three cycles of 15 minutes each to completely remove air from the tubes and fill them with the solution. The evacuated suspension is fed to the synthesis reactor 3. Hydrogen peroxide 27% and ammonium hydroxide are gradually added to the reactor with constant stirring to maintain a given acidity level of pH equal to 10. Taking into account the side reaction of catalytic decomposition of hydrogen peroxide on the surface of the synthesized manganese oxides, the

introduction of a 4-fold excess of peroxide is provided. The oxygen released in this case is proposed to be captured for further use. The resulting suspension is fed into a decanter 4 to separate and wash the resulting sediment, which is then sent to a drying oven 5 at 200°C for 1.5 hours. The resulting dried product is transferred to a grinder 6. The ground powder is sent to a warehouse 7.

7.2. Material balance

Chemical synthesis of the sample CS-2, the composition of which, according to Chapter 2, was determined as 45% Mn_3O_4 , 15% Mn_2O_3 , 12% MnO_2 with the addition of 28% HNTs, proceeds according to the reaction equations (7.1 - 7.3).



Catalytic decomposition of excess added hydrogen peroxide occurs according to the reaction:

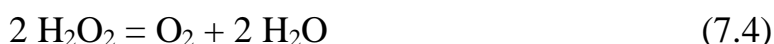


Table 7.1 shows the molar masses of the reaction components used to calculate the material balance per 1 kg of product for the proposed technological line. Further calculation is carried out to obtain 1 kg of product.

Table 7.1. Molar masses of starting substances for synthesis

Component	Molar mass / $\text{mol} \cdot \text{g}^{-1}$	Denotation
MnSO_4	150.96	M_{MnSO_4}
$(\text{NH}_4)_2\text{SO}_4$	132.14	$M_{(\text{NH}_4)_2\text{SO}_4}$
NH_4OH	35.05	$M_{\text{NH}_4\text{OH}}$
H_2O_2	34.01	$M_{\text{H}_2\text{O}_2}$
HNT	294.19	M_{HNT}
Mn_3O_4	228.81	$M_{\text{Mn}_3\text{O}_4}$

Mn ₂ O ₃	157.87	$M_{Mn_2O_3}$
MnO ₂	86.94	M_{MnO_2}
H ₂ O	18.02	M_{H_2O}
O ₂	31.99	M_{O_2}

The purity of MnSO₄ and (NH₄)₂SO₄ reagents was 97%. Reagent quantities required for the synthesis of 450 g of Mn₃O₄ are calculated below:

$$m_{MnSO_4} = \frac{m_{Mn_3O_4} \cdot 3 \cdot M_{MnSO_4}}{M_{Mn_3O_4}} = \frac{450 \cdot 3 \cdot 151}{228.81} = 890.91 \text{ g};$$

$$m_{H_2O_2} = \frac{m_{Mn_3O_4} \cdot M_{H_2O_2}}{M_{Mn_3O_4}} = \frac{450 \cdot 34.01}{228.81} = 66.89 \text{ g};$$

$$m_{NH_4OH} = \frac{m_{Mn_3O_4} \cdot 6 \cdot M_{NH_4OH}}{M_{Mn_3O_4}} = \frac{450 \cdot 6 \cdot 35.05}{228.81} = 413.60 \text{ g};$$

$$m_{(NH_4)_2SO_4} = \frac{m_{Mn_3O_4} \cdot 3 \cdot M_{(NH_4)_2SO_4}}{M_{Mn_3O_4}} = \frac{450 \cdot 3 \cdot 132.14}{228.81} = 779.64 \text{ g};$$

$$m_{H_2O} = \frac{m_{Mn_3O_4} \cdot 4 \cdot M_{H_2O}}{M_{Mn_3O_4}} = \frac{450 \cdot 4 \cdot 18.02}{228.81} = 141.75 \text{ g}.$$

Reagent quantities required for the synthesis of 150 g Mn₂O₃ were also added to the total calculation:

$$m_{MnSO_4} = \frac{m_{Mn_2O_3} \cdot 2 \cdot M_{MnSO_4}}{M_{Mn_2O_3}} = \frac{150 \cdot 2 \cdot 151}{157.87} = 286.94 \text{ g};$$

$$m_{H_2O_2} = \frac{m_{Mn_2O_3} \cdot M_{H_2O_2}}{M_{Mn_2O_3}} = \frac{150 \cdot 34.01}{157.87} = 32.31 \text{ g};$$

$$m_{NH_4OH} = \frac{m_{Mn_2O_3} \cdot 4 \cdot M_{NH_4OH}}{M_{Mn_2O_3}} = \frac{150 \cdot 4 \cdot 35.05}{157.87} = 133.21 \text{ g};$$

$$m_{(NH_4)_2SO_4} = \frac{m_{Mn_2O_3} \cdot 2 \cdot M_{(NH_4)_2SO_4}}{M_{Mn_2O_3}} = \frac{150 \cdot 2 \cdot 132.14}{157.87} = 251.10 \text{ g};$$

$$m_{H_2O} = \frac{m_{Mn_2O_3} \cdot 3 \cdot M_{H_2O}}{M_{Mn_2O_3}} = \frac{150 \cdot 3 \cdot 18.02}{157.87} = 51.37 \text{ g};$$

as well as reagent quantities required for the synthesis of 120 g of MnO₂:

$$m_{MnSO_4} = \frac{m_{MnO_2} \cdot M_{MnSO_4}}{M_{MnO_2}} = \frac{120 \cdot 151}{86.94} = 208.42 \text{ g};$$

$$m_{H_2O_2} = \frac{m_{MnSO_4} \cdot M_{H_2O_2}}{M_{MnSO_4}} = \frac{120 \cdot 34.01}{86.94} = 46.94 \text{ g};$$

$$m_{NH_4OH} = \frac{m_{MnSO_4} \cdot M_{NH_4OH}}{M_{MnSO_4}} = \frac{120 \cdot 2 \cdot 35.05}{86.94} = 96.76 \text{ g};$$

$$m_{(NH_4)_2SO_4} = \frac{m_{MnSO_4} \cdot M_{(NH_4)_2SO_4}}{M_{MnSO_4}} = \frac{120 \cdot 132.14}{86.94} = 182.38 \text{ g};$$

$$m_{H_2O} = \frac{m_{MnSO_4} \cdot M_{H_2O}}{M_{MnSO_4}} = \frac{120 \cdot 2 \cdot 18.02}{86.94} = 49.74 \text{ g}.$$

Determination of the amount of products released during the catalytic decomposition of excess of added hydrogen peroxide was made:

$$m_{H_2O} = \frac{m_{H_2O_2} \cdot M_{H_2O}}{M_{H_2O_2}} = \frac{438.42 \cdot 2 \cdot 18.02}{2 \cdot 34.01} = 232.26 \text{ g};$$

$$m_{O_2} = \frac{m_{H_2O_2} \cdot M_{O_2}}{M_{H_2O_2}} = \frac{438.42 \cdot 31.99}{2 \cdot 34.01} = 206.16 \text{ g}.$$

It has been experimentally established that the yield of the product is 80%. Also, ammonium sulfate and manganese sulfate contain 2% impurities, which do not participate in the reaction. Taking this into account, Table 7.2 shows the total values of the reaction components for obtaining 1 kg of the product.

Table 7.2. Material balance for the production of a composite CS-2 containing HNTs

Input			Output		
Component	Mass / g	Content / %	Component	Mass / g	Content / %
MnSO ₄ total:	1697.47	6.13	CS-2	1000	3.61
MnSO ₄ (pure)	1663.52	6.01			
MnSO ₄ (impurities)	33.95	0.12			
(NH ₄) ₂ SO ₄ total:	1486.04	5.37	O ₂	247.39	0.89
(NH ₄) ₂ SO ₄ (pure)	1456.32	5.26			
(NH ₄) ₂ SO ₄ (impurities)	29.72	0.11			

H ₂ O ₂	701.47	2.53	(NH ₄) ₂ SO ₄	2912.06	10.51
NH ₄ OH	772.28	2.79	H ₂ O total	23270.61	84.04
HNT pure	336	1.21	Losses	200	0.72
H ₂ O	22700.47	81.97	Impurities	63.67	0.23
Total	27693.73	100	Total	27693.73	100

7.3. Energy balance

The heat balance of the process is compiled according to the material balance of thermal processes occurring in the reactor, taking into account the supply or removal of heat with the aim of stabilizing the temperature regime in the reactor.

$$Q_{reactants} = Q_{products} + Q_{loss} + Q_{removed} \quad (7.5)$$

where Q_{react} is the amount of heat introduced by the reactants; $Q_{products}$ is the amount of heat released with the reaction products; Q_{loss} is heat loss to the environment (5% of heat input); $Q_{removed}$ is the amount of heat removed.

The heat balance was calculated using material balance data for the nanocomposite CS-2 at 298.15 K. Taking into account that the process of synthesis proceeds at room temperature and does not require heating, heat capacities can be omitted and standard formation heats can be used instead of them. The heat effects of reactions were calculated by the Hess law according to the formula:

$$\Delta H = \sum n \Delta H_f^0 products - \sum n \Delta H_f^0 reactants, \quad (7.6)$$

where $\Delta H_{products}$ and $\Delta H_{reactants}$ are the standard enthalpies of formation of products and reactants respectively, kJ·mol⁻¹; n represents stoichiometric coefficients. These values are standard at 298.15 K and are presented in Table 7.3.

Table 7.3 Isobaric molar heat capacities and the standard heats of formations of components [150], [151]

Component	$C_p, \text{J mol}^{-1} \cdot \text{K}^{-1}$	$\Delta H_f^0, \text{kJ} \cdot \text{mol}^{-1}$
MnSO ₄	100.2	-1066.7
H ₂ O ₂	89.33	-187.8
NH ₄ OH	35.6	-46.19
HNT pure	232	
(NH ₄) ₂ SO ₄	187.0	-1180.0
H ₂ O	75.299	-285.83
MnO ₂	54.02	-521.5
Mn ₂ O ₃	107.5	-957.7
Mn ₃ O ₄	139.3	-1387.6
O ₂	29.35	0

Using formula 7.6 and the values of standard heats of formation from Table 7.3, the total enthalpy of the synthesis process was calculated according to the stoichiometric reaction taking into account the composition of the sample (1 kg CS-2 contains 450 g Mn₃O₄, 150 g Mn₂O₃ and 120 g MnO₂), as well as the required excess of reagents to account for 20% losses during synthesis. HNTs are not represented in the equation because nanotubes do not participate in the chemical reaction. Additionally, the cathalytic decomposition of the added excess hydrogen peroxide is taken into account. Table 7.4 presents summarized data on the thermal effects during the synthesis of the photocatalytic material CS-2.

Table 7.4 Heats of formation of reaction components for CS-2 Sample synthesis

Component	Denotation	Calculation	Value / kJ
Reactants			
MnSO ₄	Q_{MnSO_4}	$-\frac{m_{MnSO_4}}{M_{MnSO_4}} \cdot \Delta H_{f\ MnSO_4} =$ $= \frac{1663.52}{150.96} \cdot (-1066.7)$	11763.56
NH ₄ OH	Q_{NH_4OH}	$-\frac{m_{NH_4OH}}{M_{NH_4OH}} \cdot \Delta H_{f\ NH_4OH} =$ $= \frac{772.28}{35.05} \cdot (-46.19)$	1017.71
H ₂ O ₂ total	$Q_{H_2O_2}$	$-\frac{m_{H_2O_2}}{M_{H_2O_2}} \cdot \Delta H_{f\ H_2O_2} =$ $= \frac{701.47}{34.01} \cdot (-187.8)$	3873.45
Heat losses	Q_{loss}	$\frac{(Q_{MnSO_4} + Q_{NH_4OH} + Q_{H_2O_2}) \cdot 5}{100} =$ $= \frac{(11763.56 + 1017.71 + 3873.45) \cdot 5}{100}$	832.74
Total input	$Q_{reactants}$	$Q_{MnSO_4} + Q_{NH_4OH} + Q_{H_2O_2} =$ $= 11763.56 + 1017.71 + 3873.45$	16654.72
Products			
Mn ₃ O ₄	$Q_{Mn_3O_4}$	$-\frac{m_{Mn_3O_4}}{M_{Mn_3O_4}} \cdot \Delta H_{f\ Mn_3O_4} =$ $= \frac{540}{228.81} \cdot (-1387.6)$	3274.79
Mn ₂ O ₃	$Q_{Mn_2O_3}$	$-\frac{m_{Mn_2O_3}}{M_{Mn_2O_3}} \cdot \Delta H_{f\ Mn_2O_3} =$ $= \frac{180}{157.87} \cdot (-957.7)$	1091.95
MnO ₂	Q_{MnO_2}	$-\frac{m_{MnO_2}}{M_{MnO_2}} \cdot \Delta H_{f\ MnO_2} =$ $= \frac{144}{86.94} \cdot (-521.5)$	863.77

H ₂ O	Q_{H_2O}	$-\frac{m_{H_2O}}{M_{H_2O}} \cdot \Delta H_{f\ H_2O} =$ $= \frac{570,14}{18.02} \cdot (-285.83)$	9043.46
(NH ₄) ₂ SO ₄	$Q_{(NH_4)_2SO_4}$	$-\frac{m_{(NH_4)_2SO_4}}{M_{(NH_4)_2SO_4}} \cdot \Delta H_{f\ (NH_4)_2SO_4} =$ $= \frac{1455,74}{132.14} \cdot (-1180.0)$	12999.65
O ₂	Q_{O_2}	$-\frac{m_{O_2}}{M_{O_2}} \cdot \Delta H_{f\ O_2} == \frac{247.39}{31.99} \cdot 0$	0
Total output	$Q_{product}$	$Q_{Mn_3O_4} + Q_{Mn_2O_3} + Q_{MnO_2} + Q_{H_2O} +$ $+ Q_{(NH_4)_2SO_4} + Q_{O_2} = 3274.79 +$ $+ 1091.95 + 863.77 + 9043.46 +$ $+ 12999.65$	27273.62
Amount of heat released	$Q_{released}$	$Q_{product} - Q_{reactants} - Q_{loss} =$ $= 27273.62 - 16654.72 - 832.74$	9786.16

As a result of the reaction, thermal energy is released. To standardize the process and avoid influence on product quality due to uncontrolled temperature, heat exchange using a cooling jacket is necessary. The cooling of the apparatus will occur through the reactor walls.

Conclusions to Section 7

The technological parameters of synthesis of photocatalytically active composite based on Mn₃O₄ hausmannite and HNTs were evaluated in this chapter. This composite was among the most active samples of MB dye degradation study and was selected as a model for its synthesis technology development. The block flow diagram includes stages of dissolution, vacuuming, synthesis, decantation, drying, grinding and then sending it to storage. Based on the experimental results, the product yield was 80%, considering potential losses during centrifugation and decantation, which together account for 20%. The material and heat balances were calculated for the production of 1 kg of the CS-2 composite. The thermal effect of the exothermic synthesis process of the most active composite has been calculated. According to our estimates, for the

selected amount of product production (1 kg), the temperature of the reaction mixture will increase. We have provided thermostatic reaction conditions to control the process and product properties to level this effect on the product's properties.

CONCLUSIONS

Environmental pollution constantly pressures society and decreases standards of living. Overcoming it requires new approaches in accordance with the principles of sustainable development. Photocatalytic methods of organic waste material removal represent a new family of approaches that can resolve the aforementioned issues. Revisiting photocatalytic processes during the last decade has caused huge interest in oxide systems and their composites.

1. It is revealed that oxide/hydroxide materials of manganese possess advantages such as a narrow band gap, good stability, and high photocatalytic activity for the degradation of organics under visible light range irradiation. Their composites with aluminosilicate nanotubes of halloysite are shown to display the decoration and incorporation effects of manganese compound toward a nanotube, improving functionality due to the role of HNTs as photocatalyst's support and enhanced reactant supply to the photocatalyst interface.

2. Photocatalytic behaviour of individual compounds of MnO_2 , TiO_2 , HNTs was studied for PE-films degradation. The coupling effect of mechanically mixed photocatalyst of MnO_2 and TiO_2 in 1% by mass content was established. This mixed photocatalyst achieved 21.3% of mass loss versus pure MnO_2 (6.5%) and TiO_2 (14.6%) after 90h of degradation under UV-light at $\lambda = 250 \text{ nm}$ due to the 1st type of $\text{TiO}_2@ \text{MnO}_2$ heterojunction with faster accumulation of intermediates of PE oxidation as shown by FTIR data of Carbonyl, Hydroxyl, and C–O stretching vibration indexes.

3. Chemically deposited oxide/hydroxides actively decorate HNTs' interfaces in the presence of cationic species of Mn^{2+} in the deposition medium, and incorporation into lumen is observed for crystallisation of negatively charged Mn species of acid residues of the Tutton salts.

4. The photocatalytic degradation effects of cationic (Methylene Blue) and anionic (Congo Red) dyes on manganese (oxide)hydroxide composites with HNTs were studied. Cationic dye MB degradation was the most successful on HNTs@ $\text{Mn}_3\text{O}_4/\text{Mn}_2\text{O}_3$ composite ($E_g = 2.70 \text{ eV}$), whereas anionic dye degraded most

efficiently on higher valenced individual product of deposition of α -MnOOH@ γ -/ β -MnO₂ ($E_g = 1.99$ eV).

5. The positive influence of HNT's surface decoration by Mn_xO_y on photocatalytic activity of MB degradation is demonstrated, in our opinion, due to the new option of direct electron transfer of photoelectron from E_C of both HNTs & Mn_xO_y and following MB dye reduction. It is also evident from this diagram for CR dye that only CS-8 Sample has favorably aligned E_V to HOMO level of CR dye and, probably, this feature can be responsible for the faster direct oxidation of CR with holes from the valence band of CS-8 as a photocatalyst.

6. The band gap engineering of a photocatalyst toward the definite degradation process suggests combining E_C , E_V energy levels with HOMO/LUMO levels of the target molecule. The diffuse reflectance spectroscopy measurements of a semiconductor band gap, together with the Mulliken electronegativity of a photocatalyst, were reliable tools to provide a base for a successful combination explanation and prediction.

7. The series of electrodeposited MnO₂ samples was prepared using band gap engineering principles. The tasks to improve dispersity and decrease band gap were actualised by diffuse electrodeposition control and by doping with Cr(III)-ions. The phase composition was under control of 0.5M NH₄⁺-ions additive and by H₂SO₄ (2M, 0.031M, 0): the opened structures of hollandite and birnessite were stabilised by 0.5M NH₄⁺-ions (the latter occurred at pH > 2), ramsdellite structure type of γ -MnO₂ was the main phase without additives.

8. It is confirmed that manganese (oxide)hydroxide compounds used in this study are visible light photocatalysts with typical range of band gaps to within $E_g = 1.99 - 2.7$ eV. Doping by Chromium (III) ions narrowed E_g by about 0.3 – 0.5 eV due to incorporation of new electron donor levels.

9. The technological parameters of synthesis of photocatalytically active composite based on Mn₃O₄ hausmannite and HNTs were evaluated. The block flow diagram, material, and energy balances for this chemical process technology were introduced.

ACKNOWLEDGMENTS

I would like to express my gratitude to Prof. Giuseppe Lazzara for giving me the opportunity to join his research group at the University of Palermo and for being my supervisor. Your guidance, expertise, and support have been invaluable throughout my academic journey. I admire your professionalism and the ease, enthusiasm and humour with which you approach even the most difficult tasks and teach this by your example. I deeply appreciate your mentorship and encouragement, which have greatly contributed to my growth.

I sincerely thank Prof. Georgii Sokolsky for his comprehensive support, interesting ideas, and valuable discussions, which undoubtedly influenced my development as a scientist.

I wish to thank Dr. Myronyuk Oleksiy Volodymyrovych for guidance and expertise in working with the adhesive composition for applying the photocatalyst onto polyethylene film. His advice, support, and dedication have been instrumental in advancing this aspect of my research.

I am deeply thankful to Dr. Marjeta Maček Kržmanc for the warm welcome and coordination of my work at the Jožef Stefan Institute (Ljubljana, Slovenia). I am also deeply grateful for her guidance and support throughout our collaboration, as well as for the valuable knowledge and skills I acquired.

I want to thank my team from University of Palermo Maria Rita, Martina, Lorenzo, Chiara, Ludovico, Alessandro. You have become my big Italian family and thanks to you I have found my second home here in Palermo.

I would especially like to thank Giuseppe Cavallaro for his endless patience while I was writing my first article. I am grateful for the experience of following Giuseppe's course. If I ever give lectures, they are the ones I look up to.

Я хочу подякувати Богдану – якби не ти, я б ніколи не ступила на цей шлях. Я вдячна всій своїй родині, особливо мамі, папі і Ані за підтримку будь-яких моїх рішень і віру в мої сили.

REFERENCES

- [1] L. Zudina, ‘Dopovani Fe^{2+} , Co^{2+} , NH_4^+ produkty elektrokrystalizatsii oksydnoi systemy Mn(IV) z fluorovmisnykh elektrolitiv: sklad – struktura – vlastyvoli. [Doped Fe^{2+} , Co^{2+} , NH_4^+ products of electrocrystallization of the Mn(IV) oxide system from fluorine-containing electrolytes: composition – structure – properties [Unpublished dissertation of Doctor of Philosophy in Chemistry]]’, National Aviation University, Kyiv, Ukraine, 2021.
- [2] N. Haiuk, ‘Foto(elektro)katalizatory na osnovi kompozytiv $\text{TiO}_2/\text{MnO}_2/\text{HNT}/\text{INT}$ [Photo(electro)catalysts based on $\text{TiO}_2/\text{MnO}_2/\text{HNT}/\text{INT}$ composites [Unpublished dissertation of Doctor of Philosophy in Chemistry]]’, National Aviation University, Kyiv, Ukraine, 2021.
- [3] A. Kumar *et al.*, ‘Algal mediated intervention for the retrieval of emerging pollutants from aqueous media’, *J. Hazard. Mater.*, vol. 455, p. 131568, Aug. 2023, doi: 10.1016/j.jhazmat.2023.131568.
- [4] X. Liu *et al.*, ‘Frontiers in environmental cleanup: Recent advances in remediation of emerging pollutants from soil and water’, *J. Hazard. Mater. Adv.*, vol. 16, p. 100461, Nov. 2024, doi: 10.1016/j.hazadv.2024.100461.
- [5] N. Taoufik *et al.*, ‘Recent advances in the synthesis and environmental catalytic applications of layered double hydroxides-based materials for degradation of emerging pollutants through advanced oxidation processes’, *Mater. Res. Bull.*, vol. 154, p. 111924, Oct. 2022, doi: 10.1016/j.materresbull.2022.111924.
- [6] M. Procházková, M. Touš, D. Horňák, V. Miklas, M. Vondra, and V. Máša, ‘Industrial wastewater in the context of European Union water reuse legislation and goals’, *J. Clean. Prod.*, vol. 426, p. 139037, Nov. 2023, doi: 10.1016/j.jclepro.2023.139037.
- [7] European Commission, E. C., ‘Directive 2000/60/EC of the European Parliament and of the Council of 23 October 2000 establishing a framework for Community action in the field of water policy.’, *Off. J. Eur. Communities*, no. 327.43, pp. 1–72, Oct. 2000.

- [8] M. Ismail *et al.*, ‘Pollution, Toxicity and Carcinogenicity of Organic Dyes and their Catalytic Bio-Remediation’, *Curr. Pharm. Des.*, vol. 25, no. 34, pp. 3645–3663, Nov. 2019, doi: 10.2174/1381612825666191021142026.
- [9] Y. Kang *et al.*, ‘Superparamagnetic Fe₃O₄@Al-based metal-organic framework nanocomposites with high-performance removal of Congo red’, *J. Environ. Chem. Eng.*, vol. 11, no. 3, p. 109754, Jun. 2023, doi: 10.1016/j.jece.2023.109754.
- [10] D. R. Waring and G. Hallas, Eds., ‘The Chemistry and Application of Dyes’, Boston, MA: Springer US, 1990. doi: 10.1007/978-1-4684-7715-3.
- [11] M. Zahid *et al.*, ‘Role of polymeric nanocomposite membranes for the removal of textile dyes from wastewater’, in *Aquananotechnology*, Elsevier, 2021, pp. 91–103. doi: 10.1016/B978-0-12-821141-0.00006-9.
- [12] D.-A. Xie *et al.*, ‘Remarkable purification of organic dyes by NiOOH-modified industrial waste residues’, *J. Colloid Interface Sci.*, vol. 664, pp. 136–145, Jun. 2024, doi: 10.1016/j.jcis.2024.02.190.
- [13] S. I. Siddiqui *et al.*, ‘Investigation of Congo Red Toxicity towards Different Living Organisms: A Review’, *Processes*, vol. 11, no. 3, p. 807, Mar. 2023, doi: 10.3390/pr11030807.
- [14] W. M. Dehn, ‘Comparative solubilities in water, in pyridine and in aqueous pyridine.’, *J. Am. Chem. Soc.*, vol. 39, no. 7, pp. 1399–1404, Jul. 1917, doi: 10.1021/ja02252a012.
- [15] Z. Velkova, G. Kirova, M. Stoytcheva, and V. Gochev, ‘Biosorption of Congo Red and Methylene Blue by pretreated waste *Streptomyces fradiae* biomass - Equilibrium, kinetic and thermodynamic studies’, *J. Serbian Chem. Soc.*, vol. 83, no. 1, pp. 107–120, 2018, doi: 10.2298/JSC170519093V.
- [16] F. M. Valadi, A. Ekramipooya, and M. R. Gholami, ‘Selective separation of Congo Red from a mixture of anionic and cationic dyes using magnetic-MOF: Experimental and DFT study’, *J. Mol. Liq.*, vol. 318, p. 114051, Nov. 2020, doi: 10.1016/j.molliq.2020.114051.
- [17] M. A. Adebayo, J. I. Adebomi, T. O. Abe, and F. I. Areo, ‘Removal of aqueous Congo red and malachite green using ackee apple seed–bentonite composite’,

- Colloid Interface Sci. Commun.*, vol. 38, p. 100311, Sep. 2020, doi: 10.1016/j.colcom.2020.100311.
- [18] R. O. Wright, W. J. Lewander, and A. D. Woolf, 'Methemoglobinemia: Etiology, Pharmacology, and Clinical Management', *Ann. Emerg. Med.*, vol. 34, no. 5, pp. 646–656, Nov. 1999, doi: 10.1016/S0196-0644(99)70167-8.
- [19] A. T. Matveev *et al.*, 'A New Insight into the Mechanisms Underlying the Discoloration, Sorption, and Photodegradation of Methylene Blue Solutions with and without BNOx Nanocatalysts', *Materials*, vol. 15, no. 22, Art. no. 22, Jan. 2022, doi: 10.3390/ma15228169.
- [20] A. Tamoto, N. Aratani, and H. Yamada, 'Photophysical properties and structural analysis of modified methylene blues as near infrared dyes', *J. Photochem. Photobiol. Chem.*, vol. 358, pp. 441–446, May 2018, doi: 10.1016/j.jphotochem.2017.10.031.
- [21] M. Albert, M. S. Lessin, and B. F. Gilchrist, 'Methylene blue: dangerous dye for neonates', *J. Pediatr. Surg.*, vol. 38, no. 8, pp. 1244–1245, Aug. 2003, doi: 10.1016/S0022-3468(03)00278-1.
- [22] M. K. Gibbons, Md. M. Mortula, and G. A. Gagnon, 'Phosphorus adsorption on water treatment residual solids', *J. Water Supply Res. Technol.-Aqua*, vol. 58, no. 1, pp. 1–10, Feb. 2009, doi: 10.2166/aqua.2009.017.
- [23] Y. Zhang, M.-Y. Qi, Z.-R. Tang, and Y.-J. Xu, 'Photoredox-Catalyzed Plastic Waste Conversion: Nonselective Degradation versus Selective Synthesis', *ACS Catal.*, vol. 13, no. 6, pp. 3575–3590, Mar. 2023, doi: 10.1021/acscatal.3c00301.
- [24] L. Lebreton and A. Andrady, 'Future scenarios of global plastic waste generation and disposal', *Palgrave Commun.*, vol. 5, no. 1, p. 6, Jan. 2019, doi: 10.1057/s41599-018-0212-7.
- [25] K. Su, H. Liu, C. Zhang, and F. Wang, 'Photocatalytic conversion of waste plastics to low carbon number organic products', *Chin. J. Catal.*, vol. 43, no. 3, pp. 589–594, Mar. 2022, doi: 10.1016/S1872-2067(21)63885-8.

- [26] C. Schmidt, T. Krauth, and S. Wagner, ‘Export of Plastic Debris by Rivers into the Sea’, *Environ. Sci. Technol.*, vol. 51, no. 21, pp. 12246–12253, Nov. 2017, doi: 10.1021/acs.est.7b02368.
- [27] N. Singh, D. Hui, R. Singh, I. P. S. Ahuja, L. Feo, and F. Fraternali, ‘Recycling of plastic solid waste: A state of art review and future applications’, *Compos. Part B Eng.*, vol. 115, pp. 409–422, Apr. 2017, doi: 10.1016/j.compositesb.2016.09.013.
- [28] I. Kovinchuk, G. Sokolskyi, and G. Lazzara, ‘SINGLE-STAGE AND SIMPLE FABRICATION OF PE FILMS DECORATED WITH HALLOYSITE NANOTUBES’, *KPI Sci. News*, vol. 136, no. 1–4, Art. no. 1–4, 2023, doi: 10.20535/kpissn.2023.1-4.297046.
- [29] S. Kumar, A. K. Panda, and R. K. Singh, ‘A review on tertiary recycling of high-density polyethylene to fuel’, *Resour. Conserv. Recycl.*, vol. 55, no. 11, pp. 893–910, Sep. 2011, doi: 10.1016/j.resconrec.2011.05.005.
- [30] A. Rahimi and J. Garcia, ‘Chemical recycling of waste plastics for new materials production’, *Nat. Rev. Chem.*, vol. 1, Jun. 2017, doi: 10.1038/s41570-017-0046.
- [31] W. Li, W. Zhao, H. Zhu, Z.-J. Li, and W. Wang, ‘State of the art in the photochemical degradation of (micro)plastics: from fundamental principles to catalysts and applications’, *J. Mater. Chem. A*, vol. 11, no. 6, pp. 2503–2527, Feb. 2023, doi: 10.1039/D2TA09523H.
- [32] S. M. Al-Salem, P. Lettieri, and J. Baeyens, ‘Recycling and recovery routes of plastic solid waste (PSW): A review’, *Waste Manag.*, vol. 29, no. 10, pp. 2625–2643, Oct. 2009, doi: 10.1016/j.wasman.2009.06.004.
- [33] P. Xiang, T. Zhang, Q. Wu, and Q. Li, ‘Systematic Review of Degradation Processes for Microplastics: Progress and Prospects’, *Sustainability*, vol. 15, no. 17, Art. no. 17, Jan. 2023, doi: 10.3390/su151712698.
- [34] H. Wang *et al.*, ‘A review on heterogeneous photocatalysis for environmental remediation: From semiconductors to modification strategies’, *Chin. J. Catal.*, vol. 43, no. 2, pp. 178–214, Feb. 2022, doi: 10.1016/S1872-2067(21)63910-4.

- [35] Y. Zhong *et al.*, ‘Interface engineering of heterojunction photocatalysts based on 1D nanomaterials’, *Catal. Sci. Technol.*, vol. 11, no. 1, pp. 27–42, 2021, doi: 10.1039/D0CY01847C.
- [36] L. Wang and J. Yu, ‘Principles of photocatalysis’, in *Interface Science and Technology*, vol. 35, Elsevier, 2023, pp. 1–52. doi: 10.1016/B978-0-443-18786-5.00002-0.
- [37] R. Marschall, ‘Semiconductor Composites: Strategies for Enhancing Charge Carrier Separation to Improve Photocatalytic Activity’, *Adv. Funct. Mater.*, vol. 24, no. 17, pp. 2421–2440, May 2014, doi: 10.1002/adfm.201303214.
- [38] N. Serpone, E. Borgarello, and M. Grätzel, ‘Visible light induced generation of hydrogen from H₂ S in mixed semiconductor dispersions; improved efficiency through inter-particle electron transfer’, *J Chem Soc Chem Commun*, no. 6, pp. 342–344, 1984, doi: 10.1039/C39840000342.
- [39] S. Hotchandani and P. V. Kamat, ‘Charge-transfer processes in coupled semiconductor systems. Photochemistry and photoelectrochemistry of the colloidal cadmium sulfide-zinc oxide system’, *J. Phys. Chem.*, vol. 96, no. 16, pp. 6834–6839, Aug. 1992, doi: 10.1021/j100195a056.
- [40] K. Vinodgopal, I. Bedja, and P. V. Kamat, ‘Nanostructured Semiconductor Films for Photocatalysis. Photoelectrochemical Behavior of SnO₂/TiO₂ Composite Systems and Its Role in Photocatalytic Degradation of a Textile Azo Dye’, *Chem. Mater.*, vol. 8, no. 8, pp. 2180–2187, Jan. 1996, doi: 10.1021/cm950425y.
- [41] J. Li *et al.*, ‘Advances in Z-scheme semiconductor photocatalysts for the photoelectrochemical applications: A review’, *Carbon Energy*, vol. 4, no. 3, pp. 294–331, May 2022, doi: 10.1002/cey2.179.
- [42] D. Ayodhya, ‘Semiconductors-based Z-scheme materials for photoelectrochemical water splitting: A review’, *Electrochimica Acta*, vol. 448, p. 142118, Apr. 2023, doi: 10.1016/j.electacta.2023.142118.
- [43] J. Yu, W. Wang, B. Cheng, and B.-L. Su, ‘Enhancement of Photocatalytic Activity of Mesoporous TiO₂ Powders by Hydrothermal Surface Fluorination

- Treatment', *J. Phys. Chem. C*, vol. 113, no. 16, pp. 6743–6750, Apr. 2009, doi: 10.1021/jp900136q.
- [44] A. Fujishima and K. Honda, 'Electrochemical Photolysis of Water at a Semiconductor Electrode', *Nature*, vol. 238, no. 5358, pp. 37–38, Jul. 1972, doi: 10.1038/238037a0.
- [45] R. Sanjinés, H. Tang, H. Berger, F. Gozzo, G. Margaritondo, and F. Lévy, 'Electronic structure of anatase TiO₂ oxide', *J. Appl. Phys.*, vol. 75, no. 6, pp. 2945–2951, Mar. 1994, doi: 10.1063/1.356190.
- [46] G. Sokolskyi *et al.*, 'Photoelectrocatalytic degradation of aminoazodyes of titanium dioxide with surface Ti³⁺ states', *J. Chem. Technol.*, vol. 27, pp. 130–139, Oct. 2019, doi: 10.15421/081914.
- [47] F. Sadeghfar and M. Ghaedi, 'Photocatalytic treatment of pollutants in aqueous media', in *Interface Science and Technology*, vol. 32, Elsevier, 2021, pp. 725–759. doi: 10.1016/B978-0-12-818806-4.00011-5.
- [48] F. Wang *et al.*, 'A critical review of facets and defects in different MnO₂ crystalline phases and controlled synthesis – Its properties and applications in the energy field', *Coord. Chem. Rev.*, vol. 500, p. 215537, Feb. 2024, doi: 10.1016/j.ccr.2023.215537.
- [49] R. Giovanoli, 'Thermogravimetry of manganese dioxides', *Thermochim. Acta*, vol. 234, pp. 303–313, Mar. 1994, doi: 10.1016/0040-6031(94)85154-9.
- [50] L. Zudina, G. Sokolskyi, V. Chumak, and N. Haiuk, 'OER/ORR parameters of Fe²⁺ and Co²⁺-doped manganese dioxide electrode materials', *Mater. Today Proc.*, vol. 62, pp. 7759–7766, Jan. 2022, doi: 10.1016/j.matpr.2022.05.570.
- [51] A. K. Singh, T. K. Dhiman, L. G. B. V.S., and P. R. Solanki, 'Dimanganese trioxide (Mn₂O₃) based label-free electrochemical biosensor for detection of Aflatoxin-B1', *Bioelectrochemistry*, vol. 137, p. 107684, Feb. 2021, doi: 10.1016/j.bioelechem.2020.107684.
- [52] G. Munir, H. E. A. Mohamed, K. Hkiri, S. Ghotekar, and M. Maaza, 'Phyto-mediated fabrication of Mn₂O₃ nanoparticles using Hyphaene thebaica fruit extract

- as a promising photocatalyst for MB dye degradation', *Inorg. Chem. Commun.*, vol. 167, p. 112695, Sep. 2024, doi: 10.1016/j.inoche.2024.112695.
- [53] M. Lin, M. Liu, J. Wu, G. Owens, and Z. Chen, 'Green synthesis of Mn_2O_3 activated PDS to degrade estriol in medical wastewater and its degradation pathway', *Chem. Eng. J.*, vol. 484, p. 149713, Mar. 2024, doi: 10.1016/j.cej.2024.149713.
- [54] A. Umar *et al.*, 'Porous Mn_2O_3 nanorods-based electrode for high-performance electrochemical supercapacitor', *J. Energy Storage*, vol. 81, p. 110305, Mar. 2024, doi: 10.1016/j.est.2023.110305.
- [55] Z. Chen, C.-H. Shek, C. M. L. Wu, and J. K. L. Lai, 'Characterization Strategies for Mn_2O_3 Nanomaterials', *J. Nanosci. Nanotechnol.*, vol. 14, no. 2, pp. 1693–1709, Feb. 2014, doi: 10.1166/jnn.2014.8754.
- [56] X. Li, Q. Peng, H. Yang, H. Li, M. Zhu, and J. Pan, 'The enhanced photodegradation and photocatalytic H_2 evolution of $\text{Mn}_2\text{O}_3/\text{CdS}$ hollow octahedral core-shell pn junction via MOFs auxiliary', *J. Water Process Eng.*, vol. 61, p. 105276, May 2024, doi: 10.1016/j.jwpe.2024.105276.
- [57] R. N. De Araujo *et al.*, ' α - Mn_2O_3 porous fibers synthesized by air-heated solution blow spinning (A-HSBS) technique: electrochemical assessment for oxygen evolution reaction in alkaline medium', *J. Phys. Chem. Solids*, vol. 192, p. 112086, Sep. 2024, doi: 10.1016/j.jpcs.2024.112086.
- [58] Y. Shen, J. Cai, X. Huang, Y. Zheng, and Y. Shao, 'Enhanced photocatalytic CO_2 reduction to CH_4 by $\text{Mn}_2\text{O}_3/\text{MgTi}_2\text{O}_5$ nanocomposite', *Colloids Surf. Physicochem. Eng. Asp.*, vol. 708, p. 135990, Mar. 2025, doi: 10.1016/j.colsurfa.2024.135990.
- [59] V. M. B. Crisostomo *et al.*, 'New Synthetic Route, Characterization, and Electrocatalytic Activity of Nanosized Manganite', *Chem. Mater.*, vol. 19, no. 7, pp. 1832–1839, Apr. 2007, doi: 10.1021/cm062871z.
- [60] M. Ramstedt and S. Sjöberg, 'Phase Transformations and Proton Promoted Dissolution of Hydrous Manganite (γ - MnOOH)', *Aquat. Geochem.*, vol. 11, no. 4, pp. 413–431, Dec. 2005, doi: 10.1007/s10498-005-7441-2.

- [61] C. Wei, C. Xu, B. Li, D. Nan, J. Ma, and F. Kang, 'Formation and conversion mechanisms between single-crystal gamma-MnOOH and manganese oxides', *Mater. Res. Bull.*, vol. 47, no. 7, pp. 1740–1746, Jul. 2012, doi: 10.1016/j.materresbull.2012.03.041.
- [62] Z. Bai *et al.*, 'Branched Mesoporous Mn₃O₄ Nanorods: Facile Synthesis and Catalysis in the Degradation of Methylene Blue', *Chem. - Eur. J.*, vol. 18, no. 17, pp. 5319–5324, Apr. 2012, doi: 10.1002/chem.201102944.
- [63] Y. Kong *et al.*, 'Study on the Synthesis of Mn₃O₄ Nanooctahedrons and Their Performance for Lithium Ion Batteries', *Nanomaterials*, vol. 10, no. 2, p. 367, Feb. 2020, doi: 10.3390/nano10020367.
- [64] N. Li *et al.*, 'Enhanced norfloxacin degradation by visible-light-driven Mn₃O₄/γ-MnOOH photocatalysis under weak magnetic field', *Sci. Total Environ.*, vol. 761, p. 143268, Mar. 2021, doi: 10.1016/j.scitotenv.2020.143268.
- [65] L. Qi *et al.*, 'Highly coupled MnO₂/Mn₅O₈ Z-scheme heterojunction modified by Co₃O₄ co-catalyst: An efficient and stable photocatalyst to decompose gaseous benzene', *Appl. Catal. B Environ. Energy*, vol. 353, p. 124099, Sep. 2024, doi: 10.1016/j.apcatb.2024.124099.
- [66] S.-L. Chiam, S.-Y. Pung, and F.-Y. Yeoh, 'Recent developments in MnO₂-based photocatalysts for organic dye removal: a review', *Environ. Sci. Pollut. Res.*, vol. 27, no. 6, pp. 5759–5778, Feb. 2020, doi: 10.1007/s11356-019-07568-8.
- [67] X. Cheng, G. Dong, Y. Zhang, C. Feng, and Y. Bi, 'Dual-bonding interactions between MnO₂ cocatalyst and TiO₂ photoanodes for efficient solar water splitting', *Appl. Catal. B Environ.*, vol. 267, p. 118723, Jun. 2020, doi: 10.1016/j.apcatb.2020.118723.
- [68] F. Ferrante, N. Armata, G. Cavallaro, and G. Lazzara, 'Adsorption Studies of Molecules on the Halloysite Surfaces: A Computational and Experimental Investigation', *J. Phys. Chem. C*, vol. 121, no. 5, pp. 2951–2958, Feb. 2017, doi: 10.1021/acs.jpcc.6b12876.
- [69] J. Matusik, 'Chapter 23 - Halloysite for Adsorption and Pollution Remediation', in *Developments in Clay Science*, vol. 7, P. Yuan, A. Thill, and F. Bergaya, Eds.,

- in *Nanosized Tubular Clay Minerals*, vol. 7., Elsevier, 2016, pp. 606–627. doi: 10.1016/B978-0-08-100293-3.00023-6.
- [70] P. Berthier, ‘Analyse de l’halloysite’, *Ann Chim Phys*, vol. 32, pp. 332–335, 1826.
- [71] K. Song, ‘Micro- and nano-fillers used in the rubber industry’, in *Progress in Rubber Nanocomposites*, Elsevier, 2017, pp. 41–80. doi: 10.1016/B978-0-08-100409-8.00002-4.
- [72] E. Abdullayev, A. Joshi, W. Wei, Y. Zhao, and Y. Lvov, ‘Enlargement of Halloysite Clay Nanotube Lumen by Selective Etching of Aluminum Oxide’, *ACS Nano*, vol. 6, no. 8, pp. 7216–7226, Aug. 2012, doi: 10.1021/nn302328x.
- [73] M. Massaro *et al.*, ‘Chemical modification of halloysite nanotubes for controlled loading and release’, *J. Mater. Chem. B*, vol. 6, no. 21, pp. 3415–3433, 2018, doi: 10.1039/C8TB00543E.
- [74] Y. Wu, Y. Zhang, J. Ju, H. Yan, X. Huang, and Y. Tan, ‘Advances in Halloysite Nanotubes–Polysaccharide Nanocomposite Preparation and Applications’, *Polymers*, vol. 11, no. 6, p. 987, Jun. 2019, doi: 10.3390/polym11060987.
- [75] E. Abdullayev *et al.*, ‘Self-Healing Coatings Based on Halloysite Clay Polymer Composites for Protection of Copper Alloys’, *ACS Appl. Mater. Interfaces*, vol. 5, no. 10, pp. 4464–4471, May 2013, doi: 10.1021/am400936m.
- [76] E. Abdullayev and Y. Lvov, ‘Halloysite clay nanotubes as a ceramic “skeleton” for functional biopolymer composites with sustained drug release’, *J. Mater. Chem. B*, vol. 1, no. 23, p. 2894, 2013, doi: 10.1039/c3tb20059k.
- [77] G. I. Fakhrullina, F. S. Akhatova, Y. M. Lvov, and R. F. Fakhrullin, ‘Toxicity of halloysite clay nanotubes in vivo: a *Caenorhabditis elegans* study’, *Environ. Sci. Nano*, vol. 2, no. 1, pp. 54–59, 2015, doi: 10.1039/C4EN00135D.
- [78] X. Wang, J. Gong, Z. Gui, T. Hu, and X. Xu, ‘Halloysite nanotubes-induced Al accumulation and oxidative damage in liver of mice after 30-day repeated oral administration’, *Environ. Toxicol.*, vol. 33, no. 6, pp. 623–630, Jun. 2018, doi: 10.1002/tox.22543.

- [79] H. M. Yurdacan and M. Murat Sari, 'Chapter Three - Functional green-based nanomaterials towards sustainable carbon capture and sequestration', in *Sustainable Materials for Transitional and Alternative Energy*, vol. 2, M. M. Sari, C. Temizel, C. H. Canbaz, L. A. Saputelli, and O. Torsæter, Eds., in *Advanced Materials and Sensors for the Oil and Gas Industry*, vol. 2., Gulf Professional Publishing, 2021, pp. 125–177. doi: 10.1016/B978-0-12-824379-4.00004-5.
- [80] S. Wu, M. Qiu, B. Guo, L. Zhang, and Y. Lvov, 'Nanodot-Loaded Clay Nanotubes as Green and Sustained Radical Scavengers for Elastomer', *ACS Sustain. Chem. Eng.*, vol. 5, no. 2, pp. 1775–1783, Feb. 2017, doi: 10.1021/acssuschemeng.6b02523.
- [81] E. Abdullayev and Y. Lvov, 'Halloysite Clay Nanotubes for Controlled Release of Protective Agents', *J. Nanosci. Nanotechnol.*, vol. 11, pp. 10007–26, Nov. 2011, doi: 10.1166/jnn.2011.5724.
- [82] W. O. Yah, A. Takahara, and Y. M. Lvov, 'Selective Modification of Halloysite Lumen with Octadecylphosphonic Acid: New Inorganic Tubular Micelle', *J. Am. Chem. Soc.*, vol. 134, no. 3, pp. 1853–1859, Jan. 2012, doi: 10.1021/ja210258y.
- [83] G. V. Sokolskyi *et al.*, 'Effects of electrolyte doping on electrodeposited nanostructured manganese oxide and chromium oxide', *Surf. Coat. Technol.*, vol. 400, p. 126211, Oct. 2020, doi: 10.1016/j.surfcoat.2020.126211.
- [84] X. u Zhao, Z. Li, Y. Chen, L. Shi, and Y. Zhu, 'Solid-phase photocatalytic degradation of polyethylene plastic under UV and solar light irradiation', *J. Mol. Catal. Chem.*, vol. 268, no. 1–2, pp. 101–106, May 2007, doi: 10.1016/j.molcata.2006.12.012.
- [85] J.-H. Arndt, R. Brüll, T. Macko, F. Perez, and J. Panitzky, 'Solubility of Polyethylene in *n* -Hexane and Cyclohexane: Experimental Determination and Comparison with Solid–Liquid Equilibria-Based Predictions', *Ind. Eng. Chem. Res.*, vol. 60, no. 41, pp. 14968–14976, Oct. 2021, doi: 10.1021/acs.iecr.1c02406.
- [86] S. Vyazovkin, A. K. Burnham, J. M. Criado, L. A. Pérez-Maqueda, C. Popescu, and N. Sbirrazzuoli, 'ICTAC Kinetics Committee recommendations for performing

- kinetic computations on thermal analysis data', *Thermochim. Acta*, vol. 520, no. 1, pp. 1–19, Jun. 2011, doi: 10.1016/j.tca.2011.03.034.
- [87] O. Gutiérrez and H. Palza, 'Effect of carbon nanotubes on thermal pyrolysis of high density polyethylene and polypropylene', *Polym. Degrad. Stab.*, vol. 120, pp. 122–134, Oct. 2015, doi: 10.1016/j.polymdegradstab.2015.06.014.
- [88] T. Saha, A. K. Bhowmick, T. Oda, T. Miyauchi, and N. Fujii, 'Influence of layered nanofillers on the mechanical properties and thermal degradation of polyacrylic ester polymer: Theoretical and experimental investigations', *Compos. Part B Eng.*, vol. 169, pp. 65–78, Jul. 2019, doi: 10.1016/j.compositesb.2019.03.084.
- [89] I. Blanco, L. Abate, M. L. Antonelli, and F. A. Bottino, 'The regression of isothermal thermogravimetric data to evaluate degradation Ea values of polymers: A comparison with literature methods and an evaluation of lifetime predictions reliability. Part II', *Polym. Degrad. Stab.*, vol. 98, no. 11, pp. 2291–2296, Nov. 2013, doi: 10.1016/j.polymdegradstab.2013.08.012.
- [90] C.-H. Kim, Z. Akase, L. Zhang, A. H. Heuer, A. E. Newman, and P. J. Hughes, 'The structure and ordering of ϵ -MnO₂', *J. Solid State Chem.*, vol. 179, no. 3, pp. 753–774, Mar. 2006, doi: 10.1016/j.jssc.2005.11.042.
- [91] M. Nagao *et al.*, 'Further Understanding of Reaction Processes in Electrolytic Manganese Dioxide Electrodes for Lithium Cells', *J. Electrochem. Soc.*, vol. 152, no. 7, p. E230, 2005, doi: 10.1149/1.1926667.
- [92] D. Balachandran, D. Morgan, G. Ceder, and A. Van De Walle, 'First-principles study of the structure of stoichiometric and Mn-deficient MnO₂', *J. Solid State Chem.*, vol. 173, no. 2, pp. 462–475, Jul. 2003, doi: 10.1016/S0022-4596(03)00023-9.
- [93] M. C. Celina, E. Linde, and E. Martinez, 'Carbonyl Identification and Quantification Uncertainties for Oxidative Polymer Degradation', *Polym. Degrad. Stab.*, vol. 188, p. 109550, Jun. 2021, doi: 10.1016/j.polymdegradstab.2021.109550.

- [94] A. Benitez, J. Sánchez, M. Arnal, A. Müller, O. Rodriguez Fernandez, and G. Morales, 'Abiotic degradation of LDPE and LLDPE formulated with a pro-oxidant additive', *Polym. Degrad. Stab.*, vol. 98, pp. 490–501, Jan. 2013, doi: 10.1016/j.polymdegradstab.2012.12.011.
- [95] M. C. Antunes, J. A. M. Agnelli, A. S. Babetto, B. C. Bonse, and S. H. P. Bettini, 'Abiotic thermo-oxidative degradation of high density polyethylene: Effect of manganese stearate concentration', *Polym. Degrad. Stab.*, vol. 143, pp. 95–103, Sep. 2017, doi: 10.1016/j.polymdegradstab.2017.06.012.
- [96] M. C. Celina, 'Review of polymer oxidation and its relationship with materials performance and lifetime prediction', *Polym. Degrad. Stab.*, vol. 98, no. 12, pp. 2419–2429, Dec. 2013, doi: 10.1016/j.polymdegradstab.2013.06.024.
- [97] W. W. Focke, R. P. Mashele, and N. S. Nhlapo, 'Stabilization of low-density polyethylene films containing metal stearates as photodegradants', *J. Vinyl Addit. Technol.*, vol. 17, no. 1, pp. 21–27, 2011, doi: 10.1002/vnl.20248.
- [98] A. Ramakrishnan *et al.*, 'Enhanced performance of surface-modified TiO₂ photocatalysts prepared via a visible-light photosynthetic route', *Chem. Commun.*, vol. 48, no. 68, p. 8556, 2012, doi: 10.1039/c2cc34243j.
- [99] M. A. Butler and D. S. Ginley, 'Prediction of Flatband Potentials at Semiconductor-Electrolyte Interfaces from Atomic Electronegativities', *J. Electrochem. Soc.*, vol. 125, no. 2, p. 228, Feb. 1978, doi: 10.1149/1.2131419.
- [100] F. Bessaha, N. Mahrez, K. Marouf-Khelifa, A. Çoruh, and A. Khelifa, 'Removal of Congo red by thermally and chemically modified halloysite: equilibrium, FTIR spectroscopy, and mechanism studies', *Int. J. Environ. Sci. Technol.*, vol. 16, no. 8, pp. 4253–4260, Aug. 2019, doi: 10.1007/s13762-018-2041-z.
- [101] T. S. Anirudhan and S. R. Rejeena, 'Photocatalytic Degradation of Eosin Yellow Using Poly(pyrrole-co-aniline)-Coated TiO₂ /Nanocellulose Composite under Solar Light Irradiation', *J. Mater.*, vol. 2015, pp. 1–11, Oct. 2015, doi: 10.1155/2015/636409.
- [102] G. Zhang *et al.*, 'Improved structural stability and adsorption capacity of adsorbent material Li_{1.6}Mn_{1.6}O₄ via facile surface fluorination', *Colloids Surf.*

Physicochem. Eng. Asp., vol. 629, p. 127465, Nov. 2021, doi: 10.1016/j.colsurfa.2021.127465.

- [103] W. Li *et al.*, ‘Enhanced adsorption capacity of ultralong hydrogen titanate nanobelts for antibiotics’, *J. Mater. Chem. A*, vol. 5, no. 9, pp. 4352–4358, 2017, doi: 10.1039/C6TA09116D.
- [104] G. V. Sokolskyi *et al.*, ‘(PDF) TOWARD TiO₂ — MnO₂ NANOCOMPOSITE PHOTOELECTRODES FOR ORGANIC DYE DEGRADATION’, *Promis. Mater. Process. Inapplied Electrochem.*, pp. 48–58, 2019, doi: 10.1007/978-617-7506-48-4.
- [105] I. Kovinchuk, N. Haiuk, G. Lazzara, G. Cavallaro, and G. Sokolskyi, ‘Enhanced photocatalytic degradation of PE film by anatase/ γ -MnO₂’, *Polym. Degrad. Stab.*, vol. 210, p. 110295, Apr. 2023, doi: 10.1016/j.polymdegradstab.2023.110295.
- [106] G. Sokolskyi, S. Ivanova, N. Ivanova, E. Boldyrev, T. Lobunets, and T. Tomila, ‘Doped manganese (IV) oxide in processes of destruction and removal of organic compounds from aqueous solutions’, *J. Water Chem. Technol.*, vol. 34, pp. 227–233, Sep. 2012, doi: 10.3103/S1063455X12050037.
- [107] F. Ferrante, M. Bertini, C. Ferlito, L. Lisuzzo, G. Lazzara, and D. Duca, ‘A computational and experimental investigation of halloysite silicic surface modifications after alkaline treatment’, *Appl. Clay Sci.*, vol. 232, p. 106813, Feb. 2023, doi: 10.1016/j.clay.2022.106813.
- [108] S. Sadjadi, M. M. Heravi, and M. Daraie, ‘Heteropolyacid supported on amine-functionalized halloysite nano clay as an efficient catalyst for the synthesis of pyrazolopyranopyrimidines via four-component domino reaction’, *Res. Chem. Intermed.*, vol. 43, no. 4, pp. 2201–2214, Apr. 2017, doi: 10.1007/s11164-016-2756-8.
- [109] J. T. Klopogge, ‘Characterisation of Halloysite by Spectroscopy’, in *Developments in Clay Science*, vol. 7, Elsevier, 2016, pp. 115–136. doi: 10.1016/B978-0-08-100293-3.00006-6.
- [110] L. Lisuzzo, G. Cavallaro, P. Pasbakhsh, S. Milioto, and G. Lazzara, ‘Why does vacuum drive to the loading of halloysite nanotubes? The key role of water

- confinement', *J. Colloid Interface Sci.*, vol. 547, pp. 361–369, Jul. 2019, doi: 10.1016/j.jcis.2019.04.012.
- [111] L. Lisuzzo, G. Cavallaro, S. Milioto, and G. Lazzara, 'Halloysite Nanotubes Coated by Chitosan for the Controlled Release of Khellin', *Polymers*, vol. 12, no. 8, p. 1766, Aug. 2020, doi: 10.3390/polym12081766.
- [112] G. Viscusi, E. Lamberti, F. D'Amico, L. Tammaro, and G. Gorrasi, 'Fabrication and Characterization of Bio-Nanocomposites Based on Halloysite-Encapsulating Grapefruit Seed Oil in a Pectin Matrix as a Novel Bio-Coating for Strawberry Protection', *Nanomaterials*, vol. 12, no. 8, p. 1265, Apr. 2022, doi: 10.3390/nano12081265.
- [113] S. Sahebian, S. M. Zebarjad, S. A. Sajjadi, Z. Sherafat, and A. Lazzeri, 'Effect of both uncoated and coated calcium carbonate on fracture toughness of HDPE/CaCO₃ nanocomposites', *J. Appl. Polym. Sci.*, vol. 104, no. 6, pp. 3688–3694, Jun. 2007, doi: 10.1002/app.25644.
- [114] X. Tang and S. Alavi, 'Structure and Physical Properties of Starch/Poly Vinyl Alcohol/Laponite RD Nanocomposite Films', *J. Agric. Food Chem.*, vol. 60, no. 8, pp. 1954–1962, Feb. 2012, doi: 10.1021/jf2024962.
- [115] M. M. Calvino, L. Lisuzzo, G. Cavallaro, G. Lazzara, and S. Milioto, 'Halloysite based geopolymers filled with wax microparticles as sustainable building materials with enhanced thermo-mechanical performances', *J. Environ. Chem. Eng.*, vol. 10, no. 6, p. 108594, Dec. 2022, doi: 10.1016/j.jece.2022.108594.
- [116] Yu. A. Dzenis, 'Effect of aggregation of a dispersed rigid filler on the elastic characteristics of a polymer composite', *Mech. Compos. Mater.*, vol. 22, no. 1, pp. 12–19, 1986, doi: 10.1007/BF00606002.
- [117] J. W. Sikora, I. Gajdoš, and A. Puszka, 'Polyethylene-Matrix Composites with Halloysite Nanotubes with Enhanced Physical/Thermal Properties', *Polymers*, vol. 11, no. 5, p. 787, May 2019, doi: 10.3390/polym11050787.
- [118] L. Lisuzzo, G. Cavallaro, S. Milioto, and G. Lazzara, 'Halloysite nanotubes filled with MgO for paper reinforcement and deacidification', *Appl. Clay Sci.*, vol. 213, p. 106231, Nov. 2021, doi: 10.1016/j.clay.2021.106231.

- [119] E. Paineau, G. Sokolskyi, M. Zahornyi, A. Ragulya, N. Gayuk, and I. Kovinchuk, *INTs/MnO₂/TiO₂/PANI Composites: Toward New Applications and Enforced Functionality*. Odesa,: IEEE 11th International Conference “Nanomaterials: Applications & Properties” (NAP-2021), 2021.
- [120] P. Ruetschi, ‘Cation-Vacancy Model for MnO₂’, *J. Electrochem. Soc.*, vol. 131, no. 12, p. 2737, Dec. 1984, doi: 10.1149/1.2115399.
- [121] N. Doebelin and R. Kleeberg, ‘*Profex* : a graphical user interface for the Rietveld refinement program *BGMN*’, *J. Appl. Crystallogr.*, vol. 48, no. 5, pp. 1573–1580, Oct. 2015, doi: 10.1107/S1600576715014685.
- [122] E. A. Bakr, H. G. El-Attar, and M. A. Salem, ‘Efficient catalytic degradation of single and binary azo dyes by a novel triple nanocomposite of Mn₃O₄ /Ag/SiO₂’, *Appl. Organomet. Chem.*, vol. 34, no. 8, p. e5688, Aug. 2020, doi: 10.1002/aoc.5688.
- [123] X. Yang *et al.*, ‘Enhanced electrocatalytic performance for methanol oxidation of Pt nanoparticles on Mn₃O₄-modified multi-walled carbon nanotubes’, *Int. J. Hydrog. Energy*, vol. 37, no. 15, pp. 11167–11175, Aug. 2012, doi: 10.1016/j.ijhydene.2012.04.153.
- [124] Y. Wang, C. Hou, X. Lin, H. Jiang, C. Zhang, and G. Liu, ‘Dye degradation studies of hausmannite manganese oxide (Mn₃O₄) nanoparticles synthesized by chemical method’, *Appl. Phys. A*, vol. 127, no. 4, p. 277, Apr. 2021, doi: 10.1007/s00339-021-04428-6.
- [125] T. Kohler, T. Armbruster, and E. Libowitzky, ‘Hydrogen Bonding and Jahn–Teller Distortion in Groutite, α -MnOOH, and Manganite, γ -MnOOH, and Their Relations to the Manganese Dioxides Ramsdellite and Pyrolusite’, *J. Solid State Chem.*, vol. 133, no. 2, pp. 486–500, Nov. 1997, doi: 10.1006/jssc.1997.7516.
- [126] M. Augustin *et al.*, ‘Manganese oxide phases and morphologies: A study on calcination temperature and atmospheric dependence’, *Beilstein J. Nanotechnol.*, vol. 6, pp. 47–59, Jan. 2015, doi: 10.3762/bjnano.6.6.

- [127] J. Slivnik, A. Rahten, and D. Gantar, ‘Study of Tutton’s Salts $(\text{NH}_4)_2\text{M}(\text{SO}_4)_2 \cdot 6\text{H}_2\text{O}$ with Mixed Metal Ions in the Structure’, *Croat. Chem. Acta*, vol. 58, no. 3, pp. 289–294, 1985.
- [128] G. C. Dismukes *et al.*, ‘Development of Bioinspired Mn_4O_4 –Cubane Water Oxidation Catalysts: Lessons from Photosynthesis’, *Acc. Chem. Res.*, vol. 42, no. 12, pp. 1935–1943, Dec. 2009, doi: 10.1021/ar900249x.
- [129] Ivanova N.D., Boldyrev, E. I, Pimennova K.N., Z. Sokolskyi, G. V., and Makeeva, I. S., ‘Electrochemical preparation of manganese dioxide from fluorine-containing electrolytes’, *J. Appl. Chem.*, vol. 71, pp. 1269–1271, 1998.
- [130] W. A. Dollase, ‘Correction of intensities for preferred orientation in powder diffractometry: application of the March model’, *J. Appl. Crystallogr.*, vol. 19, no. 4, pp. 267–272, Aug. 1986, doi: 10.1107/S0021889886089458.
- [131] D. M. Tinsley and J. H. Sharp, ‘Thermal analysis of manganese dioxide in controlled atmospheres’, *J. Therm. Anal.*, vol. 3, no. 1, pp. 43–48, Mar. 1971, doi: 10.1007/BF01911769.
- [132] D. Lv, X. Huang, H. Yue, and Y. Yang, ‘Sodium-Ion-Assisted Hydrothermal Synthesis of $\gamma\text{-MnO}_2$ and Its Electrochemical Performance’, *J. Electrochem. Soc.*, vol. 156, no. 11, p. A911, 2009, doi: 10.1149/1.3206586.
- [133] G. V. Sokolskyi, S. V. Ivanov, E. I. Boldyrev, N. D. Ivanova, and T. F. Lobunets, ‘ Li^+ -Doping-Induced Changes of Phase Composition in Electrodeposited Manganese(IV) Oxide Materials’, *Solid State Phenom.*, vol. 230, pp. 85–92, Jun. 2015, doi: 10.4028/www.scientific.net/SSP.230.85.
- [134] P. Raizada *et al.*, ‘Surface defect engineering of metal oxides photocatalyst for energy application and water treatment’, *J. Materiomics*, vol. 7, no. 2, pp. 388–418, Mar. 2021, doi: 10.1016/j.jmat.2020.10.009.
- [135] G. V. Sokolskyi, Ivanova N.D., L. V. Zudina, N. V. Gayuk, and Kovinchuk, I. V., ‘Electrolytic doping and implementation of a bifunctional electrochemical system’, in *9th Ukrainian Congress of Electrochemistry Achievements Problems and Prospects*, 2021, pp. 56–57. doi: 10.33609/978-966-8398-64-3.01.2021.1-191.

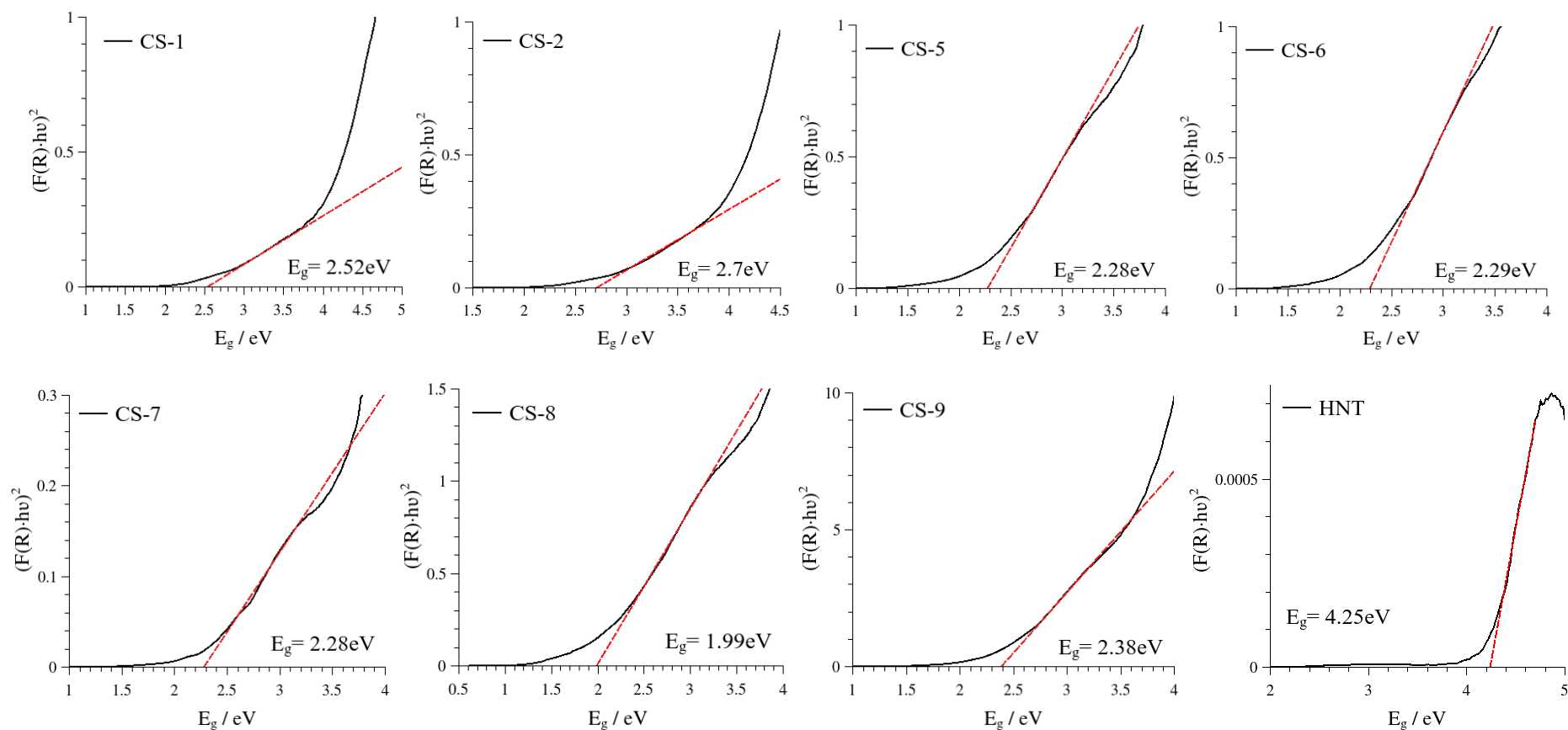
- [136] S. L. Suib, 'Porous Manganese Oxide Octahedral Molecular Sieves and Octahedral Layered Materials', *Acc. Chem. Res.*, vol. 41, no. 4, pp. 479–487, Apr. 2008, doi: 10.1021/ar7001667.
- [137] L. Guadagno, C. Naddeo, V. Vittoria, G. Camino, and C. Cagnani, 'Chemical and morphological modifications of irradiated linear low density polyethylene (LLDPE)', *Polym. Degrad. Stab.*, vol. 72, no. 1, pp. 175–186, Jan. 2001, doi: 10.1016/S0141-3910(01)00024-6.
- [138] X. Zhao, Z. Li, Y. Chen, L. Shi, and Y. Zhu, 'Enhancement of photocatalytic degradation of polyethylene plastic with CuPc modified TiO₂ photocatalyst under solar light irradiation', *Appl. Surf. Sci.*, vol. 254, no. 6, pp. 1825–1829, Jan. 2008, doi: 10.1016/j.apsusc.2007.07.154.
- [139] W. Liang, Y. Luo, S. Song, X. Dong, and X. Yu, 'High photocatalytic degradation activity of polyethylene containing polyacrylamide grafted TiO₂', *Polym. Degrad. Stab.*, vol. 98, no. 9, pp. 1754–1761, Sep. 2013, doi: 10.1016/j.polymdegradstab.2013.05.027.
- [140] L. Costa, M. P. Luda, and L. Trossarelli, 'Ultra high molecular weight polyethylene—II. Thermal- and photo-oxidation', *Polym. Degrad. Stab.*, vol. 58, no. 1, pp. 41–54, Jan. 1997, doi: 10.1016/S0141-3910(97)00010-4.
- [141] G. Liu, S. Liao, D. Zhu, J. Cui, and W. Zhou, 'Solid-phase photocatalytic degradation of polyethylene film with manganese oxide OMS-2', *Solid State Sci.*, vol. 13, no. 1, pp. 88–94, Jan. 2011, doi: 10.1016/j.solidstatesciences.2010.10.014.
- [142] M. I. Tayouri *et al.*, 'Degradation of polymer nanocomposites filled with graphene oxide and reduced graphene oxide nanoparticles: A review of current status', *Polym. Degrad. Stab.*, vol. 206, p. 110179, Dec. 2022, doi: 10.1016/j.polymdegradstab.2022.110179.
- [143] T. G. Darshan, S. Veluri, B. Kartik, C. Yen-Hsiang, and C. Fang-Chyou, 'Poly(butylene succinate)/high density polyethylene blend-based nanocomposites with enhanced physical properties – Selectively localized carbon nanotube in pseudo-double percolated structure', *Polym. Degrad. Stab.*, vol. 163, pp. 185–194, May 2019, doi: 10.1016/j.polymdegradstab.2019.03.009.

- [144] N. V. Hung *et al.*, ‘Highly effective adsorption of organic dyes from aqueous solutions on longan seed-derived activated carbon’, *Environ. Eng. Res.*, vol. 28, no. 3, Jun. 2023, doi: 10.4491/eer.2022.116.
- [145] S. S. M. Bhat and N. G. Sundaram, ‘Efficient visible light photocatalysis of Bi₄TaO₈Cl nanoparticles synthesized by solution combustion technique’, *RSC Adv.*, vol. 3, no. 34, p. 14371, 2013, doi: 10.1039/c3ra40240a.
- [146] D. Heger, J. Jirkovský, and P. Klán, ‘Aggregation of Methylene Blue in Frozen Aqueous Solutions Studied by Absorption Spectroscopy’, *J. Phys. Chem. A*, vol. 109, no. 30, pp. 6702–6709, Aug. 2005, doi: 10.1021/jp050439j.
- [147] P. C. Hiemenz and R. Rajagopalan, Eds., *Principles of Colloid and Surface Chemistry, Revised and Expanded*, 3rd ed. Boca Raton: CRC Press, 2016. doi: 10.1201/9781315274287.
- [148] D. Hahn, ‘Light Scattering Theory’, *Dep. Mech. Aerosp. Eng. Univ. Fla.*, vol. 18, 2009.
- [149] E. Pretsch, P. Bühlmann, and Affolter, *Structure determination of organic compounds—Tables of spectra data*. Berlin: Springer, 2000.
- [150] Perry, John, *Chemical Engineers’ Handbook*. — 7th ed., 7th ed. United States of America, 1999. Accessed: Feb. 03, 2025. [Online]. Available: <https://pubs.acs.org/doi/10.1021/ed019p449.2>
- [151] G. V. Samsonov, Ed., *Handbook of the Physicochemical Properties of the Elements*. Boston, MA: Springer US, 1968. doi: 10.1007/978-1-4684-6066-7.

APPENDIXES

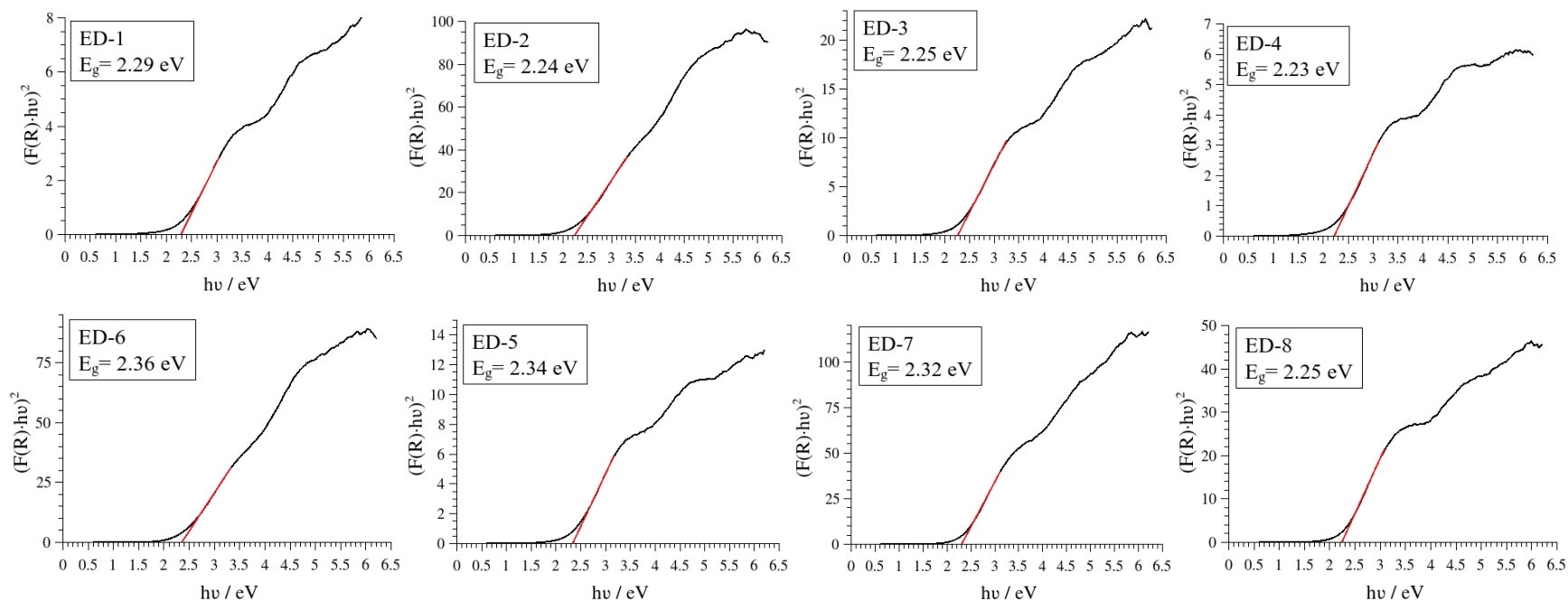
Appendix A.

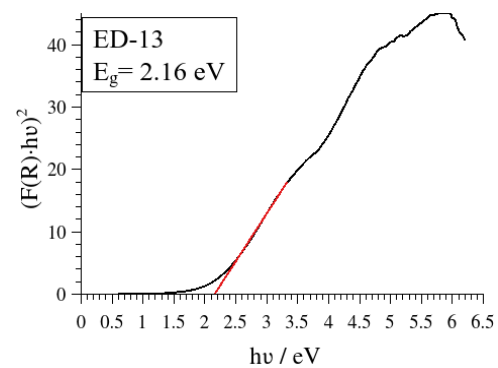
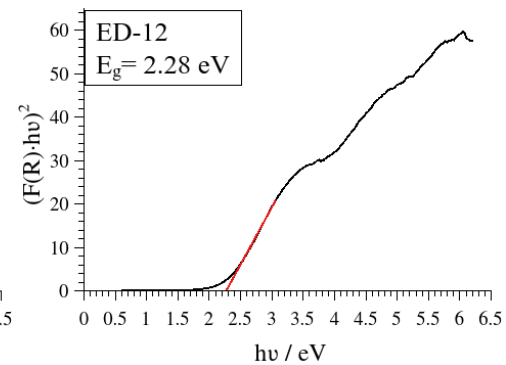
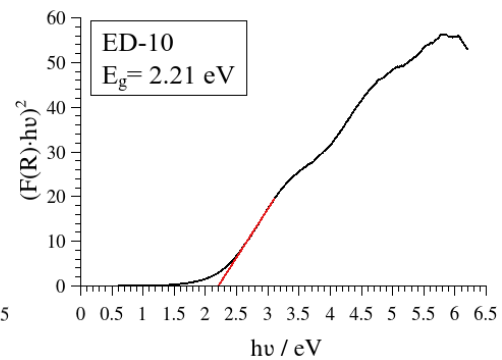
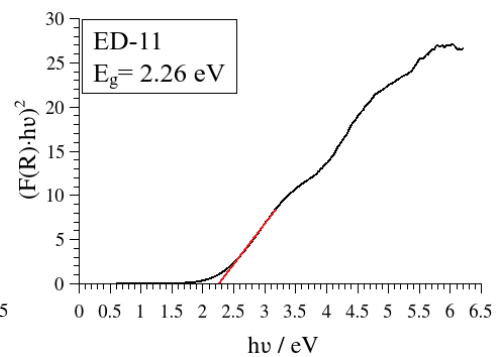
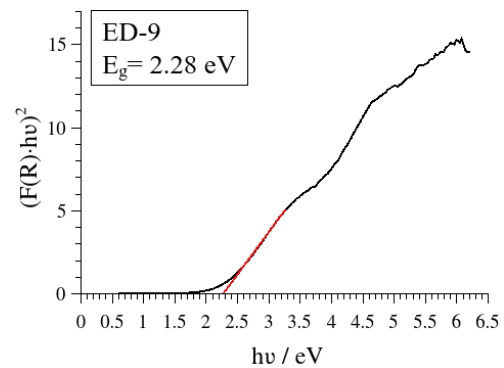
Kubelka-Munk function versus energy plots for determination of band gap of chemically sintesized samples.



Appendix B

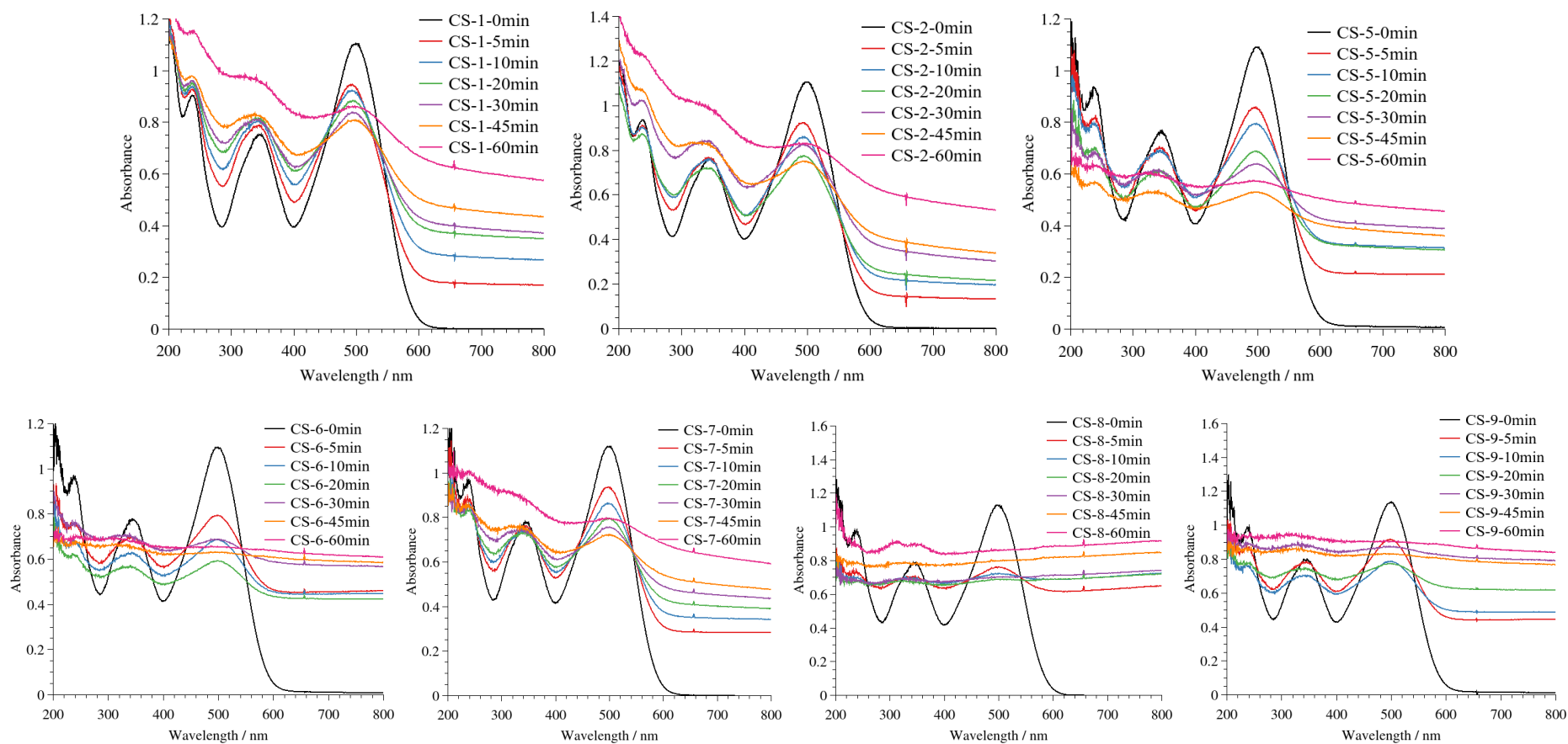
Kubelka-Munk function versus energy plots for determination of band gap of electro deposited samples.





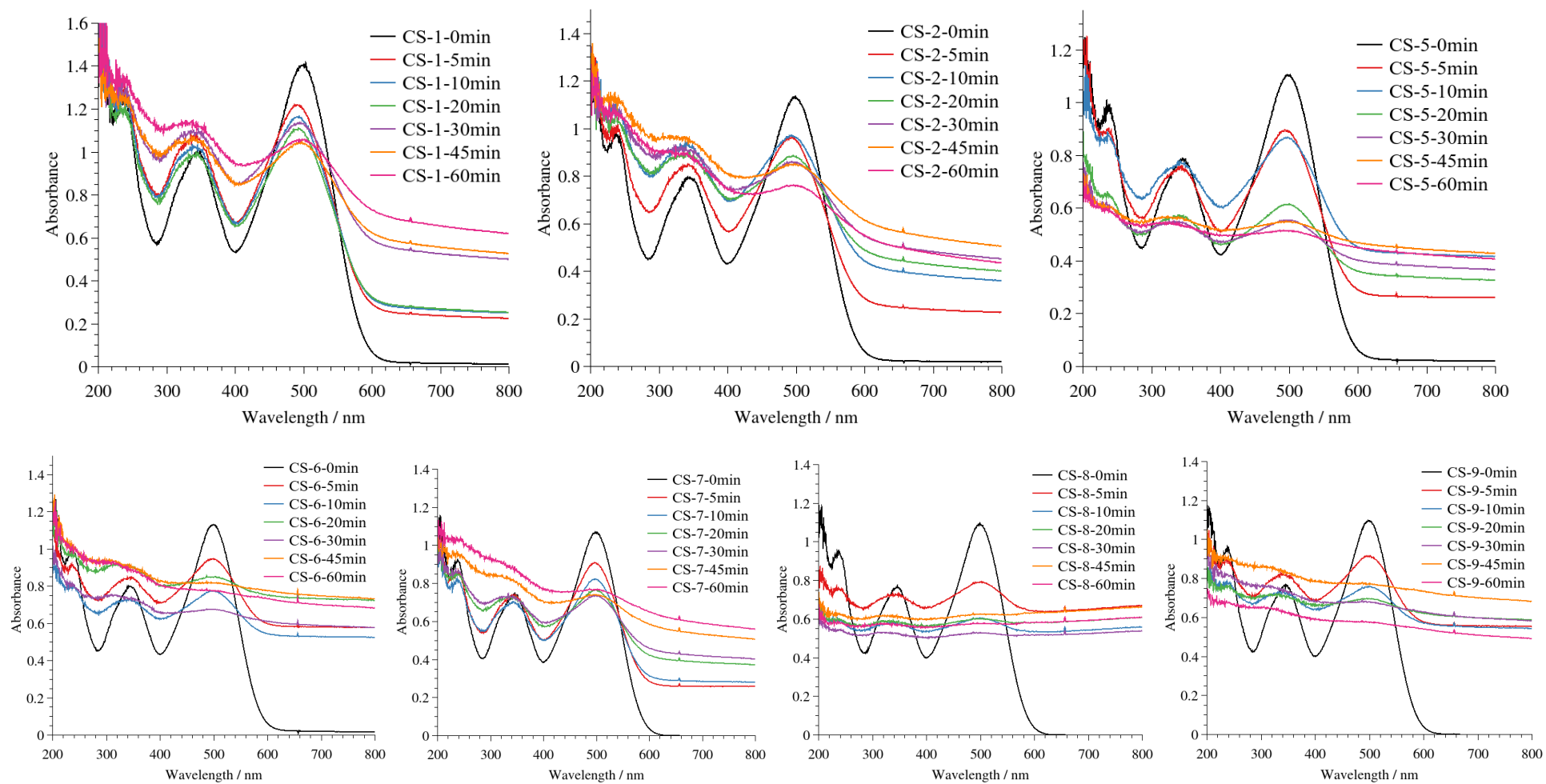
Appendix C

Absorption spectra of Congo red solutions with CS photocatalysts material under the influence of UV radiation



Appendix D

Absorption spectra of Congo red solutions with CS photocatalysts material under dark conditions



Appendix E

Absorption spectra of Methylene blue with CS photocatalysts material under UV irradiation

